Traceurs de gaz et de poussières du milieu interstellaire local

Quentin Remy

► To cite this version:

Quentin Remy. Traceurs de gaz et de poussières du milieu interstellaire local. Astrophysique [astro-ph]. Université Sorbonne Paris Cité, 2016. Français. NNT : 2016USPCC193 . tel-01745844

HAL Id: tel-01745844
https://theses.hal.science/tel-01745844

Submitted on 28 Mar 2018

Thèse de doctorat

de l'Université Sorbonne Paris Cité

Préparée à l'Université Paris Diderot

Ecole doctorale STEP'UP – ED N°560

CEA Saclay / Laboratoire SAp-AIM

Traceurs de gaz et de poussières du milieu interstellaire local

Par Quentin Remy

Thèse de doctorat de Physique de l'Univers

Dirigée par Isabelle Grenier

Présentée et soutenue publiquement à Saclay le 6 décembre 2016

Président du jury : Le Bourlot, Jacques / Professeur / Université Paris Diderot
Rapporteur : Boulanger, François / Directeur de recherche / Université Paris Sud
Rapporteur : Jean, Pierre / Professeur / Université Toulouse III
Examinateur : Joncas, Gilles / Professeur / Université Laval, Canada
Examinatrice : Lallement, Rosine / Directrice de recherche / Observatoire de Paris
Directrice de thèse : Grenier, Isabelle / Professeur / Université Paris Diderot

Résumé

Cette thèse présente les résultats d'une étude du milieu interstellaire local basée sur les mesures de rougissement dû aux poussières (excès de couleur $E(\mathrm{B-V})$), de l'émission thermique des poussières à 353 GHz (épaisseur optique des grains τ_{353}), du rayonnement diffus γ produit par l'interaction des rayons cosmiques avec le gaz, de l'émission free-free du gaz ionisé et des raies d'émissions des atomes Hɪ et des molécules CO. Ces traceurs permettent de sonder la quantité totale de gaz ainsi que celle dans les différentes phases du milieu interstellaire. L'objectif de cette étude est de tester la capacité de ces traceurs à estimer les quantités de gaz, de chercher des effets d'environnement et de comparer les tendances observées aux prédictions des modèles théoriques.

Nous avons étudié plus particulièrement la région de l'anticentre Galactique. L'information sur la vitesse du gaz apportée par les raies d'émission Hɪ et CO a été utilisée pour séparer dans l'espace position-vitesse six complexes de nuages locaux et pour les séparer de l'arrière plan Galactique. Ces complexes incluent les nuages bien connus de Taurus-Auriga, California, et Perseus.

La forme du spectre d'émissivité de rayons γ mesuré dans chaque nuage est compatible avec le spectre de rayons cosmiques local moyen ce qui témoigne de la fiabilité de l'émission γ à tracer le gaz total. Les cartes de densité de colonne de gaz déduites de l'émission de rayons γ d'origine interstellaire ont été utilisées pour mesurer les rapports $\tau_{353}/N_{\mathrm{H}}$ et $E(\mathrm{B-V})/N_{\mathrm{H}}$ dans les différents nuages. Ces rapports permettent de suivre les propriétés d'émission et d'extinction des poussières. Les variations observées de ces rapports apportent des contraintes sur la capacité des traceurs de poussières à estimer la quantité totale de gaz dans les différentes phases. On trouve que l'opacité, $\tau_{353}/N_{\mathrm{H}}$, mesurée augmente avec la densité de colonne de gaz jusqu'à un facteur 4 dans les régions moléculaires comparé au milieu diffus. Les variations du rapport $E(\mathrm{B-V})/N_{\mathrm{H}}$ sont moins marquées mais on note des fluctuations très locales à l'intérieur des régions moléculaires. Ces changements dans les propriétés d'émission et d'extinction des poussières sont liés à des évolutions structurelles et chimiques des grains prédites par les modèles.

Le facteur X_{CO}, permettant de convertir l'intensité des raies CO en densité de colonne de H_2, est mesuré indépendamment dans chaque nuage grâce aux traceurs de poussières et au rayonnement γ. Les valeurs de X_{CO} déduites de l'épaisseur optique, τ_{353}, sont systématiquement plus grandes que celles déduites du rougissement $E(\mathrm{B-V})$ ou de l'émission de rayons γ, et ce d'autant plus à mesure que l'opacité des grains $\tau_{353}/N_{\mathrm{H}}$ augmente. La mesure de X_{CO} peut donc être biaisée par l'évolution des propriétés d'émission des grains.

Nos mesures indiquent que le rapport X_{CO} moyen d'un nuage diminue pour des nuages plus compacts et brillants en CO. Cette tendance s'accorde avec la diminution du facteur X_{CO} prédite par les modèles depuis les enveloppes diffuses des nuages, plus exposées à la photo-dissociation, jusqu'aux cœurs moléculaires denses, mieux écrantés. Les valeurs de $X_{\mathrm{CO}} \lesssim 10^{20}$ cm^{-2} K^{-1} km^{-1} s mesurées pour les nuages locaux (dans cette thèse et par les précédentes analyses γ) sont nettement plus faibles que celles obtenues par les simulations du milieu interstellaire visant à reproduire des extinctions A_{V} et des densités volumiques de gaz équivalentes à celles sondées dans ces nuages. Ces différences confirment que les simulations prédisent généralement une émission CO trop peu lumineuse à faible densité de colonne.

Les émissions des raies Hɪ et CO ne tracent pas le gaz du sombre (DNM : Dark Neutral Medium) composé de Hɪ dense (optiquement épais) et de H_2 diffus à l'interface atomique-moléculaire des nuages.. L'information supplémentaire apportée conjointement par les traceurs de poussières et l'émission de rayons γ permet d'estimer les densités de colonne de gaz dans le DNM. Le DNM représente environ 20 % de la masse totale des nuages étudiés. On note une augmentation de la masse de DMN dans les enveloppes des nuages proportionnelle à la racine carrée de la masse de gaz moléculaire tracée par l'émission CO. Cette relation devra être testée dans d'autres types de nuages (grande masse, métalicité différente, fort cisaillement,...) pour à estimer la quantité de gaz du DNM dans les parties distantes de la Galaxie et les galaxies externes. Afin d'étudier les seuils de transition Hɪ-H_2 et H_2-CO nous avons mesuré l'évolution des fractions de gaz dans les différentes phases et l'évolution de la fraction de gaz sombre dans la phase moléculaire. Ces mesures peuvent servir à tester les modèles de formation et de photo-dissociation des molécules H_2 et CO.

Mots clefs : Rayons gamma, Rayons cosmiques, Galaxie, Bras Local, Milieu interstellaire, Poussières interstellaires, Nuages moléculaires.

Abstract

This thesis presents the results of a study of the local interstellar medium based on measurements of the stellar reddening due to dust (E(B−V) color excess), thermal emission of dust at 353 GHz (optical thickness of grains τ_{353}), diffuse γ-ray emission produced by the interaction of cosmic rays with gas, the free-free emission of ionized gas and the emission lines of HI atoms and CO molecules. These tracers probe the total quantity of gas as well as that in the different phases of the interstellar medium. The objective of this study is to test the reliability of these tracers to estimate gas quantities, to look for environmental effects and to compare observed trends with predictions of theoretical models.

In particular, we have studied the region of the Galactic anticenter. Information on the velocity of the gas provided by the HI and CO emission lines was used to separate six local cloud complexes in the position-velocity space and to separate them from the Galactic background. These complexes include the well-known clouds of Taurus-Auriga, California, and Perseus.

The shape of the γ-ray emissivity spectrum measured in each cloud is compatible with the average local cosmic ray spectrum which indicates the reliability of the γ-ray emission to trace the total gas. The gas column density maps deduced from γ-ray interstellar emission were used to measure the ratios $\tau_{353}/N_{\mathrm{H}}$ and $E(\mathrm{B-V})/N_{\mathrm{H}}$ in different clouds. These ratios allow to follow the emission and extinction properties of the dust. The variations observed in these ratios provide constraints on the capability of dust tracers to estimate the total amount of gas in the different phases. We have found that opacity, $\tau_{353}/N_{\mathrm{H}}$, measured increases with gas column density up to a factor of 4 in molecular regions compared to diffuse medium. The variations of the $E(\mathrm{B-V})/N_{\mathrm{H}}$ ratio are less marked but there are very local fluctuations within the molecular regions. These changes in the dust emission and extinction properties are related to structural and chemical changes of the grains predicted by the models.

The X_{CO} factor, which converts the intensity of CO lines into column density of H_2, is measured independently in each cloud by dust tracer and γ-ray emission. The values of X_{CO} deduced from the optical thickness, τ_{353}, are systematically greater than those deduced from the stellar reddening E(B−V) or the γ-ray emission, and especially as the opacity of the grains $\tau_{353}/N_{\mathrm{H}}$ increases. The measurement of X_{CO} can therefore be biased by the evolution of the emission properties of the grains.

Our measurements indicate that the average X_{CO} ratio of a cloud decreases in more compact and bright CO clouds. This trend is consistent with model predictions which expect a X_{CO} factor decrease from diffuse cloud envelopes, which are more exposed to photo-dissociation, to dense, better screened molecular cores. The values of $X_{\mathrm{CO}} \lesssim 10^{20}$ cm^{-2} K^{-1} km^{-1} s measured for local clouds (in this thesis and by previous γ-ray analyses) are significantly lower than those obtained by simulations of the interstellar medium for equivalent extinctions A_{V} and volume densities of gas to those surveyed in these clouds. These differences confirm that the simulations generally predict under-luminous CO emission at low column density.

The emissions of the HI and CO lines do not trace the Dark Neutral Medium (DNM) gas, which is composed of dense HI (optically thick) and diffuse H_2 at the atomic-molecular interface of clouds. The additionnal information provided by the dust tracers and the γ-ray emission allow to estimate the column gas densities in the DNM. The DNM represents about 20% of the total mass of the clouds studied. There is an increase in the mass of DMN in the envelopes of the clouds proportional to the square root of the mass of molecular gas traced by the CO emission. This relation will have to be tested in other types of clouds (large mass, different metalicity, high shear,...) to estimate the quantity of gas of the DNM in the distant parts of the Galaxy and the external galaxies. In order to study the transition thresholds HI-H_2 and H_2-CO we measured the evolution of the gas fractions in the different phases and the evolution of the dark gas fraction in the molecular phase. These measurements can be used to test the formation and photo-dissociation models of the H_2 and CO molecules.

Key words : Gamma rays, Cosmic Rays, Galaxy, Local arm, Interstellar Medium, Interstellar dust, Molecular clouds.

Sommaire

Introduction aux traceurs de gaz et de poussières du milieu interstellaire

Identification et séparation des nuages en positions, vitesses et distances

Analyse multi-longueurs d'onde et contraintes des propriétés du milieu interstellaire

Relations entre l'émission et l'extinction des poussières et les propriétés des grains

Transitions de phases dans le gaz interstellaire

Avant-propos

“Ce qui est admirable, ce n’est pas que le champ des étoiles soit si vaste, c’est que l’homme l’ait mesuré. ”
— Anatole France, *Le jardin d’Epicure* (1894)

À l’époque où cette citation fut écrite la plupart des observations étaient réalisées par photométrie, c’est à dire en mesurant la puissance du rayonnement des objets dans le visible comme le font nos yeux. Les physiciens venaient à peine de découvrir le rayonnement infrarouge et les raies d’absorption atomiques dans le spectre de la lumière. Les astronomes, exploitant ces découvertes, commençaient à utiliser des spectrographes, comme Angelo Secchi pour classifier les étoiles, ou Williams Huggins qui pu ainsi déceler la présence de gaz dans l’explosion de novae et dans les nébuleuses. Quel serait donc l’émerveillement de l’écrivain de constater qu’aujourd’hui, un siècle plus tard, nous observons bien plus que des étoiles mais toute une gamme d’objets à toutes les échelles de l’univers, et ce sur l’ensemble du spectre électromagnétique (la lumière au delà du visible, voir figure 1). Les objets qui nous intéressent ici sont les atomes, les molécules, et les grains de poussière du milieu interstellaire, ils n’ont rien de très exotiques mais sont la base de la matière baryonique composant les galaxies (et celle qui nous compose). On ne trouve pas de meilleur objet que le gaz interstellaire pour être observé sur une aussi grande gamme de fréquence du spectre électromagnétique (voir figure 2). Mais que ce gaz ne soit pas ”exotique” et largement observé ne signifie pas pour autant que les processus physiques ayant lieu dans le milieu interstellaire soient parfaitement compris. Chaque nouvelles observations, de plus en plus précises, nous font avancer des tendances globales aux propriétés locales en apportant de nouvelles questions, qui nous aident à apprécier la subtile complexité du milieu interstellaire.

L’objectif de cette étude est d’utiliser l’information combinée de plusieurs traceurs de gaz et de poussières pour contraindre les propriétés du milieu interstellaire dans les nuages de gaz locaux, c’est à dire à moins de 500 parsec du Soleil, soit à peu près un vingtième de la distance nous séparant du centre de la Galaxie. La première partie introduit les différents traceurs utilisés et les fréquences du spectre électromagnétique auxquels ils sont associés. La seconde partie présente comment l’émission du gaz est décomposée pour être associée à des nuages indépendants et comment ces nuages sont séparés en position, vitesse, et distance. La troisième partie introduit, au travers d’un premier article, le principe de notre analyse multi-longueurs d’onde couplant émissions du gaz, des poussières, et de rayons γ. Cet article présente également des résultats sur la détection du gaz sombre neutre, l’émission du gaz ionisé, le facteur de conversion X_{CO} (reliant l’émission de la molécule CO à la quantité d’hydrogène moléculaire), et les propriétés d’émission des poussières. La quatrième partie présente les résultats du troisième article faisant le lien entre les variations d’émission et extinction des poussières observées et les propriétés structurelles des grains données par les modèles théoriques. La cinquième partie associée au second article se concentre sur les quantités de gaz dans les différentes phases du milieu interstellaire et en particulier sur le gaz sombre neutre à la transition de la phase atomique à moléculaire. La sixième partie rappelle les principaux résultats, et propose sur la base de ces résultats une série de pistes pour de futures études du milieu interstellaire.

Concernant les liens hypertextes : les violets renvoient à des éléments l’intérieur du document, les oranges pointent vers la bibliographie pour les articles indisponibles sur l’ADS, et les bleus renvoient à des pages internet notamment pour accéder directement aux articles sur l’ADS.

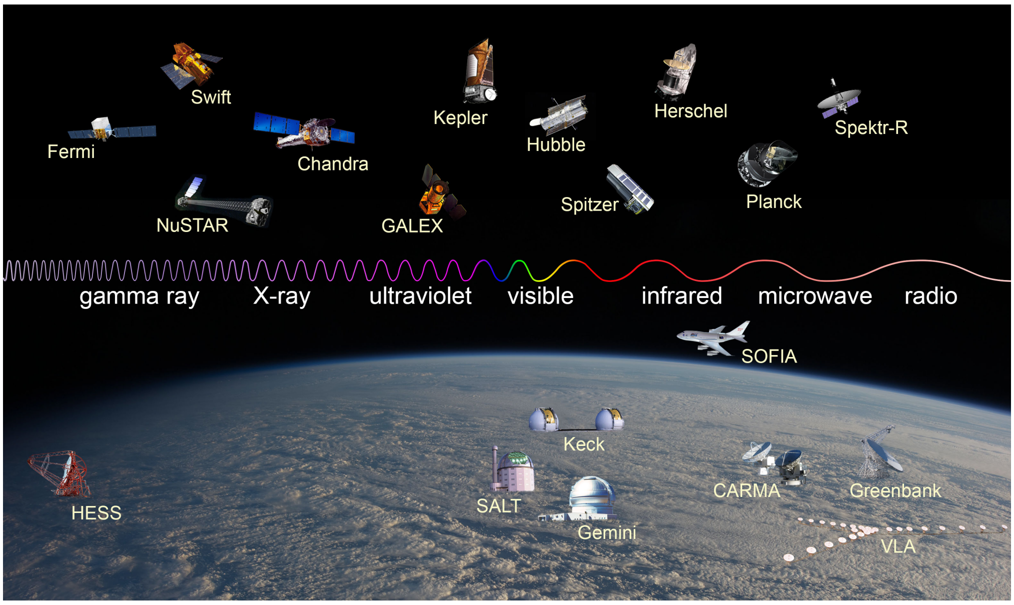

FIGURE 1 – Un aperçu des télescopes au sol et en orbite en fonction de la longueur d'onde du spectre électromagnétique observée (crédit : NASA).

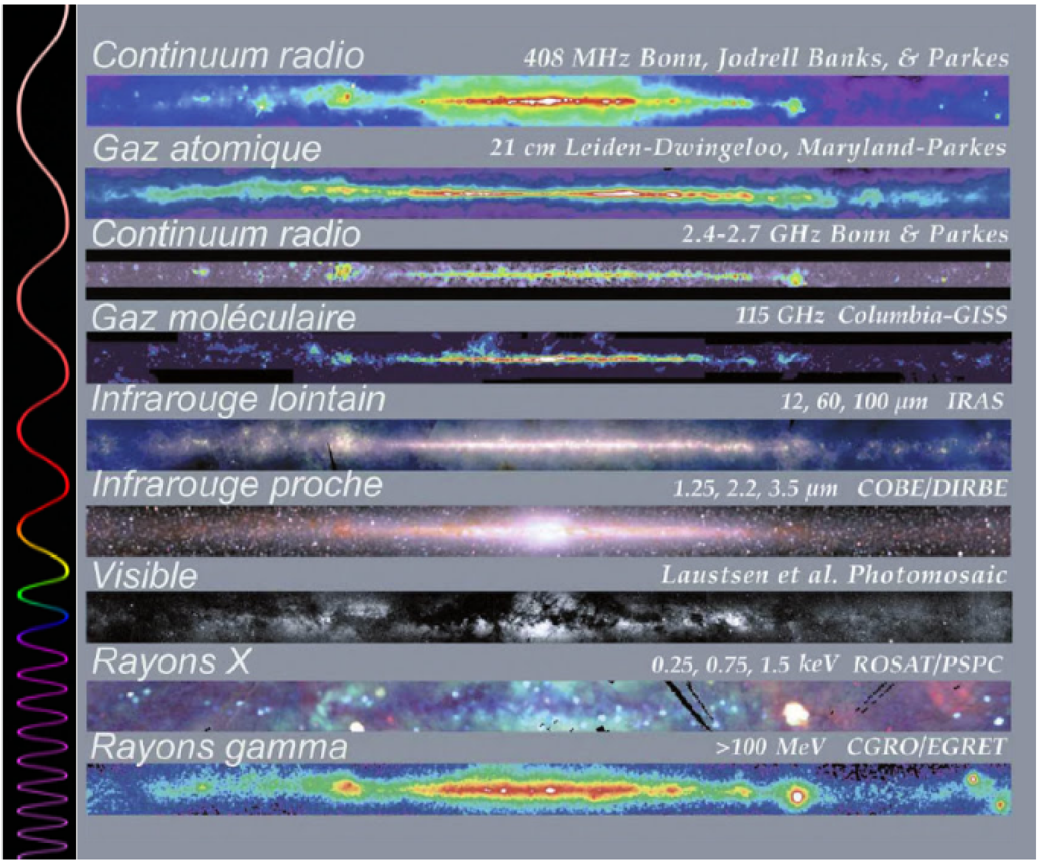

FIGURE 2 – Observations de notre Galaxie à différentes longueurs d'ondes (décroissantes de haut en bas de la figure). Chaque image correspond à une bande allant de ±5° en latitude autour au plan Galactique (axe vertical) et de $-180°$ à $+180°$ en longitude (de droite à gauche) (crédit : Digel, NASA)

Première partie

Introduction aux traceurs de gaz et de poussières du milieu interstellaire

1 Traceurs des phases du gaz neutre

1.1 Raie à 21 cm de l'hydrogène atomique

Le gaz atomique essentiellement composé d'hydrogène neutre, HI, est tracé par son émission radio à 21 cm. Cette émission correspond à une transition hyperfine d'un état de spin parallèle à anti-parallèle (propriété quantique de l'électron et du proton qui compose l'atome). Elle a été prédite par van de Hulst (1945) [1] puis observée quelques années plus tard par Ewen & Purcell (1951) et en parallèle par Muller & Oort (1951). Le décalage en fréquence de la raie par l'effet Doppler permet de connaitre l'écart de vitesse projetée sur la ligne de visée. Après la découverte de la raie confirmée, cette information en vitesse a rapidement été utilisée pour contraindre la structure des bras spiraux et la courbe de rotation de notre Galaxie (Oort & Muller 1952; van de Hulst et al. 1954). L'émission de la raie 21 cm est devenue une des observables les plus utilisées en astrophysique pour l'étude de notre Galaxie et des galaxies externes. De plus elle présente un intérêt très particulier en cosmologie pour tracer le gaz dans la période des âges sombres, entre la recombinaison et la réionisation, pour laquelle aucun autre rayonnement n'est mesurable.

Pour en revenir à la cartographie de notre Galaxie par l'émission à 21 cm, les relevés modernes couvrent l'ensemble du ciel avec une résolution spatiale allant de 0.6 à 0.067 degré et une résolution en vitesse allant 1.44 km s^{-1} à 0.18 km s^{-1}. Le relevé GALFA [2] (Peek et al. 2011) présentant à la fois la meilleure résolution en vitesse et spatiale ne couvre qu'une portion limitée du ciel. Le relevé LAB [3] (Kalberla et al. 2005) possédant la moins bonne résolution spatiale et une résolution en vitesse de 1.25 km s^{-1} couvre l'ensemble du ciel. La combinaison des relevés EBHIS [4] (Winkel et al. 2016) et GASS [5] (Kalberla et al. 2010; Kalberla & Haud 2015), couvrant respectivement les hémisphères nord et sud, permet d'obtenir un couverture complète du ciel avec une résolution spatiale environ 3 fois plus fine que celle du LAB. Les propriétés de ces relevés sont données en détail dans la Table 1 de l'article de Winkel et al. (2016). En plus des mesures en émission, la raie 21 cm est également observée en absorption dans le spectre continu de sources radio distantes (*ex.* : Heiles & Troland 2003a; Roy et al. 2013b).

Les relevés HI donnent la température de brillance de l'émission en fonction de la longitude, latitude et de la vitesse du gaz. La quantité de gaz totale le long d'une ligne de visée est mesurée par la densité de colonne exprimée en cm^{-2}. Les équations du transfert radiatif nous donnent des relations permettant de faire le lien entre la densité de colonne N_{H} le long d'une ligne de visée, l'épaisseur optique de la raie τ_ν, la température de spin T_S (température d'excitation de la transition), et la température de brillance T_b :

$$N_{\mathrm{H}} = 1.83 \times 10^{18}\, T_S \int \tau_\nu \, dv \tag{1}$$

$$T_b - T_{\mathrm{BG}} = (T_S - T_{\mathrm{BG}})\,(1 - e^{-\tau_\nu}) \tag{2}$$

---

[1] l'article original en néerlandais est traduit en anglais dans le livre *Classics in Radio Astronomy* (Sullivan 1982)

[2] GALFA : Galactic Arecibo L-band Feed Array

[3] LAB : Leiden/Argentine/Bonn

[4] EBHIS : Effelsberg-Bonn HI Survey

[5] GASS : Galactic All Sky Survey

avec $T_{\rm BG}$ la température de fond, si elle est négligeable on a :

$$T_b = T_S\,(1 - e^{-\tau_\nu}) \tag{3}$$

Cette relation nous permet de remplacer τ_ν dans l'équation 1 et donc d'exprimer la densité de colonne en fonction de la température de brillance :

$$N_{\rm H} = 1.83 \times 10^{18}\ {\rm cm^{-2}}\ \ {\rm T_S} \int \ln\left(\frac{\rm T_S}{\rm T_S - T_b}\right) {\rm dv} \tag{4}$$

Si la raie est optiquement mince alors $T_S >> T_b$ et τ_ν est faible. Un développement limité au premier ordre en τ_ν dans l'équation 3 nous donne $T_b = T_S \tau_\nu$ en utilisant cette relation dans l'équation 1 on a :

$$N_{\rm H} = 1.83 \times 10^{18}\ {\rm cm^{-2}} \int {\rm T_b\ dv} \tag{5}$$

La densité de colonne ne peut être déduite directement de la température de brillance que dans le cas où la raie est optiquement mince, sinon il faut une contrainte indépendante pour estimer la température de spin (généralement une mesure de la raie en absorption). L'analyse des nuages de l'anticentre Galactique présentée dans l'article I ajuste une température de spin moyenne sur l'ensemble de la région pour contraindre cette inconnue. Les valeurs de températures de spin varient en fonction des phases dans lequel se trouve le gaz atomique neutre. Le gaz chaud et plus diffus (WNM : Warm Neutral Medium) possède des températures de spin allant de 4000 à 9000 K, le gaz froid et plus dense, des températures de spin allant de 40 à 200 K. Entre les deux le gaz est dans une phase thermodynamiquement instable avec des températures variant de 200 à 5000 K (voir introduction de l'article II et, Liszt 2001; Heiles & Troland 2003b; Dickey et al. 2003, 2009; Roy et al. 2013b; Kim et al. 2014; Murray et al. 2015).

1.2 Raie à 2.6 mm de la molécule de monoxyde de carbone

Le gaz moléculaire, essentiellement composé de dihydrogène H_2, est tracé indirectement par l'émission de la molécule de monoxyde de carbone, CO. Dans le milieu interstellaire, les molécules CO gagnent de l'énergie rotationnelle par collision avec d'autres molécules. Les transitions rotationnelles permettant la désexcitation des molécules vont s'accompagner d'émission de photons micro-ondes. En particulier c'est l'émission à 2.6 mm (115 GHz) de la transition ramenant la molécule dans son état fondamental (J :1 → 0) qui va nous intéresser pour tracer le gaz moléculaire.

L'émission à 115 GHz du CO a été détectée pour la première fois par Wilson et al. (1970) en observant la nébuleuse d'Orion. Un historique détaillé des différents relevés CO depuis les années 70 est disponible dans la revue de Heyer & Dame (2015) (voir figure 1 pour un historique des télescopes ayant réalisé les observations et figure 2 pour l'évolution de la couverture en longitude galactique). Aujourd'hui les relevés CO ont sondé la majeure partie de la Galaxie à l'exception de hautes latitudes au dessus du plan dans l'hémisphère sud. Les deux principaux relevés composites actuels compilent les observations du télescope de 1.2-m du Harvard-Smithsonian Center for Astrophysics (Cfa; Dame et al. 2001; Dame & Thaddeus 2004) et du télescope de 4-m de l'université de Nagoya (NANTEN; Mizuno & Fukui 2004). Une partie du signal observé par le satellite *Planck* dans ses bandes à 100, 217 et 353 GHz provient de l'émission à 115, 230 and 345 GHz des transitions rotationnelles des molécules CO (J :1 → 0, J :2 → 1, J :3 → 2). Cette information a été utilisée pour cartographier l'intensité de l'émission CO sur tout le ciel (Planck Collaboration 2014b) mais contrairement aux mesures des radio-télescopes, les mesures de *Planck* n'apportent pas d'information sur la vitesse du gaz.

Comme pour les relevés HI, les relevés CO des radio-télescopes donnent la température de brillance de l'émission en fonction de la longitude, latitude et de la vitesse du gaz. La quantité de gaz moléculaire tracée par l'émission CO est proportionnelle à l'intensité CO intégrée le long d'un ligne de visée s'exprimant en K km s^{-1} :

$$W_{\rm CO} = \int T_b\, dv \tag{6}$$

elle peut être reliée à la densité de colonne d'hydrogène moléculaire par le facteur de conversion CO–H_2 (Lebrun et al. 1983), exprimé en cm^{-2} K^{-1} km^{-1} s :

$$X_{\rm CO} = \frac{N_{\rm H_2}}{W_{\rm CO}} \tag{7}$$

Le fait que l'émission CO à 115 GHz permette de tracer la quantité de gaz moléculaire alors que la raie est optiquement épaisse peut s'expliquer si on considère que les complexes moléculaires sont constitués d'un ensemble de petits nuages suffisamment dispersés dans l'espace position-vitesse pour ne pas pas s'écranter les uns les autres, ainsi $W_{\rm CO}$ l'intensité intégrée dans une direction est proportionnelle au nombre de petits nuages sur la ligne de visée, et donc à la masse totale de gaz moléculaire dans ces nuages (Morris & Rickard 1982). Bien que la mesure de $W_{\rm CO}$ trace raisonnablement bien la densité de colonne de gaz moléculaire $N_{\rm H_2}$, il faut garder à l'esprit que le ciel vu par l'émission CO est principalement une image de la chimie du CO (Liszt et al. 2010). Dans les enveloppes diffuses des nuages, les molécules de H_2 plus nombreuses et donc mieux auto-écrantées contre la photo-dissociation, vont survivre plus facilement que les molécules CO (van Dishoeck & Black 1988; Wolfire et al. 2010). Ce gaz moléculaire diffus non tracé par l'émission CO forme, avec le HI optiquement épais, le milieu sombre neutre (DNM : Dark Neutral Medium). Le gaz du DNM est détecté indirectement à l'aide de l'information apportée par les traceurs de la quantité totale de gaz présentés dans la partie suivante (Grenier et al. 2005; Planck Collaboration 2011; Paradis et al. 2012).

L'article I présente des mesures du facteur $X_{\rm CO}$ dans les nuages locaux de l'anticentre Galactique et compare ces résultats à ceux obtenus par des études antérieures à différentes échelles (locale ou galactique) et avec différents traceurs de la densité de colonne de gaz (rayons γ et poussières). Les limites de la capacité de l'émission CO à 115 GHz à tracer l'ensemble du gaz moléculaire sont discutées dans les articles I et II, en faisant le lien avec des travaux théoriques sur la formation et la photo-dissociation du CO.

2 Traceurs de la quantité totale de gaz

2.1 Émission thermique des poussières interstellaires

La désignation de poussières fait référence aux plus grosses molécules du milieu interstellaire (par exemple les hydrocarbures aromatiques polycycliques) et aux grains composés de carbonates et de silicates d'une taille allant de 1 à 100 nanomètres. Nous allons nous intéresser plus particulièrement aux grains les plus gros qui sont responsables de l'extinction du rayonnement stellaire dans le visible (sur laquelle nous reviendrons ensuite). Les gros grains de poussières chauffés par le champ de rayonnement interstellaire vont atteindre un équilibre thermique en émettant un rayonnement de corps noir modifié. L'émission thermique des gros gains constitue l'essentiel de l'émission des poussières aux longueurs d'onde allant du millimétrique à l'infrarouge lointain. A ces longueurs d'onde le milieu interstellaire est essentiellement optiquement mince, ce qui permet de sonder aussi bien les nuages locaux que des régions éloignées de la Galaxie. Pour plus de détails sur les modèles de grains et l'émission associée aux différentes populations de grains on peut se référer par exemple aux articles de Draine (2003); Draine & Li (2007); Jones et al. (2013).

Les mesures infrarouges à 100 et 240 μm (3000 et 1250 GHz) de DIRBE[6] et IRAS[7] ont été utilisées pour cartographier l'émission de poussière sur l'ensemble du ciel avec une résolution allant de 0.7 degrés (DIRBE) à 6.1 arc-minutes (IRAS) (Schlegel et al. 1998). Plus récemment les mesures à 850, 550 et 530 μm (353, 545, 857 GHz) du satellite Planck combinées aux données d'IRAS à 100 μm ont été utilisées pour produire une carte de l'épaisseur optique des poussières à une résolution de 5 arc-minutes sur l'ensemble du ciel (Planck Collaboration 2014a).

Pour un fréquence ν donnée, l'intensité de l'émission thermique des grains s'exprime comme le produit de la fonction de Planck B_ν , et de l'épaisseur optique des poussières τ_ν (à cette fréquence) :

$$I_\nu = \tau_\nu B_\nu(T) = \tau_{\nu_0} B_\nu(T_{\rm d})(\nu/\nu_0)^\beta \tag{8}$$

avec β l'index spectral des grains et τ_{ν_0} l'épaisseur optique à la fréquence de référence ν_0. L'épaisseur optique des poussières est proportionnelle à l'émissivité des grains et à la densité colonne de poussière. Si l'émissivité des grains est constante et si les poussières sont uniformément mélangées avec le gaz alors l'épaisseur optique trace linéairement la densité de colonne de gaz totale. Cela peut être vérifié en mesurant l'opacité des poussières, définie comme :

$$\sigma_\nu = \frac{\tau_\nu}{N_{\rm H}} \tag{9}$$

Ces dernières années de nombreux travaux ont signalé une augmentation de l'opacité depuis les environnements diffus jusqu'aux nuages moléculaires denses, attribuée à l'évolution des propriétés des grains (Stepnik et al. 2003; Martin et al. 2012; Roy et al. 2013a; Ysard et al. 2013; Flagey et al. 2009; Planck Collaboration 2014a,c; Planck and Fermi Collaborations 2015). Nous avons mesuré l'opacité dans différentes phases du milieu interstellaire dans

---

[6] DIRBE : Diffuse Infrared Background Experiment

[7] IRAS : Infra-Red Astronomical Satellite

la région de l'anticentre Galactique et les variations d'opacité observées sont discutées dans les articles I et III, en faisant le lien avec des travaux théoriques sur l'évolution structurelle et chimique des grains.

2.2 Extinction du rayonnement stellaire causé par les poussières

Au début du XX$^{\text{ème}}$ siècle la présence de nébuleuses de gaz dans la Galaxie était établie mais la présence de poussières capables d'absorber le rayonnement stellaire faisait débat. Trumpler (1930) apporta une preuve de l'extinction interstellaire en étudiant les distances de 100 amas ouverts dans la galaxie. En comparant les distances déduites d'une part de la mesure du diamètre angulaire des amas, et d'autre part de la mesure de leur luminosité apparente, il montra que les distances photométriques des amas les plus éloignés étaient systématiquement plus grandes que les distances déduites du diamètre angulaire, signe que la magnitude apparente était surestimée à cause d'une extinction croissante avec la distance.

Formellement pour une longueur d'onde λ, la magnitude apparente m_λ s'exprime en fonction de la magnitude absolue M_λ, de la distance d, et de l'extinction A_λ comme :

$$m_\lambda = M_\lambda + 5\log\left(\frac{\mathrm{d}}{10\ \mathrm{pc}}\right) + \mathrm{A}_\lambda \tag{10}$$

Étant donné qu'a priori on ne connait pas la distance et la magnitude apparente de la source, on mesure généralement l'excès de couleur causé par l'extinction $E(\mathrm{B}-\mathrm{V}) = \mathrm{A}_\mathrm{B} - \mathrm{A}_\mathrm{V}$, où B et V sont des bandes photométriques de référence du visible correspondant respectivement à des longueurs d'ondes de 430 et 550 nm. En choisissant une troisième longueur d'onde de référence on peut définir l'extinction sélective normalisée qui est utilisée pour contraindre la courbe d'extinction en fonction de la longueur d'onde

$$\frac{E(\lambda-\mathrm{V})}{E(\mathrm{B}-\mathrm{V})} = R_\mathrm{V}\left(\frac{A_\lambda}{A_\mathrm{V}} - 1\right) \tag{11}$$

avec,

$$R_\mathrm{V} = \frac{A_V}{E(\mathrm{B}-\mathrm{V})} \tag{12}$$

Le facteur d'extinction R_V est communément estimé à 3.1 dans le milieu diffus (Cardelli et al. 1989). Il peut atteindre des valeurs de 5 dans les nuages moléculaires les plus denses (Foster et al. 2013), probablement en raison de l'évolution structurelle des grains de poussières (Köhler et al. 2015).

On peut également définir l'intensité du rayonnement stellaire reçu comme $I(\lambda) = I_0(\lambda)\ e^{-\tau_\lambda^{\mathrm{ext}}}$, avec $\tau_\lambda^{\mathrm{ext}}$ l'épaisseur optique d'extinction qui est proportionnelle à A_λ.

$$A_\lambda = -2.5\log\left(\frac{\mathrm{I}(\lambda)}{\mathrm{I}_0(\lambda)}\right) = 1.086\ \tau_\lambda^{\mathrm{ext}} \tag{13}$$

En explicitant $\tau_\lambda^{\mathrm{ext}}$ en fonction des propriétés des grains et du rapport gaz-sur-poussière on peut relier l'extinction à la densité de colonne de gaz (voir article III).

2.3 Émission de rayons γ

Les débuts de l'astronomie γ remontent aux années 50 (Morrison 1958) mais elle s'est réellement développée au cours des années 60-70 avec le lancement des premiers satellites scientifiques dédiés à l'observation des rayons γ. La première cartographie de l'émission diffuse de rayons γ provenant du plan de la Galaxie a été effectuée par le satellite COS-B sensible à des photons d'énergies allant de 20 MeV à 5 GeV (Bignami et al. 1975; Cesarsky et al. 1977; Lebrun & Paul 1978).

Ces successeurs EGRET[8] (Kanbach et al. 1989) puis *Fermi* LAT[9] (Atwood et al. 2009) ont étendu ces observations et en ont amélioré la précision, à la fois spatialement et en énergie. Le LAT à bord du satellite *Fermi*, en activité depuis 2008 et toujours opérationnel, peut mesurer des photons à des énergies allant de 20 MeV à 2 TeV avec une résolution allant d'environ 3°à 100 MeV jusqu'à 0.04°à 100 GeV.

Pour notre étude des nuages de gaz locaux nous avons exploité les données γ dans une plage en énergie allant de 400 MeV à 100 GeV. Les observations à plus haute énergie ont des comptages de photons γ trop faibles pour une étude précise du milieu interstellaire et celles à plus basse énergie présentent une résolution trop faible pour pouvoir séparer convenablement les différentes composantes de l'émission issues des différentes phases de gaz.

---

[8] EGRET : Energetic Gamma Ray Experiment Telescope

[9] LAT : Large Area Telescope

Le rayonnement γ diffus émis dans la Galaxie est produit par l'interaction des rayons cosmiques (électrons et nucléons se propageant dans la Galaxie à des vitesses relativistes) avec d'autres particules via les processus suivant :

- le rayonnement de freinage lorsqu'un électron relativiste interagit avec le champ Coulombien d'un noyau ;
- la diffusion Compton Inverse lors de l'interaction d'un électron relativiste avec un photon de fond infrarouge ou micro-onde ;
- les collisions entre des nucléons relativistes et les nucléons du milieu interstellaire. Ces collisions produisent d'autres particules pouvant se désintégrer en émettant des photons. En particulier les mésons π_0 se désintègrent en deux photons (pic d'émission à environ 70 MeV).

Les rayons γ d'origine interstellaire d'énergie supérieure à 100 MeV sont essentiellement produits par l'interaction des nucléons des rayons cosmiques avec le gaz interstellaire. La comparaison de l'émission de rayons γ au dessus de 1 Gev et de l'émission des poussières, présentée dans la figure 3, montre que ces deux traceurs révèlent des structures de gaz similaires.

L'intensité des rayons γ d'origine interstellaire produits par les collisions de nucléons sur une ligne de visée s'exprime comme (Dermer 1986, 2012) :

$$I_\gamma^{\mathrm{ISM}} = \frac{dN_\gamma}{dS\ dt\ d_\Omega\ dE_\gamma} = \int_{los} n_{\mathrm{gas}}(l)\ dl \int_{T_p>E_\gamma}^{\infty} k\ j_p(T_p,l)\,\beta_p\ \frac{d\sigma_{pp\to2\gamma}(T_p,E_\gamma)}{dE_\gamma}\ dT_p \tag{14}$$

avec n_{gas} la densité volumique des nucléons de gaz, T_p l'énergie cinétique des protons incidents, E_γ l'énergie des γ produits, $j_p(T_p,l) = \frac{dN_p}{dS\ dt\ d_\Omega\ dT_p}$ le flux de rayons cosmiques, $\beta_p = v_p/c$ le facteur de vitesse relativiste, $\sigma_{pp\to2\gamma}$ la section efficace pour les collisions $p+p$ produisant deux γ, et k une constante de correction nucléaire pour prendre en compte les collisions p_{CR} + $\mathrm{He_{ISM}}$, et $\mathrm{He_{CR}}$ + $\mathrm{p_{ISM}}$.

L'intensité γ produite dans un nuage (exprimée en photon cm^{-2} s^{-1} sr^{-1} MeV^{-1})) est proportionnelle au taux d'émission de photon γ par nucléon de gaz, $q_{\gamma\,\mathrm{H}}(E)$, et à la densité de colonne de gaz, N_{H}, (Casandjian 2012; Planck and Fermi Collaborations 2015). Le taux d'émission de rayon γ par nucléon de gaz dépend du flux de rayons cosmiques (voir l'intégrale en énergie dans l'équation 14). Le flux de rayons cosmiques dans un nuage peut varier (déplétion ou concentration) lorsqu'ils diffusent sur les perturbations magnétiques de petites échelles (ondes d'Alfven) ou si ils sont piégés par des variations de plus grandes échelles du champ magnétique (miroirs magnétiques). Toute irrégularité dans la propagation des rayons cosmiques à travers un nuage résultant de l'interaction avec un champ magnétique est associée à des variations en énergie qui peuvent être mesurées dans le spectre de l'émissivité de rayons γ (Skilling & Strong 1976; Cesarsky & Volk 1978). On peut mesurer $q_{\gamma\,\mathrm{H}}(E)$ indépendamment dans chaque nuage. Comme illustré dans la figure 4, la forme spectrale donnée par les mesures de $q_{\gamma\,\mathrm{H}}(E)$ est la même dans le bras Local et les nuages proches observés. Cette propriété a été vérifiée dans l'analyse des nuages locaux de l'anticentre Galactique présentée dans l'article I.

Différents nuages n'ont pas nécessairement la même flux de rayons cosmiques, donc la normalisation du spectre de l'émissivité de rayons γ peut varier d'un nuage à un autre. Mais pour tracer la quantité totale de gaz il est important de ne pas détecter de variations spectrales de la phase atomique à la phase moléculaire d'un même nuage. Si les rayons cosmiques pénètrent uniformément à travers un nuage, alors l'intensité γ fournit une mesure de la quantité totale de gaz, indépendamment de l'état chimique et thermodynamique du gaz.

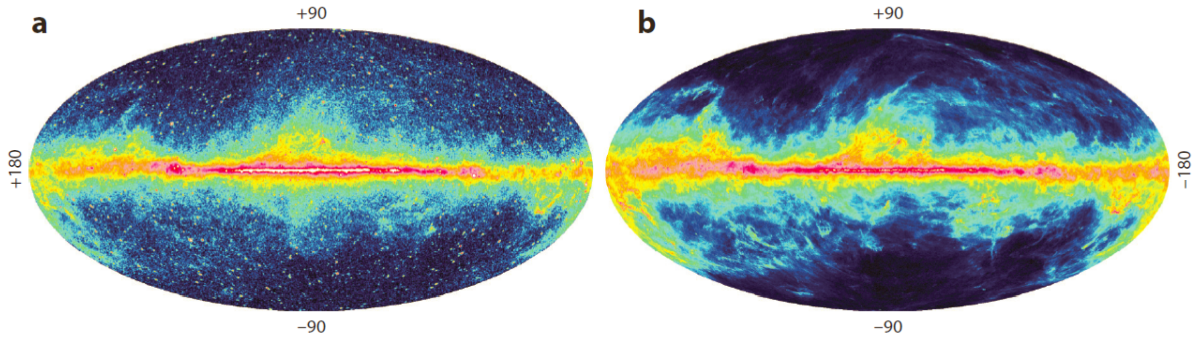

FIGURE 3 – Cartes du ciel en coordonnées Galactiques d'après Grenier et al. (2015) : (a) Intensité des rayons γ enregistrée par *Fermi*-LAT au dessus de 1 GeV en six années d'observations (`http://fermi.gsfc.nasa.gov/ssc/`) et (b) Épaisseur optique des poussières à 353 GHz déterminée à partir des mesures de Planck et IRAS (Planck Collaboration 2014a). Les deux cartes tracent la densité de colonne totale de gaz, pondérée par la densité de rayons cosmiques pour les rayons γ, et par le rapport de masse gaz-poussière et le taux de chauffage du rayonnement stellaire pour la carte de poussières. Ces cartes présentent des similitudes évidentes reflétant la structure du gaz qu'elles tracent. Le carte d'émission γ contient également de nombreuses sources ponctuelles et des composantes diffuses faibles non liées aux gaz.

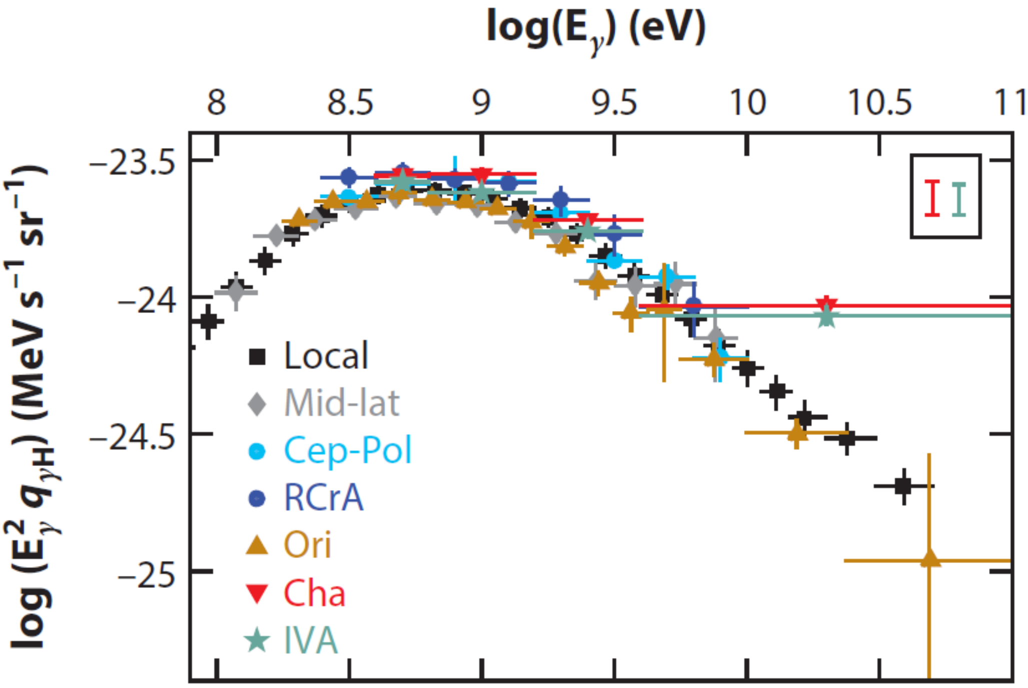

FIGURE 4 – Spectre d'émissivité de rayons γ par atome d'hydrogène interstellaire, $q_{\gamma\,\mathrm{H}}$, mesuré avec *Fermi*-LAT dans le gaz atomique de nuages proches et dans le bras Local (Abdo et al. 2010; Ackermann et al. 2012a,b; Planck and Fermi Collaborations 2015), d'aprèsGrenier et al. (2015). Les erreurs sont statistiques, et l'encadré illustre les incertitudes potentielles données par les corrections de la profondeur optique du HI et l'exposition du Fermi-LAT. Le spectre moyen du milieu interstellaire Local (en noir) est calculé à des latitudes $10° \leqslant |b| \leqslant 70°$ (Casandjian 2012).

Deuxième partie

Identification et séparation des nuages en positions, vitesses et distances

1 Vitesse de rotation du gaz dans la Galaxie et dynamique locale des nuages

Le décalage Doppler des raies d'émission HI et CO nous fournit une information sur la vitesse de rotation du gaz de la Galaxie relativement à la nôtre, et sur la dynamique des nuages locaux. Ces vitesses sont données usuellement dans le référentiel standard local au repos (LSR : "Local Standard-of-Rest frame"). Il est défini comme un référentiel en orbite circulaire autour du centre de la Galaxie, avec un rayon égal à la distance Galacto-centrique du Soleil R_0, et prenant en compte la vitesse propre du Soleil. Le vecteur vitesse solaire en coordonnées Galactiques cartésiennes étant définies comme $(U, V, W)_\odot = (-9, +12, +7)$ km/s (Delhaye 1965). La vitesse de rotation du référentiel LSR autour du centre Galactique, θ_0, est donnée par la courbe de rotation de la Galaxie $\theta(R)$. La figure 5 illustre la dissimilarité des différentes estimations de cette courbe dans la littérature. L'Union Astronomique Internationale (UAI) recommande d'utiliser les valeurs $R_0 = 8.5$ kpc et $\theta_0 = 220$ km s^{-1} (Kerr & Lynden-Bell 1986). Néanmoins les mesures récentes de parallaxes et de mouvements propres de sources masers associées à des étoiles jeunes et massives, suggèrent des valeurs de $R_0 = 8.3$ kpc et $\theta_0 = 240$ km s^{-1} (relevé BESSEL [10], Brunthaler et al. 2011; Reid et al. 2014).

Les vitesses du gaz mesurées dans les bras distants de la Galaxie sont déterminées principalement par la structure et la dynamique galactique. La figure 6 présente un modèle composite de la Voie Lactée en coordonnées Galactiques cartésiennes et sa projection dans l'espace longitude-vitesse LSR. La longueur et l'orientation de la barre centrale est déduite à partir du catalogue de sources infrarouges GLIMPSE [11] (Benjamin et al. 2005). Les bras à 3 kpc formant une ellipse autour de la barre centrale ont été modélisés à partir de la distribution en longitude-vitesse de masers (Green et al. 2011). La structure des bras spiraux est donnée par le modèle de Cordes & Lazio (2002) décrivant sur la distribution des électrons libres contrainte par les mesures de dispersion des signaux radio des pulsars et par un ensemble de données interstellaires. Les extensions des bras au-delà des limites de ce modèle sont ajoutées en y rattachant des bras spiraux logarithmiques (Wainscoat et al. 1992), ajustés en prenant en compte la distribution des masers de Reid et al. (2014). La projection des bras en vitesse utilise un modèle de courbe de rotation universelle (Persic et al. 1996), adapté à la Voie Lactée d'après les mesures de Reid et al. (2014) (courbe noire sur la figure 5). Ce modèle nous permet de replacer dans le contexte de la structure Galactique les vitesses des raies d'émission observées. Les études présentées dans cette thèse portant principalement sur le milieu interstellaire local, la compilation des équations et des paramètres des bras et des courbes de rotation ou encore les relations permettant la transformation de l'espace des positions à celui des vitesses, ne seront pas détaillées. Cela pourrait ultérieurement faire l'objet d'un document annexe "A synthetic view of the Galactic structure in space and velocity" présentant l'influence de différents modèles de bras et courbes de rotation sur la structure en vitesse (et notamment la position des points tangents, *i.e.* les directions en longitude tangentielles aux bras) en comparaison aux vitesses des raies HI et CO mesurées.

La distribution des vitesses du gaz tracé par l'émission de la raie HI en fonction de la longitude galactique est comparée à celle du modèle dans la figure 7. En direction de la Galaxie interne ($-90° < l < 70°$) les vitesses du gaz du bras local sont très proches de zéro mais difficilement séparables des multiples composantes des autres bras,

---

[10] BESSEL : The Bar and Spiral Structure Legacy

[11] GLIMPSE : Galactic Legacy Infrared Mid-Plane Survey Extraordinaire

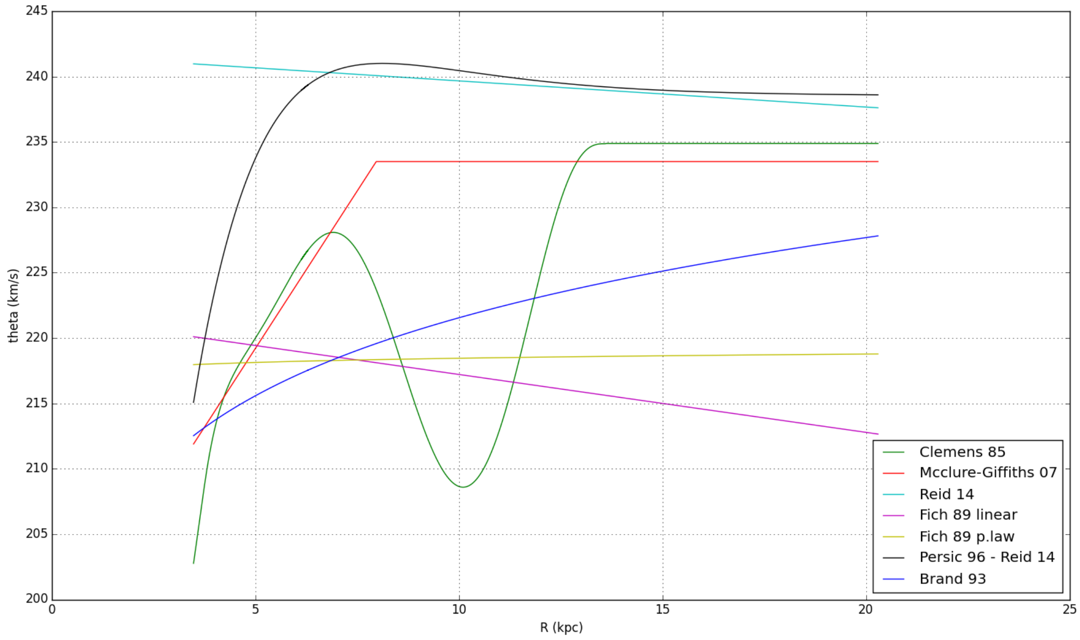

Figure 5 – Courbes de rotation de la Galaxie, $\theta(R)$, mesurées par différentes études : Clemens (1985); McClure-Griffiths & Dickey (2007); Reid et al. (2014); Fich et al. (1989); Persic et al. (1996); Brand & Blitz (1993)

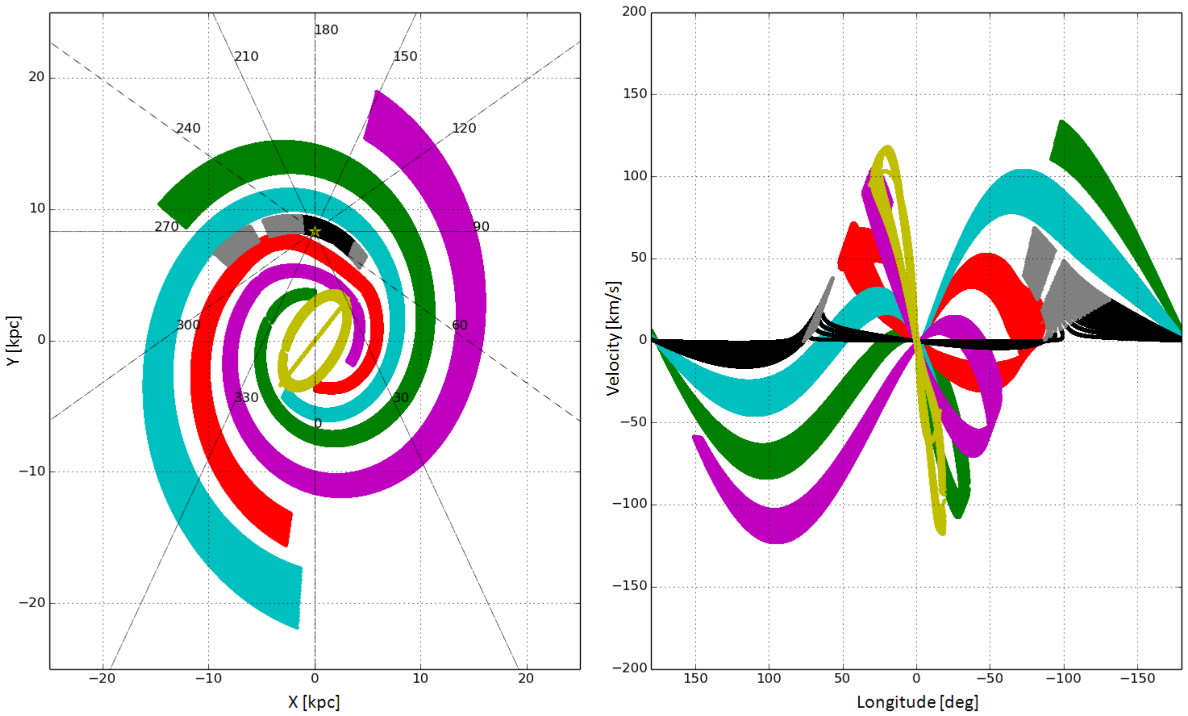

Figure 6 – Modèle de structure Galactique (à gauche) et projection dans l'espace longitude-vitesse LSR (à droite). Dans le plan cartésien à gauche, la longitude Galactique est donnée par les lignes en pointillés larges. Dans les deux figures les couleurs correspondent aux mêmes structures avec : En jaune le barre centrale et les bras à 3 kpc, en cyan le bras de Persée, en rouge le bras de Sagitarius-Carina, en magenta le bras de Scutum-Centaurus, en vert le bras de Norma-Externe, en noir le bras Local, et en gris de possibles extensions de gaz au-delà du bras Local. La largeur des bras représentés augmente exponentiellement avec la distance au centre de la galaxie pour prendre en compte le HI qui s'étend en marge de la structure spirale (Levine et al. 2006; Reid et al. 2014). La projection en vitesse se base sur la courbe de rotation de Persic et al. (1996); Reid et al. (2014) (en noir sur la figure 5).

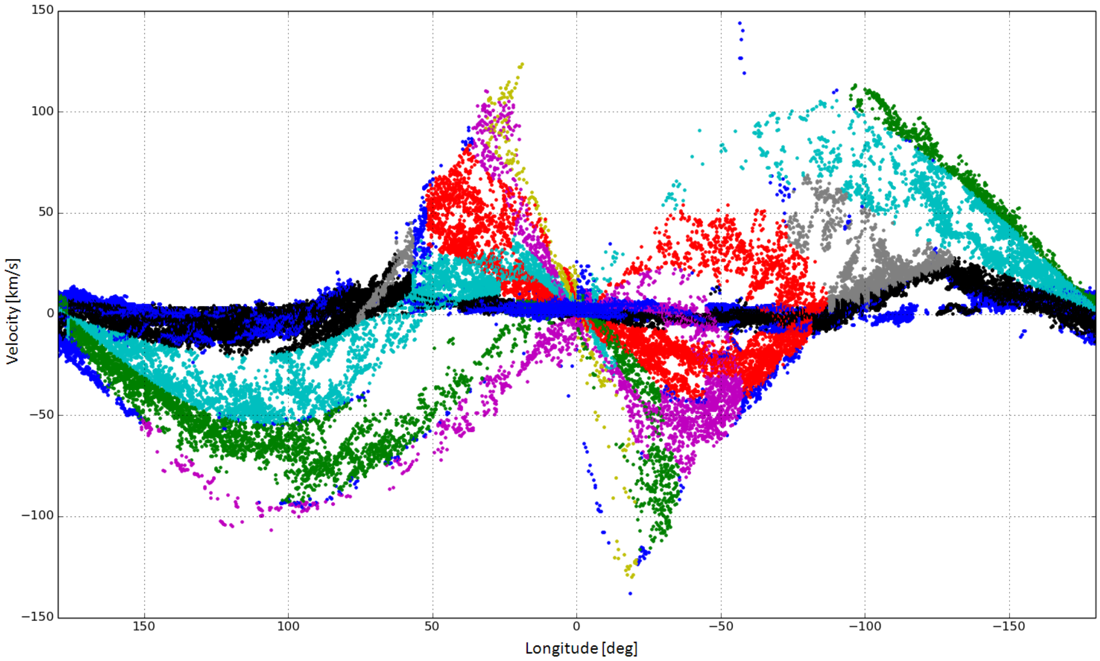

Figure 7 – Vitesse centrale des raies Hi en fonction de la longitude galactique, obtenue par la décomposition des données du relevé LAB (Kalberla et al. 2005) pour chaque direction du ciel, avec la méthode décrite dans la section 2. Les vitesses mesurées ont été associées à celles attendues pour le modèle de structure Galactique en suivant le même code couleur que dans la figure 6. Pour chaque longitude, l'association en vitesse correspond au plus proche voisin dans un intervalle de 1.5 σ autour de la vitesse centrale de la raie, où σ est la largeur du profil de raie Hi ajustée (en moyenne 6 km/s). Les points bleus possèdent des vitesses inconstantes avec le modèle ou sont à $|b| > 10°$, il s'agit pour l'essentiel de nuages locaux avec des vitesses proches de zero.

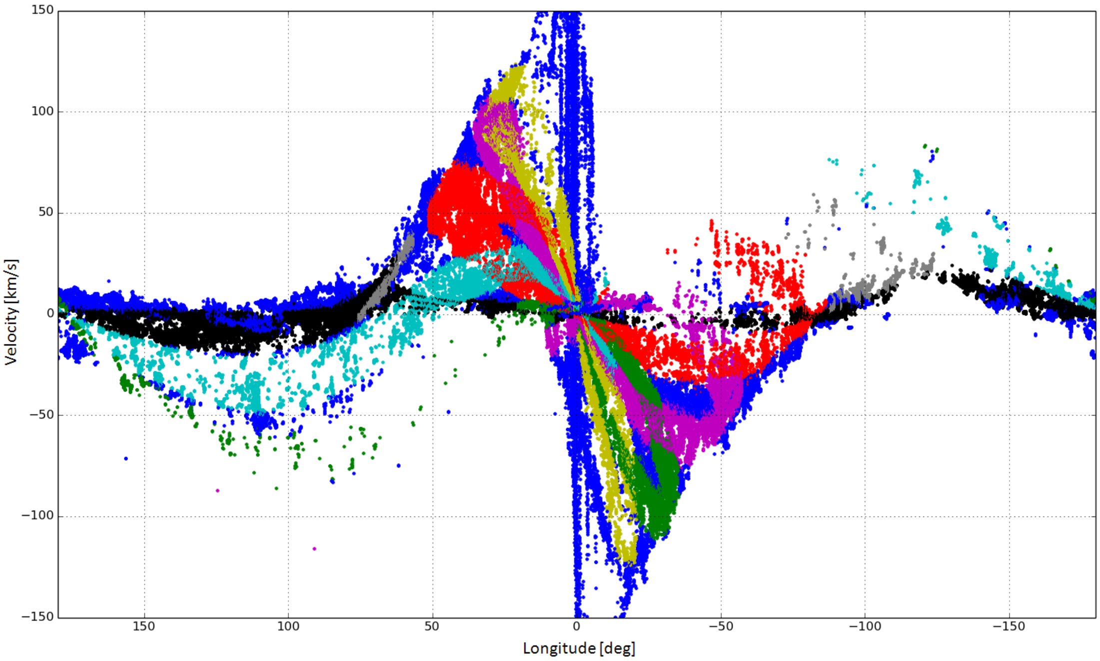

Figure 8 – Vitesse centrale des raies CO en fonction de la longitude galactique, obtenue par la décomposition des données des relevés du Cfa (Dame et al. 2001; Dame & Thaddeus 2004). Le code couleur est le même que pour les figures 6 et 7. Pour chaque longitude, l'association en vitesse correspond au plus proche voisin dans un intervalle de 2 σ autour de la vitesse centrale de la raie, où σ est la largeur du profil de raie CO ajustée (en moyenne 1.6 km/s)

alors que vers l'extérieur de la Galaxie il n'y a pas d'ambiguïté en vitesse pour séparer les différents bras. Dans la Galaxie externe, les vitesses du bras Local prédites par le modèle sont strictement positives dans l'intervalle $70° < l < 180°$ et strictement négatives dans l'intervalle $-180° < l < -90°$, par contre les données Hɪ montrent une dispersion en vitesse au-delà de ces limites pouvant aller jusqu'à environ ± 15 km s^{-1}. Ces variations dépendent essentiellement des vitesses propres aux nuages locaux.

Par exemple dans le voisinage du Soleil les nuages de la ceinture de Gould présentent des vitesses variant quasi-sinusoïdalement entre −8 et 12 km s^{-1} en fonction de la longitude Galactique (Perrot & Grenier 2003). Dans la figure 7, l'arc bleu allant de vitesses positives à $l = 180°$ vers des vitesses proches de zéro à $l = 120°$ et remontant vers des vitesses plus positives à $l = 60°$ est caractéristique de la dynamique de la ceinture de Gould.

La décomposition en vitesse de l'émission Hɪ et CO peut donc nous permettre de séparer les nuages locaux de l'émission de l'arrière-plan Galactique mais aussi séparer les nuages entre eux en identifiant des structures en vitesse particulières.

2 Séparation en vitesse des raies d'émission Hɪ et CO

La décomposition la plus simple de l'émission est réalisée en découpant directement les profils de températures de brillance observés en fonction de la vitesse, $T_b(v)$, à chacun des minima locaux. Cependant les profils peuvent être modélisés comme une somme de Gaussiennes donnant chacune l'étalement en vitesse de l'émission des raies. La coupure directe aux minima d'émission n'attribue donc pas correctement le signal des ailes gaussiennes se superposant quand les raies d'émission sont trop proches, ou les ailes des raies s'étendant au-delà de l'intervalle de vitesses considéré. Une méthode permettant une décomposition plus fiable a été proposée pour l'étude des propriétés du gaz dans la région du Chamaeleon (Planck and Fermi Collaborations 2015) et nous l'avons améliorée par la suite dans le cadre de l'étude des nuages locaux de l'anticentre Galactique (article I).

La séparation en vitesse est réalisée indépendamment dans chaque direction du ciel. L'algorithme inclut deux étapes : la détection des raies et l'ajustement du modèle de décomposition sur les données. Tout d'abord nous cherchons la position des raies d'émission dans les intervalles où la dérivée seconde du profil $T_b(v)$ est négative, ce qui nous permet de détecter les pics d'intensité et les épaules apparaissant dans le profil quand deux raies sont très proches en vitesse. Ensuite nous ajustons simultanément un profil pseudo-Voigh pour chacune des raies détectées. Le choix d'un profil pseudo-Voigh permet de prendre en compte la dispersion en vitesse Lorentzienne du gaz observé dans certaines directions du ciel. Ce profil est défini par

$$\mathrm{pV} = \eta \mathrm{L} + (1 - \eta)\mathrm{G} \tag{15}$$

avec $0 < \eta < 1$ le facteur de forme, L une Lorentzienne, and G une Gaussienne, respectivement définies comme :

$$L = \frac{h}{1 + \left(\frac{v - v_0}{\sigma}\right)^2} \qquad \text{et,} \qquad \mathrm{G} = \mathrm{h} \exp\left(\frac{\mathrm{v} - \mathrm{v}_0}{\sigma}\right)^2 \tag{16}$$

avec h la hauteur , σ la largeur, et v_0 la vitesse centrale de la raie.

Afin de prendre en compte l'incertitude sur la détection de la position de la raie, la vitesse centrale est autorisée à varier autour la position initiale de quelques intervalles dv, correspondant à la résolution en vitesse du relevé. Donc pour chaque raie détectée les paramètre ajustés sont η, h, σ, and v_0. Le meilleur ajustement du modèle sur les données est déterminé par une minimisation du χ^2. Les résidus entre les données et le modèle sont redistribués dans chaque intervalle dv au prorata de l'intensité des composantes séparées. La figure 9 donne un exemple de détection des raies d'émission Hɪ et de la décomposition obtenue après l'ajustement des profils pseudo-Voigh.

Cette décomposition a été appliquée avec une résolution spatiale d'un huitième de degré aux données Hɪ du relevé GASS (Kalberla & Haud 2015) dans la région du Chamaeleon et des relevés GALFA (Peek et al. 2011) et EBHIS (Winkel et al. 2016) dans la région de l'anticentre Galactique, ainsi qu'aux relevés CO du Cfa (Dame et al. 2001; Dame & Thaddeus 2004) pour l'ensemble des directions couvertes. De plus nous avons effectué un ajustement des profils Hɪ du relevé LAB (Kalberla et al. 2005) à plus basse résolution spatiale (demi-degré) sur l'ensemble du ciel afin d'avoir un aperçu de la distribution globale des vitesses dans la Galaxie (voir figure 7) et pour identifier les régions où la dispersion en vitesse Lorentzienne est plus importante ce qui pourrait témoigner d'une dynamique particulière (mais nous n'avons pas étudié ce point plus en détail)

Par ailleurs l'identification et la paramétrisation des pics d'émission dans les courbes de lumière des pulsars est un problème de décomposition similaire mais avec des profils moins réguliers. Ainsi dans le cadre d'une étude sur les pulsars milliseconde (Renault-Tinacci et al. 2016 in prep.), nous avons adapté la méthode en exploitant la flexibilité de profils pseudo-Voigt asymétriques pour autoriser une paramétrisation différente de la partie montante et descendante de l'émission de ces pulsars. La robustesse de l'algorithme pour ajuster un modèle de décomposition sur des données aussi différentes en fait un excellent outil qui pourrait être réutilisé dans d'autres études présentant un problème similaire.

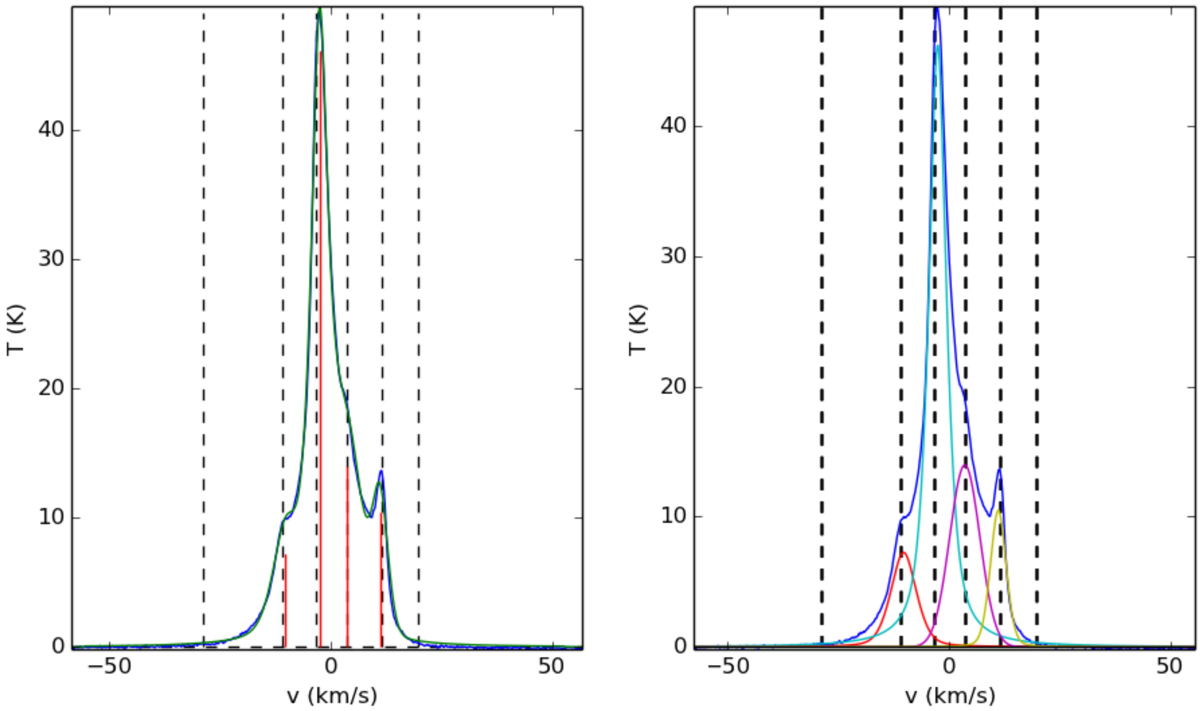

Figure 9 – Exemple de profil d'émission HI donnant la température de brillance en fonction de la vitesse dans le référentiel LSR et décomposition associée. La courbe bleu foncé correspond aux données (dans les deux figures), la courbe verte au modèle total (à gauche), et les autres courbes à la décomposition du modèle (à droite). Les lignes pointillées indiquent les vitesses des raies détectées et les lignes rouges (à gauche) correspondent aux raies ajustées.

2.1 Vitesses du gaz et largeurs des bandes diffuses interstellaires

Les bandes diffuses interstellaires (DIB) sont des bandes d'absorption larges dans les spectres stellaires. Les différents porteurs des DIBs ne sont pas encore clairement identifiés mais ils appartiennent au milieu interstellaire. Le gaz atomique tracé par l'émission HI est le plus répandu dans la Galaxie et nous donne donc une contrainte globale sur la distribution en vitesse du gaz interstellaire. L'amplitude en vitesse de l'émission HI doit donc englober celle des bandes diffuses interstellaires. De ce fait le résultat de la décomposition en vitesse de l'émission HI a été utilisé pour contraindre la largeur maximale autorisée pour identifier des DIBs. Cette contrainte (parmi d'autres) a été utilisée pour établir un catalogue des DIBs à 1.5273 μm dans les spectres des étoiles chaudes de calibration du relevé APOGEE[12] (Elyajouri et al. 2016).

La largeur maximale autorisée pour la détection d'une DIB dans chaque spectre stellaire est contrainte comme suit. Nous avons décomposé en vitesse l'émission HI donné par le relevé LAB dans un bin de $0.5° \times 0.5°$ centré sur la direction de l'étoile cible (par la méthode décrite dans la section précédente). Nos collaboratrices ont ensuite associé une DIB individuelle avec une largeur de $\sigma_0 = 1.4$ Å à chacune des vitesses données par la décomposition HI (voir figure 4 de l'article dans l'annexe A). Ce choix de σ_0 correspondant au pic de la distribution des σ des DIBs à 1.5273 μm ajustées sur l'ensemble du relevé APOGEE par Zasowski et al. (2015). Le produit des DIBs individuelles donne une DIB virtuelle dont la largeur en longueur d'onde (Å) est compatible avec l'amplitude en vitesse (km/s) de l'émission de la raie HI. La largeur de cette DIB virtuelle, notée $\sigma_{\mathrm{H_I\ 21cm}}$, est utilisée pour contraindre la largeur maximale de la DIB à 1.5273 μm et ainsi rejeter les détections incompatibles avec la distribution en vitesse dans la Galaxie.

---

[12] APOGEE : APO Galactic Evolution Experiment

3 Partitionnement des structures de gaz en nuages indépendants

Pour en revenir au milieu interstellaire local, la décomposition de l'émission HI et CO indépendamment sur chaque ligne de visée n'est que la première étape pour identifier l'émission provenant de chaque nuage, il faut ensuite les séparer dans l'espace position-vitesse c'est-à-dire en longitude, latitude galactique et vitesse LSR (l, b, v).

La séparation de structures en 3D est un problème commun en astrophysique traité par des algorithmes de partitionnement de données. Généralement on peut différencier deux types d'approche dans ces algorithmes : soit les points sont connectés à leur plus proche voisin dans l'espace des paramètres choisi et on forme ainsi des structures par association (comme les algorithmes CLUMPFIND, Williams et al. 1994, ou CROPS, Rosolowsky & Leroy 2006), soit les données sont réduites hiérarchiquement en sous-ensembles de plus en plus restreints sur la base d'un critère de dissimilarité (comme l'algorithme SCIMES [13], Colombo et al. 2015). La figure 10 présente une décomposition du complexe d'Orion en plusieurs nuages par différentes méthodes, réalisée par Colombo et al. (2015).

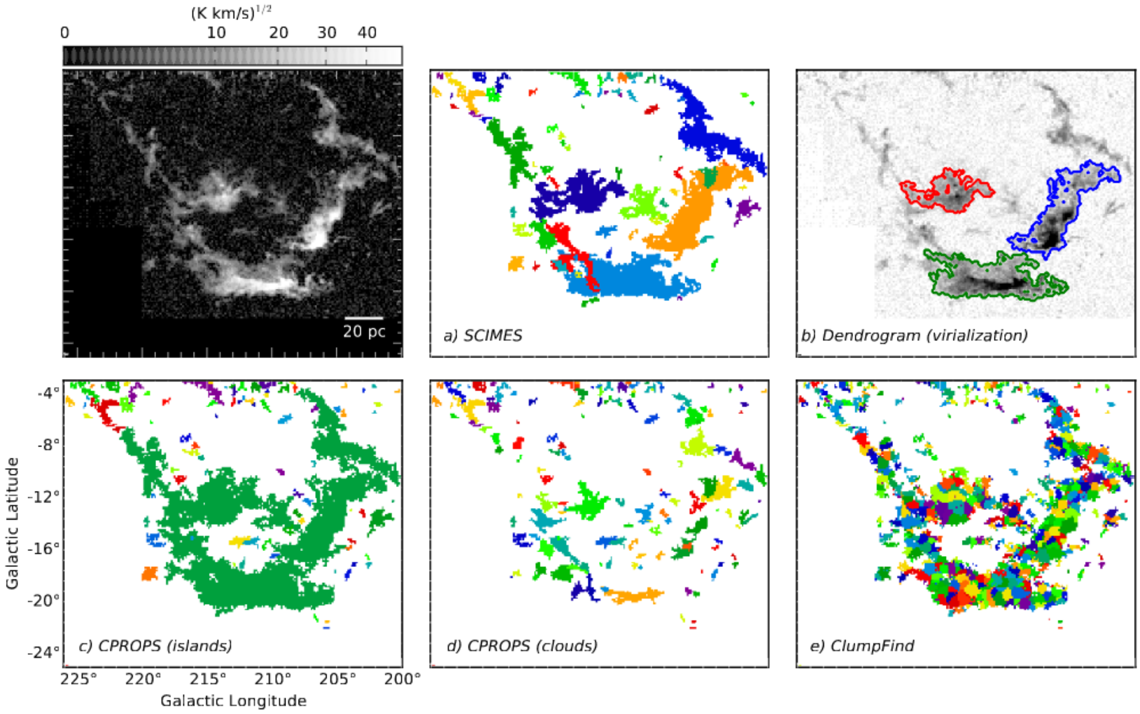

FIGURE 10 – Émission de la raie CO dans le complexe d'Orion et ses décompositions par différents algorithmes, d'après (Colombo et al. 2015). Chaque couleur représente un nuage indépendant issue de la décomposition. *a)* structures identifiées par SCIMES (Colombo et al. 2015). *b)* les plus grandes structures gravitationnellement liées, données par (Rosolowsky et al. 2008). *c)* et *d)* structures identifiées respectivement par les méthodes 'island' et 'physical priors' de CPROPS (Rosolowsky & Leroy 2006). *e)* structures identifiées par CLUMPFIND (Williams et al. 1994).

En travaillant directement sur l'information brute des cubes de données, donnant la température de brillance en fonction des longitudes, latitudes, et vitesses, les résultats peuvent être biaisés par les propriétés du relevé telle que la résolution ou la sensibilité. Des résolutions trop faibles (en position et/ou vitesse) amènent les algorithmes à confondre les différents nuages alors que des résolutions plus hautes peuvent mener à un partitionnement trop fin (des sous-structures étant identifiées comme des nuages isolés). De même pour des milieux très grumeleux ("clumpy") les cœurs compacts peuvent être séparés de leur enveloppe. Ces effets sont particulièrement marqués dans les décompositions du complexe d'Orion par les algorithmes CROPS et CLUMPFIND, illustrées dans la figure 10. L'algorithme SCIMES, basé sur une décomposition hiérarchique, identifie plus convenablement les différentes structures des petites aux grandes échelles. Cependant l'algorithme nécessite des hypothèses supplémentaires (notamment la distance du nuage) pour dériver les paramètres physiques qui servent de critère de sélection.

---

[13] SCIMES : Spectral Clustering for Molecular Emission Segmentation

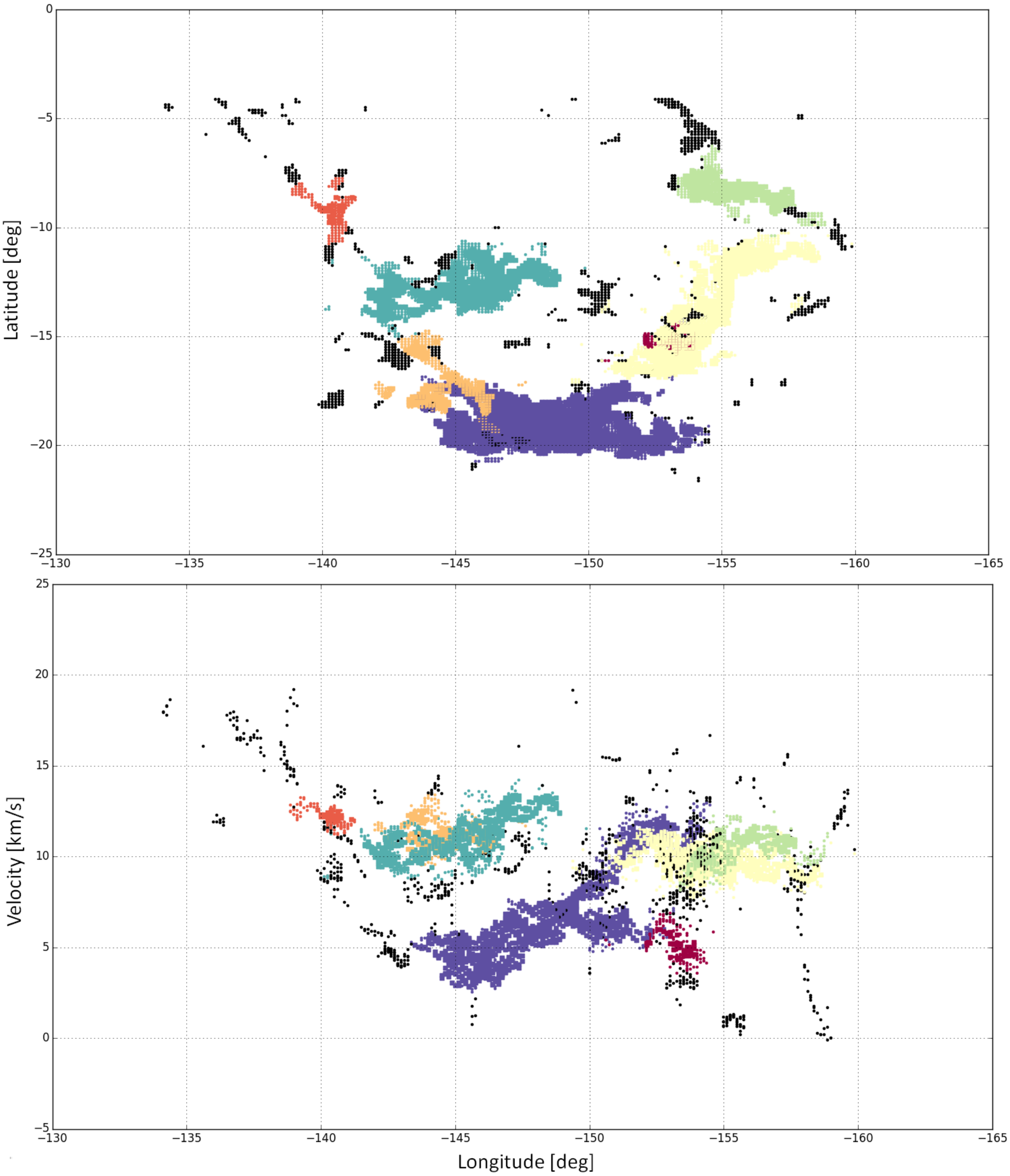

Figure 11 – Décomposition de l'émission CO du complexe d'Orion par DBSCAN, projetée dans les plans longitude-latitude (haut) et longitude-vitesse (bas). Chaque couleur représente un nuage indépendant issue de la décomposition, les points noirs sont des structures d'un niveau de densité inférieur à celui sondé qui peuvent être associées aux structures trouvées en choisissant une autre échelle de distance ϵ.

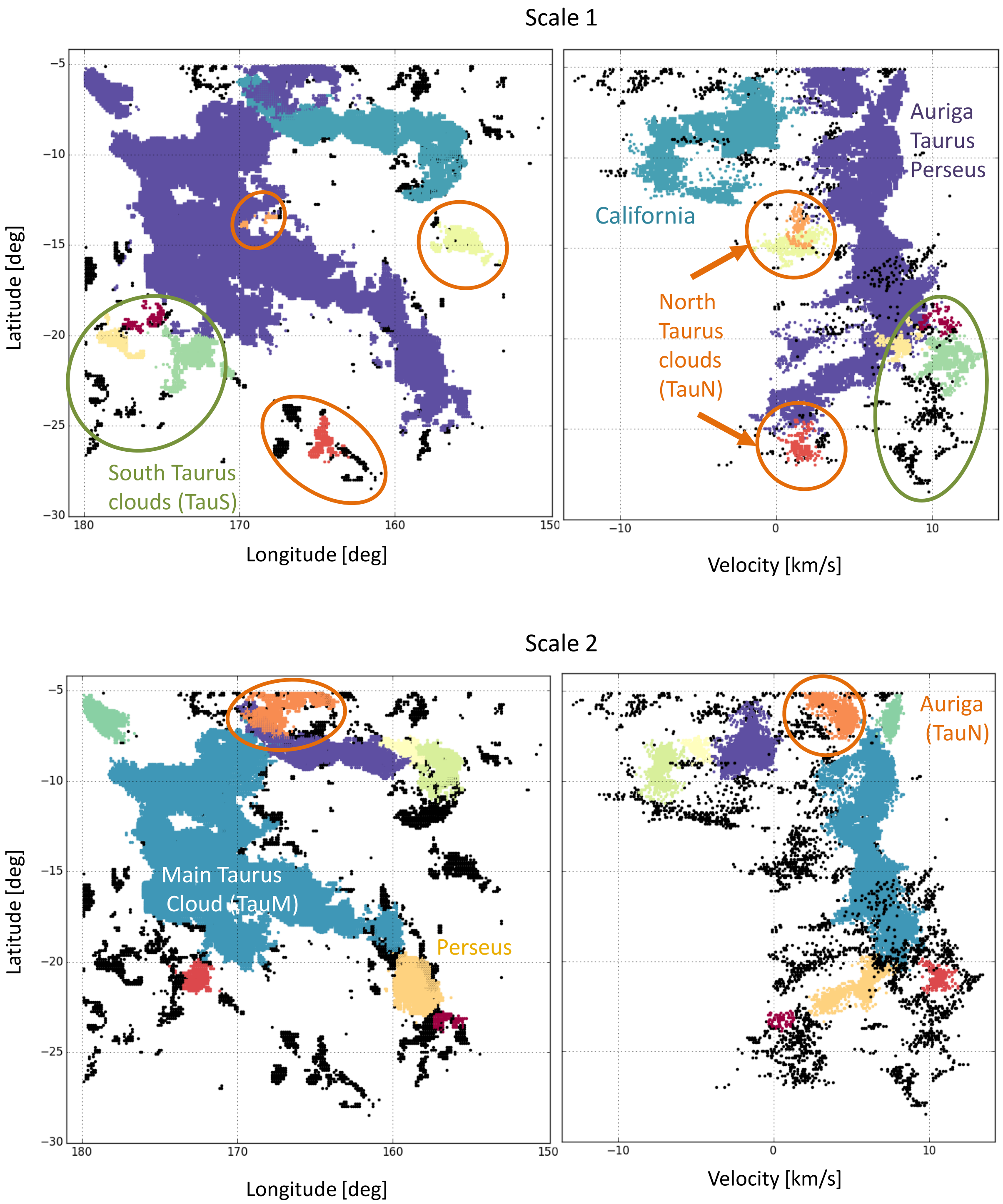

Figure 12 – Décomposition de l'émission CO dans les nuages locaux de l'anticentre Galactique par DBSCAN, projetée dans les plans longitude-latitude (à gauche) et vitesse-latitude (à droite), pour deux échelles de distance ϵ. Chaque couleur représente une structure indépendante issue de la décomposition, entre les deux échelles les couleurs ne correspondent pas. La première échelle (en haut) permet d'isoler le nuage de California du complexe d'Auriga-Taurus-Persée, ainsi que des groupes de petits nuages possédant des vitesses différentes de celles du complexe principal. La seconde échelle (en bas), plus fine, permet de séparer les nuages d'Auriga et Perseus du principal nuage de Taurus (TauM). Pour l'analyse présentée dans l'article I, les petits nuages isolés présentant des vitesses positives proches de 10 km/s ont été associés pour former ensemble nommé Taurus Sud (TauS), et les nuages de vitesses plus proches de zéro ont été associés pour former un ensemble nommé Taurus Nord (TauN), incluant le nuage d'Auriga.

Nous proposons une méthode de séparation des nuages utilisant uniquement l'information des positions (longitude, latitude Galactique) et des vitesses centrales des raies obtenues par la décomposition de l'émission (voir section 2). Aucune hypothèse supplémentaire sur les nuages n'est utilisée, ni même les valeurs de la température de brillance, qui pour un même nuage peuvent varier abruptement de l'enveloppe au cœur pouvant causer un sur-partitionnement des structures. L'information donnée par la température de brillance a été traitée indépendamment et plus finement dans la décomposition de l'émission, elle est donc implicitement contenue dans l'information sur la vitesse centrale des raies.

En discrétisant ainsi l'espace des vitesses on peut appliquer une méthode de partitionnement basée sur la densité locale des données pour identifier les structures dans l'espace position-vitesse. La méthode utilisée se base sur l'algorithme bien connu DBSCAN[14] (Ester et al. 1996). L'algorithme nécessite deux paramètres : N_{min} le nombre minimal de points nécessaires pour former le noyau d'un ensemble et ϵ la distance maximale d'un point à ses voisins pour qu'il puisse être associé à un ensemble. Ainsi les points connectés à au moins N_{min} points en dessous d'une distance ϵ appartiennent au noyau de l'ensemble et les points pouvant être connectés à au moins un point du noyau dans une distance ϵ forment la bordure de l'ensemble.

Le choix des paramètres ϵ et N_{min} dépend de la densité et donc des échelles que l'on veut sonder. N_{min} dépend de la dimension du problème et de la taille de l'échantillon, on choisit de fixer le paramètre N_{min} au nombre de premiers voisins d'un point sur une grille en $N_{\rm dim}$ dimensions soit $N_{min} = \sum_{k=1}^{N_{\rm dim}} 2 \times 3^{k-1}$. Pour fixer le paramètre ϵ, Ester et al. (1996) recommande de calculer la distance moyenne des N_{min} plus proches voisins de chacun des points et de représenter cette KNN-distance ("K-Nearest Neighbor") triée pour identifier les ruptures de pente marquant une transition de structures. La figure présente ce graphique calculé pour le cas du complexe moléculaire d'Orion avec $N_{min} = 26$ (courbe verte). Le choix du paramètre ϵ en fonction de la KNN-distance permet de sonder des structures à différentes échelles. Sonder un ensemble d'échelles pertinentes revient à échantillonner successivement la courbe en cherchant les points de courbure maximale sur des segments de la courbe. Initialement on cherche l'écart maximum entre la courbe et le segment reliant ces extrémités, ceci nous donne un nouveau point permettant de découper la courbe en deux segments. Le processus continue itérativement en découpant la courbe en 2^n segments (procédure illustrée par les courbes rouges sur la figure 13). Les bornes de ces segments servent comme échelles de distances ϵ car ce sont les lieux dans l'espace (l,b,v) où on détecte des écarts dans la distribution des données.

Le point faible de DBSCAN est souvent considéré comme son incapacité à séparer simultanément des structures de densités différentes. De multiples implémentations ont été développées pour améliorer cet aspect au prix d'un temps de calcul généralement plus long. Parmi ces algorithmes on peut citer notamment OPTICS[15] associant le principe de DBSCAN à un classement hiérarchique des structures, visualisé dans un dendrogramme (Ankerst et al. 1999).

Dans la mesure où l'étude du milieu interstellaire nécessite de se concentrer soit sur les grands complexes de gaz, soit sur des nuages isolés, soit sur les sous-structures de ces nuages, notre décomposition discrète par échelle de distance ϵ avec DBSCAN est suffisante pour étudier les différentes structures indépendamment.

La figure 11 présente le résultat de la décomposition par DBSCAN de l'émission CO du complexe d'Orion en nuages de taille intermédiaire. Il est intéressant de constater que cette décomposition aboutit à des structures similaires à celle obtenue par Colombo et al. (2015) avec SCIMES. Par contre notre séparation des structures n'utilise que l'information en position-vitesse des raies et non un critère basé sur d'autres propriétés physiques comme la luminosité, nécessitant d'exploiter l'information de la température de brillance et d'ajouter une hypothèse de distance. Les propriétés dynamiques des nuages tracées par la vitesse centrale des raies semblent donc porter l'essentiel de l'information nécessaire pour séparer les nuages.

Les méthodes de partitionnement se prêtent bien à la décomposition de l'émission CO mais fonctionnent nettement moins bien sur l'émission HI car les structures sont moins discernables en raison de l'absence de discontinuité spatiale dans l'émission HI. Par contre on observe que les vitesses centrales des raies HI et CO sont bien corrélées et comme les nuages moléculaires sont entourés par le gaz atomique, on peut donc définir des iso-surfaces communes dans l'espace position vitesse englobant l'émission HI et CO. Ainsi pour l'étude des nuages de l'anticentre Galactique nous avons identifié les principaux complexes moléculaires avec la décomposition par DBSCAN de l'émission CO (voir figure 12) puis nous avons cherché les minima de densité entourant les complexes isolés en longitude, latitude, et vitesse centrale des raies HI. Les lignes de minimum de densité en longitude-vitesse et latitude-vitesse définissent les coupures communes à la décomposition de l'émission HI et CO. Les carte finales de densité de colonne, $N_{\rm HI}$, et d'intensité CO intégrée, $W_{\rm CO}$, pour les différents nuages locaux séparés dans la région de l'anticentre Galactique sont données dans l'article I (figure 1).

---

[14] DBSCAN : Density-Based Spatial Clustering of Applications with Noise

[15] OPTICS : Ordering Points To Identify the Clustering Structure

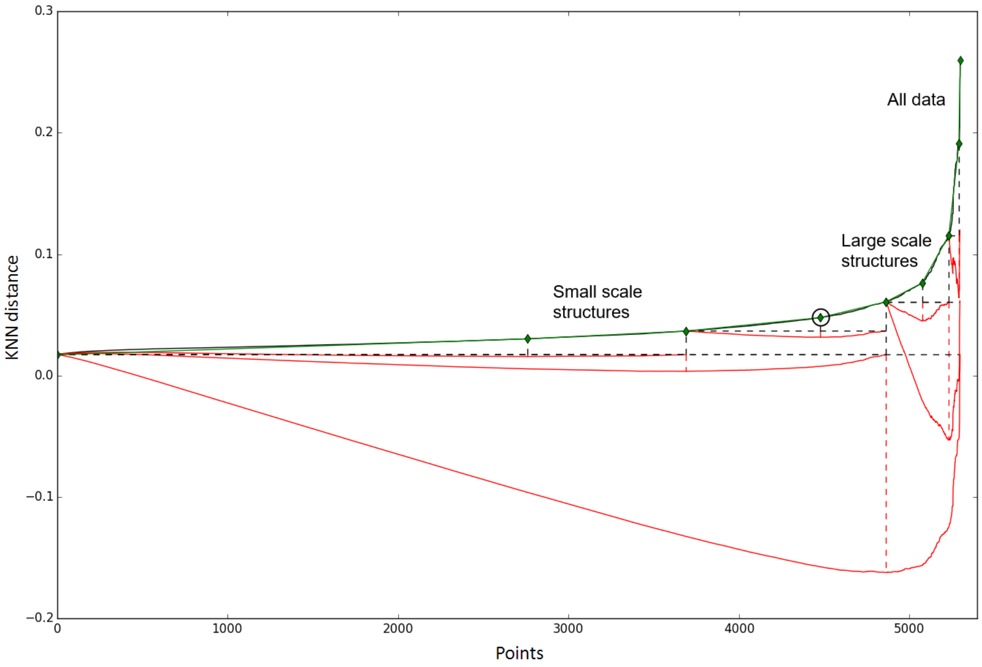

Figure 13 – KNN-distance des points dans l'espace position-vitesse pour le cas du complexe moléculaire d'Orion. La courbe noire correspond aux données, la courbe verte à sa segmentation, les courbes rouges donnent la distance relative entre la courbe et les segments (en pointillés noirs horizontaux). Les pointilles rouges verticaux donnent la distance maximale servant à déterminer la position du prochain point de la segmentation (en vert). Chaque point donne une valeur de ϵ permettant de sonder des structures à différentes échelles. Le point entouré correspond à l'échelle sélectionnée pour la décomposition illustrée dans la figure 11.

4 Contraintes sur les distances du gaz

4.1 Association des structures gaz–poussière

Après avoir identifié les nuages et les avoir séparés en position-vitesse, il reste à leur associer une distance. La méthode la plus courante consiste à exploiter les données stellaires photométriques dans différentes bandes pour contraindre simultanément l'extinction causée par les poussières et les distances, permettant ainsi de reconstituer indirectement la distribution tri-dimensionnelle des poussières (Marshall et al. 2006; Green et al. 2014, 2015). Les poussières étant mélangées avec le gaz, l'identification morphologique des structures de gaz, que nous avons décomposées, aux structures de poussière, données par les méthodes d'extinction 3D, permet d'associer une distance aux différents nuages séparés en vitesse.

Nous avons contribué au développement d'une nouvelle méthode bayésienne utilisant les données photométriques infrarouges de 2MASS[16] et le modèle de population stellaire de Besançon (Robin et al. 2003) pour contraindre l'extinction et les distances dans les nuages locaux (Marshall et al. 2015). Le problème est décrit par quatre paramètres : la distance du nuage, l'extinction du nuage, l'extinction diffuse, et la dispersion de l'extinction. Cette description se limite aux directions où il y a un nuage seul sur la ligne de visée mais pourrait être étendue à plusieurs nuages. L'algorithme utilise une méthode MCMC[17] pour explorer l'espace des paramètres et estimer la distribution de probabilité de chaque paramètre. La méthode est toujours en cours d'amélioration, notamment pour permettre d'exploiter simultanément les données photométriques infrarouges et visibles (ce qui tend à augmenter la précision des cartes d'extinction comme discuté dans la partie 5). Les résultats préliminaires montrent un bon accord avec les distances de référence des nuages moléculaires locaux les plus massifs de l'anticentre Galactique (voir figure 14).

---

[16] 2MASS : Two Micron All Sky Survey
[17] MCMC : Monte Carlo Markov Chain

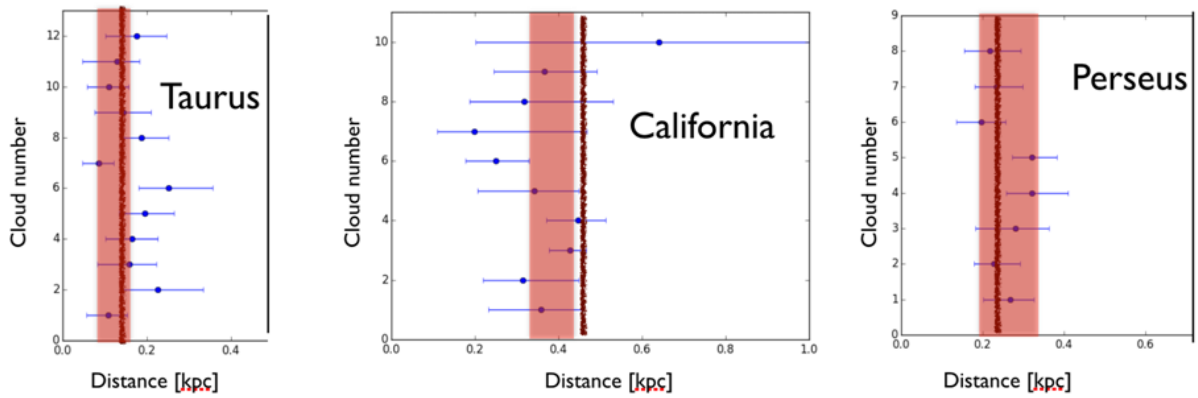

Figure 14 – Distances dans les principaux nuages locaux de l'anticentre Galactique. Les points bleus correspondent aux distances en direction de sous-structures des différents nuages (identifié avec DBSCAN) trouvées avec la nouvelle méthode décrite dans Marshall et al. (2015). Les lignes rouges marquent les valeurs de références trouvées dans la littérature. Les zones rouges correspondent à la plage de distances des sous-structures apparaissant dans le catalogue de Schlafly et al. (2014b).

4.2 Identification des raies interstellaires en émission–absorption

En se basant sur les données spectroscopiques on peut comparer les vitesses du gaz tracé par les raies d'absorption dans les spectres stellaires (par exemple pour les atomes de NaI et KI) et les raies d'émission HI et CO. Si les vitesses des différentes formes de gaz associées à un même nuage sont bien corrélées alors la détection ou non-détection des raies d'absorption en fonction de la distance de l'étoile fournit une contrainte sur la distance du gaz. Des observations spectroscopiques dans la région de Cepheus ont été réalisées et d'autres sont programmées pour tester la corrélation en vitesse entre les raies d'absorption et d'émission, ainsi que leur potentiel à apporter des contraintes sur les distances du gaz en les combinant aux mesures de parallaxes de Gaia. La figure 15 présente un exemple de corrélation des raies en émission et absorption, observé dans trois directions du nuage de Cepheus, avec une détection progressive du gaz en fonction de la distance de l'étoile.

Par ailleurs le détection ou non-détection des bandes diffuses interstellaires (DIB) en fonction de la distance de l'étoile peuvent également apporter une contrainte sur la distance des nuages (même si les porteurs des DIB ne sont pas clairement identifiés, ils appartiennent quand même au gaz ou aux poussières). La figure 16 illustre la corrélation entre le seuil de détection de la DIB à 1.5273 μm dans le catalogue de Elyajouri et al. (2016) et la distance déduite des estimations d'extinction 3D dans les nuages de Taurus et Cetus. Cette possibilité d'exploitation des données de DIB reste encore largement à étudier et à développer.

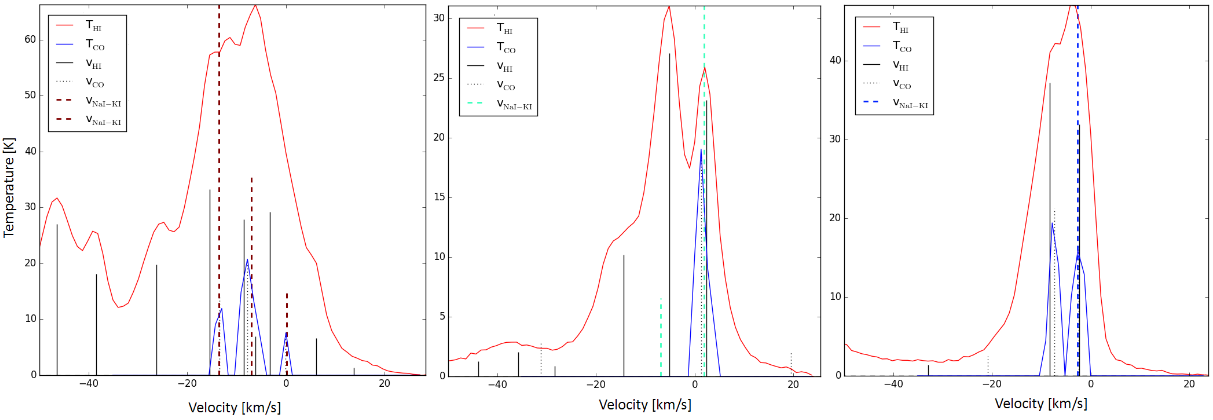

FIGURE 15 – Température de brillance, T_b, de l'émission HI (courbe rouge) et CO (courbe bleue) en fonction de la vitesse dans le référentiel LSR. Aux différents profils $T_b(v)$ sont associés les vitesses centrale des raies d'émission du gaz HI (ligne noire pleine) et CO (ligne noire pointillée) issues de notre décomposition. L'émission CO a été mise à l'échelle du HI pour visualiser la corrélation des différentes composantes. Les vitesse centrales des raies d'absorption interstellaire (pour les atomes de NaI et KI) sont affichées en lignes pointillées colorées. La hauteur de la ligne est proportionnelle à l'intégrale de la raie et la gradation de couleur rouge, vert, bleu est associée à une distance stellaire décroissante. Dans les trois directions sélectionnées on note une bonne corrélation entre les raies d'émission et absorption. L'étoile la plus proche ne détecte que la composante de gaz à des vitesses proche de zero, alors que les étoiles plus lointaines détectent plus de composantes.

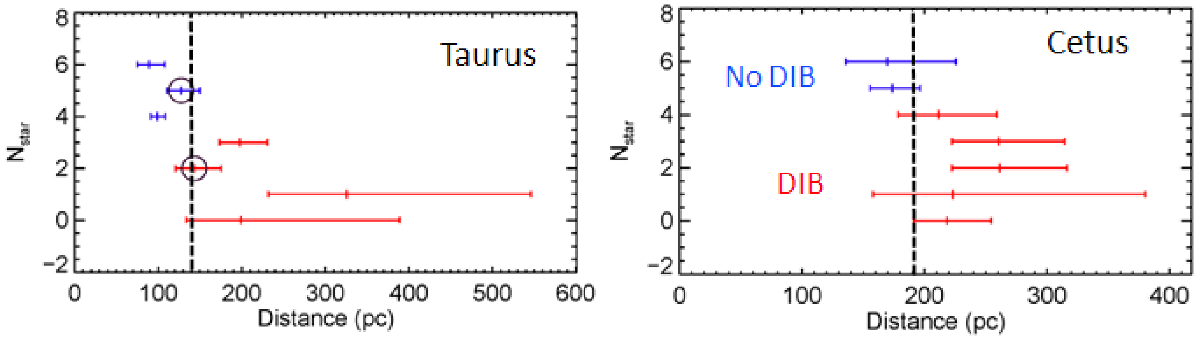

FIGURE 16 – Détection de la bande diffuse interstellaire (DIB) à 1.5273 μm dans les spectres stellaires APOGEE (Elyajouri et al. 2016) en fonction de la distance de l'étoile (catalogue HIPPARCOS[19], de Zeeuw et al. 1999; van Leeuwen 2007). Pour ces deux nuages, le seuil de détection de la DIB correspond bien à la distance moyenne des sous-structures du nuage (ligne pointillée noire) calculée à partir du catalogue de Schlafly et al. (2014b).

---

[19] HIPPARCOS : HIgh Precision PARallax COllecting Satellite

Troisième partie

Analyse multi-longueurs d’onde et contraintes des propriétés du milieu interstellaire

Comme nous l’avons vu dans la première partie, si l’émissivité des grains et le rapport gaz-sur-poussière restent uniformes, alors l’émission de poussières est proportionnelle à la quantité de gaz. Parallèlement, si les rayons cosmiques produisant les rayons γ par interaction avec le gaz interstellaire pénètrent uniformément à travers les nuages, alors le nombre de photons γ émis est proportionnel à la quantité de gaz. Ainsi l’émission des poussières et l’émission de rayons γ, corrélées à la quantité totale de gaz, peuvent être modélisées par une combinaison linéaire des contributions du gaz appartenant aux différents phases du milieu interstellaire. La phase moléculaire, la phase atomique neutre, et la phase ionisée peuvent être respectivement tracées par les émissions CO, HI et free-free. En utilisant les mesures de l’épaisseur optique des poussières et le rayonnement γ conjointement avec ces données, nous pouvons donc, d’une part, vérifier la capacité des différents traceurs à estimer la quantité totale de gaz et, d’autre part, contraindre les propriétés du gaz et des poussières. Le premier article, présenté dans cette partie, traite ces deux aspects en reprenant et en améliorant la méthode d’analyse précédemment appliquée au nuage du Chamaeleon (Planck and Fermi Collaborations 2015).

En particulier cette analyse nous permet de :

- mesurer le spectre en énergie des rayons γ d’origine interstellaire permettant de vérifier l’uniforme pénétration des rayons cosmiques dans les nuages ; suivre l’évolution de l’opacité des poussières (épaisseur optique par atome de gaz) en fonction de la densité de colonne de gaz ;
- cartographier le gaz sombre neutre (DNM) composé de HI opaque et de H_2 diffus, non détecté par les relevés HI et CO (van Dishoeck & Black 1988; Grenier et al. 2005; Wolfire et al. 2010; Planck Collaboration 2011) ;
- estimer les densités de colonne de gaz ionisé ;
- estimer la contribution relative des différentes phases à la quantité totale de gaz ;
- mesurer le facteur de conversion X_{CO} permettant de relier l’émission de la molécule CO à la quantité d’hydrogène moléculaire.

Notre étude se focalise sur la région de l’anticentre Galactique. En appliquant les méthodes de séparation des nuages décrites dans la partie 2, l’émission des raies HI et CO a été décomposée en vitesse et associée à différentes composantes. On obtient 6 complexes de nuages proches, isolés de l’arrière plan Galactique. Nous avons estimé la distance moyenne de ces complexes à partir de celle de sous-structures apparaissant dans le catalogue de Schlafly et al. (2014b). Les complexes nommés, Taurus-Main, Taurus-Sud, Taurus-Nord, Cetus, Perseus et California, ont respectivement pour distance moyenne (en parsecs) : 140±30 pc, 160±10 pc, 190±50 pc, 190±20 pc, 270±20 pc et 410±20 pc.

L’article commence par introduire la méthode utilisée et les différents tests effectués pour la valider, ensuite il discute des propriétés du gaz et des poussières dans les différents nuages. Voici un résumé des principaux points abordés :

Concernant la méthode et sa validation

L’analyse couple la modélisation de l’émission des poussières et des rayons γ. Initialement le gaz tracé par l’épaisseur optique des poussières à 353 GHz, τ_{353}, est modélisé uniquement par la combinaison des composantes HI, CO et free-free. La différence entre le modèle et les données nous fournit une carte de résidus dont nous déduisons la structure de la composante de gaz sombre (DNM). Le gaz tracé par l’émission de rayons γ est ensuite modélisé par la combinaison des composantes HI, CO et free-free ainsi que le gaz sombre déduit du modèle "τ_{353} ". La vraisemblance maximale de l'ajustement du modèle "γ " augmente significativement quand nous ajoutons cette composante, ceci implique qu'elle est clairement détectée dans l'émission de rayons γ (à plus de 80 σ). L'ajustement du modèle "γ " nous fournit également une carte de gaz sombre que nous injectons ensuite dans le modèle "poussière" pour en améliorer la qualité puisque cette phase, présentant des densités de colonne comparables aux autres phases neutres, était absente dans le modèle initial de poussière. Nous ajustons ensuite itérativement les deux modèles jusqu'à atteindre une saturation dans la vraisemblance maximale de l'ajustement du modèle "γ ".

Au final dans les différentes bandes en énergie sélectionnées, les résidus de l'ajustement du modèle d'émission des rayons γ, sont compatibles avec le bruit Poissonnien et ce à toutes les échelles angulaires sauf en directions des pics d'émission CO où le modèle sur-prédit légèrement les données (à moins de 1σ). Il reste à petite échelle des écarts entre la profondeur optique dans les observations et le modèle qui peuvent s'expliquer par la résolution inférieure de la composante de gaz sombre issue du modèle "γ " utilisée pour l'ajustement "poussière", et par les variations d'opacité des poussières discutées par la suite.

Nous avons également effectué un "Jackknife" test pour vérifier la stabilité des paramètres de l'ajustement quand des sous-ensembles de la région sont masqués aléatoirement. La distribution des résultats indique que statistiquement les paramètres de l'ajustement s'appliquent bien à toute la région et ne dépendent pas d'un sous-ensemble des données.

Par ailleurs les résultat de l'ajustement du modèle "γ " dans les différentes bandes en énergie indiquent que la forme du spectre des rayons γ mesuré dans les différentes phases de gaz est compatible avec la forme du spectre interstellaire local (Casandjian 2015). Les rayons cosmiques de basse énergie sont plus sensibles aux processus affectant leur pénétration dans les nuages ce qui peut se traduire par des modifications de la forme du spectre des rayons γ produits. Cette absence de changement spectral dans les phases plus denses (DNM et CO) indique que les rayons cosmiques pénètrent uniformément au travers des nuages étudiés et donc que l'émission de rayons γ est un traceur fiable de la quantité de gaz.

Concernant la détection du gaz neutre sombre

Le gaz non tracé par l'émission HI et CO a été séparé en deux composantes correspondant à des environnements différents. Dans les régions où l'émission CO est inférieure à 7 K km s^{-1} le gaz additionnel est associée aux enveloppes étendues de DNM à la transition HI–H$_2$, alors que quand l'émission CO est forte (> 7 K km s^{-1}) ce gaz correspond essentiellement à du H$_2$ supplémentaire dans les structures moléculaires denses où l'émission CO sature (on le nomme CO$_{\text{sat}}$). Nous avons vérifié que la vraisemblance maximale de l'ajustement du modèle "γ " augmente significativement quand nous effectuons cette séparation.

Comme nous avons réalisé la coupure en 2D et non en 3D, en direction des nuages moléculaires une partie du gaz de la composante CO$_{\text{sat}}$ inclut les enveloppes de DNM d'avant et d'arrière plan. Cependant au vu des différences de densités de colonne, la contribution du DNM à la composante de CO$_{\text{sat}}$ est estimée à seulement 5 à 10 %.

Les composantes de DNM déduites de l'émission des rayons γ et de l'épaisseur optique des poussières sont très similaires en structure et en densité de colonne. De plus elles sont clairement différentiable des composantes HI et CO ce qui prouve qu'il s'agit bien de gaz supplémentaire tracé indépendamment par l'émission des poussières et de rayons γ. L'évolution de la contribution du gaz sombre dans les quantités de gaz total et de gaz moléculaire est discutée plus en détail dans l'article II traitant de la transition HI-H$_2$.

Concernant la détection du gaz ionisé

Les régions HII NGC1499 et G156.6-18.5 sont détectées dans l'émission des poussières et des rayons γ. Au vu des flux de rayons γ mesurés il ne peut pas s'agir de diffusion Inverse Compton du rayonnement interstellaire et stellaire par les électrons relativistes (CRs). La source est plus vraisemblablement hadronique causée par l'interaction des noyaux relativistes (CRs) avec le gaz ionisé. A partir de la densité de colonne de gaz ionisé déduite de l'émission de rayons γ, et pour une température électronique moyenne supposée de 8000 K, nous estimons que la densité électronique moyenne dans la régions HII NGC1499 est de 4.3±0.6 cm^{-3}. Ce résultat est compatible avec la valeur que nous avons déduite des modèles d'émission free-free et Hα dans la régions HII NGC1499, ce qui renforce l'idée d'une origine hadronique de l'émission γ associée.

Concernant le facteur X_{CO}

Les résultats de l'ajustement du modèle d'émission des poussières et des rayons γ nous permettent de mesurer indépendamment le facteur de conversion X_{CO} dans les différents nuages séparés en vitesse. Comme observé dans l'analyse du Chamaeleon (Planck and Fermi Collaborations 2015), les valeurs de X_{CO} mesurées avec l'émission des poussière sont systématiquement supérieures à celles mesurées avec les rayons γ. On note des écarts allant de 30% jusqu'à 130% en lien avec l'augmentation de l'opacité des poussières, ceci indique que le X_{CO} déduit de l'émission des poussières est biaisé à la hausse par l'évolution des propriétés d'émission des grains, discutée par la suite.

Le facteur X_{CO} moyen déduit du modèle "γ" dans les différent nuages varie de $(1.04\pm0.05)\times 10^{20}$ cm^{-2} K^{-1} km^{-1} s à $(0.44 \pm 0.04)\times 10^{20}$ cm^{-2} K^{-1} km^{-1} s. Il décroit avec l' intensité W_{CO} moyenne dans le nuage, la largeur moyenne de raies CO et avec le rapport de surface cœur/enveloppe (mesurant la compacité du nuage). Les modèles de formation et de photo-dissociation du CO prédisent un plus grand rapport X_{CO} dans les enveloppes diffuses, plus exposées au champ de rayonnement UV dissociant, que dans les cœurs denses, bien écrantés. La diminution du rapport X_{CO} moyen mesuré dans les nuages plus compacts et plus brillant en CO, donc plus denses, s'accorde avec cette prédiction. Par contre pour des densités de gaz et des extinctions moyennes équivalentes à celles des nuages locaux, les valeurs de X_{CO} prédites par les simulations sont systématiquement plus grandes que celles observées (Bell et al. 2006; Glover & Mac Low 2011). Cet écart déjà noté par Sonnentrucker et al. (2007); Levrier et al. (2012) semble indiquer une lacune dans notre compréhension de la photo-dissociation ou de la chimie du gaz aux faibles densités de colonnes.

Concernant l'opacité des poussières

Nous avons observé une augmentation progressive de l'opacité des poussières, τ_{353}/N_H, avec la densité de colonne de gaz, N_H, et la fraction de gaz moléculaire. L'opacité moyenne augmente d'un facteur 2 dans le DNM jusqu'à un facteur 4 dans les régions moléculaires, en comparaison des valeurs mesurées dans les régions diffuses. Ces variations d'opacité limitent la plage de densités de colonne dans laquelle l'épaisseur optique des poussières trace linéairement la quantité de gaz à $N_H < 3\times10^{21}$ cm^{-2}. La hausse de l'opacité est associée à une diminution de la température de couleur des grains, on note une augmentation d'un facteur 6 entre 20 et 14 K. Ces variations sont associées à des évolutions chimiques et structurelles des grains modifiant leurs propriétés d'émission. Cet aspect est discuté plus en détail dans la partie suivante et l'article dédié.

Astronomy & Astrophysics manuscript no. tau16_paper1_v6 ©ESO 2016
December 4, 2016

Cosmic rays, gas and dust in nearby anticentre clouds: I – CO-to-H_2 conversion factors and dust opacities

Q. Remy$^{(1)}$, I. A. Grenier$^{(1)}$, D.J. Marshall$^{(1)}$, and J. M. Casandjian$^{(1)}$

^{1} Laboratoire AIM, CEA-IRFU/CNRS/Université Paris Diderot, Service d'Astrophysique, CEA Saclay, F-91191 Gif sur Yvette, France
e-mail: `quentin.remy@cea.fr`
e-mail: `isabelle.grenier@cea.fr`

December 4, 2016

ABSTRACT

Aims. We have explored the capabilities of dust emission and γ rays for probing the properties of the interstellar medium in the nearby anti-centre region, using γ-ray observations with the *Fermi* Large Area Telescope (LAT), and the thermal dust optical depth inferred from *Planck* and *IRAS* observations. We have studied massive star-forming clouds including the well known Taurus, Auriga, Perseus, and California molecular clouds, as well as a more diffuse structure which we refer to as Cetus. In particular, we aim at quantifying potential variations in cosmic-ray density and dust properties per gas nucleon across the different gas phases and different clouds, and at measuring the CO-to-H_2 conversion factor, $X_{\rm CO}$, in different environments.

Methods. We have separated six nearby anti-centre clouds, coherent in velocities and distances, from the Galactic-disc background in H I 21-cm and ^{12}CO 2.6-mm line emission. We have jointly modelled the γ-ray intensity recorded between 0.4 and 100 GeV, and the dust optical depth τ_{353} at 353 GHz as a combination of H I -bright, CO-bright, and ionised gas components. The complementary information from dust emission and γ rays is used to reveal the gas not seen, or poorly traced, by H I , free-free, and ^{12}CO emissions, namely (i) the opaque H I and diffuse H_2 present in the Dark Neutral Medium at the atomic-molecular transition, and (ii) the dense H_2 to be added where ^{12}CO lines saturate.

Results. The measured interstellar γ-ray spectra support a uniform penetration of the cosmic rays with energies above a few GeV through the clouds, from the atomic envelopes to the ^{12}CO-bright cores, and with a small ±9% cloud-to-cloud dispersion in particle flux. We detect the ionised gas from the H II region NGC1499 in the dust and γ-ray emissions and we measure its mean electron density and temperature. We find a gradual increase in grain opacity as the gas (atomic or molecular) becomes more dense. The increase reaches a factor of four to six in the cold molecular regions that are well shielded from stellar radiation. Consequently, the $X_{\rm CO}$ factor derived from dust is systematically larger by 30% to 130% than the γ-ray estimate. Additionally, we evaluate the average γ-ray $X_{\rm CO}$ factor for each cloud, and find that $X_{\rm CO}$ tends to decrease from diffuse to more compact molecular clouds, as expected from theory, but our results highlight large quantitative discrepancies in ^{12}CO intensities between simulations and observations at low molecular gas densities. We find $X_{\rm CO}$ factors in the anti-centre clouds close to or below 10^{20} cm^{-2} K^{-1} km^{-1} s, in agreement with other estimates in the solar neighbourhood. Together, they confirm a long-standing unexplained discrepancy, by a factor of two, between the mean $X_{\rm CO}$ values measured at parsec scales in nearby clouds and those obtained at kiloparsec scale in the Galaxy.

Key words. Gamma rays: ISM – Galaxy: solar neighbourhood – ISM: clouds – ISM: cosmic rays – ISM: dust

1. Introduction

The structural, dynamical and thermodynamical evolution of interstellar clouds is often probed with observations of the H I 21-cm line for the atomic gas (Kalberla et al. 2005, 2010; Peek et al. 2011) and of CO rotational emission lines for the molecular gas (Heyer & Dame 2015). Yet, measuring gas column densities in the dense media, both atomic and molecular, is hampered by the opacity of the interstellar medium (ISM) to these radiations and we have no efficient means to correct for line opacities in the absence of absorption data against background point sources. Complementary information can be gained from the sub-millimeter and infrared thermal emission of large dust grains mixed with the gas (Planck Collaboration 2014a), and from γ rays produced in interactions of high-energy cosmic rays (CRs) with interstellar gas nucleons (Lebrun et al. 1982). Dust grains and CRs trace all chemical and thermodynamical forms of the gas to large depths into the clouds (Planck and Fermi Collaborations 2015), but they trace only integrals of the gas column densities, $N_{\rm H}$, along sight lines, and they bear no kinematic information. Their use relies on critical assumptions, namely a uniform dust-to-gas mass ratio and uniform grain emissivity across a cloud and, likewise, a uniform CR flux through a cloud. Those assumptions still need to be tested in a variety of clouds and across complex phase changes, especially on consideration that dust grains and their radiation properties vary from the diffuse ISM to molecular clouds (Stepnik et al. 2003; Martin et al. 2012; Roy et al. 2013a; Ysard et al. 2013; Flagey et al. 2009; Planck Collaboration 2014a,b; Planck and Fermi Collaborations 2015). One can also test the uniformity of the γ-ray emissivity spectrum of the gas in well-sampled nearby clouds to verify the smooth penetration of CRs with energies above ~1 GeV (Skilling & Strong 1976; Cesarsky & Volk 1978; Morlino & Gabici 2015).

The recent progress in H I , CO, dust, and γ-ray observations opens excellent opportunities to confront these observations at a resolution of a few parsecs inside nearby clouds in order to probe biases in the different tracers and to search for missing gas in the census. The comparison can shed light on the highly opaque atomic gas forming the cold neutral medium (CNM), where the H I brightness temperature probes the excitation (spin) temperature of the gas rather than the column density (Murray et al. 2015, and references therein). One can also probe how the ^{12}CO, J=1→0, emission rapidly saturates at high column density and how it fades out in the diffuse molecular gas where CO lines are too weakly excited and/or CO molecules are too efficiently photodissociated to map the corresponding molecular hydrogen (van Dishoeck & Black 1988; Wolfire et al. 2010). Large H I opacities and the lack of CO emission both conspire to hide large gas masses at the H–H_2 interface. This dark neutral medium (DNM) can be jointly revealed by cosmic rays and dust (Grenier et al. 2005).

A more precise census of the gas column densities is key to establishing and quantifying variations in dust opacity (optical depth per gas nucleon) across cloud structures. Mapping those variations as a function of grain temperature, T, and opacity spectral index, β gives important diagnostics for grain evolution through mantle accretion, coagulation, and ice coating (Köhler et al. 2015).

With an approach similar to the multi-tracer analysis of the Chamaeleon complex (Planck and Fermi Collaborations 2015), we present an analysis of the anticentre region, which exhibits more massive clouds, with higher levels of star-formation activity, so we can test the properties of the gas tracers to larger column densities and molecular fractions. The analysed region spans a few hundred parsecs in distance in the local ISM (see below). It encompasses the well-known Taurus, Auriga, and Perseus molecular clouds (Ungerechts & Thaddeus 1987; Lombardi et al. 2010; Schnee et al. 2008), the massive complex associated with the California nebula (Lada et al. 2009), and a nearby, diffuse, hardly molecular cloud, which we refer to as Cetus.

Our goal is to test the dust and γ-ray emission as tracers of the total gas against linear combinations of the emission line intensities recorded in the H I and CO observations, a new free-free emission map of the ionised gas, plus the DNM gas which escapes the radio and millimeter spectroscopic surveys at the atomic-molecular interface. We have separated the H I and CO clouds in space (i.e., direction, velocity, and distance) to study their individual contributions to the total dust and γ-ray signals. We have used the model results to derive scaling factors such as the CO-to-H_2 conversion factor, $X_{\rm CO}$, in each cloud, and the average dust opacity in the different gas phases for each cloud. We have then used the multi-wavelength data to follow dust evolution with increasing $N_{\rm H}$ in several molecular clouds with masses spanning nearly two orders of magnitude. A companion paper will present the results on the transitions between gas phases, and on the mass fractions and contribution of CO-dark H_2 to the molecular phase in individual regions.

The paper is structured as follows: the data are presented in Sect. 2 and the models are described in Sect. 3. The model results and the detection of gas in the DNM, CO-saturated, and ionised phases are detailed in Sect. 4. The CR content of the clouds, the $X_{\rm CO}$ ratios, and the dust opacities are discussed in Sect. 5, 6, and 7, respectively. Additionally, we present the H I and CO component separation into nearby cloud complexes in appendix A, the derivation of the free-free intensities in appendix B, the dependence of the goodness of fit on the H I spin temperature in appendix C, the best-fit coefficients of the dust and γ-ray models in appendix D, and a table with historical γ-ray measurements of $X_{\rm CO}$ factors in E.1.

2. Data

The analysis region extends from 139° to 191° in Galactic longitude and from −56° to −3° in Galactic latitude. We have masked regions with large column densities from the background Galactic disc, at $-9° < b < -3°$ for $l > 183°$ and $l < 152°$ and regions with small column densities at declinations below −5°where the H I maps have lower angular resolution. All maps in Fig. 1 have been projected onto the same 0.°125-spaced Cartesian grid as that of the CfA CO survey (Dame et al. 2001). We have checked that the use of the Cartesian projection, instead of equal-area bins, does not significantly bias the results. The largest differences are less than a fifth of the uncertainties found in the jackknife tests discussed in Sect. 4.2.

2.1. HI and CO data

For this analysis we have used the 4′-resolution GALFA-HI survey where available (Peek et al. 2011) and we have complemented it with the 10.8′-resolution EBHIS survey elsewhere (Winkel et al. 2016). As shown in Fig. 1, the GALFA survey covers 74% of the region. GALFA data-cubes [1] were re-sampled into the 0.°125-spaced Cartesian grid. We have used the narrow-band cubes with their original velocity resolution of 0.18 km/s in the local standard of rest (LSR). The EBHIS frequency sampling is coarser, with a velocity resolution of 1.44 km/s. In the analysed region covered by both survey we have found a tight correlation in column densities between the two:

$$N_{\rm H}^{\rm GALFA} = 1.0013 \times N_{\rm H}^{\rm EBHIS} - 8.17 \times 10^{17} {\rm cm}^{-2} \quad (1)$$

In order to trace the molecular gas we have used ^{12}CO J=1→0 observations at 115 GHz from the moment-masked CfA CO survey of the Galactic plane (Dame et al. 2001; Dame & Thaddeus 2004). Most of the survey is based on a 0.°125-spaced Cartesian grid except for the high-latitude clouds, at $b \lesssim -50°$, which have been interpolated from 0.°25 to 0.°125.

2.2. HI and CO velocity separation

We have decomposed the H I and CO spectra into individual lines and we have used this information to identify six nearby entities that are coherent in velocity, position (in Galactic coordinates), and distance, in addition to the emission from the background Galactic disc. The H I velocity resolution in the region covered by the EBHIS survey is coarser, but still adequate to separate the main structures because of the limited confusion along sight lines at medium-to-high latitudes. The separation process is three-fold and is described by Planck and Fermi Collaborations (2015) and in Appendix A. The choice of six main entities has been guided by the structure in (l, b, v) density and by distance information obtained from stellar reddening (Schlafly et al. 2014). Details on the (l, b, v) cuts are given in Table A.1. The main structures found in the local ISM, namely Cetus, Main Taurus, South Taurus, North Taurus, Perseus, and California, together with the background Galactic structures are depicted in $N_{\rm HI}$ column densities and in $W_{\rm CO}$ intensities in Fig. 1. The set of H I maps includes all of the H I emission observed in this region except for the high velocity clouds (Wakker et al. 2008). In order to investigate the effect of the unknown H I optical depth, we have derived all the $N_{\rm HI}$ maps for a sample of uniform spin temperatures (150, 200, 300, 400, 500, 600, 700, and 800 K) and for the optically thin case.

---

[1] `https://purcell.ssl.berkeley.edu`

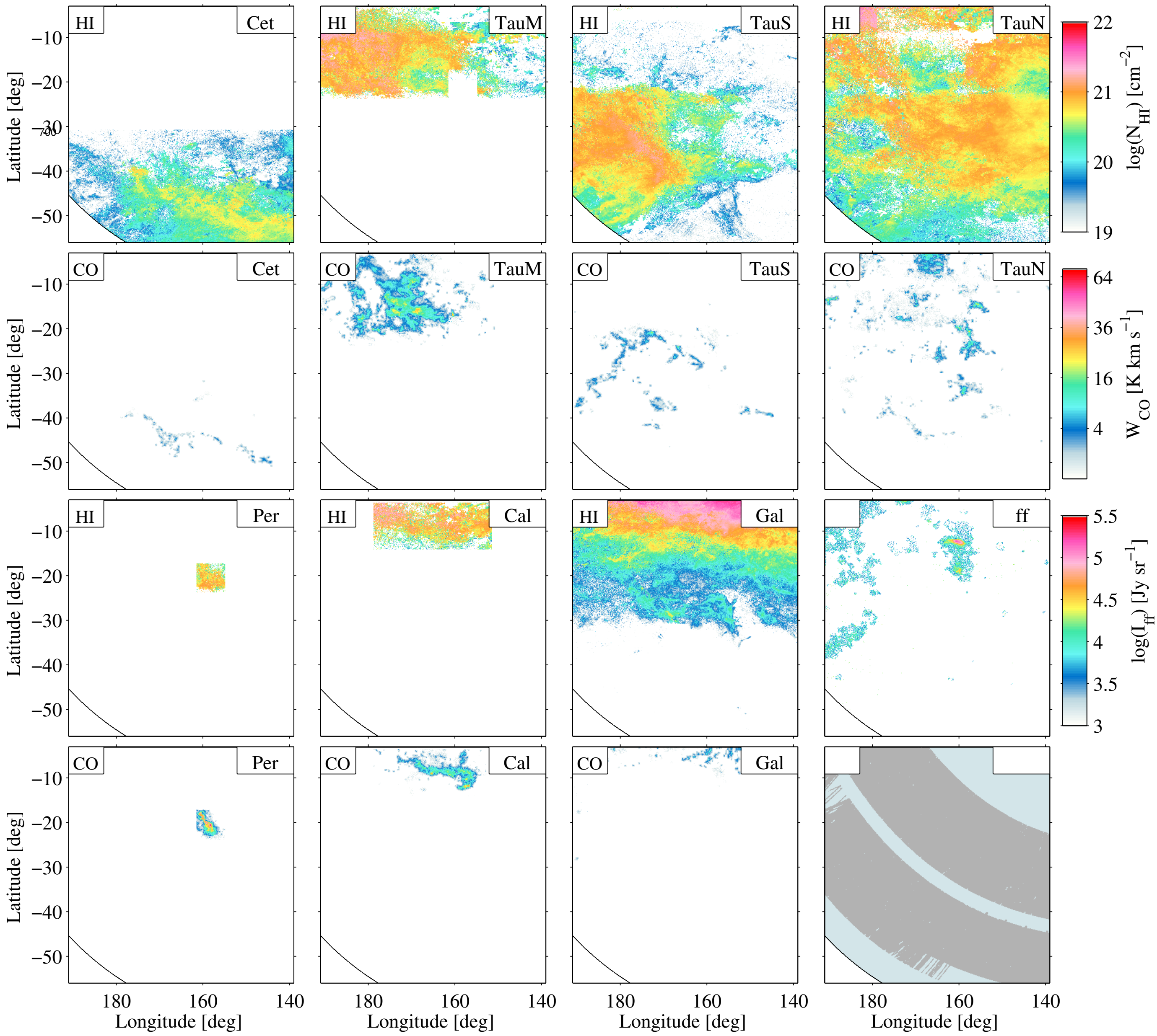

Fig. 1. Maps of the Cetus (Cet), Main Taurus (TauM), South Taurus (TauS), North Taurus (TauN), Perseus (Per), and California (Cal) clouds, and of the Galactic disc background (Gal) in H I column density, $N_{\rm HI}$, for a spin temperature of 400 K, and in CO intensity, $W_{\rm CO}$. The $N_{\rm HI}$ and $W_{\rm CO}$ maps are respectively labelled HI and CO. The map labelled ff shows the intensity $I_{\rm ff}$ of free-free emission toward this region. The last subplot shows the coverage of the GALFA (dark grey) and EBHIS (light blue) H I data.

Distance estimates to the local clouds have been compiled from the photometric measurements of PanSTARRS-1 and the detection of reddening fronts toward stellar groups (Schlafly et al. 2014). We have selected the stars along lines of sight intersecting each (and only one) cloud within its $W_{\rm CO}$ contour at 0.5 K km s^{-1} and we have calculated the average distance in each sample. For the reddening fronts to the stars toward Cetus, Main Taurus, South Taurus, North Taurus, Perseus, and California we find average distances of 190±30 pc, 140±30 pc, 160±10 pc, 190±50 pc, 270±20 pc, and 410±20 pc, respectively. They compare reasonably with the geometry inferred from the modelling of the far-UV continuum emission (Lim et al. 2013). The North Taurus component is dominated by the Auriga cloud near the northern edge of our analysis region; it also includes MBM 12 molecular cloud from Magnani et al. (1985) catalogue. The South Taurus component includes MBM 6, MBM 12 and MBM 18.

2.3. Dust data

In order to trace the dust column density, we have used the optical depth, τ_{353}, obtained at 353 GHz by Planck Collaboration (2014a). They have modelled the spectral energy distributions of the thermal emission of the large grains with modified blackbody curves in specific intensity, $I_\nu = \tau_{\nu_0} B_\nu(T_{\rm d})(\nu/\nu_0)^\beta$. The optical depth τ_{ν_0} at frequency ν_0, the dust colour temperature $T_{\rm d}$, and the spectral index β were fitted to the data from *Planck* and the Infrared Astronomical Satellite (IRAS) across the sky at 30′ resolution. The fits were then repeated at 5′ resolution by fixing β as obtained in the first step. This procedure limited the

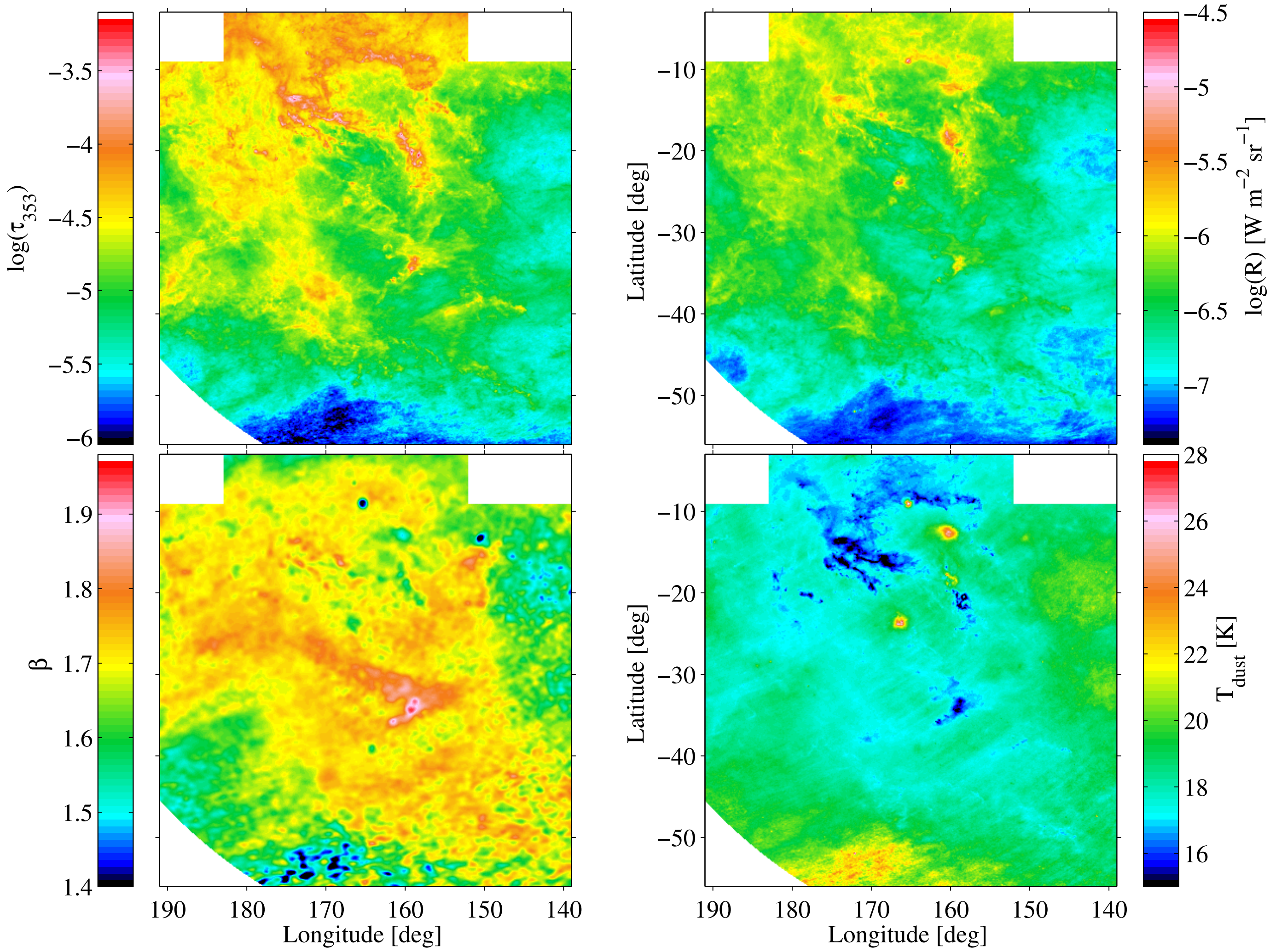

Fig. 2. Maps of dust optical depth at 353 GHz (top left), radiance (top right), spectral β index (bottom left), and colour temperature (lower right), from Planck Collaboration (2014a).

noise impact on the T_d–β degeneracy in faint regions. The modelled intensities were checked to be consistent with the data at all frequencies (see Fig. 11 in Planck Collaboration 2014a). The contamination from CO line emission in the 353 GHz filter band amounts to a few per cent of the total signal. It was not removed so as to avoid increasing the noise in directions away from CO clouds.

The optical depth, τ_ν, and opacity, σ_ν, of the dust at frequency ν follow the relations :

$$\tau_\nu = \frac{I_\nu}{B_\nu(T_\mathrm{d})} = \sigma_\nu N_H \quad (2)$$

We have also calculated the total power radiated by the dust, also referred to as radiance:

$$\mathcal{R} = \int \tau_{353}\, B_\nu(T_\mathrm{d}) \left(\frac{\nu}{353\,\mathrm{GHz}}\right)^\beta d\nu \quad (3)$$

Figure 2 shows the dust properties thus measured across the analysis region.

The corresponding analysis of the Chamaeleon region (Planck and Fermi Collaborations 2015) compared different dust tracers, namely the optical depth and an estimate of the dust extinction, A_{VQ}, empirically corrected for starlight intensity. The latter distribution best followed the gas column densities in the Chamaeleon region, but we have checked that this is not true in the anticentre region in particular toward regions of dust temperatures exceeding 23 K,, so we present the results of our analyses using only the τ_{353} optical depth. Understanding why the empirical correction used for A_{VQ} is less efficient in the anticentre region will be investigated separately.

2.4. Ionised gas

Ionised gas is visible in Hα emission (Finkbeiner 2003) in the California nebula around $l = 160.^\circ 1$ and $b = -12.^\circ 4$, in the G159.6-18.5 H II region, and along the Eridanus loop. The Califonia Nebula, alias NGC 1499 or S 220, is ionised by ξ Persei, an O7.5III star located at a distance of 380 ± 70 pc (van Leeuwen 2007) that has run away from the Perseus OB 2 association (Shinohara & Ishida 1976). The $1.^\circ 2$-diameter region G159.6-18.5 has been seen by IRAS and the Wide-Field Infrared Survey Explorer (WISE) (Andersson et al. 2000; Anderson et al. 2014). It is excited by another run-away O9.5V star, HD 278942, at a distance of 190 ± 40 pc (van Leeuwen 2007), which would place it in front rather than behind the Perseus cloud (Bally et al. 2008).

The composite Hα map varies in angular resolution from 6′ to 1° across the region of interest and Hα emission can be efficiently absorbed behind dense clouds (see for instance the dusty absorption lane across G159.6-18.5 in Fig. 8 of Bally et al. 2008). We have therefore preferred measures of the free-free intensity at mm wavelengths to trace the ionised gas.

The *Planck* LFI map at 70 GHz (release 2.01 data, Planck Collaboration 2015) shows free-free emission in spatial coincidence with the Hα emission. The angular resolution of 14′ of LFI better suits our analysis than the 1°-resolution of the free-free map inferred at 22 GHz from the 9-year WMAP data (Bennett et al. 2013). To separate the free-free intensity in the 70 GHz data, we have successively removed the contributions from the Cosmological Microwave Background (CMB), from dust emission, and from point sources. The method we have used to extract the free-free emission is described in Appendix B.

The resulting free-free dominated map is displayed in Fig. 1. It closely resembles the Hα intensity map of the region (Finkbeiner 2003), but for a uniform resolution of 14′ and a reduced contrast, by a factor 2 to 8, between the intensities of G159.6-18.5 and NGC 1499. because the Perseus clouds are more transparent to mm waves.

The integral of the free-free intensity along a sight line through ionised gas with temperature T_e and electron and ion number densities, n_e and n_i, scales at 70 GHz as :

$$I_{\rm ff} = 63.4 \text{ Jy sr}^{-1} \left(\frac{T_e}{10^4\,\text{K}}\right)^{-0.28} \int n_e\, n_i\, ds \tag{4}$$

where the emission measure $\int n_e\, n_i\, ds$ is expressed in cm^{-6} pc (Karzas & Latter 1961; Carson 1988). If the observed intensity results from discrete and homogeneous nebulae with comparable uniform electron densities, $\overline{n}_e$, $I_{\rm ff}$ roughly scales with the ion column density,

$$N_{\rm HII} \approx 4.87\, 10^{16} \text{ cm}^{-2}\ (I_{\rm ff}/1 \text{ Jy sr}^{-1})\ (T_e/10^4\text{ K})^{0.28} (\overline{n}_e/1\text{ cm}^{-3})^{-1}, \tag{5}$$

so we have used the $I_{\rm ff}$ map as a template for the $N_{\rm HII}$ distribution in the gas model and we discuss the scaling ratio obtained in the fit between $N_{\rm HII}$ and $I_{\rm ff}$ in Sec. 4.4.

2.5. Gamma-ray data

We have used six years of the Pass 8 photon data from *Fermi*-LAT, the associated instrument response functions (IRFs, P8R2_CLEAN_V6), and the corresponding isotropic spectrum for the extragalactic and residual instrumental backgrounds (Atwood et al. 2013; Acero et al. 2015). We have applied tight rejection criteria (CLEAN class selection, photon arrival directions within < 100° of the Earth zenith and in time intervals when the LAT rocking angle was inferior to 52°) in order to reduce the contamination by residual CRs and Earth atmospheric γ rays in the photon data (see Nolan et al. 2012, for details). We have sampled the IRFs, the exposure map, the γ-ray emissivity spectrum, $q_{\rm LIS}$, of the local interstellar gas (Casandjian 2015), and the spectrum of the isotropic background in 14 energy bins, 0.2 dex in width and centred from $10^{2.3}$ to $10^{4.9}$ MeV.

To ensure photon statistics robust enough to follow details in the spatial distributions of the different interstellar components, we have analysed the data in broad and independent energy bands, bounded by $10^{2.6}$, $10^{2.8}$, $10^{3.2}$, $10^{3.6}$, and 10^5 MeV. We have also analysed the data in the integrated $10^{2.6}$ – 10^5 MeV band. The low-energy threshold was set to take advantage of the best LAT point-spread function (PSF), which strongly degrades at low energy. The analysis of the data in two lower-energy bands ($10^{2.2}$–$10^{2.4}$ and $10^{2.4}$–$10^{2.6}$ MeV) proved to be less reliable to separate the gas phases in compact clouds. To optimize the angular resolution, we have selected all detected photons above 1.6 GeV, but only those at lower energy that converted to pairs in the front section of the tracker (Atwood et al. 2009; Ackermann et al. 2012a). Given the broad ranges of the energy bands, we have not corrected the fluxes for the energy resolution, which is better than 14% at these energies (Atwood et al. 2013). To account for the spill-over of emission produced outside the analysis region, but reconstructed inside it, we have modelled point sources and interstellar contributions in a region 4° wider than the analysis region. This choice corresponds to the 99.5% containment radius of the PSF in the lowest energy band. For the H I emission outside the analysis region not covered by EBHIS and GALFA surveys we have used the Leiden/Argentine/Bonn (LAB) survey (Kalberla et al. 2005).

The positions and the flux spectra of the γ-ray sources in the field are provided by the *Fermi*-LAT Third Source Catalog (Acero et al. 2015). The observed γ-ray emission also includes a contribution from the large-scale Galactic inverse Compton (IC) emission emanating from the interactions of CR electrons with the ISRF. The GALPROP[2] parameter file 54-LRYusifovXCO4z6R30-Ts150-mag2 has been used to generate an energy-dependent template of the Galactic IC emission across the analysis region (Ackermann et al. 2012e).

3. Models and analyses

To first order, the dust and γ-ray emissions should both trace the total gas column density, $N_{\rm H}$. In order to compare them in Fig. 3, we have convolved the dust optical depth with the LAT PSF on the one hand, and we have subtracted non-gaseous γ-ray emissions obtained by the fitting (Sec. 4) from the γ-ray data on the other hand. Fig. 3 shows strong similarities in the spatial distributions of both tracers, but it also reveals differences in their dynamical range in several places.

To detect neutral gas unaccounted for in $N_{\rm HI}$ and $W_{\rm CO}$, we have used the fact that it is permeated by both cosmic rays and dust grains. We have therefore extracted the significant γ-ray and dust residuals over the $N_{\rm HI}$, $W_{\rm CO}$, and $N_{\rm HII}$ expectations and we have used the spatial correlation between those residuals to infer the additional gas column densities (see Sec 3.3). We have separated the residuals for two types of environments: in regions of weak or no CO intensity, below 7 K km s^{-1}, which correspond to the DNM at the H-H$_2$ transitions; and in regions toward large CO intensities, above 7 K km s^{-1}, to capture additional H$_2$ gas where ^{12}CO emission saturates and rarer isotopologues such as ^{13}CO or C^{18}O should be used. We refer to this saturated-CO molecular component as "CO$_{\rm sat}$".

3.1. Dust model

In the case of a uniform dust-to-gas mass ratio and uniform mass emission coefficient of the grains, the dust optical depth linearly scales with the total $N_{\rm H}$. We have therefore modelled $\tau_{353}(l, b)$ in each direction as a linear combination of the gaseous contributions from the different phases (H II , H I , DNM, CO-bright, CO$_{\rm sat}$), with free normalisations to be fitted to the data, as in Planck and Fermi Collaborations (2015). We have added a free isotropic term, $y_{\rm iso}$, to account for the residual noise and the uncertainty in the zero level of the dust data (Planck Collaboration

---

[2] `http://galprop.stanford.edu`

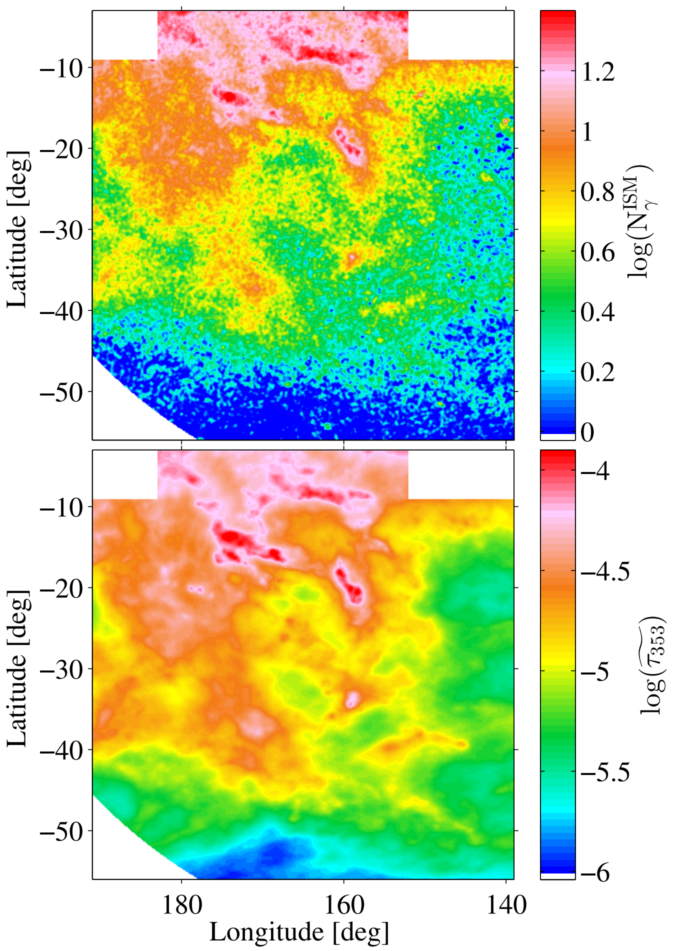

Fig. 3. *Top:* γ-ray counts of gaseous origin recorded in the 0.4–100 GeV energy band in a 0°.125 pixel grid. γ-ray emissions other than due to cosmic-ray interactions in the gas have been subtracted. The map has been smoothed with a Gaussian kernel of 0°.14 dispersion for display. *Bottom:* dust optical depth measured at 353 GHz and displayed at the *Fermi*-LAT angular resolution for comparison.

2014a). The $\tau_{353}(l, b)$ model can be expressed as:

$$\begin{aligned}\tau_{353}(l,b) &= \sum_{i=1}^{7} y_{\rm HI,i} N_{\rm HI,i}(l,b) + \sum_{i=1}^{7} y_{\rm CO,i} W_{\rm CO,i}(l,b) + y_{\rm ff} I_{\rm ff}(l,b)\\ &+ \; y_{\rm DNM} N_{\rm H}^{\rm DNM}(l,b) + y_{\rm COsat} N_{\rm H}^{\rm COsat}(l,b) + y_{\rm iso} \qquad (6)\end{aligned}$$

where $N_{\rm HI,i}(l,b)$, $W_{\rm CO,i}(l,b)$, and $I_{\rm ff}(l,b)$ respectively denote the $N_{\rm HI}$, $W_{\rm CO}$, and free-free maps of the clouds depicted in Fig. 1. $N_{\rm H}^{\rm DNM}(l,b)$ and $N_{\rm H}^{\rm COsat}(l,b)$ stand for the column densities in the DNM and CO$_{\rm sat}$ components deduced from the coupled analyses of the γ-ray and dust data (see Sect. 3.3).

The y model parameters have been estimated using a χ^2 minimization. We expect the model uncertainties to exceed the measurement errors in $\tau_{353}(l,b)$ because of potential variations in grain properties through the clouds and because of the limitations of the gas tracers (survey sensitivities, emission saturation, self-absorption, etc.). As we cannot precisely determine the model uncertainties, we have set them to a fractional value of the data and we have determined this fraction to be 19% by reaching a reduced χ^2 of unity. This fraction is larger than the 3% to 9% error in the measurement of τ_{353} across this region (Planck Collaboration 2014a).

3.2. Gamma-ray model

Earlier studies have indicated that the bulk of the Galactic CRs radiating at 0.4–100 GeV have diffusion lengths far exceeding typical cloud dimensions and that they permeate all the H I - bright, DNM, and CO-bright gas phases. The observed γ-ray emission can therefore be modelled, to first order, by a linear combination of the same gaseous components as in the dust model. We have assumed that the emissivity spectrum of the gas follows the average one obtained in the local ISM ($q_{\rm LIS}(E)$, Casandjian 2015), but we have left a free normalisation in each energy band to account for possible deviations in CR density and spectrum. The model includes other radiation components such as the Galactic IC radiation, $I_{\rm IC}(l,b,E)$, the isotropic intensity mentioned above, $I_{\rm iso}(E)$, and point sources with individual flux spectra $S_j(E)$. We have verified that the soft emission from the Earth limb is not detected in the present energy range for the choice of maximum zenith angle. The soft and transient emission from Sun and Moon is not expected to be detected as the number of γ-ray photons they emit over 6 years is negligible compared to those of the ISM components in the energy range studied. The γ-ray intensity $I(l,b,E)$, expressed in cm^{-2} s^{-1} sr^{-1} MeV^{-1}, can thus be modelled as :

$$\begin{aligned}I(l,b,E) &= q_{\rm LIS}(E) \times [\, \sum_{i=1}^{7} q_{\rm HI,i}(E)\, N_{\rm HI,i}(l,b)\\ &+ \sum_{i=1}^{7} q_{\rm CO,i}(E)\, W_{\rm CO,i}(l,b) + q_{\rm ff}(E) I_{\rm ff}(l,b)\\ &+ q_{\rm DNM}(E)\, \tau_{353}^{\rm DNM}(l,b) + q_{\rm COsat}(E)\, \tau_{353}^{\rm COsat}(l,b)\ ]\\ &+ q_{\rm IC}(E)\, I_{\rm IC}(l,b,E)) + q_{\rm iso}(E)\, I_{\rm iso}(E)\\ &+ \sum_{j} q_{S_j}(E)\, S_j(E)\, \delta(l-l_j, b-b_j)\\ &+ q_{S\,{\rm ext}}(E)\, S_{\rm ext}(l,b,E) \qquad (7)\end{aligned}$$

with the $\tau_{353}^{\rm DNM}$ and $\tau_{353}^{\rm COsat}$ maps extracted from the coupled dust and γ-ray analyses (see Sect. 3.3).

The input $q_{\rm LIS}$ spectrum was based on four years of LAT data and on the correlation between the γ radiation and the $N_{\rm HI}$ column densities derived from the LAB survey, for a spin temperature of 140 K, at latitudes between 7° and 70° (Casandjian 2015). The $q_{\rm HI,i}$ scale factors in the model can therefore compensate for differences in the H I data (calibration, angular resolution, spin temperature) and potentially for cloud-to-cloud variations in CR flux. Such differences will affect the normalizations equally in all energy bands whereas a change in CR penetration in a specific cloud will show as an energy-dependent correction. For each cloud, the average γ-ray emissivity spectrum per H atom in the atomic phase is estimated from the product of the $q_{\rm LIS}$ spectrum and the best-fit $q_{\rm HI,i}$ normalization. This emissivity can be used to estimate the gas mass present in the other DNM, CO, and CO$_{\rm sat}$ parts of the cloud if one assumes a uniform CR flux across the whole structure.

The model includes 126 points sources from the 3FGL catalogue (Acero et al. 2015) inside the analysis region. Their flux spectra, $S_j(E)$, have been computed with the spectral characteristics provided in the catalogue. Their $q_{S_j}(E)$ normalization in the model allows for possible changes due to the longer exposure and different photon reconstruction dataset used in the present analysis (six years of Pass 8 data instead of four years of Pass 7 reprocessed data for 3FGL) and due to the use of a different interstellar background for source detection in 3FGL. The sources have been fitted simultaneously. The sources present

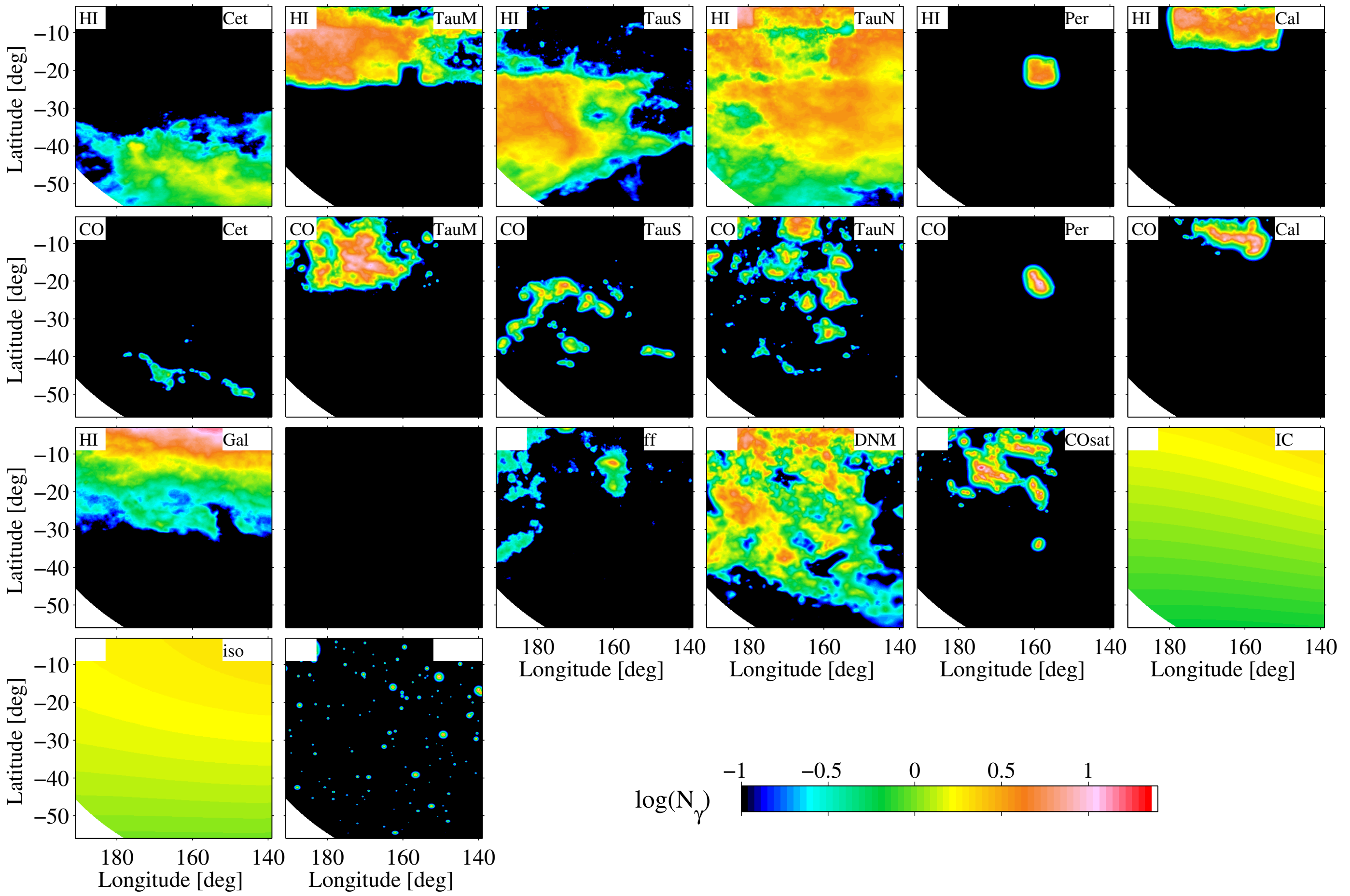

Fig. 4. Photon yields arising in the γ-ray model in the 0.4–100 GeV band from the H I (HI label) and CO-bright (CO label) phases of the Cetus, Main Taurus, South Taurus, North Taurus, Perseus, California, and Galactic disc clouds, from the ionised gas (ff label), from the DNM and CO_{sat} gas column densities, from the Galactic IC emission, and from the isotropic background (iso label) and γ-ray point sources.

in the 4°-wide peripheral band around the analysis region have been merged into a single map, $S_{ext}(l, b, E)$, and its normalization, $q_{S_{ext}}$, has been left free in each energy band. The IC emission has been derived from a GALPROP model (Ackermann et al. 2012e) and isotropic emission has been determined over the whole sky with a different interstellar background model (Casandjian 2015), so we have left their scaling free in each energy band.

In order to compare with the LAT photon data in the different energy bands, we have multiplied by the exposure and convolved by the LAT PSF each model component. Figure 4 gives the photon yields in the total energy band obtained by the fitting (Sec. 4) from those components. It shows that the emission originating from the gas dominates over other types of emission and that the LAT angular resolution allows the spatial separation of the various clouds, and of the different gas phases within the clouds. The q model parameters have been fitted to the LAT photon data in each energy band using a binned maximum-likelihood with Poisson statistics.

3.3. Analysis iterations

An important aspect of our analysis is the iterative coupling of the dust and γ-ray models in order to extract the common DNM and CO_{sat} gas components which are present in both datasets, but for which we have no a priori templates. Both components show up as positive residuals over the expectations from the H I -bright, CO-bright, and free-free-bright gas components. To extract them, we have built maps of the positive residuals between the data (dust or γ rays) and the best-fit contributions from the N_{HI}, W_{CO}, free-free, and ancillary (other than gas) components. We have kept only the positive residuals above the noise (see below). We have separated the residuals into DNM and CO_{sat} maps according to the W_{CO} intensity in each direction (below and above 7 K km/s for the DNM and CO_{sat}, respectively). The DNM and CO_{sat} templates estimated from the dust are provided to the γ-ray model (τ_{353}^{DNM} and τ_{353}^{COsat} in equation 7); conversely, the DNM and CO_{sat} column densities derived from the γ rays are provided to the dust model (N_H^{DNM} and N_H^{COsat} in equation 6). We have started the iterative process by fitting the dust optical depth with the H I , CO, free-free, and isotropic components to build the first DNM and CO_{sat} maps for the γ-ray model. We have then iterated between the γ-ray and dust models until a saturation in the log-likelihood of the fit to γ-ray data is reached (from the third to the fourth iteration).

The estimates of the q and y model coefficients and the DNM and CO_{sat} templates improve at each iteration since there is less and less need for the other components, in particular the H I and CO ones, to compensate for the missing gas. They still do at some level because the DNM and CO_{sat} templates provided by the γ rays or dust emission have limitations (e.g., dust emissivity variations, limited γ-ray sensitivity).

Care must be taken in the extraction of the positive residuals because of the Gaussian noise around zero. A simple cut at zero

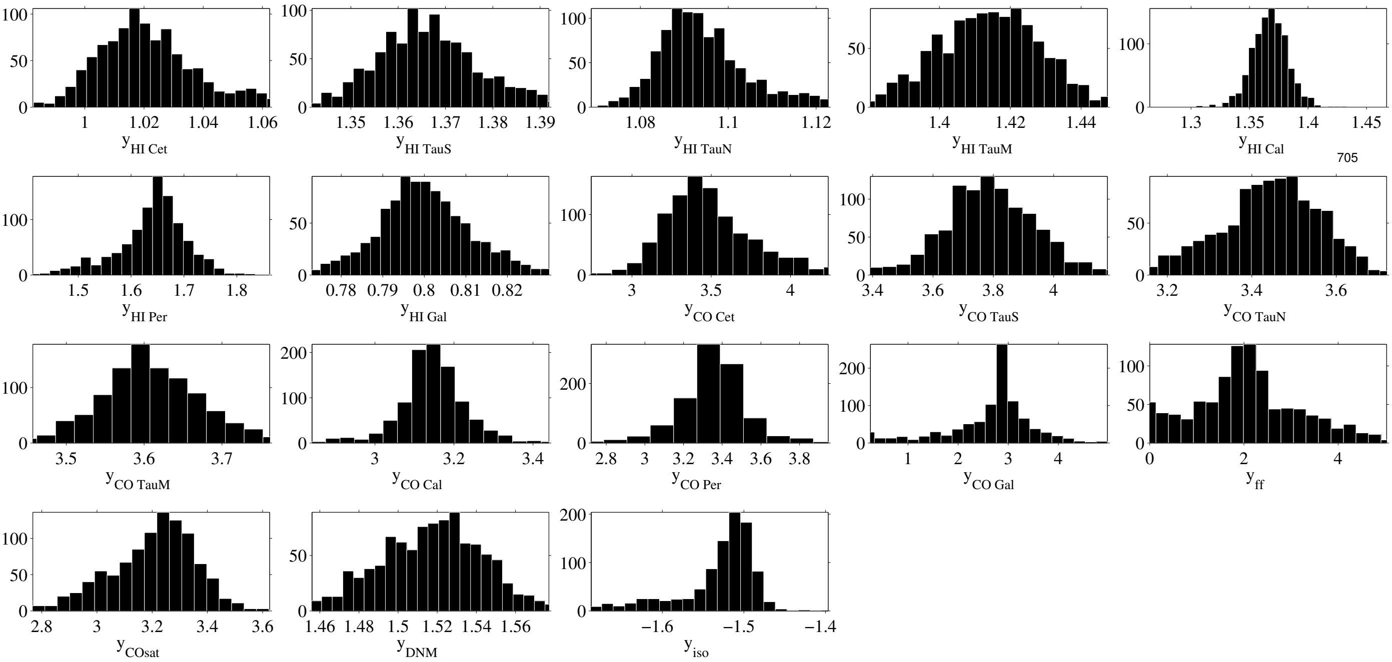

Fig. 5. Number distribution of the dust model coefficients over 1000 jackknife fits for an H I spin temperature of 400 K. $y_{\rm HI,i}$, $y_{\rm COsat}$, and $y_{\rm DNM}$ are in units of 10^{-26} cm^2, $y_{\rm CO,i}$ in 10^{-6} K^{-1} km^{-1} s, $y_{\rm ff}$ in 3.8 10^{-11} Jy^{-1} sr and y_{iso} in 10^{-6}.

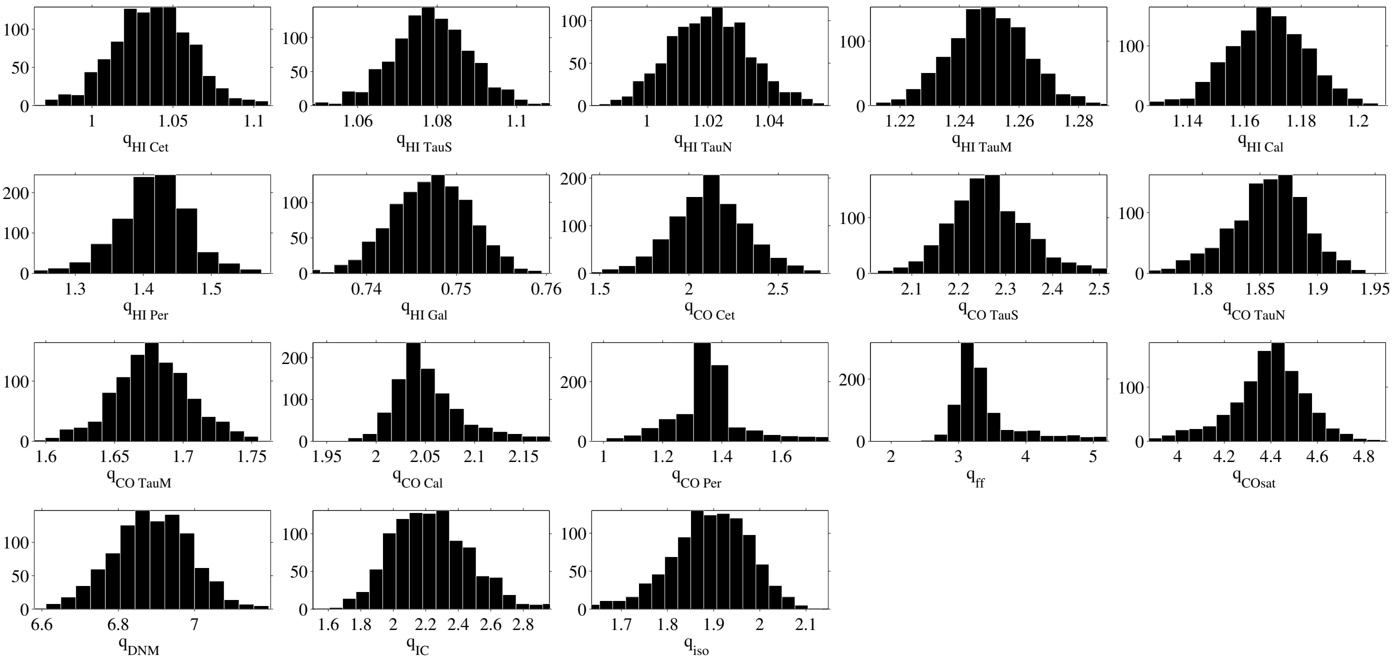

Fig. 6. Number distribution of the γ-ray model coefficients obtained for 1000 jackknife fits for an H I spin temperature of 400 K. $q_{\rm CO,i}$ are in units of 10^{20} cm^{-2} K^{-1} km^{-1} s, $q_{\rm ff}$ in 3.8 10^{15} cm^{-2} Jy^{-1} sr, $q_{\rm DNM}$ and $q_{\rm COsat}$ in 10^{25} cm^{-2}. $q_{\rm HI,i}$, $q_{\rm IC}$ and q_{iso} are normalisation factors.

would induce an offset bias, so we have de-noised the residual maps using the multi-resolution support method implemented in the MR filter software (Starck & Pierre 1998). The stability of the iterative analysis and the results of the dust and γ-ray fits are discussed in the following sections.

4. Results

4.1. H I optical depth correction

The unknown level of H I opacity in the different maps induces systematic uncertainties on the $N_{\rm HI}$ column densities, therefore on the H I contributions to the models. The γ rays can help constrain the *average* level of H I optical-depth correction applicable to the whole region by comparing the $T_{\rm S}$-dependent contrast of the $N_{\rm HI}$ maps with the structure of the γ-ray flux emerging from the H I gas. We have not tested different spin temperatures for each cloud complex. The maximum log-likelihood value of

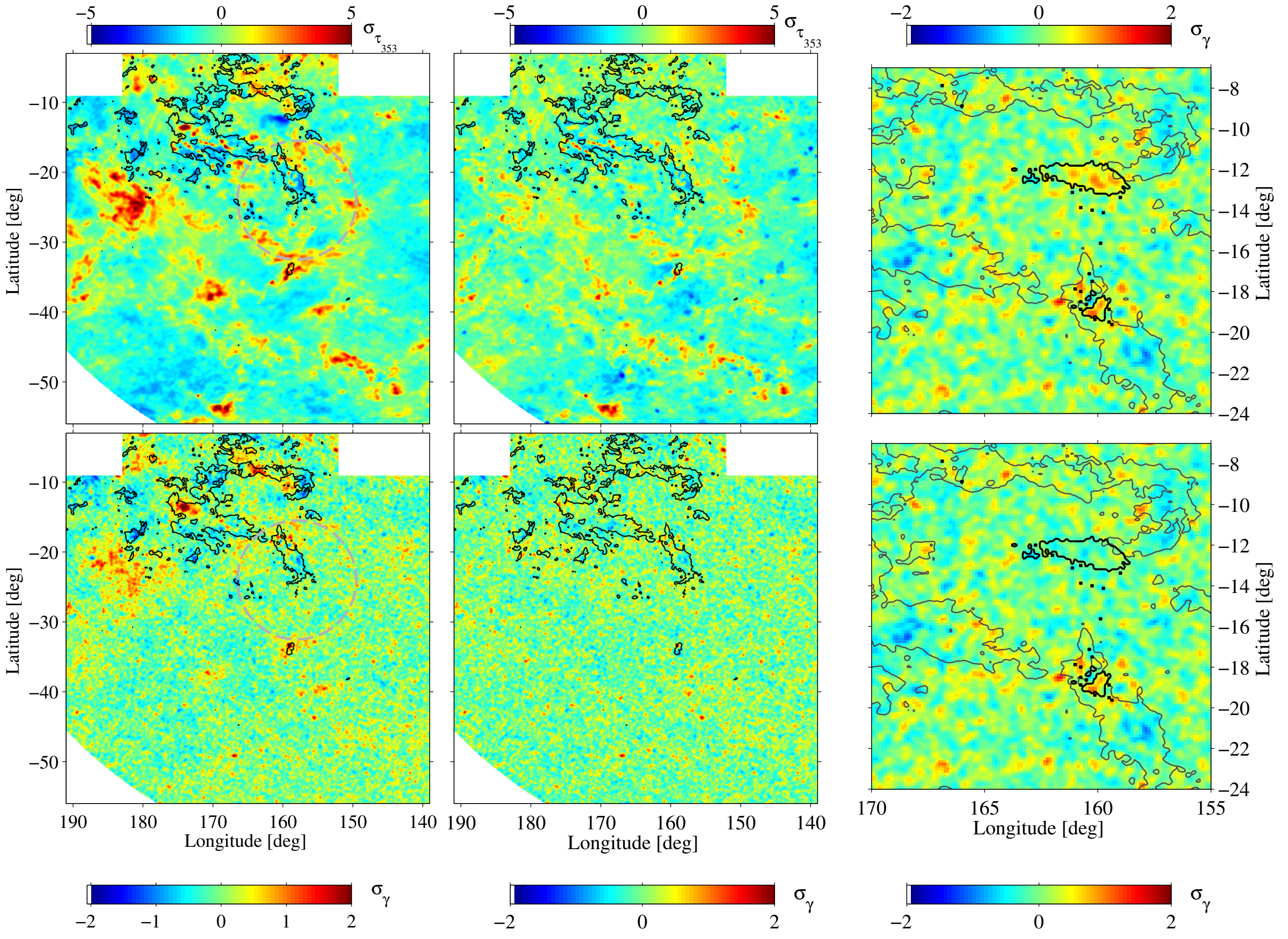

Fig. 7. Residual maps (data minus best-fit model, in sigma units) in dust optical depth ($\sigma_{\tau_{353}}$) and in γ-ray counts in the 0.4–100 GeV band (σ_γ) obtained when including different sets of gaseous components in the models: without (*left*) and with (*middle*) the DNM and COsat components in addition to the H I , CO, and free-free templates; a close-up view (*right*) of the γ-ray residuals without (*top*) and with (*bottom*) the free-free map. The grey circles in the left-hand column highlight a DNM shell. The thin black contours outline the shape of the CO clouds at the 7 K km s^{-1} level chosen to separate DNM and CO$_{\rm sat}$ components. The thick black contours in the right-hand column outline the shape of the NGC 1499 and G159.6-18.5 H II regions at the 2×10^4 Jy sr^{-1} level in free-free emission at 70 GHz. The models are derived for an H I spin temperature of 400 K.

the γ-ray fit peaks for an H I spin temperature near 400 K (see Fig. C.1 in Appendix C). In the following, we present the results obtained for this temperature, unless otherwise mentioned.

Spin temperatures are generally measured from pairs of H I emission and absorption spectra against bright radio sources (Heiles & Troland 2003; Mohan et al. 2004; Kanekar et al. 2011; Roy et al. 2013b; Murray et al. 2015). Line-of-sight harmonic means assume a single spin temperature along a sight line over the whole H I line or per velocity channel, as in the present work (monophasic $T_{\rm S}$). The average value near 400 K that we find is consistent with the sparse distribution of previous monophasic spin measurements in this region (Mohan et al. 2004; Kanekar et al. 2011) and with the temperature span of 200–600 K found at high Galactic latitudes for the range of $N_{\rm HI}$ column densities dominating the present maps. But the monophasic assumption is known to bias the spin temperatures to higher values and to characterize the mixture of the cold and warm neutral mediums (CNM and WNM) along the line of sight, rather than the physical temperatures of individual structures (Murray et al. 2015). Monophasic temperatures tend to decrease with increasing $N_{\rm HI}$ column densities because of the increasing proportion of CNM along the line of sight (Kanekar et al. 2011).

4.2. Best fits and jackknife tests

The best dust and γ-ray fits that could be achieved with the models described by equations 6 and 7 include all the free-free, H I , DNM, CO, and CO$_{\rm sat}$ templates for the gaseous components. Table D.1 gives the corresponding best-fit coefficients and Sec. 4.5 discuss the goodness of fit with these models. Sections 4.3 and 4.4 further discuss how the models have improved by adding gas templates other than H I and CO. We focus here first on the determination of the uncertainties associated with each parameter in the models.

The large spatial extents of the maps and the existence of tight correlations between the gas, dust, and γ-ray distributions yield small statistical errors on the best-fit coefficients. They have been inferred from the information matrix of the fit (Strong 1985) and they include the effect of correlations between parameters. The gas parameters of the local clouds have precisions of 1–5% and 1–4% in dust and γ rays, respectively. Only the small contributions of the H ii regions and of the Cetus CO clouds to the γ-ray data have respective uncertainties of 10% and 14%.

We have checked the magnitude of systematic uncertainties in our linear modelling approximations, hence of spatial changes in the model and/or in the mean level of H i and CO self-absorption. We did so by repeating the last dust and γ-ray fits a thousand times over subsets of the analysis region, namely after masking out 20% of the pixels with a sum of 2.625°-wide, randomly selected squares. In γ rays, the jackknife tests have been performed only for the total 0.4–100 GeV energy band.

Figures 5 and 6 show the distributions thus obtained for the best-fit coefficients that are significantly detected. Most of them show Gaussian-like distributions, thereby indicating that the results presented in Tables D.1 are statistically stable and that the average coefficients that describe our models are not driven by subset regions in each cloud complex. Several distributions exhibit long, non-Gaussian tails when the corresponding clouds subtend small solid angles (e.g., the H ii regions or the CO clouds from the Galactic disc or Perseus). The long tails reflect the indeterminacy of the parameter when a large fraction of their maps are masked.

The standard deviations found in the jackknife distributions amount to 1–3% and 1–4% for the extended H i and DNM components in dust and γ rays, respectively. The deviations are slightly larger, respectively 1–5% and 2–10%, for the more compact CO clouds in the local ISM.

We have quadratically added the 1 σ fitting error and the standard deviation of the jackknife distributions to give the statistical errors listed in Table C.1. The jackknife tests have been carried out for the total energy band. We have assumed the same relative deviations, σ_q/q, for the individual energy bands as for the total one since the jackknife samples test potential non-uniformities in the models at larger scales than the angular resolution of the data.

The results indicate that the small contribution of the faint Cetus CO clouds to the total γ-ray photon counts is only detected below 4 GeV. Similarly, the faint CO clouds from the edge of the Galactic disc are not detected against the much larger γ-ray contribution from the Galactic atomic gas (see Fig. 4). In the dust fit, all components are significantly detected.

We have checked the convergence of the iterative scheme described in Sect. 3.3 by monitoring the increase in the maximum log-likelihood value of the γ-ray fit as we progressed into the iterations until saturation. The log-likelihood ratio $2\Delta \ln(L)$ of 1180 between the last and first iterations indicates a large improvement in the quality of the fits because of a better separation of the different gas structures. The initial fits yielded too-large H i and CO parameters to compensate for the missing gas. As the construction of the DNM and $\mathrm{CO_{sat}}$ maps improved through the iterations, the bias on the H i and CO parameters relaxed. Between the first and last iterations, the H i and CO γ-ray emissivities dropped by 5-21% and 4-22%, respectively, depending on the cloud complex and its spatial overlap with DNM and $\mathrm{CO_{sat}}$ structures. Similarly, the dust opacities of the H i and CO clouds decreased by 10-42% and 36-87%, respectively.

4.3. Detection of DNM and $\mathrm{CO_{sat}}$ gas

Prior to building the complete models, we have checked for the presence of substantial amounts of gas that are not traced by the H i and CO line intensities or free-free emission, but that are perceptible in parallel in the independent γ-ray and dust data sets. To do so, we have performed the dust and γ-ray fits with only the H i , CO, and free-free templates for the gaseous components. We find that the data exceed the model predictions in several extended regions (see the positive residuals in the left column of Figure 7) and that the excesses correlate in space in the independent dust and γ-ray data. Adding the DNM and $\mathrm{CO_{sat}}$ templates to the models significantly improves the quality of the fits (see the middle column of Figure 7). The log-likelihood ratio of 6427 between the γ-ray fits with and without the DNM and $\mathrm{CO_{sat}}$ components implies that those components are detected at a formal confidence level greater than 80 σ (Neyman & Pearson 1933). Hadronic interactions between cosmic rays and dust grains, or IC up-scattering of the dust thermal radiation would yield too few γ rays to explain such a correlation (Grenier et al.

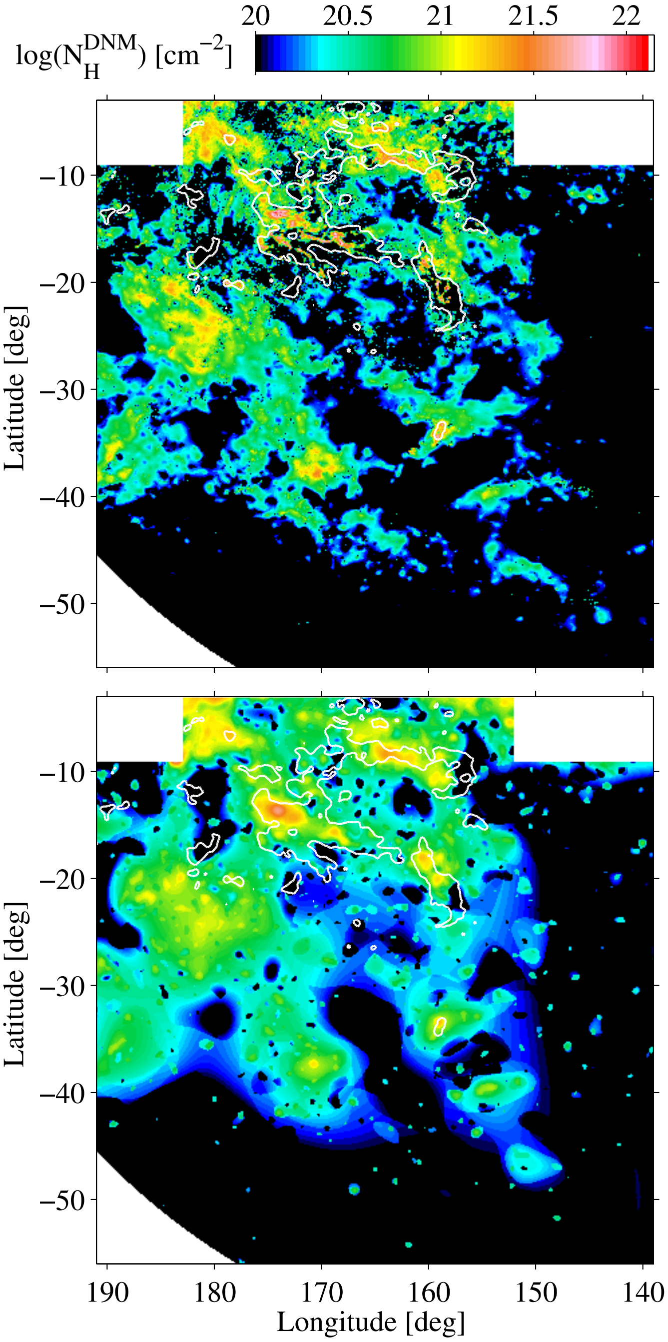

Fig. 8. Hydrogen column density maps in the DNM and $\mathrm{CO_{sat}}$ components, derived from the dust (*top*) and γ-ray (*bottom*) data. The demarcation between the two components is outlined by the white contour at 7 K km/s in CO line intensity.

2005). A coincident variation both in CR density and in dust-to-gas ratio is very improbable, so the CRs and dust jointly reveal gas in excess of the H I , CO, and ionised expectations in those directions. The spectrum of the γ-ray emission associated with both components is consistent with that found in the other gas phases over the 0.4-100 GeV energy range (see Sect. 5). This gives further support to a gaseous origin of the γ-ray emission in the DNM and CO_{sat} structures and to a smooth penetration of the CRs from the atomic envelopes to the dense parts of the clouds with saturated CO lines.

A log-likelihood ratio of 1404 between the models with different or with equal emissivities for the DNM and CO_{sat} components strongly supports their separation into distinct components. The DNM map traces column densities of dense H I and/or diffuse H_2 at the atomic–molecular transition of the clouds whereas the CO_{sat} map reveals dense H_2 in excess of that linearly traced by W_{CO} because of the saturation of the CO lines (W_{CO} remains constant as N_{H_2} keeps increasing). Without kinematic information, we cannot separate the DNM and CO_{sat} contributions from the different cloud complexes when they overlap in direction. To extract the column densities displayed in Fig. 8, we have assumed that the DNM and CO_{sat} gas is pervaded by the average CR density measured in the atomic phase of the different clouds in the region (Grenier et al. 2005; Planck and Fermi Collaborations 2015). We show in Sect. 5 that the small cloud-to-cloud dispersion in γ-ray emissivity per gas nucleon justifies the use of the average.

We defer the discussion of the DNM and CO_{sat} gas masses and their relation to the H I -bright, ^{12}CO-bright, and ^{13}CO-bright phases to a companion paper.

4.4. Detection of ionised gas

We have also checked the significance of the addition of the free-free template to the final γ-ray and dust models, and we have tested the gaseous origin of the corresponding γ-ray signal. We develop both points in this section.

The log-likelihood ratio of 116 between the models with and without the free-free template supports a γ-ray detection of the H II regions at a formal confidence level greater than $10\,\sigma$. The close-up view in Fig. 7 shows the clear detection of a γ-ray excess toward the bright NGC 1499 region and the more marginal gain in adding the small column densities of ionised hydrogen from the fainter G159.6-18.5 region. By replacing the free-free map by a broad Gaussian source located toward the centre of NGC 1499, we have checked that the fit significantly requires an extended excess ($7\,\sigma$), with a FWHM comprised between 1.4° and 3.6° at the 95% confidence level. The Gaussian source, however, yields a poorer fit than the more elongated free-free emission.

The two H II regions, NGC 1499 and G159.6-18.5, are respectively excited by a giant and a main-sequence O star. Part of their intense stellar light is upscattered to γ rays by the local CR electrons (Orlando & Strong 2007). Given the distance, luminosity, and effective temperature of each star, we have calculated the IC γ-ray flux produced in its vicinity and we have integrated the flux over the angular sizes of the H II region, in the 0.4–100 GeV energy band. We find IC fluxes of $\sim 2.9 \times 10^{-11}$ cm^{-2} s^{-1} and $\sim 5.9 \times 10^{-12}$ cm^{-2} s^{-1}, respectively, that cannot account for the γ-ray fluxes of $(2.5 \pm 0.4) \times 10^{-8}$ cm^{-2} s^{-1} and $(2.3 \pm 0.4) \times 10^{-9}$ cm^{-2} s^{-1} seen in correlation with the free-free emission. Hence, the γ-ray excesses seen toward NGC 1499 and partially toward G159.6-18.5 are more likely due to hadronic interactions of the local CRs in the ionised gas.

The weak correlation between the dust optical depth τ_{353} and the free-free template highlighted by the jackknife test probably reflects the difficulty of estimating τ_{353} toward regions of strong spectral gradients (see Fig. 2), in particular because the β index and the grain temperature have been derived at different angular resolutions (Planck Collaboration 2014a).

Assuming a uniform CR flux in the H I and H II gas phases, we have used the average γ-ray emissivity of the atomic gas in the region (see Sect. 5) and the best-fit q_{ff} parameter obtained for the 0.4–100 GeV band to convert the free-free intensities to hydrogen column densities and compare them with the values expected from equation 5. The electron temperature of H II regions is known to vary with Galactocentric radius because of the metallicity gradient (Alves et al. 2012). Adopting a mean value in the solar neighbourhood between 7000 K and 8000 K, we find an average electron density of (4.3 ± 0.6) cm^{-3} in the H II regions sampled here.

At the distance $d \approx 380$ pc to ξ Persei inside NGC 1499 (van Leeuwen 2007), the 80′ radius of the ionised region is $L = 9$ pc. The fractional thickness of the shell, relative to L, is estimated to be $l = 0.38$ (Shinohara & Ishida 1976) and the nebula subtends a solid angle $4\pi\tilde{\sigma}$ with $\tilde{\sigma} = 0.21$ at the exciting star. The H_α flux is corrected for the interstellar absorption as $F_{\alpha 0} = 10^{0.292 A_V} F_\alpha$, with A_V the visual extinction up to 500 pc derived from the 3D extinction map of Green et al. (2015). According to Shinohara & Ishida (1976) for equal electron and ion volume densities, the mean electron density of a shell-like nebula such as NGC 1499 can be expressed as $\overline{n}_e = S\,V^{\frac{1}{2}}$ with the effective volume

$$V = \frac{4}{3}\pi L^3 \tilde{\sigma}[1 - (1 - l)^3] \tag{8}$$

and the excitation parameter

$$\frac{S}{\mathrm{cm^{-3/2}}} = \left(\frac{1}{9.46 \times 10^{-60}}\right)\left(\frac{F_{\alpha 0}}{1\,\mathrm{erg\,cm^{-2}\,s^{-1}}}\right)\left(\frac{d}{1\,\mathrm{pc}}\right)^2\left(\frac{T_e}{1\,\mathrm{K}}\right)^{0.87} \tag{9}$$

The electron temperature T_e of the nebula can be estimated by comparing the free-free and H_α emissions. The H_α intensity in Rayleigh units is expressed as a function of the emission measure $\int n_e n_i ds$ as :

$$I_{H_\alpha} = \frac{1}{2.75}\left(\frac{T_e}{10^4\,\mathrm{K}}\right)^{-0.9} \int n_e n_i ds \tag{10}$$

Combining equations (4) and (10), we obtain

$$T_e = 2.43\,\mathrm{K}\left(\frac{I_{ff}}{I_{H_\alpha}}\right)^{\frac{1}{0.62}} \tag{11}$$

Given this temperature, we can estimate the mean electron density.

If we apply those calculations to NGC 1499 within a low contour at $I_{ff} = 2 \times 10^4$ Jy sr^{-1}, we find a mean temperature of (6100 ± 2700) K and a mean electron density $\overline{n}_e = (15.1 \pm 6.7)$ cm^{-3}. If we adopt a more restrictive contour where the γ-ray residuals exceed 0.8σ in the best-fit model without the free-free template, we find $\overline{T}_e = (7700 \pm 1700)$ K and a mean density $\overline{n}_e = (5.0 \pm 1.1)$ cm^{-3} in good agreement with the gas density estimate inferred from the correlation between the γ rays and the nebular free-free emission. This agreement gives further weight to a hadronic origin of the γ rays associated with NGC 1499.

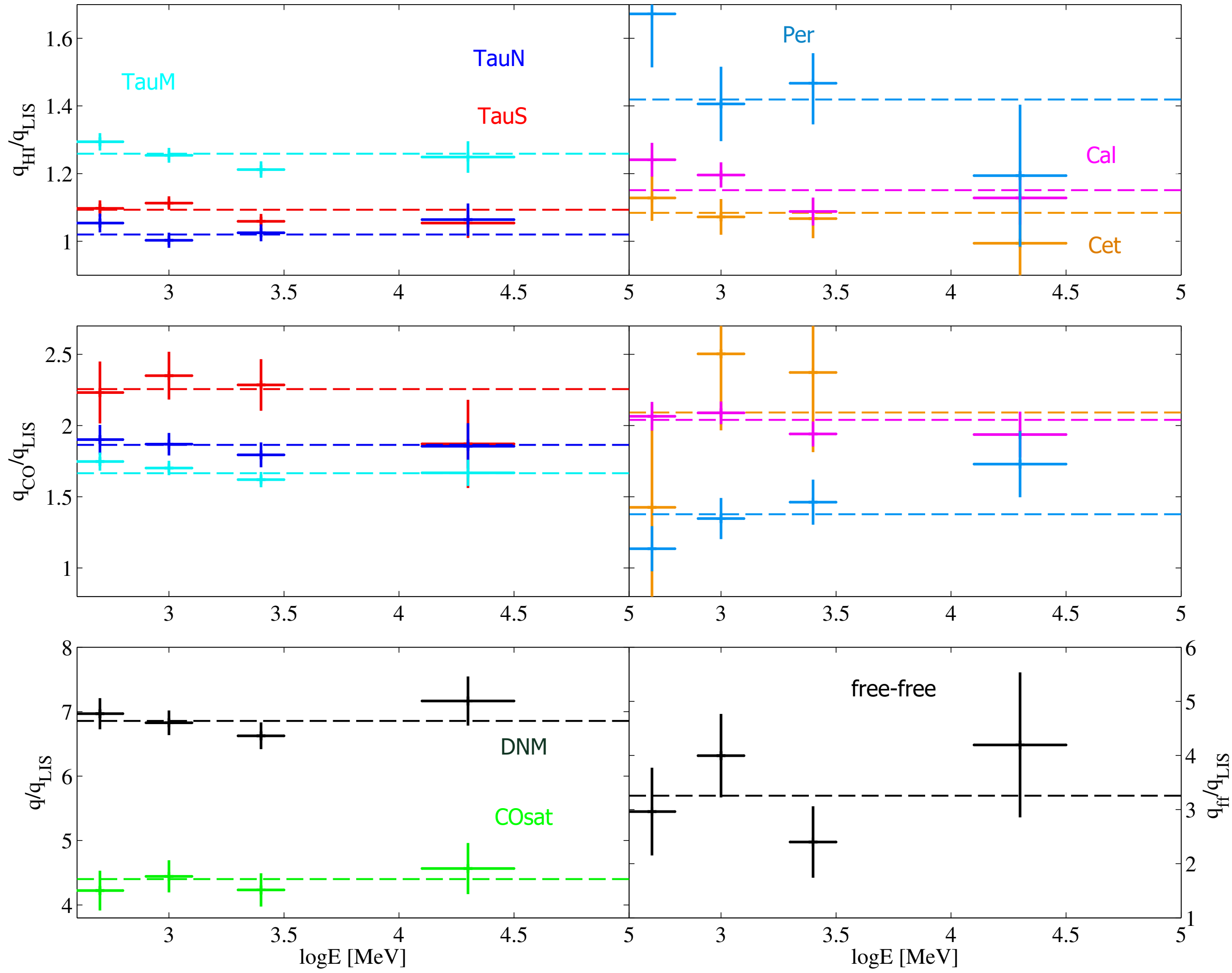

Fig. 9. Spectral evolution, relative to the local interstellar spectrum $q_{\rm LIS}$, of the γ-ray emissivities of the local gas components. $q_{\rm CO}$ is given in units of $10^{20}{\rm cm}^{-2}$ (K km s^{-1})$^{-1}$ and $q_{\rm DNM}$ in $10^{25}{\rm cm}^{-2}$. The $q_{\rm HI}$ normalizations are given for a spin temperature of 400 K. The dashed lines compare the results obtained for the whole 0.4–100 GeV band to the results of the four independent bands. All error bars are symmetrical; horizontal error bars at the boundaries are truncated.

4.5. Final model residuals

The residuals obtained between the dust and γ-ray data and the best fits that include all gaseous components are presented in the middle column of Fig. 7. They show that the linear model provides an excellent fit to the γ-ray data in the overall energy band, as well as in the separate energy bands which are not shown. The residuals are consistent with noise at all angular scales except, marginally, toward the brightest CO peaks where the model tends to over-predict the data. Significant positive residuals remain at small angular scales in the dust fit. They closely follow the spatial distribution of the DNM and they are likely due to the limitations in angular resolution and in sensitivity of the γ-ray DNM template compared to its dust homologue. Small-scale clumps in the residual structure can also reflect localized variations in dust properties per gas nucleon that are not accounted for in the linear models, in particular toward the brightest CO regions. These effects are discussed in Sect. 7.

A wide, 17°-diameter shell, centred on l = 158° and b = −24° is apparent in the initial dust residuals, and also marginally in the γ-ray residuals (see the left column of Fig. 7). The shell is rich in DNM gas (see Fig. 8). We have found no coincident structure at other wavelengths that could explain this shell in terms of a nearby H II region or old supernova remnant.

5. γ-ray emissivity of the gas

The γ-ray emissivity spectra of the local gaseous components are presented in Fig. 9. We note that all the $q_{\rm HI}$ normalizations exceed one because the present fits preferred a larger H I spin temperature than the value of 140 K adopted for the derivation of $q_{\rm LIS}$ across the whole sky off the Galactic plane (Casandjian 2015). We find no significant spectral variations except in Perseus for which we observe opposite trends for $q_{\rm HI}$ decreasing and $q_{\rm CO}$ increasing with energy. This behaviour can be attributed to the cross talk between the very compact set of H I and CO clouds in Perseus as the LAT PSF degrades at low energies.

The results indicate that the CR population permeating the various phases of the different clouds has the same energy distribution as the average in the local ISM (Casandjian 2015). We find no spectral signature that would betray exclusion or concentration processes in a particular cloud or with increasing gas density, from the diffuse atomic gas in Cetus up to the densities of 10^{3-4} cm^{-3} sampled by 2.6-mm CO line emission. Together with similar findings in the Chamaeleon clouds (Planck and Fermi Collaborations 2015), these results support the theoretical predictions that CRs with energies between a few hundreds of MeV and a few tens of GeV smoothly diffuse through the H I -bright and CO-bright parts of the ISM (Skilling & Strong 1976; Cesarsky & Volk 1978; Padovani & Galli 2011), up to column densities of 10^{21-22} cm^{-2} (Morlino & Gabici 2015). The volume densities of the gas covered by H I and CO observations are modest, but they hold the bulk of the interstellar gas mass, γ rays should reliably trace most of the interstellar gas.

We can compare the γ-ray emissivities measured in the anticentre clouds for a spin temperature of 150 K with the average value found in the local ISM for $T_{\rm spin}$ = 140 K (Casandjian 2015), as shown in Fig. 10. The 35±1% lower emissivity that we find for the atomic gas in the Galactic-disc background is not useful for comparison as it integrates all distances beyond the local ISM, through regions of decreasing CR density along lines of sight outward through the Galaxy (Abdo et al. 2010; Ackermann et al. 2011) and to high altitudes above the Galactic disc (Tibaldo et al. 2015). Within a few hundred parsecs, we find small cloud-to-cloud differences in γ-ray emissivity. The Cetus, South Taurus, and North Taurus clouds compare well with the average in the local ISM whereas the California, Main Taurus and Perseus clouds appear to be $15 \pm 3\%$, $12 \pm 2\%$, and $36 \pm 6\%$ more emissive than the average, respectively. Except for Perseus, these variations are commensurate with previous measurements. Figure 10 shows a cloud-to-cloud dispersion of ±9% that does not relate to the cloud altitude above the Galactic disc, nor to the cloud location with respect to the local spiral arm (Galactocentric distance). This dispersion largely stems from uncertainties in the derivation of the $N_{\rm HI}$ column densities. We note indeed that the $q_{\rm HI}$ emissivity is 10% to 20% larger in the Cepheus-Polaris, Main Taurus, California, RCrA and Chamaeleon clouds where $N_{\rm HI}$ column densities in the 80th percentile exceed 10^{21} cm^{-2}, a level at which H I optical depth corrections become significant.

The emissivity in Perseus is at variance with the other nearby clouds, but less so at high energy where the LAT PSF allows a firmer separation between the compact atomic and molecular phases of the cloud. The origin of the high emissivity will be investigated using photon selections with improved angular resolution as soon as the photon statistics permit the analysis. For the anticentre region under study, we derive very consistent averages regardless of whether we include the Perseus data to the other five measurements or not. We have used this average emission rate in the 0.4–100 GeV band, $\overline{q}_{\rm HI} = (6.0 \pm 0.3) \times 10^{-27} \gamma$ s^{-1} sr^{-1} H^{-1}, in the atomic gas to infer column densities in the other gas phases.

6. $X_{\rm CO}$ factors

The $X_{\rm CO}$ factor is often applied to convert $W_{\rm CO}$ intensities to hydrogen-equivalent $N_{\rm H_2}$ column densities in the molecular phase. In γ rays, under the assumption of a uniform CR flux in the H I -bright and CO-bright phases, it is derived as $X_{{\rm CO}\gamma} = q_{\rm CO}/(2q_{\rm H_I})$, independently in each energy band. This ratio also assumes that helium is uniformly mixed by number with hydrogen in the ISM. Likewise, assuming a uniform dust-to-gas mass ratio and a uniform emission coefficient κ_{353} of the grains at 353 GHz, the $X_{\rm CO}$ factor is derived in the dust fit as $X_{{\rm CO}\tau} = y_{\rm CO}/(2y_{\rm H_I})$. The results of the two methods for the six CO clouds selected in our analysis are given in Table 1. The γ-ray results in the individual energy bands are displayed in Fig. 11.

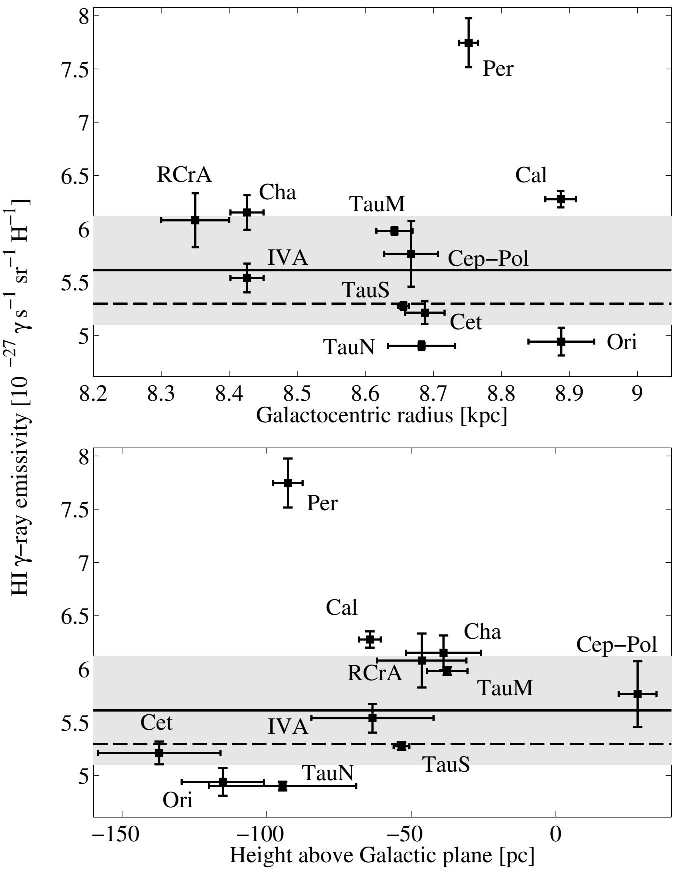

Fig. 10. Distribution with Galactocentric radius (top) and altitude above the Galactic disk (bottom) of the 0.4–10 GeV emissivities measured in the atomic gas of nearby clouds for H I spin temperatures between 125 and 150 K. The solid and grey band respectively give the average emissivity and ± 1 rms dispersion in the sample. The dashed line marks the average emissivity measured across the sky at $|b| \geq 7°$ (Casandjian 2015).

Table 1. $X_{\rm CO}$ factors in 10^{20} cm^{-2}K^{-1}km^{-1}s for the dust and γ-ray fits.

Cloud	τ_{353}	γ rays
Cetus	1.58±0.08±0.07	1.01±0.16±0.07
Taurus South	1.44±0.04±0.04	1.04±0.05±0.05
Taurus North	1.55±0.03±0.05	0.90±0.03±0.05
Taurus Main	1.24±0.02±0.06	0.67±0.01±0.04
California	1.11±0.03±0.07	0.87±0.03±0.03
Perseus	1.03±0.05±0.12	0.44±0.04±0.04

Notes. The first uncertainties are statistical, the second give the standard deviations obtained by varying the H I spin temperature.

6.1. $X_{\rm CO}$ measurements in γ rays

We find $X_{\rm CO}$ values for the present clouds that compare well with previous γ-ray measurements in other nearby clouds. For $X_{\rm CO}$ factors obtained with *Fermi* LAT at comparable angular resolution, we can cite the values of $0.63 \pm 0.02^{+0.09}_{-0.07}$ in the Cepheus-Polaris complex (Abdo et al. 2010), of $0.99 \pm 0.08^{+0.18}_{-0.10}$ in the RCrA cloud (Ackermann et al. 2012c), of 1.21±0.02 in the Orion

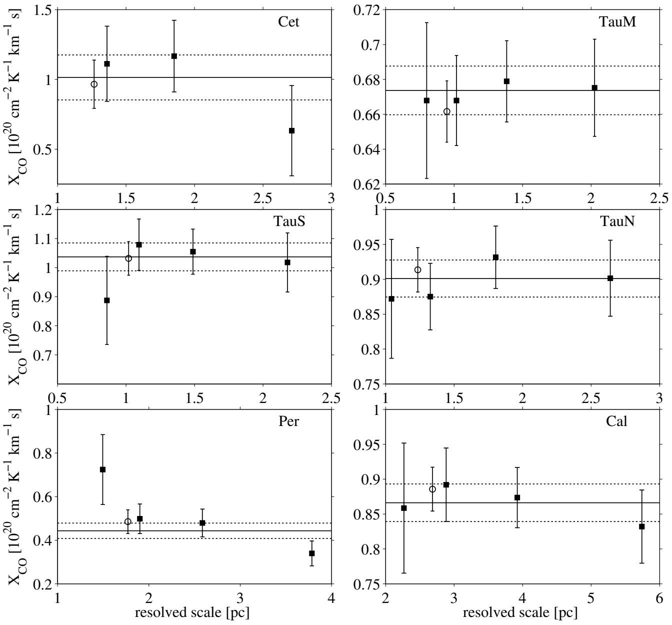

Fig. 11. Evolution of the X_{CO} factor, as measured in γ rays for various linear resolutions in the different clouds. The open circle marks the value obtained in the overall 0.4–100 GeV band, in close agreement with the weighted average of the four independent energy bands (black line) and its 1σ errors (dashed lines).

clouds (Ackermann et al. 2012b), and of $0.69 \pm 0.02^{+0.03}_{-0}$ in the Chameleon clouds (Planck and Fermi Collaborations 2015), in units of 10^{20} cm^{-2} K^{-1} km^{-1} s. We note that the X_{CO} factors in those well-resolved clouds are all close to or lower than 10^{20} cm^{-2} K^{-1} km^{-1} s. Table E.1 lists historical γ-ray estimates of X_{CO}. It shows that the estimates in nearby clouds have remained stable or only slightly decreased as the angular resolutions of the H I , CO, and γ-ray surveys have improved. The lower level of cross-correlation between the H I and CO structures on the one hand, a better separation of the γ radiation produced in the atomic and molecular phases on the other hand, and a lower contamination from unresolved γ-ray point sources has primarily improved the precision of the measurements. The latest analyses with <10.8′ FWHM resolution in H I , 8.5′ resolution in CO, and *Fermi* LAT data consistently yield low X_{CO} values, ranging between 0.5 $\times 10^{20}$ cm^{-2} K^{-1} km^{-1} s and 1.2 $\times 10^{20}$ cm^{-2} K^{-1} km^{-1} s. Systematic uncertainties on the N_{HI} column densities due to H I optical depth corrections impact the estimation of the γ-ray emissivities per gas nucleon. Analyses for different H I spin temperatures show that the resulting systematic uncertainty on the X_{CO} factors amount to (0.1-0.2) $\times 10^{20}$ cm^{-2} K^{-1} km^{-1} s.

The values listed in Table E.1 highlight a recurrent discrepancy between the X_{CO} measurements at small scale in nearby clouds and the two-to-three times larger values found at kiloparsec scales when averaging over a population of molecular complexes in spiral arms or in Galactocentric rings. We return to this point at the end of this section.

In Fig. 11 we take advantage of the energy-dependent PSF of the LAT to probe various linear scales within the present nearby clouds. The scale is derived using the half-width at the half-maximum of the PSF integrated over the energy band for the q_{LIS} spectral shape. We find no evidence of X_{CO} changes at parsec scales except in Perseus.

Because the q_{HI} and q_{CO} variations in Perseus are inversely coupled in energy, the resulting change in X_{CO} is likely due to an increased level of cross-correlation between the compact H I and CO phases as the LAT PSF degrades (Figs. 4 and 9). If we force the γ-ray emissivity of the H I gas to be the same as the average found among the other clouds, we obtain a larger X_{CO} value of (0.68 ± 0.04)$\times 10^{20}$ cm^{-2} K^{-1} km^{-1} s, close to that measured above 4 GeV with the best LAT angular resolution. However, the use of this value implies a significant ($4.6\,\sigma$) degradation of the fit quality at lower energies. The likelihood analysis significantly supports a lower X_{CO} factor in Perseus. A low value is also indicated by the average of 0.3$\times 10^{20}$ cm^{-2} K^{-1} km^{-1} s found at 0.4-pc resolution in the dust, H I , and CO study of Lee et al. (2014).

Figure 12 compares γ-ray measurements of X_{CO} in nearby clouds from Planck and Fermi Collaborations (2015) and this work. We restrict the sample to estimates obtained in the Chamaeleon and anti-centre clouds because they are based on the same analysis method, the same γ-ray energy bands to ensure the same angular resolution of the LAT, and the same sampling resolution in the H I and CO data. They both include the DNM gas in the models. In Fig. 12 we explore whether the average X_{CO} factor in a cloud varies with parameters characterizing the cloud state. The distributions show that the average X_{CO} factor does not depend on the H_2 mass mapped in CO, nor on the dynamics of the cloud characterized by the velocity dispersion of the CO lines. But X_{CO} appears to depend on the cloud structure and in particular on its diffuseness. To reflect changes in the latter, we have explored several characteristics:

- the mean W_{CO} intensity, $\overline{W_{CO}}$, in a cloud, taken above 1 K km/s to avoid noise fluctuations;
- the surface fraction of dense regions with large W_{CO} intensity within a cloud, $SF_{dense} = S_{W_{CO}>7\ Kkm/s}/S_{W_{CO}>1\ Kkm/s}$ (with S a solid angle), which gauges the relative weight of diffuse and dense molecular regions in the determination of X_{CO};
- the mean visual extinction toward a cloud, $\overline{A_V^{CO}}$, taken from the NICER M2a 12′-resolution A_J map (Juvela & Montillaud 2016), translated into A_V using a colour ratio of 3.55 according to the extinction law of Cardelli et al. (1989). Only values in directions with W_{CO} > 1 K km/s and A_V > 0.8 mag. have been retained in the average to avoid noise contamination;
- the average CO line width, $\overline{\sigma_v^{CO}}$, in a cloud since optically-thick lines tend to be wider and X_{CO} should decrease with $\overline{\sigma_v^{CO}}$ (Shetty et al. 2011b).

Figure 12 shows that, for all these diagnostics, X_{CO} tends to decrease from diffuse to more compact clouds. The decrease remains significant if we use the Perseus X_{CO} value found when forcing the H I γ-ray emissivity to the local average, or if we exclude the Perseus data point. A uniform X_{CO} factor is strongly rejected ($> 30\sigma$) for all the diffuse diagnostics, whether we modify or exclude the Perseus data point or not.

The trend is consistent with the expectation that X_{CO} decreases from the diffuse envelopes, exposed to the photodissociating radiation field, to the shielded cores of the CO clouds (Polk et al. 1988; Sheffer et al. 2008; Liszt et al. 2010; Glover & Mac Low 2011; Shetty et al. 2011a; Liszt & Pety 2012; Lee et al. 2014). The turbulence level and the degree of virialization of the cloud (e.g., the ratio of kinetic to gravitational energy) also influences the average X_{CO} factor by allowing the ISRF to penetrate more or less deeply into the turbulent layers of the cloud (Bell et al. 2006; Bertram et al. 2016). Hence, we expect the average X_{CO} over a cloud to vary with the relative solid angle subtended

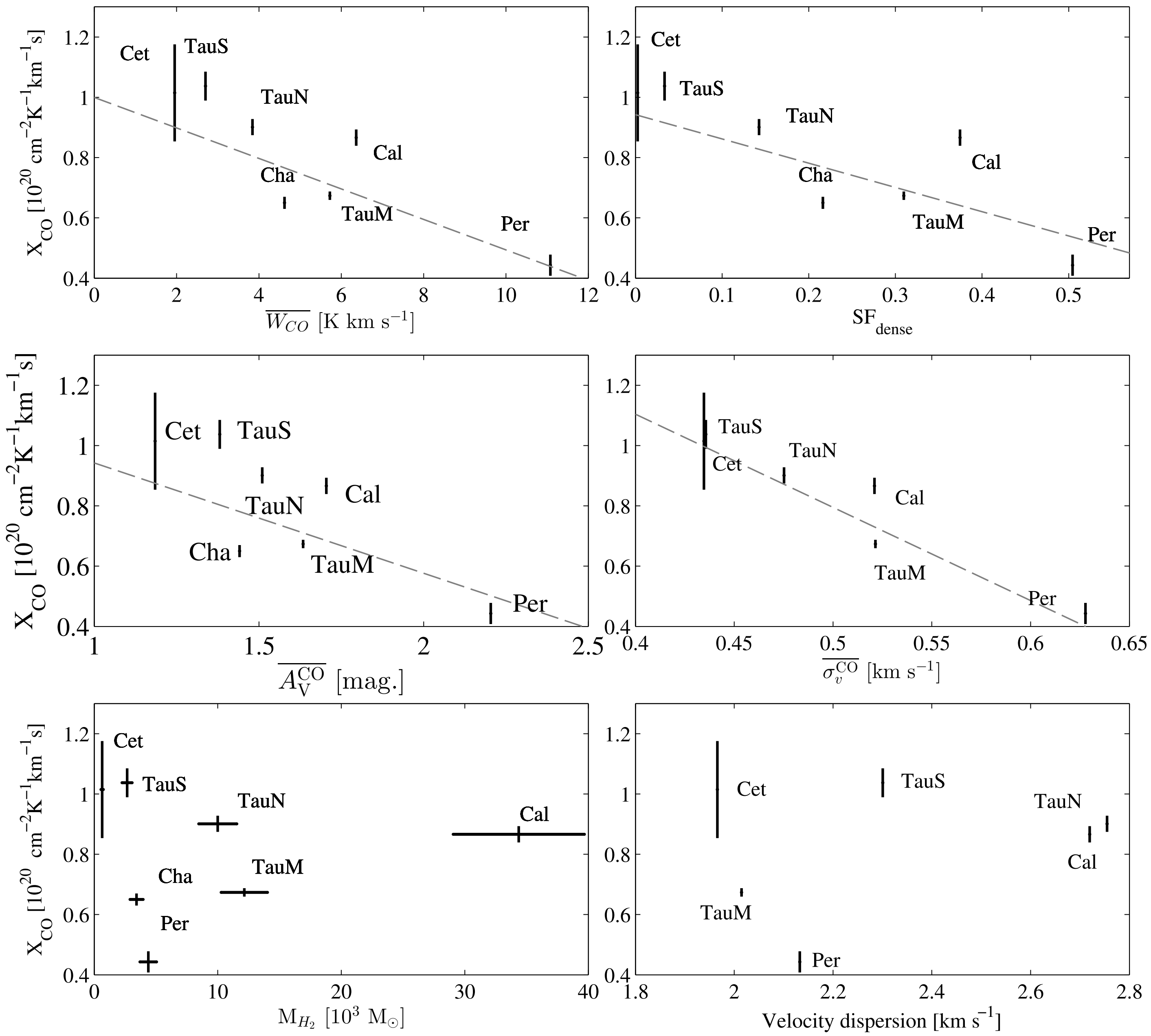

Fig. 12. Evolution of the X_{CO} factor measured in γ rays as a function of the average W_{CO} intensity, $\overline{W_{CO}}$, the surface fraction of dense gas, SF_{dense}, the mean visual extinction in the CO-bright phase, $\overline{A_V^{CO}}$, the average CO line width, $\overline{\sigma_v^{CO}}$, the H_2 mass in the CO-bright phase, M_{H_2}, and the velocity dispersion of the CO line. Dashed lines give the best (χ^2) linear regressions

by the diffuse and dense parts of the clouds, the former exhibiting weak CO emission and large X_{CO} values, the latter being CO-bright and having low X_{CO} values.

According to X_{CO} calculations as a function of visual extinction A_V (Bell et al. 2006), X_{CO} should drop by more than two orders of magnitude with increasing A_V, down to a minimum at $1 \lesssim A_V \lesssim 3$ mag. For long-lived clouds, exposed to the local cosmic-ray ionization rate of 1.4×10^{-17} s^{-1} (Grenier et al. 2015) and to the local ISRF, the minimum X_{CO} value reaches below 10^{20} cm^{-2} K^{-1} km^{-1} s for hydrogen densities larger than 10^3 cm^{-3} and/or for turbulent velocities larger than 1 km/s. Yet, the measured CO lines have widths below 0.7 km/s and the clouds in our sample are not massive enough to sustain such large average densities through most of their volume. Moreover, models of dense clouds show a steady increase in X_{CO} at all N_{H_2} column densities (Shetty et al. 2011a), at variance with the declining trends found in Fig. 12.

We have also compared the mean visual extinction, $\overline{A_V^{CO}}$, mean CO intensity, $\overline{W_{CO}}$, and X_{CO} factor in each cloud with the simulation results of Glover & Mac Low (2011). The $X_{CO}(\overline{W_{CO}})$ trend seen in Fig. 12 roughly compares in slope with the simulation expectations, but not in absolute values, even though the efficiency of the radiation screening compares well in the observations and simulations. We show in Sect. 7.1 that the A_V/N_H ratio measured in the clouds compares well with the Bohlin et al. (1978) value adopted in the simulations. For a given $\overline{A_V^{CO}}$ in a cloud, the simulations under-predict the mean $\overline{W_{CO}}$ intensity by a factor 20, and overpredict X_{CO} by a factor 40. The comparison should be taken with care because both the observation and simulation samples are sparse, because the observations span a smaller dynamical range in $\overline{W_{\rm CO}}$ than the simulations, and because the $\overline{W_{\rm CO}}$ and $\overline{A_{\rm V}^{\rm CO}}$ averages depend on the threshold applied to define CO cloud edges, which differs in both datasets. Nevertheless, the comparison highlights that, for initial volume densities ≤ 300 cm^{-3} applicable to the set of observed clouds, the simulations produce underluminous CO clouds at low densities compared to the observations. This was noted by Levrier et al. (2012). The CO deficit in their simulation reached a factor of 10 in column density in the peripheral regions exposed to the UV radiation, where $N_{\rm H_2} \lesssim 2 \times 10^{20}$ cm^{-2}. At larger column densities, the simulations and data compare much better. So, there seems to be a general problem with our understanding of chemistry at low gas density in the photo-dominated regions (PDR), either in the treatment of the UV attenuation or in the absence of warm chemistry driven by intermittent energy deposition in regions where the interstellar turbulence is dissipated (Godard et al. 2014).

The list of historical $X_{\rm CO}$ measurements given in Table E.1 and the values we are adding with the present sample of anticentre clouds confirm a recurrent discrepancy that exists between the mean $X_{\rm CO}$ factors measured with parsec resolution in nearby clouds and the $X_{\rm CO}$ averages obtained at the scale of spiral arms (Local and Perseus arms) or of the Galactic disk. The former are two to three times lower than the large-scale values, which are close to 2 $\times 10^{20}$ cm^{-2} K^{-1} km^{-1} s (see Table E.1). The change in $X_{\rm CO}$ with scale may be due to measurement biases induced by the sampling resolution, such as the increased difficulty at large distance to separate the clumpy CNM clouds and the DNM envelopes from the CO-bright phase. Misattributing a small part of the dense atomic gas or diffuse $\rm H_2$ would significantly bias the $X_{\rm CO}$ factor upward. For instance, confusing 10–20% of the CNM with the CO-related signal could explain the observed change in $X_{\rm CO}$ (Planck and Fermi Collaborations 2015). In nearby galaxies, Sandstrom et al. (2013) have indeed measured a systematically larger $X_{\rm CO}$ factor in highly inclined galaxies than in face-on ones where the pile-up along sight lines is reduced. Alternatively, the change in $X_{\rm CO}$ with scale may be due to the intrinsic structure of clouds and to the presence of $X_{\rm CO}$ gradients across them, as proposed by theory (Bell et al. 2006; Glover & Mac Low 2011) and supported by the data in Fig. 12. Such gradients impact how one averages $X_{\rm CO}$ over an ensemble of clouds in different states. $X_{\rm CO}$ averages in spiral arms can exceed local values if a large fraction of the molecular mass lies in diffuse, gravitationally unbound clouds where $X_{\rm CO}$ factors can reach very large values of 10^{20-22} cm^{-2} K^{-1} km^{-1} s (Bell et al. 2006; Shetty et al. 2011a). Another possibility is that the average is driven by the giant molecular clouds which are expected to exhibit $X_{\rm CO}$ values of a few 10^{20} cm^{-2} K^{-1} km^{-1} s because the gas is predominantly in the optically-thick CO regime. More tests are needed to disentangle the origin of the $X_{\rm CO}$ changes with scale. With larger photon statistics at high γ-ray energies, we should be able to investigate how the angular resolution and confusion between gas phases affect the calibration of $X_{\rm CO}$ beyond the solar neighbourhood.

6.2. $X_{\rm CO}$ measurements with dust

The results of the dust model provide an independent measure of $X_{\rm CO}$. Figure 13 shows that the dust-derived $X_{\rm CO}$ factors are systematically 30% to 130% larger than the γ-ray values. Systematic discrepancies had already been noted in previous studies (Planck Collaboration 2011a; Bolatto et al. 2013), but on the basis of different H I and CO surveys, different correlation methods, and different angular resolutions. In the present study, as in Planck and Fermi Collaborations (2015), the dust and γ-ray models are fitted to the same $N_{\rm HI}$ and $W_{\rm CO}$ maps, at the same resolution. Bolatto et al. (2013) proposed that the inclusion of the DNM gas in γ-ray analyses and its absence in dust analyses could explain the lower $X_{\rm CO}$ values obtained in γ rays, but, by construction, the inclusion of the DNM map cannot bias the $X_{\rm CO}$ estimate (Grenier et al. 2005; Planck and Fermi Collaborations 2015). Furthermore, the recent analyses include the DNM in both the dust and γ-ray fits and we have verified in this work that the $X_{\rm CO}$ values change by less than 20% when the DNM phase is added or not in the fits.

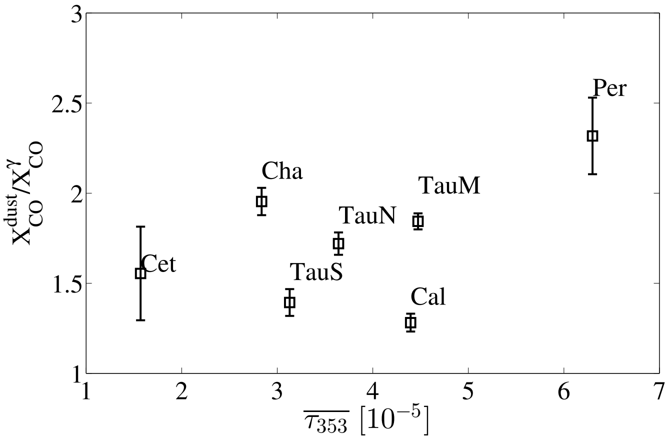

Fig. 13. Ratio of $X_{\rm CO}$ measurements with dust and γ rays in clouds of different average dust optical depth $\overline{\tau_{353}}$.

Alternatively, the standard derivation of the $X_{\rm CO}$ factor as $X_{\rm CO\tau} = y_{\rm CO}/(2y_{\rm H_I})$ is based on a uniform dust opacity, $\tau_{353}/N_{\rm H}$, across the gas phases. A change in dust emission properties, in particular an increase in $\tau_{353}/N_{\rm H}$ at large gas column densities, can significantly bias the $X_{\rm CO}$ factor upward (Planck and Fermi Collaborations 2015). We show in Sect. 7.2 evidence for such a departure from linearity in dense CO regions where $\tau_{353}/N_{\rm H}$ can increase by a factor of up to six due to grain evolution compared to their properties in the atomic gas. Outside the densest molecular parts (brightest in CO), the molecular hydrogen is more diffuse and the increase in $\tau_{353}/N_{\rm H}$ is more modest, by a factor ranging between 1.2 and about 2, so the resulting bias on the derivation of the average value of $X_{\rm CO}$ across a cloud is less than a factor of two.

Dust reddening and extinction maps have also been used to evaluate $X_{\rm CO}$ in nearby clouds. We find values in close agreement with the extinction study of Chen et al. (2015) in the main Taurus and Perseus clouds (their Taurus and Perseus E1 values). The present Taurus South complex overlaps their Taurus E1, E2, and E3 structures with respective $X_{\rm CO}$ factors of (0.84±0.01), (1.41 ± 0.02), and (1.69 ± 0.04)× 10^{20} cm^{-2} K^{-1} km^{-1} s bracketing our result in Taurus South.

Using the 2MASS extinction map of Dobashi et al. (2013), Paradis et al. (2012) found $X_{\rm CO}$ = (2.27 ± 0.9)× 10^{20} cm^{-2} K^{-1} km^{-1} s in the Taurus-Perseus region, without decomposing the different clouds. Their $A_{\rm V}/N_{\rm H}$ estimate of 5.33× 10^{-22} mag. cm^2 in this region is 20% lower than the all-sky $|b| > 10°$ average, but this difference is not sufficient to reconcile their measurement based on dust reddening with our values based on dust emission. The determination of $A_{\rm V}/N_{\rm H}$ in the H I phase directly impacts the derivation of $X_{\rm CO}$ in the embedded molecular phase. The different methods used to infer $A_{\rm V}$ from stellar data yield system-

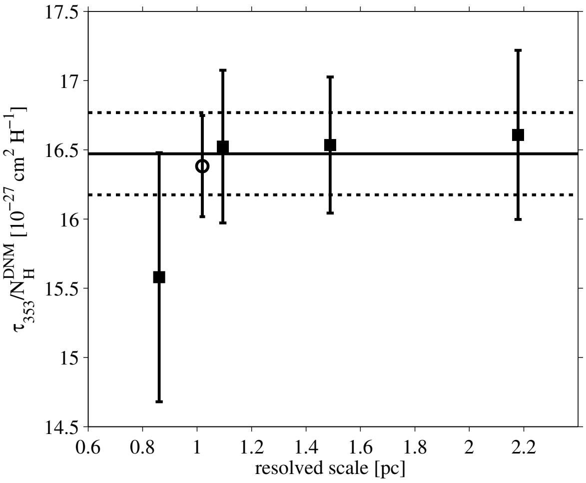

Fig. 14. Average dust opacities in the DNM measured in γ rays for different linear resolutions in the clouds. The open circle marks the measurement in the 0.4–100 GeV energy band, in close agreement with the weighted average of the four independent energy bands (black line) and its $\pm 1\sigma$ errors (dashed lines).

atic differences as large as 1 magnitude at low $A_{\rm V}$, toward the atomic and diffuse ISM (Dobashi et al. 2013; Green et al. 2015; Juvela & Montillaud 2016), so further analyses are necessary to evaluate their impact on $X_{\rm CO}$ measurements.

Pineda et al. (2010) have used 2MASS data and the NICER method to map the dust reddening and to derive $X_{\rm CO}$ near 2.1×10^{20} cm^{-2} K^{-1} km^{-1} s in the Taurus Main complex. In this case, the difference with our result can be explained because they did not separate the extinction related to H I along the CO sight lines, but they attributed all the dust to the molecular phase. In our analyses, we separate the dust or γ rays associated with each phase along all sight lines.

7. Dust evolution

7.1. Average dust opacities per gas phase

Our analyses yield average dust properties per H atom in each gas phase. The best-fit $y_{\rm HI}$ coefficients directly give the average dust opacities, $\overline{\tau_{353}/N_{\rm H}}^{\rm HI}$, in the H I structures. We have used the γ-ray estimates of the $X_{\rm CO}$ factors to derive the average dust opacities in the CO-bright phase of each complex, $\overline{\tau_{353}/N_{\rm H}}^{\rm CO} = y_{\rm CO}/(2X_{\rm CO\gamma})$. The results are listed in Table 2 together with similar measurements in the Chamaeleon clouds (Planck and Fermi Collaborations 2015). To ease the comparison with other dust reddening measurements, we have converted the dust opacities to $N_{\rm H}/E$(B-V) ratios using the $E({\rm B}-{\rm V})/\tau_{353}$ slope of $(1.49\pm0.03)\times10^4$ found in a large correlation study between τ_{353} and reddening measurements toward 53 399 quasars (Planck Collaboration 2014a). We did not attempt to estimate dust opacities in the ionised gas because of the large temperature gradients which impact the τ_{353} derivation toward the H II regions, with uncertainties in τ_{353} doubling near the hotspots.

The correlation existing between the γ-ray intensity and dust optical depth in the DNM yields an important measure of the average dust opacity in this phase. The value $\overline{\tau_{353}/N_{\rm H}}^{\rm DNM} = q_{\rm HI}/q_{\rm DNM}$ assumes a uniform CR flux across the H I and DNM phases, an assumption that is corroborated by the fact that both phases exhibit comparable γ-ray emissivity spectra and moderate gas volume densities. According to Fig. 14, we find no opacity changes at parsec scales in the extended DNM structures. The average, $\overline{\tau_{353}/N_{\rm H}}^{\rm DNM} = (16.5\pm0.3)\times10^{-27}$ cm^2, compares very well with the value of $(17.2\pm0.5)\times10^{-27}$ cm^2 obtained in the DNM surrounding the Chamaeleon clouds (Planck and Fermi Collaborations 2015).

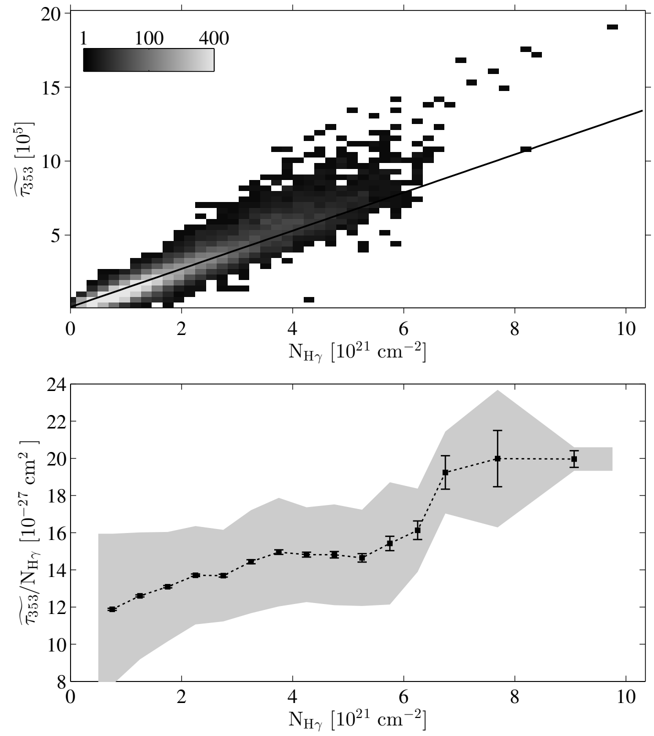

Fig. 15. Upper : 2D histogram of the correlation between the total gas column density, $N_{\rm H\gamma}$, measured with the 0.4–100 GeV interstellar γ rays, and the dust optical depth at 353 GHz, convolved with the LAT response for an interstellar spectrum. The maps were sampled at a $0^{\circ}\!.375$ resolution. Lower : evolution of the dust opacity in $N_{\rm H}$ bins. The error bars give the standard errors of the means and the grey band gives the standard deviation of the opacities in each bin.

Using optically thin H I , Planck Collaboration (2014a) found marked gradients in dust opacity across the sky, with values ranging from 6.6 to about 11×10^{-27} cm^2 in the atomic gas, and a high-latitude value of $(7.0\pm2.0)\times10^{-27}$ cm^2 in good agreement with the opacity of $(7.1\pm0.6)\times10^{-27}$ cm^2 derived in high-latitude cirruses with a different analysis method (Planck Collaboration 2014b). The opacities continued to increase in the CO-bright phase, up to 18×10^{-27} cm^2 for an $X_{\rm CO}$ factor of 10^{20} cm^{-2} K^{-1} km^{-1} s. Our results confirm that dust opacities vary from cloud to cloud and they can reach values well in excess of the high-latitude value, both in the atomic and molecular phase.

We find 50% to 135% larger opacities in the anticentre H I clouds than in the more diffuse H I cirruses, even though we have corrected the $N_{\rm HI}$ column densities for a spin temperature of 400 K. The systematic uncertainties on $\tau_{353}/N_{\rm H}$ due to the H I optical depth correction are listed in Table 2 as the second set of errors. Given the likelihood variations shown in Fig. C.1, we have taken the standard deviation in the set of measurements as a function of spin temperature for each parameter to represent such an uncertainty. Considerations of those uncertainties cannot reconcile the individual cloud measurements and the cir-

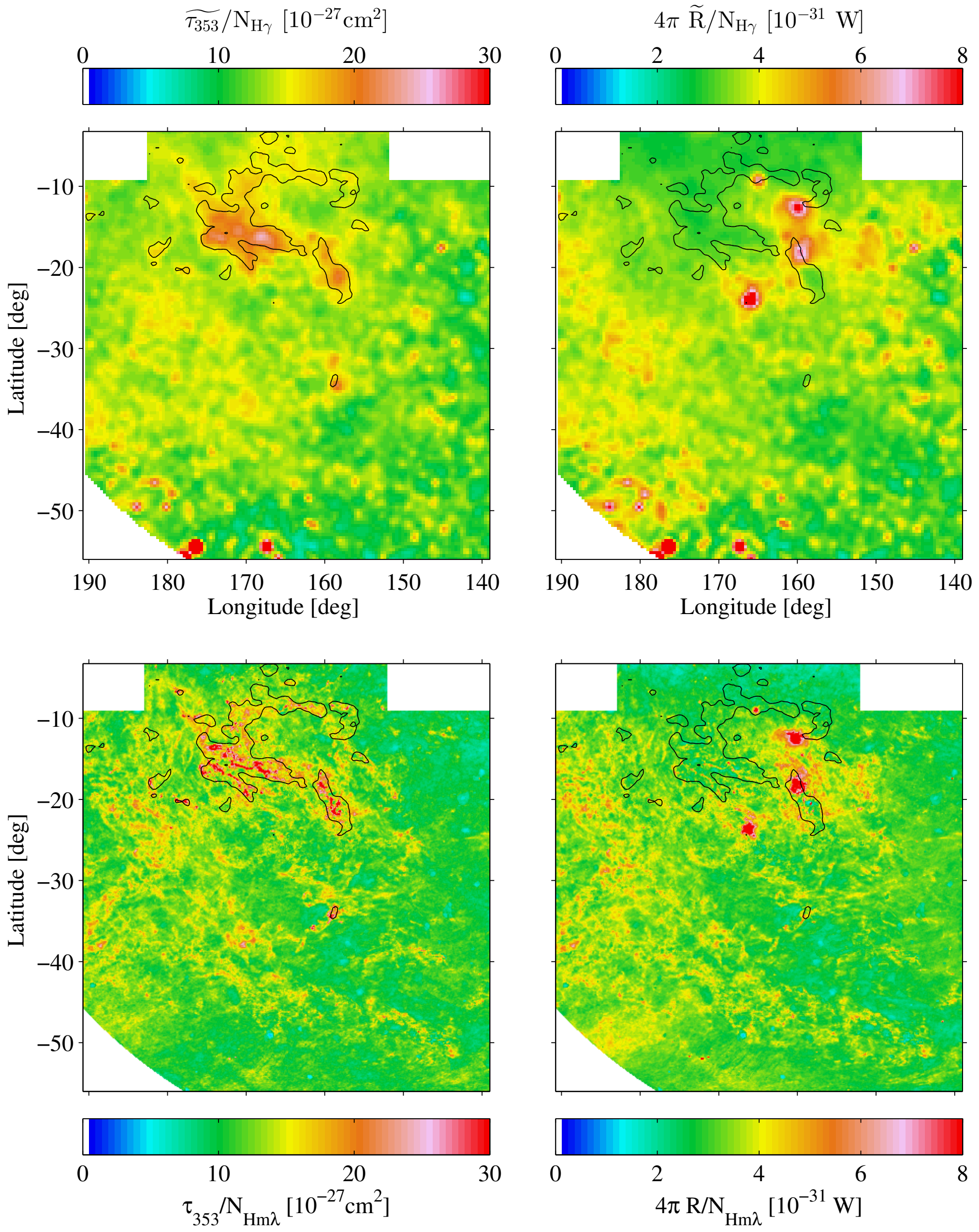

Fig. 16. Spatial variations of the dust opacities (left) and specific power (right) with the total gas measured by $N_{H\gamma}$ at 0°.375 resolution (top) and by $N_{Hm\lambda}$ at 0°.125 resolution (bottom). The tilded quantities are convolved with the LAT response for an interstellar spectrum. The black contours outline the shape of the CO clouds at the 7 K km s^{-1} level chosen to separate DNM and CO$_{sat}$ components.

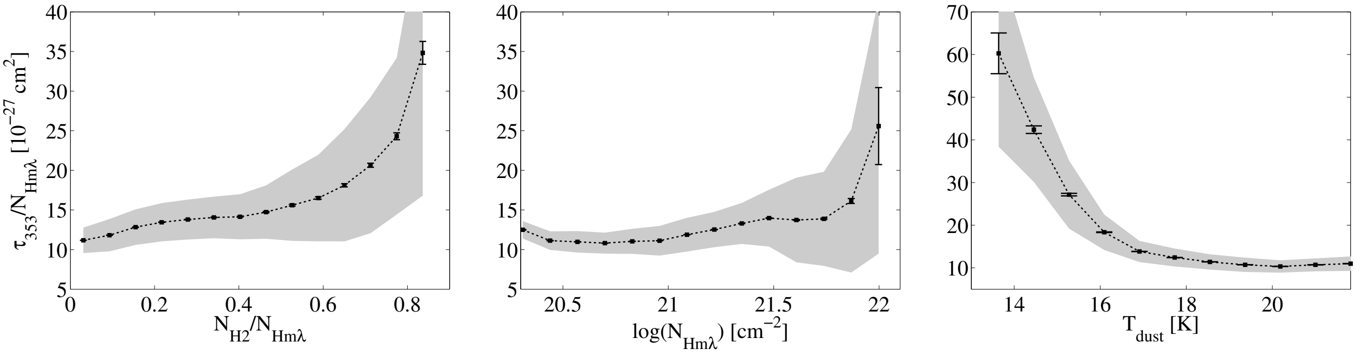

Fig. 17. Evolution of the dust opacities as a function of the molecular fraction in the gas column (left), the total gas column density N_H (middle) and the dust color temperature (right). To estimate the molecular fraction, the DNM is assumed to be 50% molecular. The error bars give the standard errors of the means and the grey band gives the standard deviation of the opacities in each bin.

Table 2. Average dust opacities, $\tau_{353}/N_{\rm H}$, and $N_{\rm H}/E(B-V)$ ratios in the gas phases of the different clouds.

Cloud	$\overline{\tau_{353}/N_{\rm H}}^{\rm HI}$ [10^{-27} cm^2]	$\overline{\tau_{353}/N_{\rm H}}^{\rm CO}$ [10^{-27} cm^2]	$\overline{\left[\frac{N_{\rm H}}{E({\rm B-V})}\right]}_{\rm HI}$ [10^{21} cm^{-2}]	$\overline{\left[\frac{N_{\rm H}}{E({\rm B-V})}\right]}_{\rm CO}$ [10^{21} cm^{-2}]
Cet	10.3±0.1±0.2	17.9±4.1±1.2	6.54±0.19±0.15	3.75±0.94±0.25
TauS	13.7±0.1±0.4	18.3±1.5±1.1	4.91±0.12±0.15	3.67±0.38±0.22
TauN	11.0±0.1±0.3	18.8±1.0±1.0	6.12±0.16±0.18	3.56±0.27±0.19
TauM	14.2±0.1±0.6	27.0±1.0±1.5	4.73±0.13±0.20	2.48±0.14±0.14
Cal	13.7±0.2±0.5	17.7±1.0±0.7	4.91±0.16±0.17	3.80±0.28±0.15
Per	16.5±0.5±1.0	34.4±5.1±4.6	4.08±0.20±0.26	1.95±0.33±0.25
Cha[a]	$16.3 \pm 0.2^{+0}_{-0.8}$	$32 \pm 1^{+0}_{-2}$	$4.11 \pm 0.10^{+0.23}_{-0}$	$2.1 \pm 0.2^{+0.1}_{-0}$
Cha – IVA[a]	$14.8 \pm 0.2^{+0}_{-0.6}$		$4.5 \pm 0.1^{+0.2}_{-0}$	

Notes. [a] from Planck and Fermi Collaborations (2015).
The first uncertainties are statistical, the second give the standard deviations obtained by varying the H I spin temperature.

rus value, even for the rather tenuous H I clouds in Cetus and Taurus North. The cloud-to-cloud dispersion indicates environmental effects beyond the latitude dependence noted by Liszt (2014) in the atomic gas. The $\overline{\tau_{353}/N_{\rm H}}^{\rm HI}$ opacities listed in Table 2 do not relate to the H I mass of the corresponding clouds. The 15% dispersion in this sample rather relates to the mean visual extinction of the H I cloud and to the surface fraction of large and small $N_{\rm HI}$ column densities across the cloud. We present in the next section evidence for gradual opacity changes as the gas density increases that explain why the average opacity in an H I cloud depends on its structure. The observation of opacity variations within the atomic phase at column densities below 10^{21} cm^{-2} challenges the current dust evolution models discussed in the next section.

We find systematically larger mean opacities in the CO-bright phase than in the H I phase, thereby confirming the continued increase in $\tau_{353}/N_{\rm H}$ at large H_2 column densities. The latter has been evaluated independently in each cloud (independent $X_{\rm CO}$ factors), so the cloud-to-cloud changes in $\overline{\tau_{353}/N_{\rm H}}^{\rm CO}$ that Planck Collaboration (2014a) have noted across the sky are not due to their use of a uniform $X_{\rm CO}$ factor. In Table 2, the mean opacity increases by 30% to 100% between the H I and CO-bright phases, independent of the H_2 mass locked in the cloud. The dispersion in $\overline{\tau_{353}/N_{\rm H}}^{\rm CO}$ rather relates to the surface fraction of dense regions with large $W_{\rm CO}$ intensities, SF$_{\rm dense}$, in the averaging. To study environmental changes in $\tau_{353}/N_{\rm H}$ within molecular clouds, we must take into account the added complication of spatial gradients in $X_{\rm CO}$.

7.2. Environmental changes in dust opacity

In order to follow changes in dust opacity across the clouds, we have built two maps of the total $N_{\rm H}$ column density in the region. The first one, $N_{{\rm H}\gamma}$, takes advantage of the CR interactions with gas in all chemical forms and thermodynamical states. The γ-ray intensity from the gas has been obtained from the LAT data in the overall energy band after subtraction of the γ-ray counts unrelated to gas in the best-fit model. In order to reduce the Poisson noise and get more robust photon statistics, we have degraded the resolution to 0°375. We have converted this γ-ray intensity into $N_{\rm H}$ using the average emission rate, $\overline{q}_{\rm HI}$, obtained in the atomic phase in the region. The second map, $N_{{\rm H\,m}\lambda}$, uses the higher-resolution information from the H I , CO, and dust data, and the mass scaling provided by the best-fit γ-ray model (uniform H I spin temperature of 400 K, $X_{{\rm CO}\gamma}$ factors in the clouds, γ-ray emissivity in the DNM, ionised, and CO$_{\rm sat}$ gas as in the H I). The opacity distribution at the smallest angular scales should be considered with care because the scaling factors used to construct $N_{{\rm H\,m}\lambda}$ have been derived at the scale of a whole cloud.

Figure 15 shows the 2D histogram of the correlation between the sightline integrals in dust optical depth and in $N_{{\rm H}\gamma}$ column density. The distribution deviates from linearity above about 4×10^{21} cm^{-2}. The opacity maps, shown in Fig. 16, indicate that $\tau_{353}/N_{\rm H}$ evolves progressively within the clouds, especially when the medium becomes molecular, in the diffuse DNM and even more so in the CO-bright parts. The increase in opacity does not relate to an increase in the specific power, $4\pi R/N_{\rm H}$, radiated by the grains, so the rise in opacity cannot be attributed to a larger heating rate (if we consider that the large grains are in thermal equilibrium to equate the radiated and absorbed powers). The largest opacities rather correspond to a ~30% lower heating rate in the well-shielded CO regions.

Thanks to the total gas tracing capability of the CRs and to the complementarity of the $N_{{\rm H}\gamma}$ and $N_{{\rm H\,m}\lambda}$ maps, it is very unlikely that opacity variations as large as those seen in Fig. 16 are caused by large deficits in the gas column densities. Our results give strong support to earlier indications that the big grains in the CO filaments of the Taurus cloud have larger sub-mm emissivities than in the more diffuse media. The previous studies noted opacity changes by a factor ranging from ~2 (Flagey et al. 2009; Planck Collaboration 2011b; Ysard et al. 2013) to $3.4^{+0.3}_{-0.7}$ (Stepnik et al. 2003) above the diffuse-ISM value. In the present analysis, we find opacity enhancements exceeding a factor of three and reaching a factor of six toward the CO clouds, even though we provide a measure of the additional H_2 gas that is not linearly traced by $W_{\rm CO}$ in the CO$_{\rm sat}$ directions. The largest opacities do not rise as high in the Taurus clouds as they do in the Chamaeleon ones (Planck and Fermi Collaborations 2015), but a quantitative comparison would require the

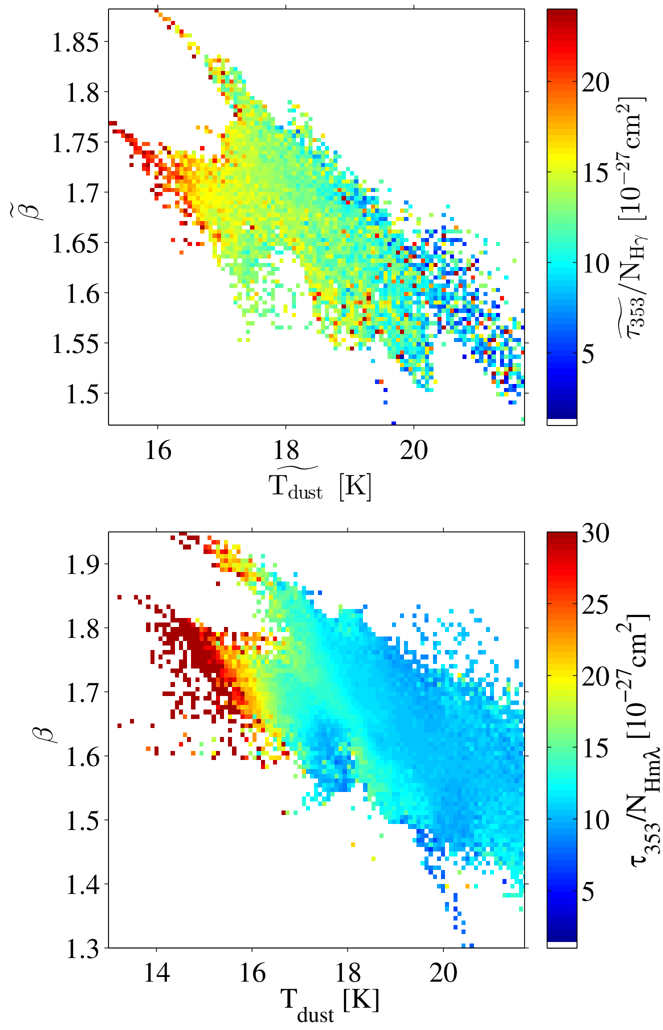

Fig. 18. Evolution of the dust opacities with the total gas measured by $N_{H\gamma}$ at 0°.375 resolution (top) and by $N_{Hm\lambda}$ at 0°.125 resolution (bottom) as a function of the dust color temperature (x-axis) and spectral β index (y-axis)

separation of the DNM and CO_{sat} components in a new analysis of the Chamaeleon region. We also find that the opacity starts to increase in the DNM, therefore at lower gas densities than the few thousand per cm^3 sampled in CO. The grain opacity at the H I –H_2 transition compares very well with that in the DNM surrounding the Chamaeleon clouds (Planck and Fermi Collaborations 2015).

In order to determine how the opacity gradient depends steeply on the ambient ISM, Fig. 17 shows how the opacity varies with the molecular fraction in the gas column, f_{H_2}, with the total $N_{Hm\lambda}$ column density as traced by the multi-wavelength data, and with the dust colour temperature. We observe a gradual increase as the gas becomes molecular and a steeper change at N_H above 5×10^{21} cm^{-2} due to two factors: change in molecular fraction and in grain properties in the molecular gas. The amplitude of the gradient is best traced by the drop in grain temperature. Figure 16 further shows that the ambient molecular gas density is not the only factor of evolution because we detect notable cloud-to-cloud differences in the opacity gradients. Compare for instance the large opacities that often exceed $25{\times}10^{-27}$ cm^2 along the Main Taurus and Perseus CO clouds with the 50% lower values obtained toward comparable W_{CO} intensities near both ends (in longitude) of the California cloud.

Several studies have noted that the opacity enhancement occurred together with a reduction of the IR emission from polycyclic aromatic hydrocarbons (PAHs) and from very small grains stochastically heated by the ambient ISRF (e.g., Stepnik et al. 2003; Flagey et al. 2009; Ysard et al. 2013). Grain evolution in dense media was invoked to explain the radiation changes (see the previous references and Martin et al. 2012; Köhler et al. 2015). It involves accretion of aliphatic-rich carbonaceous mantles from the gas phase, grain coagulation into fluffy aggregates, and the formation of an ice mantle on the surface of the aggregates in the coldest regions. Recent theoretical studies such as Köhler et al. (2015) suggest that the spectral changes in β relate to gas density-dependent processes and that the variations in opacity, spectral index β, and colour temperature are closely connected. Figure 18 shows the quantitative relation between those three parameters in the observations. The data corroborate the prediction that the opacity should increase for β above 1.5 and temperature below 17 K. According to this model, the directions with temperatures near 16–18 K, $\beta \geq 1.5$, and $\tau_{353}/N_{Hm\lambda}$ values about twice as large as the diffuse-ISM value of $\sim 7{\times}10^{-27}$ cm^2 would be rich in grains with carbonaceous mantles. The mantle accretion would therefore occur primarily in the DNM. Aggregates would dominate the directions below 16 K, at $1.6 \lesssim \beta \lesssim 1.8$, and where τ_{353}/N_H is at least four times above the diffuse-ISM value. Such conditions are found inside the sampled CO clouds. Ice coating of the aggregates would explain the largest opacity values in Fig. 18, at the lowest temperatures and largest spectral indices, β.

8. Conclusions

We have analysed the gas, dust and CR content of several nearby anti-centre clouds including the Cetus, Taurus, Auriga, Perseus, and California clouds. We have performed an iterative fit of the total gas column density as traced by γ rays and the dust optical depth at 353 GHz. We have modelled both tracers as linear combinations of the gas column densities traced by H I , ^{12}CO, and free-free emissions, and we have extracted the morphology and column density of the DNM from the joint γ-ray and dust data. We have verified the robustness of our set of parameters through the use of jackknife tests; these parameters have enabled us to constrain the properties of the ISM in these clouds.

The main results are summarised as follows.

- **On the cosmic rays:** The γ-ray emissivity of the gas in the analysed clouds has the same energy spectrum as in other clouds of the local ISM and we find no dependence of their average γ-ray emissivity with Galactocentric radius (i.e., distance from the local spiral arm), nor with height above the Galactic plane. In the 0.4–100 GeV energy band and at the precision level of the current LAT observations, we find no evidence of CR exclusion or CR concentration in the clouds, up to the ^{12}CO-bright molecular regions.
- **On the dark gas:** The γ-ray and dust data jointly reveal significant amounts of gas in addition to that seen in H I , free-free, and ^{12}CO emissions. The diffuse large-scale structures are associated with the DNM at the transition between the atomic and molecular phases. They gather dense atomic hydrogen and diffuse H_2 in unknown proportions, but with column densities equivalent to those found in the H I and CO emitting parts. In the molecular phase, the γ rays and dust reveal filaments of dense gas in addition to that proportionality traced by W_{CO} where the ^{12}CO line intensities saturate.

- **On the H ii regions:** The H ii regions, NGC 1499 and G156.6-18.5, are jointly detected in dust and γ-ray emission. The corresponding γ-ray flux cannot be attributed to the IC up-scattering of the bright stellar radiation by the local CR electrons. It is more likely caused by the hadronic interactions of the local CR nuclei in the ionised gas. Hence for NGC 1499, we have used the average γ-ray emissivity of the atomic gas in the region to infer a mean electron density of 4.3 ± 0.6 cm^{-3} for an electron temperature of 8000 K, in good agreement with the modelling of the free-free and Hα emissions of the H ii region.
- **On the X_{CO} factors:** We provide independent measurements of the X_{CO} factor from the dust and γ-ray analyses in six different clouds, against the same H i and CO data. As in the Chamaeleon complex, we find that the dust-derived values are systematically larger, by 30% to 130%, than the γ-ray estimates. The difference is likely due to chemical and structural evolution of the dust with increasing N_H. The X_{CO} factors measured in γ rays range from $(1.04 \pm 0.05)\times 10^{20}$ cm^{-2} K^{-1} km^{-1} s in Taurus South to $(0.44 \pm 0.04)\times 10^{20}$ cm^{-2} K^{-1} km^{-1} s in Perseus. Those results confirm a recurrent discrepancy by a factor of two to three between the X_{CO} averages obtained in nearby clouds and at large scale in the Galaxy. In nearby clouds, the X_{CO} values appear to decrease with the average W_{CO} intensity of the cloud, with the average CO line width, and with the surface fraction subtended by the brightest CO clumps; the more diffuse CO clouds tend to have larger average X_{CO} factors. Models of the formation and photodissociation of H_2 and CO molecules predict a marked decline in X_{CO} from the diffuse envelopes of molecular clouds to their dense cores. Hence the X_{CO} average should qualitatively vary with the surface fraction of dense regions in the cloud structure and with the degree of saturation of the CO lines as in our data. However, given the moderate gas densities filling most of the volume of the nearby molecular clouds, the low X_{CO} values that we find are at variance with the theoretical predictions from PDR chemistry.
- **On the dust opacities:** The dust opacity at 353 GHz, τ_{353}/N_H, appears to rise by a factor of three from low column densities in the atomic gas (about 10^{-26} cm^2) to cold grains in molecular gas at $N_H \gtrsim 5 \times 10^{21}$ cm^{-2}. The rise can reach a factor of six at very low dust temperatures below 14 K. The amplitude of the rise is comparable to the variations observed in the Chamaeleon clouds (Planck and Fermi Collaborations 2015). As the observed specific power radiated by the grains decreases in the cold molecular regions the changes cannot be attributed to a larger heating rate, but they are more likely caused by a chemical or structural change in the grains. The magnitude of the rise severely limits the use of the thermal emission of the large dust grains to trace the total gas. The linear regime is limited to $N_H < 3 \times 10^{21}$ cm^{-2} in these clouds. The confirmation of large opacity variations across clouds directly impacts the gas mass estimates inferred from dust emission at sub-mm and mm wavelengths to derive star-forming efficiencies in the Galaxy and in external galaxies. We quantify the coupled changes in grain temperature, opacity, and β index of the thermal radiation to help model the grain evolution.

In a second paper we will study how the DNM and CO$_{sat}$ gas relate to the H i -bright, ^{12}CO-bright, and ^{13}CO-bright phases. We will derive the masses of the DNM and of the CO$_{sat}$ phase for a sample of substructures in the Cetus, Taurus, California and Chameleon clouds, while taking care to avoid regions of cloud confusion along sightlines. We will follow the evolution of the CO-dark H_2 fraction both within a cloud and from cloud to cloud and we will place our results in the context of other observational and theoretical studies.

In a subsequent study, we will confront the gas, γ-ray, and dust distributions in the nearby clouds using dust column densities inferred from stellar reddening. The joint comparison of dust emission and extinction data to other gas tracers will provide additional information on the relation between the total gas and dust, including the abundant dark neutral medium, and will help to better constrain the evolution of dust properties, in particular with regard to potential variations of the extinction curve (Schlafly et al. 2016).

Adding more data points to the trends shown in Fig. 12 is essential to confirm that the average X_{CO} factor in a cloud tends to decrease for increasingly dense CO molecular clouds, in response to different X_{CO} gradients spanning each cloud (Bell et al. 2006; Glover & Mac Low 2011). Particular attention should be paid to the use of the same method to derive a consistent set of X_{CO} values, and to the addition of clouds with little confusion between the different gas phases to ensure a precise separation of the total gas tracers in each phase. The current γ-ray analyses cannot yield X_{CO} maps across individual clouds. The variations in dust opacity with increasing gas column density prevent the use of dust emission maps to probe X_{CO} gradients in nearby clouds. In this context, it is essential to increase the number of clouds with measured average X_{CO} values and to confront the observed X_{CO} trends with PDR models in order to interpret the slope and dispersion of the trends presented here. Confirming that X_{CO} factors vary from cloud to cloud within the local ISM because of their different dynamical and chemical structures stresses that large-scale X_{CO} averages can vary because of a different mix of cloud states in different Galactic regions, in addition to the Galaxy-wide X_{CO} gradients expected from metallicity and ISRF gradients. For instance, it opens the way for observable differences in X_{CO} between ensembles of clouds inside and outside of the spiral arms since the inter-arm clouds that have been sheared after their passage through an arm are more susceptible to photo-dissociation, thus more prone to having large X_{CO} averages (Smith et al. 2014).

Acknowledgements. The *Fermi* LAT Collaboration acknowledges generous ongoing support from a number of agencies and institutes that have supported both the development and the operation of the LAT as well as scientific data analysis. These include the National Aeronautics and Space Administration and the Department of Energy in the United States, the Commissariat à l'Energie Atomique and the Centre National de la Recherche Scientifique / Institut National de Physique Nucléaire et de Physique des Particules in France, the Agenzia Spaziale Italiana and the Istituto Nazionale di Fisica Nucleare in Italy, the Ministry of Education, Culture, Sports, Science and Technology (MEXT), High Energy Accelerator Research Organization (KEK) and Japan Aerospace Exploration Agency (JAXA) in Japan, and the K. A. Wallenberg Foundation, the Swedish Research Council and the Swedish National Space Board in Sweden. Additional support for science analysis during the operations phase is gratefully acknowledged from the Istituto Nazionale di Astrofisica in Italy and the Centre National d'Études Spatiales in France. The authors acknowledge the support of the Agence Nationale de la Recherche (ANR) under award number STILISM ANR-12-BS05-0016.

References

Abdo, A. A., Ackermann, M., Ajello, M., et al. 2010, ApJ, 710, 133
Acero, F., Ackermann, M., Ajello, M., et al. 2015, ApJS, 218, 23
Ackermann, M., Ajello, M., Albert, A., et al. 2012a, ApJS, 203, 4
Ackermann, M., Ajello, M., Allafort, A., et al. 2012b, ApJ, 756, 4
Ackermann, M., Ajello, M., Allafort, A., et al. 2012c, ApJ, 755, 22
Ackermann, M., Ajello, M., Allafort, A., et al. 2012d, A&A, 538, A71
Ackermann, M., Ajello, M., Atwood, W. B., et al. 2012e, ApJ, 750, 3

Ackermann, M., Ajello, M., Baldini, L., et al. 2011, ApJ, 726, 81
Alves, M. I. R., Davies, R. D., Dickinson, C., et al. 2012, MNRAS, 422, 2429
Anderson, L. D., Bania, T. M., Balser, D. S., et al. 2014, ApJS, 212, 1
Andersson, B.-G., Wannier, P. G., Moriarty-Schieven, G. H., & Bakker, E. J. 2000, AJ, 119, 1325
Atwood, W., Albert, A., Baldini, L., et al. 2013, ArXiv e-prints
Atwood, W. B., Abdo, A. A., Ackermann, M., et al. 2009, ApJ, 697, 1071
Bally, J., Walawender, J., Johnstone, D., Kirk, H., & Goodman, A. 2008, The Perseus Cloud, ed. B. Reipurth, 308
Bell, T. A., Roueff, E., Viti, S., & Williams, D. A. 2006, MNRAS, 371, 1865
Bennett, C. L., Larson, D., Weiland, J. L., et al. 2013, ApJS, 208, 20
Bertram, E., Glover, S. C. O., Clark, P. C., Ragan, S. E., & Klessen, R. S. 2016, MNRAS, 455, 3763
Bloemen, J. B. G. M., Caraveo, P. A., Hermsen, W., et al. 1984, A&A, 139, 37
Bloemen, J. B. G. M., Strong, A. W., Mayer-Hasselwander, H. A., et al. 1986, A&A, 154, 25
Bobin, J., Sureau, F., & Starck, J. 2015, ArXiv e-prints
Bohlin, R. C., Savage, B. D., & Drake, J. F. 1978, ApJ, 224, 132
Bolatto, A. D., Wolfire, M., & Leroy, A. K. 2013, ARA&A, 51, 207
Bronfman, L., Cohen, R. S., Alvarez, H., May, J., & Thaddeus, P. 1988, ApJ, 324, 248
Cardelli, J. A., Clayton, G. C., & Mathis, J. S. 1989, ApJ, 345, 245
Carson, T. R. 1988, A&A, 189, 319
Casandjian, J.-M. 2015, ApJ, 806, 240
Cesarsky, C. J. & Volk, H. J. 1978, A&A, 70, 367
Chen, B.-Q., Liu, X.-W., Yuan, H.-B., Huang, Y., & Xiang, M.-S. 2015, MNRAS, 448, 2187
Dame, T. M., Hartmann, D., & Thaddeus, P. 2001, ApJ, 547, 792
Dame, T. M. & Thaddeus, P. 2004, in Astronomical Society of the Pacific Conference Series, Vol. 317, Milky Way Surveys: The Structure and Evolution of our Galaxy, ed. D. Clemens, R. Shah, & T. Brainerd, 66
Digel, S. W., Aprile, E., Hunter, S. D., Mukherjee, R., & Xu, F. 1999, ApJ, 520, 196
Digel, S. W. & Grenier, I. A. 2001, in American Institute of Physics Conference Series, Vol. 587, Gamma 2001: Gamma-Ray Astrophysics, ed. S. Ritz, N. Gehrels, & C. R. Shrader, 538–542
Digel, S. W., Grenier, I. A., Heithausen, A., Hunter, S. D., & Thaddeus, P. 1996, ApJ, 463, 609
Digel, S. W., Grenier, I. A., Hunter, S. D., Dame, T. M., & Thaddeus, P. 2001, ApJ, 555, 12
Dobashi, K., Marshall, D. J., Shimoikura, T., & Bernard, J.-P. 2013, PASJ, 65
Ester, M., Kriegel, H. P., Sander, J., & Xu, X. 1996, in Proceedings of the Second International Conference on Knowledge Discovery and Data Mining, ed. E. Simoudis, J. Han, & U. M. Fayyad (AAAI Press), 226–231
Finkbeiner, D. P. 2003, ApJS, 146, 407
Flagey, N., Noriega-Crespo, A., Boulanger, F., et al. 2009, ApJ, 701, 1450
Glover, S. C. O. & Mac Low, M.-M. 2011, MNRAS, 412, 337
Godard, B., Falgarone, E., & Pineau des Forêts, G. 2014, A&A, 570, A27
Green, G. M., Schlafly, E. F., Finkbeiner, D. P., et al. 2015, ApJ, 810, 25
Grenier, I. A., Black, J. H., & Strong, A. W. 2015, ARA&A, 53, 199
Grenier, I. A., Casandjian, J.-M., & Terrier, R. 2005, Science, 307, 1292
Heiles, C. & Troland, T. H. 2003, ApJS, 145, 329
Heyer, M. & Dame, T. M. 2015, ARA&A, 53, 583
Hunter, S. D., Bertsch, D. L., Catelli, J. R., et al. 1997, ApJ, 481, 205
Hunter, S. D., Digel, S. W., de Geus, E. J., & Kanbach, G. 1994, ApJ, 436, 216
Juvela, M. & Montillaud, J. 2016, A&A, 585, A38
Kalberla, P. M. W., Burton, W. B., Hartmann, D., et al. 2005, A&A, 440, 775
Kalberla, P. M. W., McClure-Griffiths, N. M., Pisano, D. J., et al. 2010, A&A, 521, A17
Kanekar, N., Braun, R., & Roy, N. 2011, ApJ, 737, L33
Karzas, W. J. & Latter, R. 1961, ApJS, 6, 167
Köhler, M., Ysard, N., & Jones, A. P. 2015, A&A, 579, A15
Lada, C. J., Lombardi, M., & Alves, J. F. 2009, ApJ, 703, 52
Lebrun, F., Bennett, K., Bignami, G. F., et al. 1983, ApJ, 274, 231
Lebrun, F. & Huang, Y.-L. 1984, ApJ, 281, 634
Lebrun, F., Paul, J. A., Bignami, G. F., et al. 1982, A&A, 107, 390
Lee, M.-Y., Stanimirović, S., Wolfire, M. G., et al. 2014, ApJ, 784, 80
Levrier, F., Le Petit, F., Hennebelle, P., et al. 2012, A&A, 544, A22
Lim, T.-H., Min, K.-W., & Seon, K.-I. 2013, ApJ, 765, 107
Liszt, H. 2014, ApJ, 783, 17
Liszt, H. S. & Pety, J. 2012, A&A, 541, A58
Liszt, H. S., Pety, J., & Lucas, R. 2010, A&A, 518, A45
Lombardi, M., Lada, C. J., & Alves, J. 2010, A&A, 512, A67
Magnani, L., Blitz, L., & Mundy, L. 1985, ApJ, 295, 402
Martin, P. G., Roy, A., Bontemps, S., et al. 2012, ApJ, 751, 28
Mohan, R., Dwarakanath, K. S., & Srinivasan, G. 2004, Journal of Astrophysics and Astronomy, 25, 143
Morlino, G. & Gabici, S. 2015, MNRAS, 451, L100
Murray, C. E., Stanimirović, S., Goss, W. M., et al. 2015, ApJ, 804, 89
Neyman, J. & Pearson, E. S. 1933, Philosophical Transactions of the Royal Society of London Series A, 231, 289
Nolan, P. L., Abdo, A. A., Ackermann, M., et al. 2012, ApJS, 199, 31
Orlando, E. & Strong, A. W. 2007, Ap&SS, 309, 359
Padovani, M. & Galli, D. 2011, A&A, 530, A109
Paradis, D., Dobashi, K., Shimoikura, T., et al. 2012, A&A, 543, A103
Peek, J. E. G., Heiles, C., Douglas, K. A., et al. 2011, ApJS, 194, 20
Pineda, J. L., Goldsmith, P. F., Chapman, N., et al. 2010, ApJ, 721, 686
Planck and Fermi Collaborations. 2015, A&A, 582, A31
Planck Collaboration. 2011a, A&A, 536, A19
Planck Collaboration. 2011b, A&A, 536, A25
Planck Collaboration. 2014a, A&A, 571, A11
Planck Collaboration. 2014b, A&A, 566, A55
Planck Collaboration. 2015, ArXiv e-prints
Polk, K. S., Knapp, G. R., Stark, A. A., & Wilson, R. W. 1988, ApJ, 332, 432
Roy, A., Martin, P. G., Polychroni, D., et al. 2013a, ApJ, 763, 55
Roy, N., Kanekar, N., Braun, R., & Chengalur, J. N. 2013b, MNRAS, 436, 2352
Sandstrom, K. M., Leroy, A. K., Walter, F., et al. 2013, ApJ, 777, 5
Schlafly, E. F., Green, G., Finkbeiner, D. P., et al. 2014, ApJ, 786, 29
Schlafly, E. F., Meisner, A. M., Stutz, A. M., et al. 2016, ApJ, 821, 78
Schnee, S., Li, J., Goodman, A. A., & Sargent, A. I. 2008, ApJ, 684, 1228
Sheffer, Y., Rogers, M., Federman, S. R., et al. 2008, ApJ, 687, 1075
Shetty, R., Glover, S. C., Dullemond, C. P., & Klessen, R. S. 2011a, MNRAS, 412, 1686
Shetty, R., Glover, S. C., Dullemond, C. P., et al. 2011b, MNRAS, 415, 3253
Shinohara, M. & Ishida, K. 1976, PASJ, 28, 437
Skilling, J. & Strong, A. W. 1976, A&A, 53, 253
Smith, R. J., Glover, S. C. O., Clark, P. C., Klessen, R. S., & Springel, V. 2014, MNRAS, 441, 1628
Starck, J.-L. & Pierre, M. 1998, A&AS, 128, 397
Stepnik, B., Abergel, A., Bernard, J.-P., et al. 2003, A&A, 398, 551
Strong, A. W. 1985, A&A, 150, 273
Strong, A. W., Bloemen, J. B. G. M., Dame, T. M., et al. 1988, A&A, 207, 1
Strong, A. W. & Mattox, J. R. 1996, A&A, 308, L21
Tibaldo, L., Digel, S. W., Casandjian, J. M., et al. 2015, ApJ, 807, 161
Ungerechts, H. & Thaddeus, P. 1987, ApJS, 63, 645
van Dishoeck, E. F. & Black, J. H. 1988, ApJ, 334, 771
van Leeuwen, F. 2007, A&A, 474, 653
Wakker, B. P., York, D. G., Wilhelm, R., et al. 2008, ApJ, 672, 298
Winkel, B., Kerp, J., Flöer, L., et al. 2016, A&A, 585, A41
Wolfire, M. G., Hollenbach, D., & McKee, C. F. 2010, ApJ, 716, 1191
Ysard, N., Abergel, A., Ristorcelli, I., et al. 2013, A&A, 559, A133

Appendix A: Component separation

We have decomposed the H i and CO spectra into sets of individual lines as in Planck and Fermi Collaborations (2015). The method starts with the detection and localization in velocity of isolated lines or significant peaks in the spectra. Each HI and CO spectrum is then fitted by a sum of pseudo-Voigt line profiles centred on the centroids of the detected lines or peaks, within ±2.7 to 3 km/s. The fits are generally good, with less than 15% difference between the observed and fitted integrals over all velocities. In order to preserve the observed photometry, we calculate the residuals between the observed and fitted spectra in each channel and we redistribute them among the fitted lines, proportionally to their intensity in this channel. We finally construct N_{HI} column-density and W_{CO} intensity maps of a specific cloud by integrating the fitted lines that have their velocity centroid within a chosen velocity interval for each (l, b) direction. This method corrects for potential line spill-over from one velocity interval (i.e., cloud) to the next. To determine boundaries between clouds in the position-velocity space (l, b, v), we have used the velocity centroids of all the fitted lines and their density in the (l, b, v) space to search for line clusters (i.e., clouds). To do so, we have used the Density-Based Spatial Clustering of Applications with Noise (DBSCAN) algorithm (Ester et al. 1996) to isolate arbitrarily-shaped clusters and to draw contours of minimum density around them. The six H i and CO regions used in this analysis have been delimited by following those curves of minimal number density in (l, b, v) space. The cuts follow piecewise continuous lines in (b,v) over specific longitude intervals. The latter and the points used to define the broken lines are given in Table A.1.

Appendix B: Free-free emission in the 70 GHz data

In order to separate the free-free intensity in the *Planck* LFI map at 70 GHz from non-gaseous emission components, we have proceeded as follows. We have first subtracted the CMB intensity as modelled at 70 GHz by Bobin et al. (2015) from the joint analysis of *WMAP* and *Planck* observations. We have then taken advantage of the sparse spatial correlation between the thermal dust intensity I_{70} at 70 GHz and the dust optical depth τ_{353} at 353 GHz in the wavelet domain to filter out the dust component. To do so, we have transformed both maps with eight scales of the B-spline wavelet with the `mr-transform` tool of Starck & Pierre (1998). For each scale, we have obtained the best (χ^2) linear regression between the wavelet distributions of I_{70} and τ_{353} in the regions of both significant dust optical depth ($\tau_{353} > 5\,10^{-6}$) and low free-free intensity (< 0.3 $\mathrm{mK_{CMB}}$ at 22 GHz). We have used this regression to remove the part linearly correlated with τ_{353} from the 70 GHz transform at each scale. After this correction, we have applied the inverse transform to reconstruct the filtered map. We have then used the `mr-detect` tool with the same eight wavelet scales to detect and remove point sources. Only the first scale was used for source detection. The final map has been translated into units of specific intensity (Jy/sr) using the conversion coefficients [3] for the 70 GHz band. We have applied the colour correction interpolated for the -0.14 spectral index expected for free-free emission at 70 GHz.

Appendix C: H I spin temperature

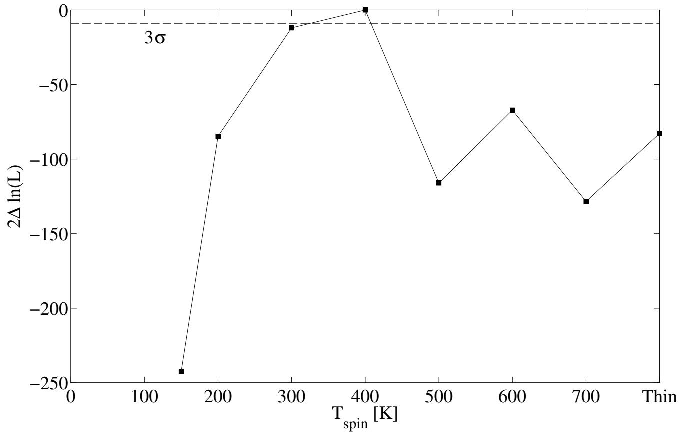

Fig. C.1. Evolution of the log-likelihood ratio of the γ-ray fit in the 0.4-100 GeV band as a function of the H I spin temperature used to calculate the N_{HI} column densities in the clouds.

The evolution of the maximum log-likelihood of the γ-ray fit in the $10^{2.6-5}$ MeV band can be used to constrain the choice of average H I spin temperature that best matches the N_{HI} column density maps of the different clouds to the structure of the γ rays produced by CR interactions in the atomic gas. We find that the fit quality peaks near 400 K (Fig. C.1). We have not attempted to use different spin temperatures for the different clouds present in the analysis region.

Appendix D: Best fit coefficients of the γ-ray and dust models

The best fit corresponds to an $\mathrm{H_I}$ spin temperature of 400 K. For each parameter we first give the statistical uncertainty from the fit and jackknife tests, then the standard deviation obtained by varying the H I spin temperature.

Appendix E: Previous γ-ray measurements of the X_{CO} conversion factor

---

[3] http://wiki.cosmos.esa.int/planckpla2015/index.php/UC_CC_Tables#LFI_Unit_Conversion_Tables

Table A.1. Limits of the H I and CO clouds in longitude, latitude, and velocity

Cloud	Cetus	Main Taurus	South Taurus	North Taurus	Perseus	California
l_{min}	135°	135°	135°	135°	155°	151°.6
l_{max}	195°	195°	195°	195°	161°.5	178°.8
(b , v) points for lower border	-22°, -14 -30°, 16 -42°, -10 -61°, -100	3°, 5.8 -2°, 6.1 -5°.5 , 5.9 -8°, 4.3 -9°, 1.7 -10°, 1.4 -11°.5 , 3. -13°, 3.1 -14°.6 , 4.2 -17°, 4.2 -18°.5 , 6.2 -22°, 1.3 -23°.9 , 4.4	3°, 5.8 -2°, 6.1 -3°, 6.1 -3°.5 , 7.2 -6°, 14 -19°, 14 -21°.2 , 9.3 -23°.9 , 4.4 -25°, 6 -34°.5 , 6 -38°.6 , 2.8 -61°, 7.2	1°.4 , -2.3 -3°.6 , -3.6 -6°, -7.2 -10°.6 , -12.2 -14°.1 , -11.8 -18°, -6 -20°, 14 -31°, -14 -35°.5 , 6 -42°, -7 -61°, -6	-17°.8 , 8°.2 -17°.3 , 6 -18°.5 , 6.2 -22°.1 , 1.3 -23°.9 , 4.4	-3°.6 , 0.8 -6°.5 , -1 -7°, -0.25 -8°.6 , 1 -10°.1 , 0.6 -14°.1 , -2 -14°.1 , -11.8
(b , v) points for upper border	-22°, -14 -31°, -14 -35°.5 , -6 -42°, -7 -61°, -6	3°, 5.8 -2°, 6.1 -3°, 6.1 -3°.5 , 7.2 -6°, 14 -19°, 14 -21°.2 , 9.3 -23°.9 , 4.4	3°, 5.8 -2°, 6.1 -3°, 6.1 -6°, 14 -6°.5 , 15.5 -10°.6 , 24.5 -61°, 24.5	1°.4 , -2.3 -3°, 5.8 -5°.5 , 5.9 -8°.4 , 4.3 -9°, 1.7 -10°, 1.4 -11°, 5.3 -13°, 3.1 -14°.6 , 4.2 -17°, 4.2 -18°.5 , 6.2 -22°.1 , 1.3 -23°.9 , 4.4 -25°, 6 -34°.5 , 6 -38°.6 , 2.8 -61°, 7.2	-17°.1 , 8.2 -17°.6 , 11.3 -19°.8 , 12.4 -21°.2 , 9.3 -23°.9 , 4.4	-3°.6 , -3.6 -6°, -7.2 -10°.6 , -12.2 -14°.1 , -11.8

Table D.1. Best-fit coefficients of the γ-ray model in each energy band.

γ-ray	Energy band [MeV]					τ_{353}	
model	$10^{2.6}$ – $10^{2.8}$	$10^{2.8}$ – $10^{3.2}$	$10^{3.2}$ – $10^{3.6}$	$10^{3.6}$ – 10^{5}	$10^{2.6}$ – 10^{5}	model	
$q_{\mathrm{HI\ Cet}}$	1.13±0.07±0.04	1.07±0.05±0.03	1.07±0.04±0.04	0.99±0.12±0.04	1.08±0.04±0.06	$y^{a}_{\mathrm{HI\ Cet}}$	1.03±0.01±0.02
$q_{\mathrm{HI\ TauS}}$	1.10±0.02±0.04	1.11±0.02±0.04	1.06±0.02±0.04	1.05±0.04±0.04	1.09±0.01±0.04	$y^{a}_{\mathrm{HI\ TauS}}$	1.37±0.01±0.04
$q_{\mathrm{HI\ TauN}}$	1.05±0.03±0.04	1.00±0.02±0.03	1.02±0.02±0.04	1.06±0.05±0.04	1.02±0.02±0.05	$y^{a}_{\mathrm{HI\ TauN}}$	1.10±0.01±0.03
$q_{\mathrm{HI\ TauM}}$	1.29±0.03±0.06	1.25±0.02±0.06	1.21±0.02±0.06	1.25±0.05±0.05	1.26±0.02±0.06	$y^{a}_{\mathrm{HI\ TauM}}$	1.42±0.02±0.06
$q_{\mathrm{HI\ Cal}}$	1.24±0.05±0.02	1.20±0.04±0.02	1.09±0.04±0.02	1.13±0.08±0.02	1.15±0.03±0.02	$y^{a}_{\mathrm{HI\ Cal}}$	1.37±0.02±0.04
$q_{\mathrm{HI\ Per}}$	1.67±0.16±0.06	1.41±0.11±0.05	1.47±0.12±0.05	1.19±0.21±0.04	1.42±0.08±0.05	$y^{a}_{\mathrm{HI\ Per}}$	1.65±0.07±0.10
$q_{\mathrm{HI\ Gal}}$	0.73±0.02±0.03	0.75±0.02±0.03	0.74±0.02±0.03	0.82±0.04±0.04	0.74±0.01±0.03	$y^{a}_{\mathrm{HI\ Gal}}$	0.80±0.04±0.02
$q_{\mathrm{CO\ Cet}}$	1.43±0.72±0.23	2.50±0.54±0.22	2.37±0.56±0.22	0.00±0.90±0.00	2.09±0.37±0.20	$y^{b}_{\mathrm{CO\ Cet}}$	3.46±0.17±0.09
$q_{\mathrm{CO\ TauS}}$	2.23±0.22±0.09	2.35±0.17±0.09	2.29±0.18±0.09	1.87±0.31±0.10	2.26±0.12±0.10	$y^{b}_{\mathrm{CO\ TauS}}$	3.78±0.09±0.12
$q_{\mathrm{CO\ TauN}}$	1.90±0.10±0.04	1.87±0.08±0.04	1.79±0.09±0.04	1.86±0.16±0.03	1.86±0.06±0.03	$y^{b}_{\mathrm{CO\ TauN}}$	3.44±0.07±0.04
$q_{\mathrm{CO\ TauM}}$	1.75±0.06±0.03	1.70±0.05±0.03	1.62±0.05±0.03	1.67±0.09±0.03	1.67±0.04±0.04	$y^{b}_{\mathrm{CO\ TauM}}$	3.58±0.05±0.03
$q_{\mathrm{CO\ Cal}}$	2.07±0.10±0.04	2.09±0.08±0.04	1.94±0.09±0.04	1.94±0.16±0.05	2.04±0.06±0.04	$y^{b}_{\mathrm{CO\ Cal}}$	3.13±0.08±0.10
$q_{\mathrm{CO\ Per}}$	1.14±0.16±0.13	1.35±0.14±0.14	1.46±0.13±0.13	1.73±0.23±0.14	1.38±0.13±0.13	$y^{b}_{\mathrm{CO\ Per}}$	3.34±0.13±0.26
$q_{\mathrm{CO\ Gal}}$	0.32±0.25±0.68	0.00±0.25±0.43	0.05±0.25±0.62	0.00±0.25±0.28	0.00±0.25±0.48	$y^{b}_{\mathrm{CO\ Gal}}$	2.91±0.44±1.19
q_{ff}	2.96±0.81±1.09	4.00±0.77±0.95	2.40±0.66±0.86	4.20±1.34±0.89	3.26±0.57±0.97	y^{c}_{ff}	2.11±0.61±1.03
q_{COsat}	4.22±0.31±0.10	4.44±0.25±0.10	4.23±0.26±0.07	4.57±0.40±0.09	4.40±0.20±0.09	y^{a}_{COsat}	3.30±0.10±0.16
q_{DNM}	6.97±0.24±0.07	6.83±0.19±0.08	6.63±0.21±0.08	7.17±0.38±0.09	6.86±0.14±0.10	y^{a}_{DNM}	1.52±0.02±0.09
q_{ic}	1.40±0.78±0.20	3.06±0.72±0.42	2.46±0.70±0.26	2.31±0.87±0.18	3.01±0.48±0.21	y^{d}_{iso}	-1.54±0.02±0.10
q_{iso}	1.96±0.27±0.04	1.89±0.30±0.15	1.43±0.29±0.06	1.85±0.29±0.04	1.58±0.16±0.08		

Notes. The q coefficients are expressed in 10^{20} cm^{-2} (K km s^{-1}) for the CO; 3.8 10^{15} cm^{-2}Jy^{-1}sr for the free-free; 10^{25} cm^{-2} for the DNM and CO$_{Sat}$; other q coefficients are simple normalization factors.
The y coefficients are expressed as follows: ^{a} in 10^{-26} cm^{2}; ^{b} in 10^{-6} K^{-1}km^{-1}s; ^{c} in 3.8 10^{-11} Jy^{-1}sr; ^{d} in 10^{-6}.
The first uncertainties are statistical, the second give the standard deviations obtained by varying the H I spin temperature.

Table E.1. Estimates of the average X_{CO} factor in units of 10^{20} cm^{-2} (K km s^{-1})$^{-1}$.

γ-ray telescope	Location	X_{CO} factor	reference
	Large Galactic scales		
COS-B	1st quadrant	2.5^{a}	Lebrun et al. (1983)
COS-B	Galactic disc	2.3^{a}	Bloemen et al. (1986)
COS-B	Galactic disc	2.3 ± 0.3	Strong et al. (1988)
EGRET	Galactic disc	1.9 ± 0.2	Strong & Mattox (1996)
EGRET	Galactic disc	1.56 ± 0.05	Hunter et al. (1997)
EGRET	$5° < \lvert b \rvert < 80°$	1.74 ± 0.03	Grenier et al. (2005)
EGRET	Local Arm 3rd quadrant	1.64 ± 0.31	Digel et al. (2001)
Fermi LAT	Local Arm 2nd quadrant	1.59 ± 0.17	Abdo et al. (2010)
Fermi LAT	Local Arm Cygnus	1.68 ± 0.05	Ackermann et al. (2012d)
Fermi LAT	Local Arm 3rd quadrant	2.08 ± 0.11	Ackermann et al. (2011)
Fermi LAT	between the Local and Perseus arms	1.93 ± 0.16	Ackermann et al. (2011)
Fermi LAT	Perseus arm	1.9 ± 0.2	Abdo et al. (2010)
	Nearby clouds		
COS-B	Oph-Sag	0.9 ± 0.4^{a}	Lebrun & Huang (1984)
COS-B	Orion	2.1 ± 1.0^{a}	Bloemen et al. (1984)
EGRET	Oph	1.1 ± 0.2	Hunter et al. (1994)
EGRET	Orion	1.35 ± 0.15	Digel et al. (1999)
EGRET	Cepheus	0.92 ± 0.14	Digel et al. (1996)
EGRET	Taurus	1.08 ± 0.10	Digel & Grenier (2001)
Fermi LAT	Orion	1.21 ± 0.02	Ackermann et al. (2012b)
Fermi LAT	Cepheus & Cassiopeia	0.87 ± 0.05	Abdo et al. (2010)
Fermi LAT	Cepheus & Polaris	0.63 ± 0.02	Ackermann et al. (2012c)
Fermi LAT	RCrA	0.99 ± 0.08	Ackermann et al. (2012c)
Fermi LAT	Chamaeleon	0.69 ± 0.02	Planck and Fermi Collaborations (2015)
Fermi LAT	$10° < \lvert b \rvert < 70°$	0.902 ± 0.007	Casandjian (2015)

Notes. [a] corrected to absolute CO radiation temperatures according to Bronfman et al. (1988)

Quatrième partie

Relations entre l'émission et l'extinction des poussières et les propriétés des grains

Cette partie présente les résultats du troisième article poursuivant la discussion sur l'évolution de propriétés des poussières initiée dans le premier article (présenté en partie 3). Nous avons repris l'étude des nuages locaux de l'anticentre Galactique avec la même méthode d'analyse couplant traceurs de poussière et émission de rayons γ, mais en substituant les données d'émission des poussières, l'épaisseur otique τ_{353} à 353 GHz, par des données d'extinction, le rougissement stellaire $E(\mathrm{B-V})$. Comme précédemment pour l'opacité $\tau_{353}/N_{\mathrm{H}}$, le rapport $E(\mathrm{B-V})/N_{\mathrm{H}}$ est calculé en utilisant la densité de colonne d'hydrogène, N_{H}, déduite de l'émission de rayons γ d'origine interstellaire. Les poussières étant mélangées avec le gaz interstellaire, l'évolution de ces rapports en fonction de la quantité de gaz totale nous fournit des contraintes sur l'évolution des propriétés des grains et du rapport gaz sur poussière, dans les milieux diffus jusqu'au cœur des nuages moléculaires. L'étude conjointe des variations des rapports $\tau_{353}/N_{\mathrm{H}}$ et $E(\mathrm{B-V})/N_{\mathrm{H}}$ en fonction de quantités liés aux propriétés des grains (index spectral d'émission thermique, température de couleur, facteur d'extinction...) permet de faire le lien avec les prédictions des modèles de grains et de comparer qualitativement et quantitativement les tendances observées.

Chronologiquement cette analyse a été réalisée en dernier au vu des données dont nous disposions. Les cartes basées sur les données photométriques infrarouges de 2MASS (Rowles & Froebrich 2009; Dobashi et al. 2013; Juvela & Montillaud 2016) couvrant toute la région permettent de sonder les nuages moléculaires et le gaz sombre et mais elles présentent un fort bruit dans les régions diffuses particulièrement à basse latitude. Selon la méthode utilisée pour dériver ces cartes (et gérer ce bruit) on note un décale des extinctions prédites ($\sim$ 0.5 magnitude). Nous avons tester la corrélation de ces cartes d'extinction à de l'épaisseur optique des poussières,τ_{353},(Planck Collaboration 2014a) et la densité de colonne de gaz, N_{H}, déduite de l'émission de rayon γ interstellaire. On note des différences systématiques qui suggèrent que les données infrarouges de 2MASS seules ne suffisent pas pour tracer la quantité de poussière mixée avec le gaz diffus. Parallèlement la carte d'extinction de Schlafly et al. (2014a) basée les données photométriques optiques de Pan-STARRS [20] présente un très faible bruit dans les régions diffuses mais ne sonde pas aussi profondément les nuages moléculaires que celles basées sur les données infrarouges de 2MASS. En combinant les données optiques et infrarouges de Pan-STARRS et 2MASS, Green et al. (2015) ont obtenu une carte d'extinction 3D allant jusqu'à plusieurs kilo-parsecs de distance du Soleil. La comparaison de cette carte (intégrée sur toute les distances) avec l'épaisseur optique des poussières et avec la densité de colonne de gaz déduite de l'émission de rayon γ interstellaire présente globalement une meilleure corrélation que les cartes basées uniquement sur les données optiques ou infrarouges seules. C'est donc seulement au cours cette dernière année que nous avons utilisé le rougissement $E(\mathrm{B-V})$ donné par Green et al. (2015) pour une analyse conjointe du rougissement des poussières et de l'émission de rayons γ. Les résultats de cette analyse n'ont pas encore été discutés en détail avec la Collaboration *Fermi*-LAT et l'article proposé est un premier brouillon avant revue interne de la Collaboration. La section 2 décrivant les données et analyses doit être consolidée en résumant les exposées correspondants déjà présentés dans l'article I.

Les résultats de l'analyse indiquent en premier lieu une excellente corrélation entre les densités de colonne de gaz déduites du modèle conjoint $E(\mathrm{B-V})+\gamma$ et celle du modèle $\tau_{353}+\gamma$ présenté dans le premier article (moins de 3% d'écart en direction des nuages moléculaires et du DNM). Ceci indique que le choix du traceur de poussière,

---

[20] Pan-STARRS : Panoramic Survey Telescope And Rapid Response System

permettant de contraindre la structure du gaz sombre (DNM) en lien avec l'émission γ, n'affecte pas significativement le calcul de la densité de colonne de gaz totale. La structure spatiale et les densités de colonne du gaz dans le DNM obtenue dans les deux analyses sont très similaires.

Sur l'ensemble de la région, nous avons mesuré un rapport $E(\mathrm{B-V})/N_\mathrm{H}$ moyen de $(2.02 \pm 0.48) \times 10^{-22}$ mag. cm^2. Les valeurs moyennes trouvées dans les nuages individuels varient seulement d'environ 10% dans la phase atomique et dans les nuages moléculaires diffus (faible émission CO). Dans les régions moléculaire plus brillantes en CO le rapport $E(\mathrm{B-V})/N_\mathrm{H}$ moyen tend à augmenter mais localement on note tout de même des variations autour de la valeur moyenne d'un nuage moléculaire à un autre et à l'intérieur des nuages. L'écart au $E(\mathrm{B-V})/N_\mathrm{H}$ moyen ne dépasse pas les 30%. L'augmentation du rapport $E(\mathrm{B-V})/N_\mathrm{H}$ entre les phases HI et CO est nettement moins marquée que celle du rapport τ_{353}/N_H, notée dans l'article I.

Dans le premier article nous avions montré que dans les différents nuages locaux de l'anticentre Galactique, les mesures du rapport X_CO basées sur l'épaisseur otique des poussières étaient systématiquement plus grandes que celles basées sur l'émission de rayons γ, et ce d'autant plus dans les nuages possédant une grande épaisseur otique. Les mesures du rapport X_CO basées sur l'extinction des poussières montre un meilleur accord avec celles basées sur l'émission de rayons γ. Ceci confirme que les larges valeurs du facteur X_CO déduites de l'épaisseur optique, τ_{353}, sont biaisées à la hausse par l'augmentation intrinsèque de l'opacité τ_{353}/N_H dans les nuages moléculaire.

Les relations entre les rapports τ_{353}/N_H et $E(\mathrm{B-V})/N_\mathrm{H}$ et les propriétés des poussières telles que l'index spectral β, la température de couleur T_dust, la facteur d'extinction R_V, la taille des grains... permettent de tester les prédictions des modèles sur l'évolution de la structure et de la composition des grains. Les résultats des articles I et III sur les variations des rapports τ_{353}/N_H et $E(\mathrm{B-V})/N_\mathrm{H}$, associés aux mesures de β, T_dust (Planck Collaboration 2014a) et R_V (Foster et al. 2013; Schlafly et al. 2016), ont été confronté aux prédictions des modèles récents d'évolution des grains (Cecchi-Pestellini et al. 2010; Ysard et al. 2013; Jones et al. 2013; Köhler et al. 2015) et nous ont amené aux conclusions suivantes :

Dans le milieu diffus les faibles variations du rapport $E(\mathrm{B-V})/N_\mathrm{H}$ sont compatibles avec l'amplitude des variations du facteur d'extinction R_V ($\sim$ 10%), la faible dispersion dans ces deux observables suggère que le rapport de masse gaz-sur-poussière ne varie pas significativement. La nette augmentation de l'opacité τ_{353}/N_H du HI diffus au DNM, d'un facteur 2 comparée à la valeur trouvée dans les cirrus à haute latitude, est donc probablement due à un changement d'émissivité des grains plutôt qu'à une augmentation du rapport de masse gaz-sur-poussière. La hausse d'opacité s'accompagne d'une augmentation de l'index spectral β et d'une baisse de la température de couleur des grains. Les opacités relevées dans le DNM sont associées à des valeurs T_dust = 16-18 K et $\beta > 1.5$, ce qui est compatible avec les valeurs de β prédites par le modèle de (Köhler et al. 2015) lors de la formation de manteau d'accrétion à la surface des grains. L'accrétion n'augmentant pas significativement la taille des grains, ni les valeurs de R_V, ce processus est compatible avec les faibles variations de $E(\mathrm{B-V})/N_\mathrm{H}$ et R_V observées dans les milieux diffus et le DNM.

La comparaison des mesures du facteur R_V et de l'index β réalisé par (Schlafly et al. 2016) présente un forte dispersion, mais montre une tendance à diminuer β quand R_V augmente. Le modèle de (Köhler et al. 2015) prédit globalement la tendance opposée, une hausse R_V avec β. Ceci semble indiquer qu'un autre processus entre aussi en jeu. Comme les mesures de T_dust et β sont anti-corrélés (Planck Collaboration 2014a), l'augmentation de R_V quand β diminue pourrait refléter une augmentation R_V avec la température de couleur des grains. On note une diminution systématique du rapport $E(\mathrm{B-V})/N_\mathrm{H}$ (inversement proportionnel à R_V) pour $T_\mathrm{dust} > 19$ et $\beta < 1.7$, en accord avec cette tendance. Des températures de couleur plus grandes sont associées à une radiance thermique des grains plus élevées ce qui indique indirectement qu'ils ont été plus chauffés par le champ de rayonnement interstellaire (IRSF). Une plus forte exposition à l'IRSF peut entrainer un assombrissement des grains augmentant R_V au cours du temps (Cecchi-Pestellini et al. 2010). Ceci pourrait expliquer la hausse R_V noté par Schlafly et al. (2016) quand β diminue (et T_dust augmente).

Dans les régions moléculaires, les modèles prédisent une augmentation de l'index spectral, de la taille des grains et du facteur d'extinction, liée à la formation de grands agrégats par coagulation des grains (Ysard et al. 2013; Köhler et al. 2015). La hausse de l'opacité τ_{353}/N_H observée s'accompagne d'une augmentation de l'index spectral compatible avec les prédictions des modèles. Cependant les variations du rapport $E(\mathrm{B-V})/N_\mathrm{H}$ autour de la moyenne dans différentes sous-structures d'un même nuage moléculaire, comme observé dans Persée, suggèrent des variations des propriétés d'extinction des grains très sensibles aux conditions locales dans ces milieux denses. Néanmoins l'extinction est moins bien contrainte dans ces régions (nombre moins important d'étoiles détectées) et les sous-structures les plus denses ne sont pas complètement résolues par les cartes de rougissement et d'émission γ utilisées. Ces variations locales pourrait s'effacer si ils étaient dues à un effet systématique ou s'accentuer avec une meilleure résolution.

Astronomy & Astrophysics manuscript no. tau16_paper3_v2
October 14, 2016

Cosmic-rays, gas, and dust in nearby anti-centre clouds : III – Dust extinction, emission, and grains properties

Q. Remy(1), I. A. Grenier(1), D.J. Marshall(1), and J. M. Casandjian(1)

[1] Laboratoire AIM, CEA-IRFU/CNRS/Université Paris Diderot, Service d'Astrophysique, CEA Saclay, F-91191 Gif sur Yvette, France
e-mail: `quentin.remy@cea.fr`
e-mail: `isabelle.grenier@cea.fr`

October 14, 2016

ABSTRACT

Aims. We have explored the capabilities of dust extinction and γ rays to probe the properties of the interstellar medium in the nearby anti-centre region. In particular, we aim at quantifying the variations of the dust properties per gas nucleon across the different gas phases and different clouds. The comparison of dust extinction and emission properties with other physical quantities of large grains (size, emission spectral index β, total-to-selective extinction factor R_V) helps the theoretical modelling of grains as they evolve from diffuse to dense cloud environments.

Methods. We have jointly modelled the γ-ray intensity, recorded between 0.4 and 100 GeV with the *Fermi* Large Area Telescope (LAT), and the stellar reddening, $E(B-V)$, inferred from *Pan-STARRS* and *2MASS* photometry, as a combination of HI-bright, CO-bright, and ionised gas components. The complementary information from dust extinction and γ rays is used to reveal the gas not seen, or poorly traced, by HI, free-free, and ^{12}CO emissions, namely (i) the opaque HI and diffuse H_2 present in the Dark Neutral Medium (DNM) at the atomic-molecular transition, and (ii) the dense H_2 to be added where ^{12}CO lines saturate (CO_{sat}). We use the total gas column density, N_H, inferred from the interstellar γ rays to measure the dust reddening per gas nucleon, $E(B-V)/N_H$. We compare the gas maps with those inferred from a similar analysis (Remy et al. 2016) of γ rays and of the optical depth of the thermal dust emission, τ_{353}, at 353 GHz, so that we can compare environmental variations in the $E(B-V)/N_H$ ratio and in the dust emission opacity, τ_{353}/N_H.

Results. The gas column densities obtained when combining γ rays with either dust reddening or dust emission compare reasonably well in the atomic and DNM gas phases and over most of the CO-bright phase, but we find localized differences in the dense media (CO_{sat} component) due to differences in the two dust tracers. Over the whole anti-centre region, we find an average $E(B-V)/N_H$ ratio of $(2.02 \pm 0.48)\times10^{-22}$ mag. cm^2 with maximum local variations of about ±30%, at variance with the 2-to-6-fold coincident increase seen in emission opacity as the gas column density increases. We show how the $E(B-V)/N_H$ ratios and opacities vary with the colour temperature and spectral index of the thermal emission of the large grains. Additionally, we find a better agreement between the $X_{CO} = N(H_2)/W_{CO}$ conversion factors derived with dust reddening or with γ rays than with those inferred from dust emission, especially toward clouds with large τ_{353} optical depths. The comparison confirms that the high X_{CO} values found with dust emission are biased by the significant rise in emission opacity inside molecular clouds.

Conclusions. In the diffuse medium, we find only small variations in the $E(B-V)/N_H$ factor compatible with the dispersion in the R_V factor reported by other studies. This implies a rather uniform dust-to-gas mass ratio in the diffuse parts of the anti-centre clouds. The small amplitude of the $E(B-V)/N_H$ variations with increasing N_H confirms that the large opacity τ_{353}/N_H rise seen toward dense CO clouds is primarily due to changes in dust emissivity. The environmental changes are qualitatively compatible with model predictions based on mantle accretion on the grains and the formation of grain aggregates.

Key words. Gamma rays: ISM – Galaxy: solar neighbourhood – ISM: clouds – ISM: cosmic rays – ISM: dust

1. Introduction

Large dust grains in the interstellar medium (ISM) absorb starlight from the UV to near infrared domain causing appreciable extinction or reddening in stellar observations (Draine 2003). These grains in thermal equilibrium with the ambient radiation field re-emit in the infrared to millimetre wavelengths. If the dust grains are well mixed with the interstellar gas, the extinction they cause and their thermal emission both provide indirect tracers of the gas column density.

The extinction caused by dust grains is generally estimated from the photometry of a set of stars in a given direction. A family of method is based on the comparison of the observed stellar colours in various photometric bands with reference colours corresponding to zero extinction (NICE, NICER, NICEST algorithms: Lada et al. 1994; Lombardi & Alves 2001; Lombardi 2009). Such colour-excess methods have been applied to 2MASS photometry to derive two-dimensional maps of the dust extinction over the whole sky (Rowles & Froebrich 2009; Juvela & Montillaud 2016). Marshall et al. (2006) have developed a method to estimate simultaneously the dust extinction and distance comparing the observed colour from 2MASS data with the intrinsic colours and distances of stars provided by the Besancon Galaxy model (Robin et al. 2003). More recently, Green et al. (2015) have used the combined information of Pan-STARRS 1 and 2MASS surveys to derive a three-dimensional extinction

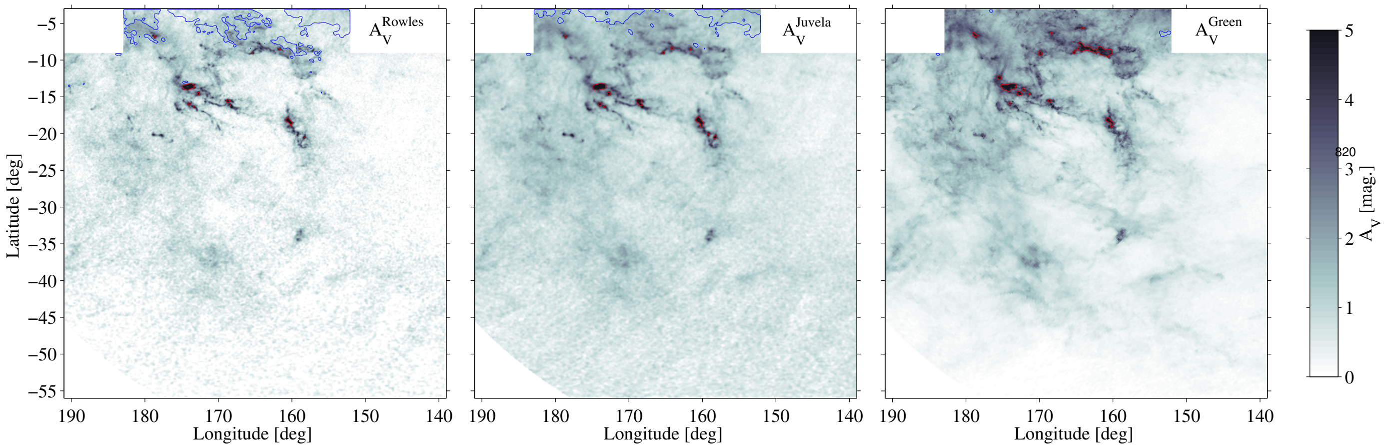

Fig. 1. Visual extinction maps derived from Rowles & Froebrich (2009); Juvela & Montillaud (2016); Green et al. (2015) (from left to right) with the extinction law of Cardelli et al. (1989). The blue and red contours correspond to cuts in A_V at respectively at $0.2 < A_V < 1.6$ and $A_V > 4$ mag. in regions where $N_H > 4.5 \times 10^{21}$ cm^{-2}.

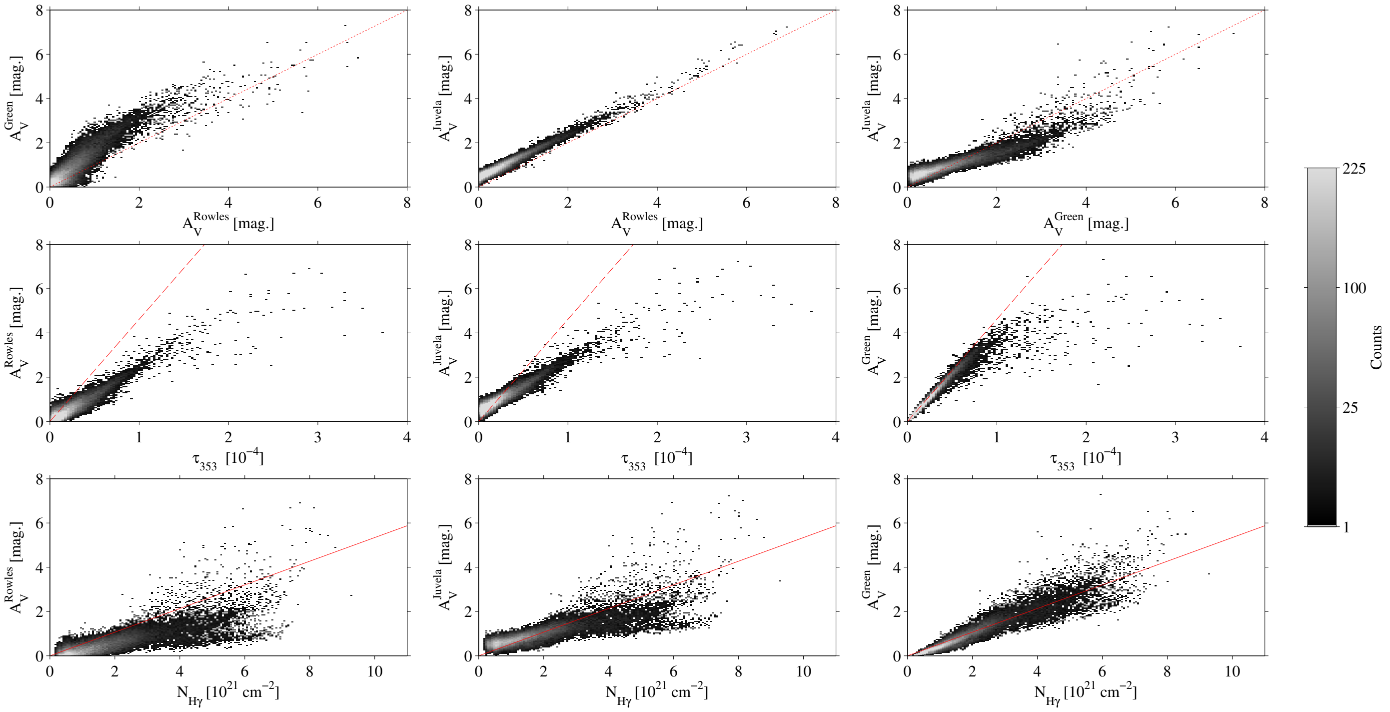

Fig. 2. *Top*: 2D histograms in 0.°25×0.°25 bins of the correlations between the visual extinction maps derived from Rowles & Froebrich (2009), Juvela & Montillaud (2016), and Green et al. (2015) with the extinction law of Cardelli et al. (1989) (R_V=3.1). *Middle*: 2D histograms of the correlations between the dust optical depth at 353 GHz (Planck Collaboration 2014a) and visual extinction maps. *Bottom*: 2D histograms of the correlations between the total gas column density, $N_{H\gamma}$, measured with the 0.4-100 GeV interstellar γ rays (Remy et al. (2016)) and visual extinction maps. The dotted line in the top plots corresponds to a one-to-one correlation. The dashed line in the middle plots corresponds to a ratio $A_V/\tau_{353} = 4.62 \times 10^4$ mag. (Planck Collaboration 2014a). The solid line in the bottom plots corresponds to a ratio $A_V/N_H = 5.34 \times 10^{-22}$ mag. cm^2 (Bohlin et al. 1978).

map in a fully probabilistic framework described in Green et al. (2014).

The dust emission at 100 and 240 μm measured with *DIRBE* and *IRAS* has been used to estimate dust optical depths over the whole sky (Schlegel et al. 1998). This map has then been scaled to E(B−V) reddenings using a set of quasar reddening measurements. In a more recent study (Planck Collaboration 2014a), the dust emission between 353 to 3000 Ghz (100 to 850 μm) measured with *Planck* and *IRAS* has been used to model the dust spectral energy distribution and derive an all-sky map of the dust optical depth at 353 GHz, τ_{353}. The latter relates to dust column density and grain emissivity. Assuming uniform dust properties (size distribution, chemical composition, and grain structure), the dust optical depth can be converted into extinction or reddening.

In addition to the information provided by dust tracers, γ rays with energies above few hundred of MeV produced by the interaction of cosmic rays (CRs) with gas nucleons provide a measure of the total gas column density assuming a uniform CR flux through a given cloud (Cesarsky & Volk 1978; Lebrun et al. 1982; Strong et al. 1988). As shown in (Remy et al. 2016), the interstellar γ-ray spectra measured in the nearby clouds of the

Galactic anti-centre region studied here, are consistent with a uniform penetration of the cosmic rays with energies above a few GeV through the different gas phases of the clouds, from the atomic envelopes to the molecular cores.

Several studies have noted an increase in dust opacity (optical depth per gas nucleon, $\tau_{353}/N_{\rm H}$) with increasing gas column density from the atomic to molecular phases. In the Taurus clouds, the opacities increase in the dense CO filaments by a factor ranging from ~2 (Flagey et al. 2009; Planck Collaboration 2011; Ysard et al. 2013) to $3.4^{+0.3}_{-0.7}$ (Stepnik et al. 2003) above the diffuse-ISM value. In a study of the Galactic anti-centre region including the Taurus clouds (Remy et al. 2016), we have found opacity enhancements reaching a factor of six toward the CO clouds, even though we provide a measure of the additional H_2 gas that is not linearly traced by $W_{\rm CO}$ in the directions where the ^{12}CO line emission saturates (CO$_{\rm sat}$). We also find that the opacity starts to increase in the Dark Neutral Medium (DNM) at the HI–H_2 transition, therefore at lower gas densities than the few thousand per cm^3 sampled in CO. The grain opacity found in the DNM of the Galactic anti-centre region compares well with that of the DNM surrounding the Chamaeleon clouds (Planck and Fermi Collaborations 2015).

The opacity increase could be caused by an evolution of the grain properties changing their mass emission coefficient, as suggested by recent theoretical works (Köhler et al. 2015), or by spatial variations in the dust-to-gas mass ratio. The latter possibility also impacts the relation between dust extinction and gas column density. In the present study we aim to study variations in the distribution of E(B−V)/nh ratios in the nearby anti-centre clouds, using γ rays to trace the gas column density. We use the same analysis method and gas data as used in the derivation of the dust opacity, $\tau_{353}/N_{\rm H}$, in these clouds (Remy et al. 2016) in order to compare environmental changes in E(B−V)/$N_{\rm H}$ and in $\tau_{353}/N_{\rm H}$.

The challenges of tracing the gas and dust in the ISM and the motivation for this work to compare the total gas column density information inferred from various tracers are presented in Sec. 1.1. To do so, we compare several extinction maps with the dust optical depth at 353 GHz from Planck Collaboration (2014a) and with the hydrogen column density derived from interstellar γ rays from Remy et al. (2016). As described in Sec. 2, the indications given by this comparison guide the choice of the extinction map to be used with the γ rays to study the E(B−V)/$N_{\rm H}$ ratios in the different gas phases (HI, DNM, and CO). The joint analysis of dust and γ-ray tracers is detailed in Remy et al. (2016) and summarized in Sec. 2.1. The result of the joint "γ+E(B−V)" analysis are given in Sec. 3 and compared to the results of the former "γ+τ_{353}" analysis. The consequences on dust properties and on the capability of these dust tracers to probe the gas column density are discussed in the last section.

1.1. Comparison of dust and gas tracers

For our analyses, we have selected the same anti-centre region as that studied in Remy et al. (2016). It extends from 139°to 191°in Galactic longitude and from -56°to -3°in latitude. Regions with large gas column densities from the Galactic disc in the background and regions with a coarser angular resolution in HI have been masked. The resulting analysis region is depicted in Fig. 1. We have selected three dust extinction maps in order to quantify the differences between dust extinctions derived with several methods and to test their relative correlation with the dust emission optical depth and gas column density over the same regions. The extinction maps are the following:

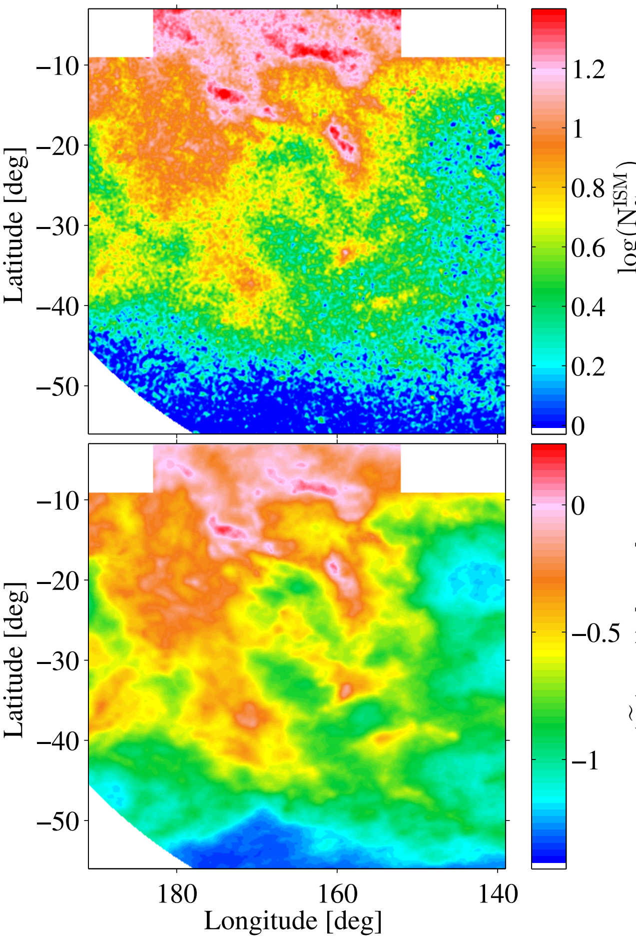

Fig. 3. *Top:* γ-ray counts of gaseous origin recorded in the 0.4–100 GeV energy band in a 0°.125 pixel grid. γ-ray emissions other than due to cosmic-ray interactions in the gas have been subtracted. The map has been smoothed with a Gaussian kernel of 0°.14 dispersion for display. *Bottom:* stellar reddening by dust displayed at the *Fermi*-LAT angular resolution for comparison.

- a visual extinction, $A_{\rm V}$, map constructed from the 2MASS stellar data, with the median colour excess of the 49 stars nearest to each direction (Rowles & Froebrich 2009);
- an extinction map in the J band, $A_{\rm J}$, derived from the 2MASS data with the NICER M2a processing at 12′-resolution (Juvela & Montillaud 2016) ;
- a three-dimensional E(B−V) map based on Pan-STARRS 1 and 2MASS stellar data integrated up to its maximal distance (Green et al. 2015).

According to the extinction law of Cardelli et al. (1989), we have converted the map of Juvela & Montillaud (2016) from $A_{\rm J}$ to $A_{\rm V}$ with a multiplicative factor 3.55 and the map of Green et al. (2015) from E(B−V) to $A_{\rm V}$ using the extinction factor $R_{\rm V}$=3.1. The resulting three visual extinction maps are presented in Fig. 1 together with contours delimiting a selection of regions where $N_{\rm H}$ and $A_{\rm V}$ are not linearly correlated. Figure 2 shows the 2D histograms of the correlations between each of these visual extinction maps and the dust optical depth at 353 GHz (Planck Collaboration 2014a). It also displays the correlations with the gas column density derived from γ rays of interstellar origin in the 0.4-5 GeV energy range from Remy et al. (2016). The histograms have been constructed in 0°.25×0°.25 bins to compare the datasets at a common angular resolution.

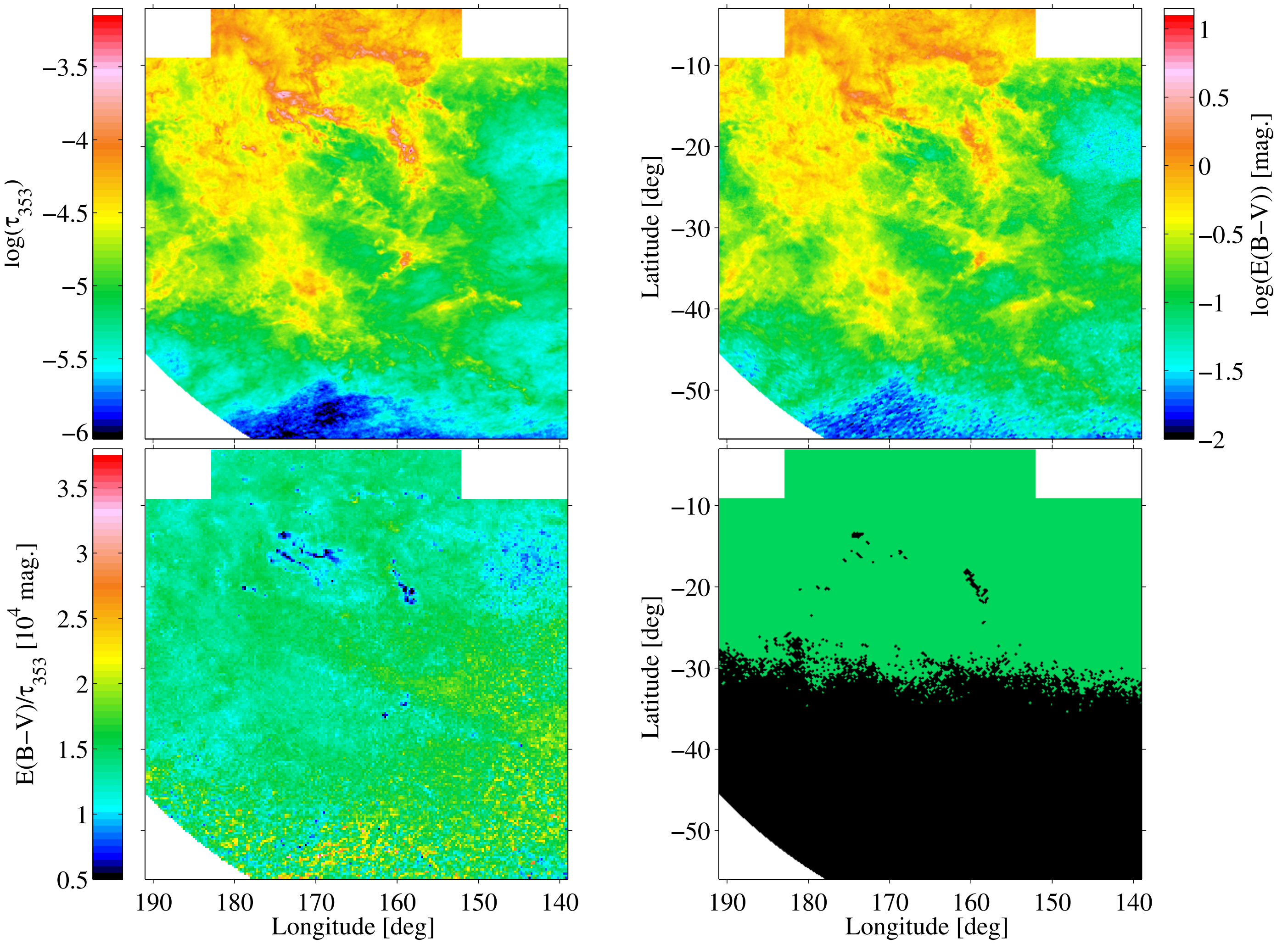

Fig. 4. Maps of the dust optical depth at 353 GHz (top left), of the stellar reddening by dust (top right), and of their ratio (bottom left). The map on the lower right shows in green the pixels with an angular resolution of 0°.11 in $E(\mathrm{B-V})$, which have been retained for mask2, and in black the pixels with a lower resolution.

Figure 2 shows that the visual extinctions obtained by Rowles & Froebrich (2009) and Juvela & Montillaud (2016) are closely correlated with increasing A_V, but the latter is shifted to higher extinction by about 0.5 mag. The map of Green et al. (2015) presents less noise at low A_V, but most of the pixels with $A_\mathrm{V} \gtrsim 1$ mag. exhibit extinctions above the values of the two others. Those differences may be explained by the use of optical data from Pan-STARRS to complement the 2MASS sample, especially in diffuse regions. The precision is also improved by larger stellar statistics. Conversely, the near-infrared data from 2MASS is essential to scan deeper into dense molecular clouds. In the nearby clouds of Orion, Taurus and Perseus, Green et al. (2015) obtain larger extinctions when combining 2MASS and Pan-STARRS photometry than with the sole use of Pan-STARRS (Schlafly et al. 2014). We also find a tighter correlation between the gas column densities derived in γ rays and the extinctions based on 2MASS and Pan-STARRS data than with Pan-STARRS-based extinctions (not illustrated here).

Figure 2 also clearly shows that the dust optical depth strongly deviates from the visual extinction above 2 or 3 mag, independently of the method employed to derive the visual extinctions. At $\tau_{353} > 10^{-4}$ the optical depth non-linearly increases above the extinction expectation. At A_V <2 mag., the distribution of Green et al. (2015) compares well with the A_V/τ_{353} ratio of 4.62×10^4 mag. found by Planck Collaboration (2014a) using colour-excess measurements toward 53 399 quasars and converted from $E(\mathrm{B-V})$ to A_V with $R_\mathrm{V} = 3.1$.

We note a significant saturation of the extinction at $N_\mathrm{H} > 4 \times 10^{21}$ cm^{-2} and A_V <2 mag in the maps of Rowles & Froebrich (2009) and Juvela & Montillaud (2016). This corresponds to regions in the Galactic disc (enclosed by blue contours in Fig. 1). At low gas column densities, $N_\mathrm{H} < 2 \times 10^{21}$ cm^{-2}, the data from Juvela & Montillaud (2016) and Green et al. (2015) show a better correlation with the gas column densities derived from the γ-ray emission. The slope is consistent with the standard ratio $A_\mathrm{V}/N_\mathrm{H} = 5.34{\times}10^{-22}$ mag. cm^2 of Bohlin et al. (1978). At larger column densities, $N_\mathrm{H} > 4 \times 10^{21}$ cm^{-2}, the dispersion in A_V increases. Large extinctions deviating from the N_H trend are found in the densest cores of molecular clouds (within red contours in Fig 1). They are possibly due to the lack of suitable stars in heavily obscured regions.

The N_H column density used in Fig. 2 for this quick look at the correlations between dust and gas tracers is based on the analysis coupling γ rays and the τ_{353} optical depth in emission to map the DNM gas (Remy et al. 2016). To be fully consistent and accurate in the determination of $E(\mathrm{B-V})/N_\mathrm{H}$ ratios, we need to derive the $N_{\rm H}$ map with the same analysis method, but using jointly γ-ray emission and dust extinction.

2. Analyses and data

2.1. Summary of dust and γ-ray models

The large dust grains responsible for the stellar reddening at near IR and optical wavelengths are supposed to be well mixed with the interstellar gas, so we have modelled the spatial distributions of the E(B−V) reddening as a linear combination of gas column densities in the various phases and different cloud complexes (see Eq. 6 of Remy et al. 2016, substituting E(B−V) for τ_{353}). As the reddening map of Green et al. (2015) presents a better correlation with both the dust optical depth and gas column densities, we use this map hereafter to study the relation between $N_{\rm H}$ and E(B−V).

We have also used the same γ-ray data as in Remy et al. (2016), namely six years of Pass 8 photon data, recorded between 0.4 and 100 GeV by the *Fermi* Large Area Telescope (LAT) and the associated instrument response function (P8R2_CLEAN_V6). At the energies relevant for the LAT observations, the particle diffusion lengths in the interstellar medium exceed the cloud dimensions and there is no spectral indication of variations in CR density inside the clouds (Remy et al. 2016), so the interstellar γ radiation can be modelled, to first order, as a linear combination of gas column-densities in the various phases and different regions seen along the lines of sight. The model also includes a contribution from the large-scale Galactic inverse-Compton (IC) emission, an isotropic intensity to account for the instrumental and extragalactic backgrounds, and point sources (see Eq. 7 of Remy et al. 2016).

To ensure photon statistics robust enough to follow details in the spatial distributions of the different interstellar components, we have analysed the data in broad and independent energy bands, bounded by $10^{2.6}$, $10^{2.8}$, $10^{3.2}$, $10^{3.6}$, and 10^5 MeV. We have assumed that the emissivity spectrum of the gas follows the average one obtained in the local ISM (Casandjian 2015) but we have left a free normalisation in each energy band to account for possible deviations in CR density and spectrum.

The positions and the flux spectra of the γ-ray sources in the field are provided by the *Fermi*-LAT Third Source Catalog (Acero et al. 2015). The observed γ-ray emission also includes a contribution from the large-scale Galactic inverse Compton (IC) emission emanating from the interactions of CR electrons with the interstellar radiation field (ISRF). The GALPROP[1] parameter file 54-LRYusifovXCO4z6R30-Ts150-mag2 has been used to generate an energy-dependent template of the Galactic IC emission across the analysis region (Ackermann et al. 2012) Details on the isotropic spectrum for the extragalactic and residual instrumental backgrounds are given in Atwood et al. (2013) and Acero et al. (2015).

In order to reduce the contamination by residual CRs tracks in the photon data and by Earth atmospheric γ rays, we have applied tight rejection criteria (CLEAN class selection, photon arrival directions within $< 100°$ of the Earth zenith and in time intervals when the LAT rocking angle was inferior to 52°, see Nolan et al. 2012, for details). To account for the spill-over of emission produced outside the analysis region, but reconstructed inside it, we have modelled point sources and interstellar contributions in a region 4° wider than the analysis region.

Figure 3 shows the γ rays of interstellar origin and the stellar reddening displayed at the angular resolution of the *Fermi* LAT (for an interstellar spectrum). As with the dust optical depth τ_{353} (see Fig. 3 of Remy et al. (2016)), Fig. 3 illustrates the striking similarities between the spatial distributions of the dust reddening and of the gas traced by CR interactions. The two have very a similar structure (as it have been shown for γ rays and τ_{353}, see Fig 3 of Remy et al. (2016)).

2.2. Choice of analysis masks

The map of E(B−V)/τ_{353} ratios, displayed in Fig. 4, shows that regions of intermediate E(B−V) (∼0.3-1 mag) have a ratio close to the value of $1.49{\times}10^4$ mag. found by Planck Collaboration (2014a). Yet, the ratio drops by a factor up to three at large extinctions in the direction of compact molecular clumps and filaments. This drop is due to the non-linear rise in dust opacity discussed for Fig. 2.

The E(B−V) map has been constructed with a resolution of 0°.11 or 0°.23 depending on the number of stars available in each pixel. Directions with a resolution below 0°.11 are shown in black in Fig. 4. They correspond to low latitudes far from the densely populated regions near the Galactic plane ($b < -30$ deg) and to dense molecular regions.

In the very diffuse environments below -30° in latitude where E(B−V) <0.3 mag, the fluctuations seen in the E(B−V)/$N_{\rm H}$ ratio may be due to uncertainties in the zero level in optical depth and/or to an increased level of noise in E(B−V) at lower stellar surface densities.

In order to compare dust emission and reddening across the whole region and to test the impact of the change in angular resolution across the E(B−V) map, we have performed the analysis with three different masks displayed in Fig. 4 and 5:

- mask0, including the full region as in the τ_{353} and γ-ray analysis of Remy et al. (2016),
- mask1, excluding latitudes below −30° to keep regions with high signal-to-noise in E(B−V),
- mask2, excluding all the pixels with an angular resolution in E(B−V) worse than 0°.11.

2.3. Gaseous components

As mentioned in the previous section, the dust extinction and γ-ray emission are modelled as linear combinations of several gaseous components including bright and dark neutral gas in the atomic and molecular phases as well as ionized gas. Details on these components are given in Remy et al. (2016) and summarized in the following.

The bright atomic gas is traced by the 21 cm line emission of the hydrogen. The region under study is covered at 74% by the GALFA-HI survey at 4′-resolution (Peek et al. 2011). Elsewhere we have used the EBHIS survey at 10.8′-resolution (Winkel et al. 2016). Both surveys were re-sampled into the 0°.125-spaced Cartesian grid used for the analyses. We have verified the tight correlation in column densities between the two surveys where both are available in our analysis region (Remy et al. 2016).

In order to trace the bright molecular gas, we have used ^{12}CO J=1→0 observations at 115 GHz from the moment-masked CfA CO survey of the Galactic plane (Dame et al. 2001; Dame & Thaddeus 2004). Most of the survey is based on a 0°.125-spaced Cartesian grid except for the high-latitude clouds, at $b \lesssim -50°$, which have been interpolated from 0°.25 to 0°.125.

HI and CO lines have been used to kinematically separate cloud complexes along the lines of sight and to separate the

---

[1] `http://galprop.stanford.edu`

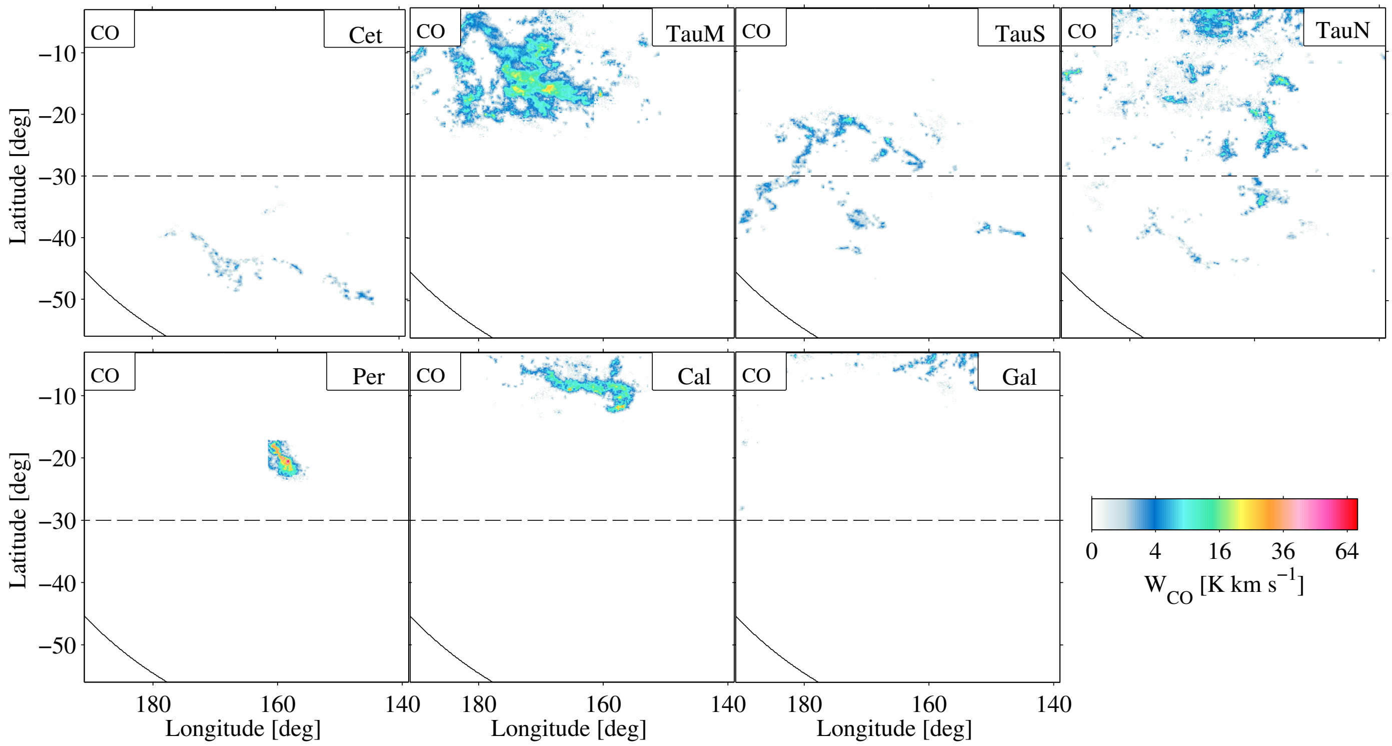

Fig. 5. Maps in CO intensity, W_{CO}, of the Cetus (Cet), Main Taurus (TauM), South Taurus (TauS), North Taurus (TauN), Perseus (Per), and California (Cal) clouds, and of the Galactic disc background (Gal). The solid curve and dashed line show the low-latitude borders of two analysis regions, respectively mask 0 and mask1.

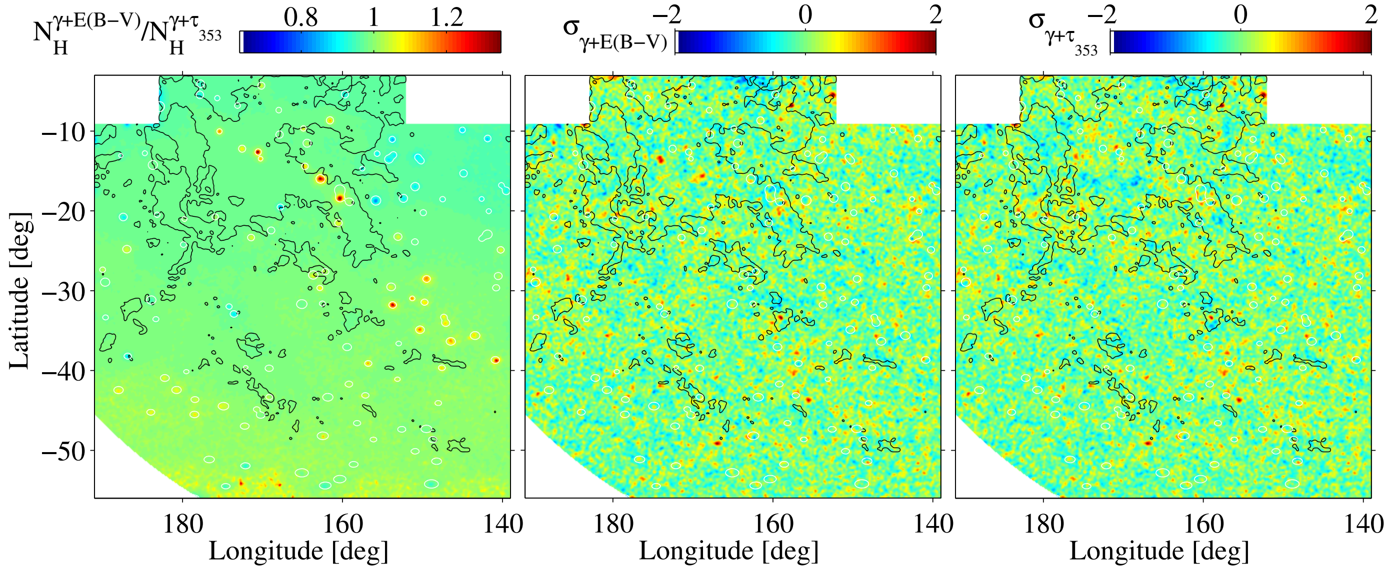

Fig. 9. *Left:* Map of the ratios of hydrogen column densities derived from interstellar γ rays in the "γ+E(B−V)" and "γ+τ_{353}" analyses, the white contours marking the position of γ-ray point sources; *Middle and right:* residual γ-ray maps (photon counts minus best-fit model, in sigma units) in the 0.4–100 GeV band for the "γ+E(B−V)" (middle) and "γ+τ_{353}" (right) analyses, for an HI spin temperature of 400 K. The black contours outline the shape of the CO clouds at the 1 K km s^{-1} level.

nearby clouds from the Galactic backgrounds. We have used the narrow-band GALFA data-cubes with their original velocity resolution of 0.18 km/s in the local standard of rest. The EBHIS frequency sampling is coarser, with a velocity resolution of 1.44 km/s, but still adequate to separate clouds in velocity. Details of the pseudo-Voigt line decompositions and selection of longitude, latitude, and velocity boundaries of the different complexes are given in Remy et al. (2016). The separation resulted in six different complexes for both HI and CO components: Cetus, South Taurus, North Taurus, Main Taurus Perseus, and California. They are shown in CO intensity, W_{CO}, in Fig. 5 and in N_{HI} column density in Fig. 1 of Remy et al. (2016). The California, Perseus, and Taurus clouds are fully kept in mask1, but Cetus is masked out in both mask1 and mask2. Those masks discard 30 and 18 % of the pixels with CO emission in the South and North Taurus clouds, respectively. 15% of the pixels toward the

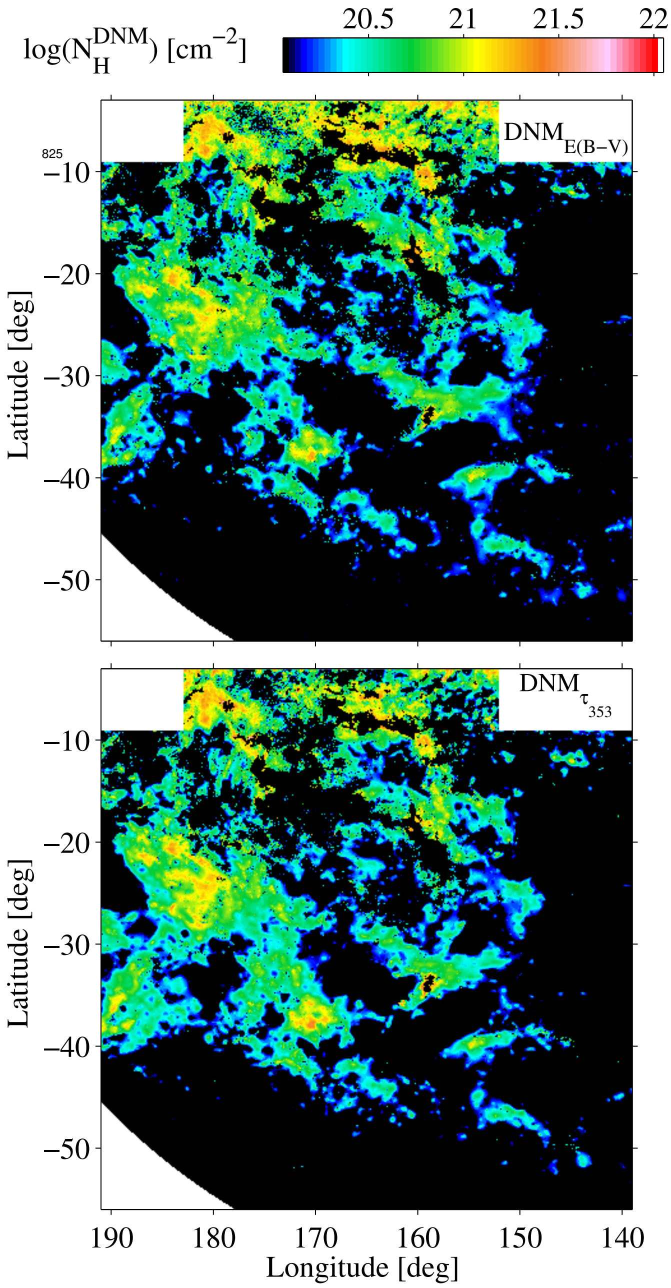

Fig. 6. Hydrogen column density maps obtained for the DNM with the "γ+E(B−V)" (top) and "γ+τ_{353}" (bottom) analyses of the full region (mask0).

Perseus cloud are masked out with mask2. Since the $X_{\rm CO}$ factor tends to decrease from the edge to the core of molecular clouds (Bell et al. 2006; Bertram et al. 2016; Remy et al. 2016) masking out sub-regions of a cloud may change the average $X_{\rm CO}$ of the cloud compared to the result obtained with mask0.

Ionised gas in the California nebula (around $l = 160\overset{\circ}{.}1$ and $b = -12\overset{\circ}{.}4$), in the G159.6-18.5 Hɪɪ region, and along the Eridanus loop is visible in Hα emission (Finkbeiner 2003) and free-free emission at mm wavelengths (Bennett et al. 2013). We have used the *Planck* LFI map at 70 GHz (release 2.01 data, Planck Collaboration 2015) with a angular resolution of 14′ to isolate the free-free emission in the analysis region. To separate the free-free intensity at 70 GHz, we have successively removed from the LFI data the contributions from the Cosmological Microwave Background (CMB), from dust emission, and from point sources (see Remy et al. (2016) for details).

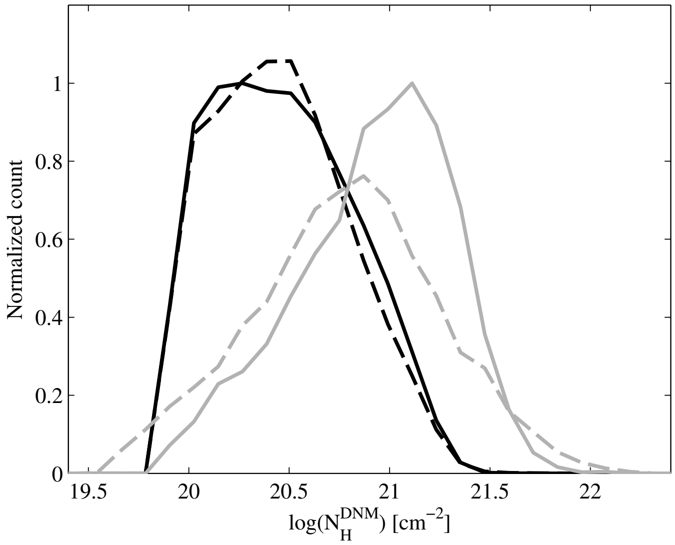

Fig. 7. Number distributions of hydrogen column densities in the DNM (black) and CO$_{\rm sat}$ (gray) components, obtained from the "γ+τ_{353}" (dashed) and "γ+E(B−V)" (solid) analyses of the full region (mask0). The curves have been normalized to the maximum value found in the "γ+E(B−V)" analysis, for each gas phase.

The analysis couples the dust and γ-ray models to constrain the structure of the additional gas not seen in Hɪ, CO and free-free emissions, namely the gas in the DNM at the Hɪ-H$_2$ transition and the CO$_{\rm sat}$ gas missed by the saturation of the ^{12}CO lines at large optical thickness. The two templates of additional gas used in the γ-ray model are inferred from the dust model and conversely. This cycle between the dust and γ-ray fits is repeated iteratively until we reach a saturation in the quality (log-likelihood) of the fit to the γ-ray data. By comparing the results of the γ-ray analyses using τ_{353} and E(B−V) as dust input, we can check for any bias in the determination of $N_{\rm H}$ column densities in γ rays, which would be indirectly induced by the dust data via the DNM and CO$_{\rm sat}$ distributions.

3. Results

3.1. Gas column density

The coupled analysis of γ rays and dust, with the latter in emission or extinction, takes advantage of the common underlying gas distribution in the two tracers to constrain the amount and structure of gas ill traced by the radio line surveys and free-free emission (i.e. DNM and CO$_{\rm sat}$). This gas is jointly revealed by its dust and CR content. We first investigate how the choice of dust tracer affects the derivation of gas column densities in the DNM and CO$_{\rm sat}$ phases, then in the total gas.

Figures 6 and 7 show that the hydrogen column densities derived from the "γ+E(B−V)" and "γ+τ_{353}" analyses in the DNM have very similar spatial structures and that the column density distributions compare well across the whole range. The total mass is the "γ+τ_{353}" map is only 9% lower than in the "γ+E(B−V)" one. The maps present small differences. In the diffuse parts below 4×10^{20} cm^{-2}, the "γ+τ_{353}" map exhibits slightly more extended structures. Above 1.5×10^{21} cm^{-2} near the Galactic plane ($b > -8°$), the "γ+E(B−V)" map yields larger column densities, probably from the Galactic disc background.

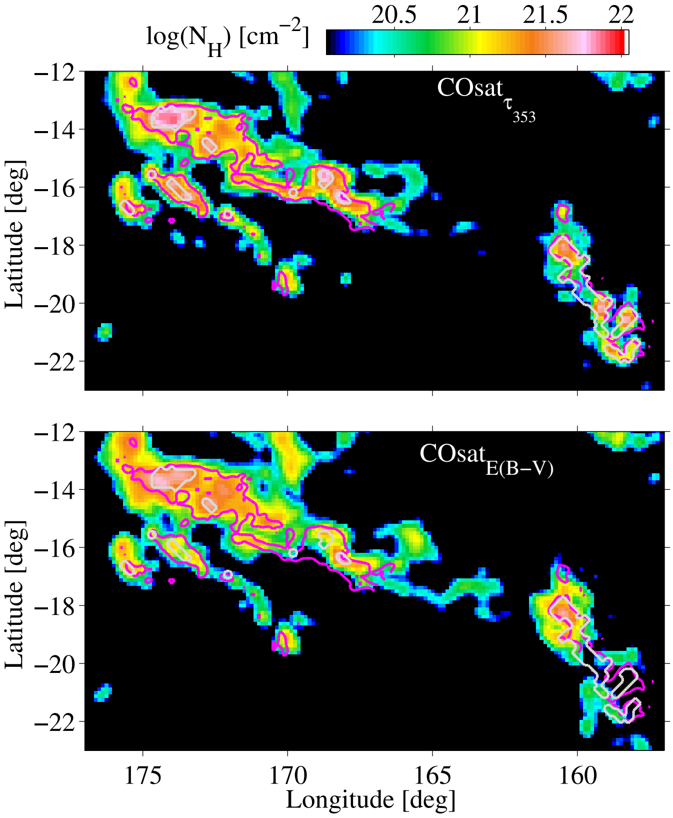

Fig. 8. Hydrogen column density map of additional gas in the ^{12}CO-saturated parts of the Taurus and Perseus clouds, derived from the "γ+τ_{353}" (top) and "γ+E(B−V)" (bottom) analyses of the full region (mask0). The pixels within the grey contours have a lower angular resolution in E(B−V) (mask2). The magenta contours enclose regions with ^{13}CO intensities above 2 K km s^{-1}.

Similarly, Fig. 8 illustrates that the CO$_{\rm sat}$ component derived in the "γ+E(B−V)" and "γ+τ_{353}" analyses presents the same overall structure. Local differences in column densities are more accentuated than in the DNM (see Fig. 7), in particular at intermediate column densities of $(1-3)\times10^{21}$ cm^{-2} where the "γ+E(B−V)" map yields larger column densities in several structures. Hence, the total CO$_{\rm sat}$ mass in the "γ+E(B−V)" map is 22% larger than in the "γ+τ_{353}" one. Conversely, the densest filaments and clumps emitting in ^{13}CO are enhanced in the "γ+τ_{353}" map (beyond 6×10^{21} cm^{-2}). This difference corresponds in Fig. 4 to the sharp rise in τ_{353} optical depth compared to the E(B−V) reddening toward the cores of the main Taurus and Perseus clouds. Those directions, however, correspond to the regions of lower angular resolution in the E(B−V) map, so the loss of contrast in these parts may be due to the change in resolution (see the grey contours in 8).

Figure 9 compares the quality of the γ-ray fits obtained in the "γ+E(B−V)" and "γ+τ_{353}" analyses by showing the residuals (photon data minus model, in sigma unit) in the overall energy band for each analysis. In both cases, the linear model provides an excellent description of the observed data in the 0.4-100 GeV band, as well as in the individual energy bands that are not shown here. The residuals remain largely consistent with noise fluctuations below $\pm1\sigma$. The small model excess noted toward the brightest CO parts of TauM, Perseus, and California in the "γ+τ_{353}" analysis (Remy et al. 2016) disappears when using dust reddening because of the reduced contrast in the E(B−V) map mentioned above. This confirms that the model excess in "γ+τ_{353}" was caused by the marked rise in dust opacity, $\tau_{353}/N_{\rm H}$, that characterises the cold population of grains present in the densest CO cores (see Fig. 17 of Remy et al. (2016)), rather than a loss of CRs.

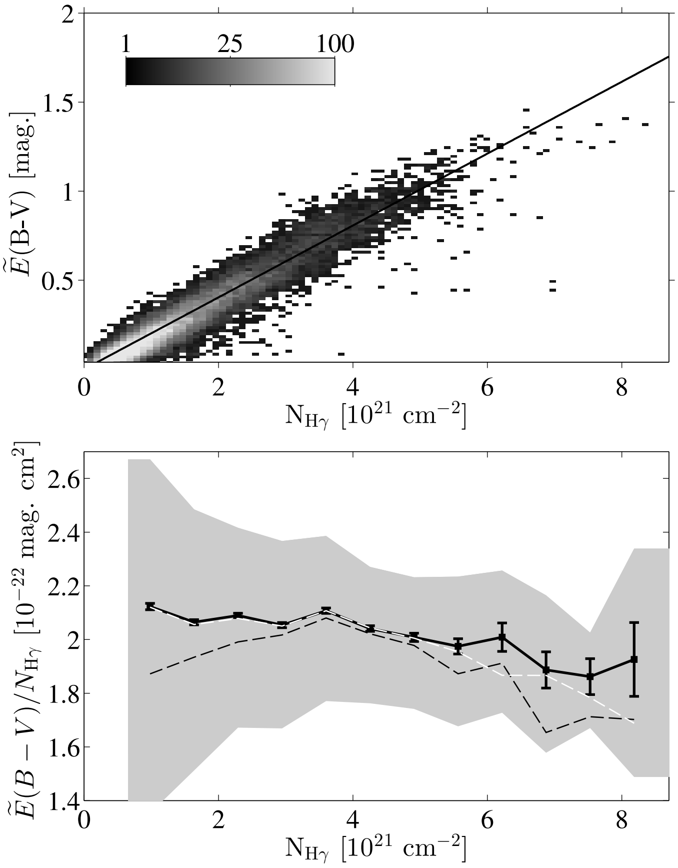

Fig. 10. *Upper*: 2D histogram of the correlation between the total gas column density, $N_{\rm H\gamma}$, measured with the 0.4-100 GeV interstellar γ rays, and the dust reddening convolved with the LAT response for an interstellar spectrum. The maps are sampled at a 0.°375 resolution. The solid line marks the average E(B−V)/$N_{\rm H}$ ratio of $(2.02\pm0.48)\times10^{-22}$ mag. cm^2 found across the whole field (mask0) and all gas phases. *Lower*: evolution of the E(B−V)/$N_{\rm H}$ ratio in equally spaced bins in $N_{\rm H\gamma}$. The shaded area gives the standard deviation in each bin using the complete analysis region (mask0). The black dashed, white dashed, and black solid curves give the means obtained with mask0, mask1, and mask2, respectively. The error bars give the standard error on the means.

Figure 9 also compares the total gas column densities, $N_{\rm H\gamma}$, derived from the gaseous γ-ray emission in the "γ+E(B−V)" and "γ+τ_{353}" analyses by showing their ratio. The total column density is derived from the γ-ray counts after subtraction of non-gaseous components estimated from the best-fit model. The γ-ray intensity is converted into $N_{\rm H\gamma}$ using the average emission rate per gas nucleon measured in the atomic phase in the region (Remy et al. 2016). The subtraction of γ-ray point sources results in very localized differences, by less than ±30%, between the gas column densities obtained in the two analyses. Only 10% of the point sources present in the region have an impact. The flux differences in the "γ+E(B−V)" and "γ+τ_{353}" models for those sources remain compatible with the individual normalisation uncertainties in the 3FGL catalogue. Away from those point sources, the two column density maps agree within ±3%, except toward the most diffuse regions, at $b<-45°$or at $l<155°$and $b<-10°$, where differences of about ±10% result from the noise

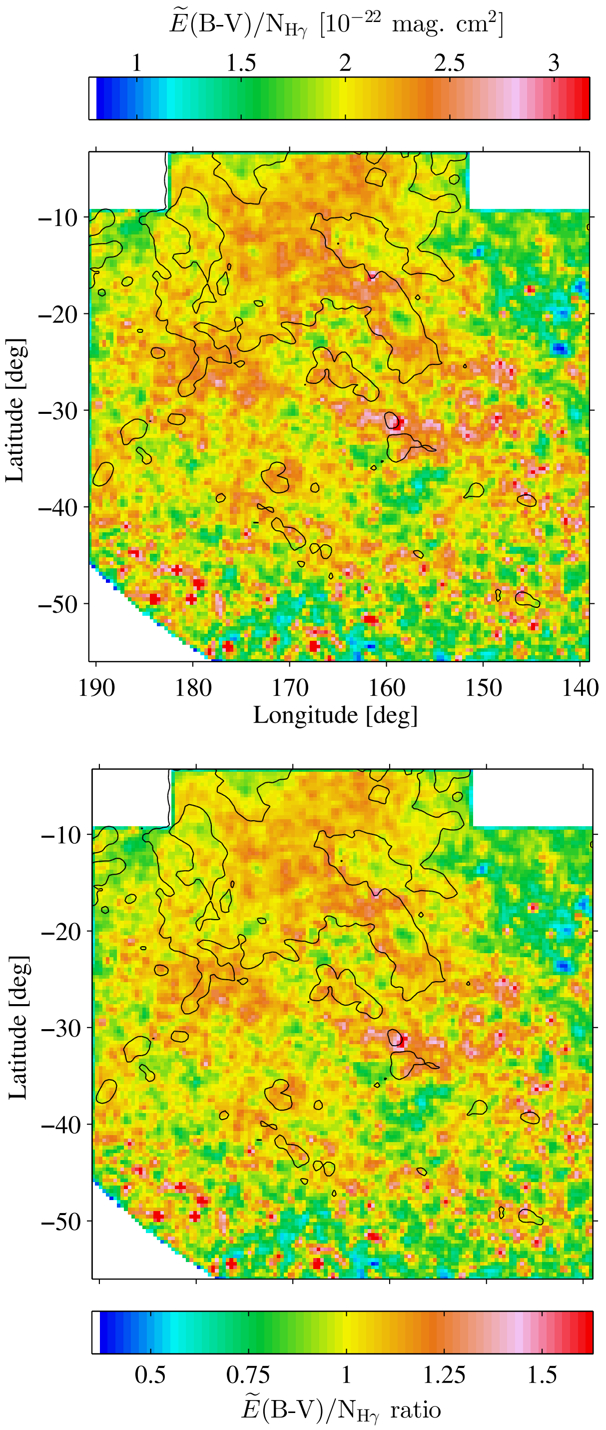

Fig. 11. Spatial variations of the amount of reddening per gas nucleon, $E(B-V)/N_H$, with the total gas measured by $N_{H\gamma}$ at 0°.375 resolution (top) and its variations relative to the average value of (2.02 ± 0.48)×10^{-22} mag. cm^2 (bottom). The tilded quantities are convolved with the LAT response for an interstellar spectrum. The black contours outline the shape of the CO clouds at the level of 1 K km s^{-1} in W_{CO} intensity.

level in the dust reddening map. Hence, the total gas column densities derived from the γ-ray fit in the local clouds are not significantly affected by the choice of dust map used to infer the DNM and CO$_{sat}$ components in the model, despite the differences discussed in Fig. 6 and 8.

3.2. Extinction per gas nucleon and opacity variations

Our analyses yield average dust properties per H atom in each gas phase. The best-fit coefficients of the N_{HI} maps in the dust model directly give the average dust opacity, τ_{353}/N_H, or the average $E(B-V)/N_H$ ratio, in the atomic envelopes of each cloud complex, depending on the dust map modelled. We have also used the best-fit coefficients of the W_{CO} maps and the γ-ray estimates of the X_{CO} factors to derive the average dust opacity, or $E(B-V)/N_H$ ratio, in the CO-bright phase of each complex.

Table 1 lists the $E(B-V)/N_H$ ratios obtained in the HI and CO phases in the "γ+E(B−V)" analysis, together with the opacities found in the "γ+τ_{353}" analysis (Remy et al. 2016) and the $\left[\frac{E(B-V)}{N_H}\right]^{(\tau)}$ ratios deduced from those opacities by applying the conversion factor $E(B-V)/\tau_{353}$ of 1.49×10^4 mag inferred from quasar colours (Planck Collaboration 2014a). The direct measurements of $E(B-V)/N_H$ ratios compare within 10% with those deduced via the dust opacity in the HI phases and in faint CO clouds (Cet, TauS, TauN). They significantly differ, however, in the brighter molecular clouds (TauM, Per, Cal), by a factor up to 2.5, because the grain opacity steeply increases inside molecular clouds (see Fig. 17 of Remy et al. (2016) and the references discussed in the following section).

We find $E(B-V)/N_H$ ratios in the atomic parts of the North Taurus and Cetus clouds close to the reference value of 1.7×10^{-22} mag. cm^2 of Bohlin et al. (1978) that applies to lines of sight with $E(B-V) < 0.5$ mag. in the solar neighbourhood and in the Galactic disc. They also agree with the ratio of (1.71 ± 0.07)×10^{-22} mag. cm^2 found in the atomic gas of the Taurus region from the visual extinction map of Dobashi et al. (2013) (Paradis et al. 2012). A nearly identical ratio of (1.69 ± 0.11)×10^{-22} mag. cm^2 has been measured in diffuse H_2 clouds up to 1 mag. in reddening from *FUSE* observations (Rachford et al. 2009). We find, however, larger ratios in the range of (1.9 − 2.1)×10^{-22} mag. cm^2 already in the atomic gas of the TauM, TauS, and Cal clouds, an average ratio of (2.09±0.15)×10^{-22} mag. cm^2 in the denser DNM, and still larger ratios in the range of (2.2 − 2.7)×10^{-22} mag. cm^2 in the CO-bright clouds. Paradis et al. (2012) had noted variations of the same magnitude between local clouds in their extinction data based on 2MASS stellar photometry. We further note that the present $E(B-V)/N_H$ ratios are systematically 1.2 to 2.2 times lower than the values obtained in parts of the TauS, TauM, and Perseus clouds by Chen et al. (2015) from their visual extinction map based on 2MASS and XSTPS-GAC stellar data. Further analyses of common regions using the same $N_{H\gamma}$ data and direct comparisons of the E(B−V) and A_V maps are necessary to find the origin of the discrepancy.

The good correlation between the hydrogen column density derived from γ rays and the dust reddening is presented in Fig. 10 together with the evolution of the $E(B-V)/N_{H\gamma}$ ratio as a function of the gas column density. The angular resolution of the E(B−V) and $N_{H\gamma}$ maps has been degraded to 0°.375 to improve the photon statistics in the histogram bins. At this resolution, E(B−V) and $N_{H\gamma}$ linearly correlate across the whole gas range. We detect no inflexion in the $E(B-V)/N_H$ ratio with increasing gas column density, contrary to the systematic rise in dust opacity across the same gas range (see Fig. 15 of Remy et al. (2016)).

The spatial distribution of the $E(B-V)/N_{H\gamma}$ ratios is shown in Fig 11. We also map their variations relative to the average value of (2.02 ± 0.48)×10^{-22} mag. cm^2 found for the whole field (mask0) and across all gas phases. The $E(B-V)/N_{H\gamma}$ values increase in the DNM and in the vicinity of the molecular clouds

Table 1. Average $E(B-V)/N_H$ ratios, in 10^{-22} mag cm^2, and dust opacities, τ_{353}/N_H in 10^{-27} cm^2, in the HI and CO-bright gas phases of the different cloud complexes (mask0).

Cloud	$\left[\frac{E(B-V)}{N_H}\right]_{HI}$	$\left[\frac{E(B-V}{N_H}\right]_{CO}$	$\overline{\tau_{353}/N_H}^{HI}$	$\overline{\tau_{353}/N_H}^{CO}$	$\left[\frac{E(B-V)}{N_H}\right]^{(\tau)}_{HI}$	$\left[\frac{E(B-V}{N_H}\right]^{(\tau)}_{CO}$
Cet	1.61±0.01	2.32±0.34	10.3±0.1	17.9±4.1	1.53±0.03	2.67±0.49
TauS	1.96±0.01	2.47±0.12	13.7±0.1	18.3±1.5	2.04±0.04	2.73±0.20
TauN	1.70±0.01	2.74±0.10	11.0±0.1	18.8±1.0	1.63±0.04	2.81±0.15
TauM	1.89±0.03	2.62±0.07	14.2±0.1	27.0±1.0	2.12±0.05	4.03±0.17
Cal	2.11±0.01	2.38±0.21	13.7±0.2	17.7±1.0	2.04±0.05	2.63±0.15
Per	2.55±0.10	2.18±0.24	16.5±0.5	34.4±5.1	2.45±0.08	5.13±0.45

Notes. $^{(\tau)}$ dust opacities converted to $E(B-V)/N_H$ ratios using the average $E(B-V)/\tau_{353}$ factor of $(1.49\pm0.03)\times10^4$ mag. of Planck Collaboration (2014a).

compared to the diffuse regions. The drop toward Perseus is due to a relative lack of reddening, possibly due to the presence of young stellar objects, rather than to an excess of gas column density. Large ratios are found in the region at $155° < l < 163°$ and $-33° < b < -30°$ where the (independent) thermal emission of the grains has a spectral index above 1.8 (see Fig. 2 of Remy et al. 2016). Across the whole region, the $E(B-V)/N_{H\gamma}$ ratios vary typically by ±30% around the average value. This is far lower than the 3-fold variations found in dust opacity toward molecular clouds, at the same angular resolution and with the same analysis method (Remy et al. 2016).

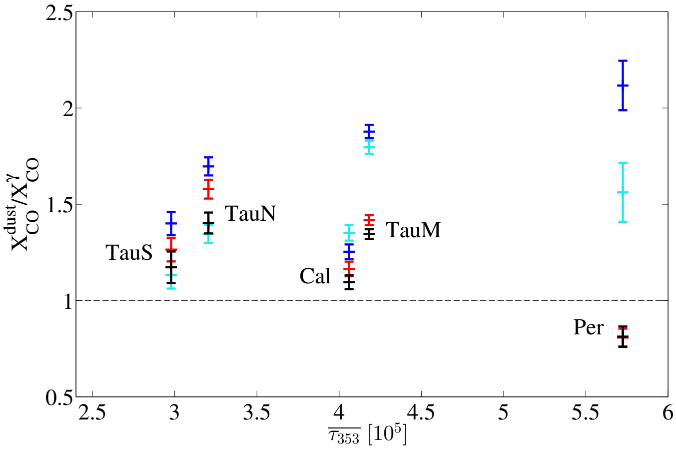

Fig. 12. Comparison by ratio of the dust and γ-ray measurements of X_{CO} in the different clouds as a function of the average dust optical depth at 353 GHz in each cloud. The colours mark the use of different dust tracers and analysis masks: $E(B-V)$ reddening with mask2 (black) and mask0 (red), and τ_{353} optical depth with mask 2 (cyan) and mask0 (blue)

3.3. Impact on the X_{CO} factor

Cloud-to-cloud variations in the X_{CO} factor and the comparison of the values in the different clouds with previous studies have been discussed in Remy et al. (2016). In the present study, we focus on the differences between the dust and γ-ray measurements and on the results obtained with different masks. The results are presented in Table 2. The γ-ray values of the X_{CO} factor in the Perseus cloud should be taken with care because of the significant level of cross-correlation between the compact HI and CO phases of the cloud when convolved with the LAT angular resolution, especially at low energies (see Sec. 6.1 of Remy et al. (2016)). This is even more true when further lowering the dynamical ranges by removing pixels in mask2.

The cloud complexes of TauM and Cal are only marginally affected by the change in mask and their average X_{CO} factors remain stable in the different analyses. On the contrary, the X_{CO} factors in Perseus vary significantly when masking out the densest gas pixels: the value found in dust emission decreases by a factor of 2.3 because the masked pixels correspond to regions where the grains have particularly large emission opacities; the change is still pronounced, but reduced to a factor of 1.6, in the "$\gamma+\tau_{353}$" analysis because the masked pixels have large column densities in the CO_{sat} component; the change is reduced to 20% in the γ-ray fit coupled to the dust reddening. Remy et al. (2016) reported significant variations in X_{CO} when averaged over clouds that are structured differently. The X_{CO} factors tend to decrease from diffuse to more compact clouds, as expected from the models of the formation and photodissociation of H_2 and CO molecules. The models predict strong gradients in the relative abundance of CO and H_2, which result in a marked decline in X_{CO} from the diffuse molecular envelopes to the dense and well-shielded cores (Bell et al. 2006; Bertram et al. 2016). Hence the X_{CO} average over a cloud should vary with the surface fraction of dense versus diffuse regions and with the degree of saturation of the CO lines in the densest parts. By masking out large fractions of the TauS and TauN complexes, we find significant changes in X_{CO} in all the analyses, thereby confirming the existence of spatial variations in X_{CO} inside a cloud complex.

Figure 12 shows the ratio of X_{CO} factors derived from the dust and γ-ray data. It illustrates that the $E(B-V)$-based measurements are systematically closer to the γ-ray ones than the measurements based on dust emission, but they still differ by 15% to 60%. Changing the dust tracer coupled to the γ-ray analysis to infer the DNM and CO_{sat} components results in modest changes, by ±24%, in the γ-ray values of X_{CO} (outside Perseus). The figure also shows that the $E(B-V)$-based factors do not increase with the average optical depth of the cloud as the τ_{353}-based factors do. The different behaviours of the X_{CO} factors measured in dust emission and reddening, and their response to the masking of the densest CO cores corroborate the existence of

Table 2. X_{CO} factors in 10^{20} cm^{-2}K^{-1}km^{-1}s for the dust and γ-ray fits.

Model	Cetus	Taurus South	Taurus North	Taurus Main	California	Perseus
τ_{353} mask0	1.58±0.03	1.44±0.02	1.55±0.01	1.24±0.01	1.11±0.01	1.03±0.01
τ_{353} mask2		0.90±0.01	1.00±0.01	1.26±0.01	1.24±0.01	0.45±0.01
$\gamma + \tau_{353}$ mask0	1.01±0.15	1.04±0.04	0.90±0.02	0.67±0.01	0.87±0.03	0.44±0.03
$\gamma + \tau_{353}$ mask2		0.79±0.05	0.73±0.02	0.70±0.01	0.92±0.03	0.27±0.03
E(B−V) mask0	1.44±0.03	1.06±0.01	1.22±0.01	0.97±0.01	0.93±0.01	0.49±0.01
E(B−V) mask1		0.74±0.01	0.83±0.01	0.94±0.01	0.91±0.01	0.45±0.01
E(B−V) mask2		0.78±0.01	0.87±0.01	0.93±0.01	0.96±0.01	0.40±0.01
γ+E(B−V) mask0	1.00±0.14	0.84±0.04	0.76±0.02	0.70±0.01	0.82±0.03	0.58±0.03
γ+E(B−V) mask1		0.63±0.04	0.56±0.02	0.70±0.01	0.81±0.03	0.58±0.03
γ+E(B−V) mask2		0.66±0.04	0.59±0.02	0.70±0.01	0.86±0.03	0.46±0.03

a strong opacity bias in X_{CO} measurements based on dust emission only.

4. Discussion and conclusions

The strong variations in dust opacity and small changes in the E(B−V)/N_{H} ratio do not coincide in direction. Several studies have reported variations of the dust opacity (e.g., Stepnik et al. 2003; Flagey et al. 2009; Martin et al. 2012; Ysard et al. 2013; Köhler et al. 2015) or changes in the extinction law (Cardelli et al. 1989; Foster et al. 2013; Schlafly et al. 2016). In both cases, they have been attributed to the evolution of the grain properties, but different physical processes are involved in the emission and absorption cross sections of the grains. As noted by Fitzpatrick & Massa (2007), the extinction curves respond sensitively to local conditions and contain unique information about the grains along the lines of sight. In the following, we recall the expression of the $\tau_{353}/N_{\mathrm{H}}$ and E(B−V)/N_{H} ratios as a function of several grain properties and we compare their variations with predictions by recent theoretical models (Jones et al. 2013; Köhler et al. 2015).

4.1. Definitions

The dust optical depth is defined as the product of the dust emission cross section per unit mass, κ_ν in cm^{-2} g^{-1}, and the dust mass column density, M_{dust}. The emission cross section can be expressed as $\kappa_\nu = \kappa_0 \left(\frac{\nu}{\nu_0}\right)^\beta$ with κ_0 the value at the reference frequency ν_0 and β the spectral index (Hildebrand 1983; Compiègne et al. 2011; Planck Collaboration 2014a). The dust mass column density is expressed as a function of the hydrogen column density, N_{H}, as $M_{\mathrm{dust}} = R_{\mathrm{DG}}\mu_{\mathrm{H}}N_{\mathrm{H}}$ with $\mu_{\mathrm{H}} = 2.27\times10^{-27}$ kg the mean gas mass per hydrogen atom, and R_{DG} the dust-to-gas mass ratio. So the dust opacity is expressed as :

$$\frac{\tau_\nu}{N_{\mathrm{H}}} = \kappa_{\nu_0}\left(\frac{\nu}{\nu_0}\right)^\beta R_{\mathrm{DG}}\mu_{\mathrm{H}} \qquad (1)$$

The dust extinction at a wavelength λ is proportional to the extinction optical depth along a line of sight, which is defined as the integral of the dust volume density, n_{dust}, and the extinction cross section $\sigma_\lambda^{\mathrm{ext}}$ (Spitzer 1998):

$$A_\lambda = 1.086\tau_\lambda^{\mathrm{ext}} = 1.086\int n_{\mathrm{dust}}\sigma_\lambda^{\mathrm{ext}}\mathrm{ds} \qquad (2)$$

Assuming the ISM grains can be described by spheres of effective radius a and mean internal mass density ρ_{gr}, we have $\sigma_\lambda^{\mathrm{ext}} = Q_\lambda^{\mathrm{ext}}\pi a^2$ with Q_λ^{ext} the efficiency factor for extinction. So the extinction optical depth can be expressed as a function of the hydrogen column density as:

$$\tau_\lambda^{\mathrm{ext}} = Q_\lambda^{\mathrm{ext}}\pi a^2 N_{\mathrm{dust}} = Q_\lambda^{\mathrm{ext}}\frac{3\mu_{\mathrm{H}}}{4\rho_{\mathrm{gr}}a}R_{\mathrm{DG}}N_{\mathrm{H}} \qquad (3)$$

Substituting this relation in the expression of the visual extinction, A_{V}, and using the definition of the total-to-selective extinction factor $R_{\mathrm{V}} = \frac{A_{\mathrm{V}}}{E(\mathrm{B-V})}$ yields:

$$\frac{E(\mathrm{B-V})}{N_{\mathrm{H}}} = 1.086\frac{3Q^{\mathrm{ext}}}{4\rho_{\mathrm{gr}}aR_{\mathrm{V}}}R_{\mathrm{DG}}\mu_{\mathrm{H}} \qquad (4)$$

A relation between the optical depth and the extinction can be obtained by combining equations (1) and (4):

$$\frac{\tau_\nu}{E(\mathrm{B-V})} = \frac{4\rho_{\mathrm{gr}}a}{3.258Q^{\mathrm{ext}}}\kappa_\nu R_{\mathrm{V}} \qquad (5)$$

4.2. Dust evolution in the diffuse medium

In the joint τ_{353} and γ-ray analysis of the nearby anti-centre clouds (Remy et al. 2016), we showed that the opacity increases by a factor of 2 in the HI and DNM phases above the diffuse-ISM value of ~7×10^{-27} cm^2 H^{-1} found in high-latitude cirruses (Planck Collaboration 2014b). Similarly, Planck Collaboration (2014a) measure a high-latitude value of (7.0 ± 2.0)×10^{-27} cm^2 H^{-1} and note variations in dust opacity in the atomic gas with values ranging from 6.6 to about 11×10^{-27} cm^2 H^{-1}. Using the Planck optical depth at 353 GHz and N_{HI} column densities from GALFA, Reach et al. (2015) report up to 3-fold variations in the diffuse ISM.

In the anti-centre region, we find that the $E(\mathrm{B-V})/N_\mathrm{H}$ ratio increases by less than 50% from the very diffuse gas to the denser HI and DNM parts of the clouds. Moreover, the average ratio of $(2.02\pm0.48)\times10^{-22}$ mag. cm^2 found across all gas phases is only 20% larger than the reference value of 1.7×10^{22} cm^2 mag. derived at $E(\mathrm{B-V}) < 0.5$ mag by Bohlin et al. (1978). Hence, the amplitude of the opacity rise in the HI and DNM phases significantly contrasts with the more uniform $E(\mathrm{B-V})/N_\mathrm{H}$ ratio.

The increase in opacity relates to an increase in spectral index, β, and a decrease in colour temperature, T_dust, of the termal emission (see Fig. 13). Recent theoretical studies such as Köhler et al. (2015) suggest that the spectral changes in β relate to gas density-dependent processes and that the variations in opacity, spectral index β, and colour temperature are closely connected. According to this model, the directions with temperatures near 16–18 K, $\beta \geq 1.5$ would be rich in grains with carbonaceous mantles. The distributions of opacities, β indices, and colour temperatures found in the anti-centre clouds suggest that the mantle accretion would occur primarily in the DNM.

At optical wavelengths, with grain size larger than 0.1 μm, the extinction efficiency factor (defined as the sum of the absorption and scattering efficiency) tends to the limit $Q^\mathrm{ext} = Q^\mathrm{abs} + Q^\mathrm{sca} = 2$ (Bohren & Huffman 1983; Desert et al. 1990). This condition is verified in the model of Köhler et al. (2015) as they find $Q^\mathrm{abs} \sim Q^\mathrm{sca} \sim 1$ up to $\lambda \sim 0.6$ μm for all the grains larger than 0.11 μm and the aggregates larger than 0.17 μm. Mantle accretion will not significantly change the size of the grains and induces only a 10% change in R_V according to the model. Such constraints are compatible with the small dispersion in $E(\mathrm{B-V})/N_\mathrm{H}$ found in the anti-centre clouds. Deviations by ±30% suggest that the population of large grains are rather stable in size distribution, absorption cross section, and in proportion to the gas mass across those clouds (see Eq. 4). Thus the increase in opacity (Eq. 1) would primarily be due to a change in grain emissivity κ_ν caused by mantle accretion in the dense HI and diffuse H_2 media, rather than to an increase in dust to gas mass ratio, R_DG.

Schlafly et al. (2016) have selected 37,000 stars with stellar parameters estimated from the APOGEE spectroscopic survey and they have used Pan-STARRS1 photometry to constrain the extinction curve from optical to infrared wavelengths and to derive the R_V factor. Up to $E(\mathrm{B-V}) \sim 2$ mag. their values of R_V vary in the 3.1-3.5 range around a mean of about 3.3. They do not systematically increase with reddening in this range. The amplitude of the R_V variations ($\sim$ 10%) are compatible with changes due to mantle accretion according to Köhler et al. (2015), and they are consistent with the dispersion we measure in $E(\mathrm{B-V})/N_\mathrm{H}$ in the anti-centre clouds. They further note that larger values of R_V relate to lower β indices. This trend is not predicted by the model of Köhler et al. (2015). Figure 13 shows the relation that we find between T_dust, β and the $E(\mathrm{B-V})/N_\mathrm{H}$ ratios in the present dataset, and how their changes relate to the gradients in N_H. At $T_\mathrm{dust} \lesssim 19$ K, the $E(\mathrm{B-V})/N_\mathrm{H}$ ratios remain close to the reference value. The lowest $E(\mathrm{B-V})/N_\mathrm{H}$ ratios, expected for larger R_V factors, are indeed found at $\beta < 1.7$, therefore at large colour temperature $T_\mathrm{dust} > 19$ K because of the anti-correlation between β and T_dust. Higher colour temperatures are associated with larger dust radiance indicating a larger heat rate by the ISRF if the large grains are in thermal equilibrium. In the proximity of UV sources or at low densities where there is less screening against UV radiation, the grains are more exposed to the ISRF which causes their darkening and an increase in R_V with time (Cecchi-Pestellini et al. 2010). This effect may explain the association of larger R_V factors with lower β indices (larger T_dust) found by Schlafly et al. (2016) and seen in Fig. 13.

4.3. Dust evolution in the molecular regions

In molecular regions, the opacity rise is steeper. Values that are 2 to 6 times above the diffuse-ISM average are commonly found (Flagey et al. 2009; Planck Collaboration 2011; Ysard et al. 2013; Stepnik et al. 2003; Remy et al. 2016). Large opacities are associated with spectral indinces $\beta > 1.7$ and colour temperatures below 17 K. According to the model of Köhler et al. (2015), these conditions are reached when grains coagulate into aggregates, with a possible formation of ice mantle on their surface. The aggregate size is about three times larger than the size of the constituting grains (at the peak of the mass-size distribution, see Fig 1. of their paper). Similarly, Ysard et al. (2013) have observed a 2-fold increase in opacity at 250 μm toward a molecular filament in the Taurus cloud and they have modelled it as the result of grain growth, by an average factor of five, due to the formation of aggregates. Moreover, directions with large extinctions ($A_\mathrm{V} > 3.3$ mag.) are associated in the Taurus clouds with the detection of water ice (Whittet et al. 1988). In this context, Köhler et al. (2015) predict a larger R_V value of 4.9 when aggregates are formed. The R_V factors measured by Schlafly et al. (2016) start to increase with increasing reddening for $E(\mathrm{B-V}) > 2$ mag., but they hardly reach values beyond 4 (only 1% of the sample), possibly because the survey does not point specifically to dense molecular regions, but scans larger scales than the compact CO filaments.

Foster et al. (2013) have used deep red-optical data from Megacam on the MMT[2], combined with near-infrared data from UKIDSS, to probe the extinction law in two 1°–size substructures of the Perseus cloud, known as B5 in the eastern end at $l = 160\overset{\circ}{.}6$ and $b = -16\overset{\circ}{.}8$, and L14484-L1451-L1455 in the western end at $l = 158\overset{\circ}{.}3$, $b = -21\overset{\circ}{.}5$. They find that the extinction law changes from the diffuse value of $R_\mathrm{V} \sim 3$ at $A_\mathrm{V} = 2$ mag. to a dense-cloud value of $R_\mathrm{V} \sim 5$ at $A_\mathrm{V} = 10$ mag. in both sub-structures. These estimates compare with the theoretical value for aggregates and suggest changes in R_V from 3 to 5 with increasing gas density in the CO-bright phase.

Combining the results on the anti-centre clouds, we find a gradual increase rather than a decrease of the mean $E(\mathrm{B-V})/N_\mathrm{H}$ ratio from $(1.84 \pm 0.10)\times10^{-22}$ mag. cm^2 in the HI phase, to $(2.09 \pm 0.15)\times10^{-22}$ mag. cm^2 in the DNM, and $(2.53 \pm 0.12)\times10^{-22}$ mag. cm^2 in the CO-bright phase. Furthermore, Fig. 11 shows that the changes in $E(\mathrm{B-V})/N_\mathrm{H}$ do not anti-correlate with the N_H map toward CO clouds, except toward Perseus. Inside the latter, the $E(\mathrm{B-V})/N_\mathrm{H}$ ratio is 30% lower than the average in the western end and 10 to 20% larger in the eastern end, while Foster et al. (2013) find the same increase in R_V in both regions. Therefore, if the grain size should increase by a typical factor of 3 in the dense clumps and the corresponding R_V factor should increase by a factor of 1.6, the relative stability of the observed $E(\mathrm{B-V})/N_\mathrm{H}$ ratio toward the anti-centre molecular clouds may hint at a significant increase in R_DG and/or in Q^ext to compensate the factor of 4.8 increase in the denominator of the $E(\mathrm{B-V})/N_\mathrm{H}$ expression in eq. 4. They may be due to the formation of ice mantles increasing the oxygen depletion (Whittet 2010) or increasing the extinction efficiency of the grain surface. Alternatively, the lack of a significant decline in the $E(\mathrm{B-V})/N_\mathrm{H}$ ratios with increasing molecular hydrogen column density may also be due to limitations in the determination of the redden-

---

[2] `https://www.mmto.org/`

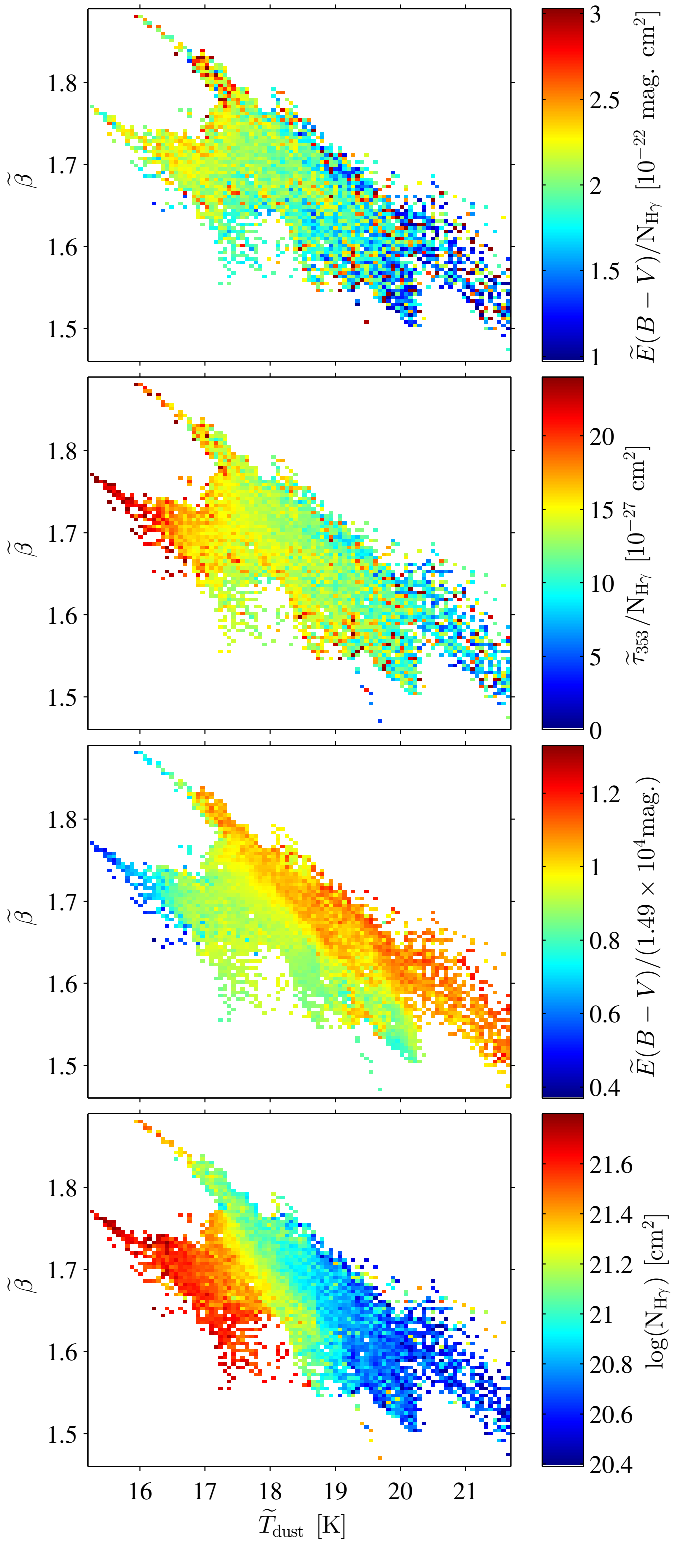

Fig. 13. Evolution of the $\widetilde{E}$(B − V)/$N_{\rm H}$ ratio (top), $\widetilde{\tau}_{353}/N_{\rm H}$ opacity (second), relative variation in the $\widetilde{E}$(B − V)/$\widetilde{\tau}_{353}$ ratio (third), and in total gas column density $N_{{\rm H}\gamma}$ derived from interstellar γ rays (bottom), in 0.°375-wide bins, as a function of the color temperature, $T_{\rm dust}$, and spectral index, β, of the thermal dust emission. The tilde quantities have been convolved with the LAT response for an interstellar spectrum. The variations in the $\widetilde{E}$(B − V)/$\widetilde{\tau}_{353}$ ratio are given with respect to the mean value of 1.49×10^4 mag. found from quasar colours through diffuse clouds (Planck Collaboration 2014a).

ing in obscured regions where few stars are available to sample the extinction. Extinction estimates are derived from magnitude limited stellar catalogues and therefore suffer from a selection bias (Sale 2015). The effect of this is that the most heavily extinguished stars are not detected and the extinction is biased towards lower values. This is especially true for lines of sight with higher column densities and partially explains the lack of a significant decline in the E(B−V)/$N_{\rm H}$ ratio.

Moreover, the compact molecular filaments associated to ice mantle formation are not fully resolved in γ rays, nor in reddening (see Fig 8 where ^{13}CO emission coincides with the lower resolution pixels). So the actual variations in E(B−V)/$N_{\rm H}$ may be steeper than presently observed.

The third plot of Fig. 13 illustrates how the extinction and emission properties of the large dust grains evolve relative to each other when sampling clouds from low gas densities, well exposed to the ISRF (at low β index and large T_{dust} temperature), to dense and obscured media. The correlation found between τ_{353} optical depths and quasar colour excesses across the sky, mostly through atomic clouds, has led to an average $\widetilde{E}$(B − V)/$\widetilde{\tau}_{353}$ ratio of 1.49×10^4 mag. (Planck Collaboration 2014a). Figure 13 shows that the bulk of the anti-centre sight lines are consistent with this mean and that the emission and extinction properties vary coherently away from this mean toward more extreme media. The E(B−V)/$N_{\rm H}$ and $\tau_{353}/N_{\rm H}$ ratios both increase from the most tenuous clouds to the more massive atomic and DNM phases. The gradients are not commensurate, but close to each other. From the DNM to the dense molecular environments, the gradients in $\tau_{353}/N_{\rm H}$ and E(B−V)/$N_{\rm H}$ diverge. The rise in opacity is more than twice larger than the coincident rise in E(B−V)/$N_{\rm H}$ ratio.

Figure 13 highlights the complicated variations of dust properties with environment. The variations in E(B−V)/τ_{353} do not follow a simple dependency on column density, nor on temperature. In this context, it is essential to take advantage of the total gas tracing capability of the γ rays spawn by cosmic rays to quantify dust opacity and E(B−V)/$N_{\rm H}$ gradients in other nearby clouds, with both larger and smaller mass than those in the anti-centre sample, in order to confirm the trends and relative amplitudes of the environmental changes in absorption/scattering versus emission properties of the large grains. The comprehensive photometry data on stars and quasars from future deep synoptic surveys, such as LSST `https://www.lsst.org/scientists/scibook`, will also clarify the robustness of the reddening measurements toward the densest molecular cores.

Acknowledgements. The *Fermi* LAT Collaboration acknowledges generous ongoing support from a number of agencies and institutes that have supported both the development and the operation of the LAT as well as scientific data analysis. These include the National Aeronautics and Space Administration and the Department of Energy in the United States, the Commissariat à l'Energie Atomique and the Centre National de la Recherche Scientifique / Institut National de Physique Nucléaire et de Physique des Particules in France, the Agenzia Spaziale Italiana and the Istituto Nazionale di Fisica Nucleare in Italy, the Ministry of Education, Culture, Sports, Science and Technology (MEXT), High Energy Accelerator Research Organization (KEK) and Japan Aerospace Exploration Agency (JAXA) in Japan, and the K. A. Wallenberg Foundation, the Swedish Research Council and the Swedish National Space Board in Sweden. Additional support for science analysis during the operations phase is gratefully acknowledged from the Istituto Nazionale di Astrofisica in Italy and the Centre National d'Études Spatiales in France. The French authors acknowledge the support of the Agence Nationale de la Recherche (ANR) under award number STILISM ANR-12-BS05-0016.

References

Acero, F., Ackermann, M., Ajello, M., et al. 2015, ApJS, 218, 23
Ackermann, M., Ajello, M., Atwood, W. B., et al. 2012, ApJ, 750, 3
Atwood, W., Albert, A., Baldini, L., et al. 2013, ArXiv e-prints
Bell, T. A., Roueff, E., Viti, S., & Williams, D. A. 2006, MNRAS, 371, 1865
Bennett, C. L., Larson, D., Weiland, J. L., et al. 2013, ApJS, 208, 20
Bertram, E., Glover, S. C. O., Clark, P. C., Ragan, S. E., & Klessen, R. S. 2016, MNRAS, 455, 3763
Bohlin, R. C., Savage, B. D., & Drake, J. F. 1978, ApJ, 224, 132
Bohren, C. F. & Huffman, D. R. 1983, Absorption and scattering of light by small particles
Cardelli, J. A., Clayton, G. C., & Mathis, J. S. 1989, ApJ, 345, 245
Casandjian, J.-M. 2015, ApJ, 806, 240
Cecchi-Pestellini, C., Cacciola, A., Iatì, M. A., et al. 2010, MNRAS, 408, 535
Cesarsky, C. J. & Volk, H. J. 1978, A&A, 70, 367
Chen, B.-Q., Liu, X.-W., Yuan, H.-B., Huang, Y., & Xiang, M.-S. 2015, MNRAS, 448, 2187
Compiègne, M., Verstraete, L., Jones, A., et al. 2011, A&A, 525, A103
Dame, T. M., Hartmann, D., & Thaddeus, P. 2001, ApJ, 547, 792
Dame, T. M. & Thaddeus, P. 2004, in Astronomical Society of the Pacific Conference Series, Vol. 317, Milky Way Surveys: The Structure and Evolution of our Galaxy, ed. D. Clemens, R. Shah, & T. Brainerd, 66
Desert, F.-X., Boulanger, F., & Puget, J. L. 1990, A&A, 237, 215
Dobashi, K., Marshall, D. J., Shimoikura, T., & Bernard, J.-P. 2013, PASJ, 65
Draine, B. T. 2003, ApJ, 598, 1017
Finkbeiner, D. P. 2003, ApJS, 146, 407
Fitzpatrick, E. L. & Massa, D. 2007, ApJ, 663, 320
Flagey, N., Noriega-Crespo, A., Boulanger, F., et al. 2009, ApJ, 701, 1450
Foster, J. B., Mandel, K. S., Pineda, J. E., et al. 2013, MNRAS, 428, 1606
Green, G. M., Schlafly, E. F., Finkbeiner, D. P., et al. 2014, ApJ, 783, 114
Green, G. M., Schlafly, E. F., Finkbeiner, D. P., et al. 2015, ApJ, 810, 25
Hildebrand, R. H. 1983, QJRAS, 24, 267
Jones, A. P., Fanciullo, L., Köhler, M., et al. 2013, A&A, 558, A62
Juvela, M. & Montillaud, J. 2016, A&A, 585, A38
Köhler, M., Ysard, N., & Jones, A. P. 2015, A&A, 579, A15
Lada, C. J., Lada, E. A., Clemens, D. P., & Bally, J. 1994, ApJ, 429, 694
Lebrun, F., Paul, J. A., Bignami, G. F., et al. 1982, A&A, 107, 390
Lombardi, M. 2009, A&A, 493, 735
Lombardi, M. & Alves, J. 2001, A&A, 377, 1023
Marshall, D. J., Robin, A. C., Reylé, C., Schultheis, M., & Picaud, S. 2006, A&A, 453, 635
Martin, P. G., Roy, A., Bontemps, S., et al. 2012, ApJ, 751, 28
Nolan, P. L., Abdo, A. A., Ackermann, M., et al. 2012, ApJS, 199, 31
Paradis, D., Dobashi, K., Shimoikura, T., et al. 2012, A&A, 543, A103
Peek, J. E. G., Heiles, C., Douglas, K. A., et al. 2011, ApJS, 194, 20
Planck and Fermi Collaborations. 2015, A&A, 582, A31
Planck Collaboration. 2011, A&A, 536, A25
Planck Collaboration. 2014a, A&A, 571, A11
Planck Collaboration. 2014b, A&A, 566, A55
Planck Collaboration. 2015, ArXiv e-prints
Rachford, B. L., Snow, T. P., Destree, J. D., et al. 2009, ApJS, 180, 125
Reach, W. T., Heiles, C., & Bernard, J.-P. 2015, ApJ, 811, 118
Remy, Q., Grenier, I. A., Marshall, D. J., & Casandjian, J. M. 2016, submitted to A&A
Robin, A. C., Reylé, C., Derrière, S., & Picaud, S. 2003, A&A, 409, 523
Rowles, J. & Froebrich, D. 2009, MNRAS, 395, 1640
Sale, S. E. 2015, MNRAS, 452, 2960
Schlafly, E. F., Green, G., Finkbeiner, D. P., et al. 2014, ApJ, 789, 15
Schlafly, E. F., Meisner, A. M., Stutz, A. M., et al. 2016, ApJ, 821, 78
Schlegel, D. J., Finkbeiner, D. P., & Davis, M. 1998, ApJ, 500, 525
Spitzer, L. 1998, Physical Processes in the Interstellar Medium, 335
Stepnik, B., Abergel, A., Bernard, J.-P., et al. 2003, A&A, 398, 551
Strong, A. W., Bloemen, J. B. G. M., Dame, T. M., et al. 1988, A&A, 207, 1
Whittet, D. C. B. 2010, ApJ, 710, 1009
Whittet, D. C. B., Bode, M. F., Longmore, A. J., et al. 1988, MNRAS, 233, 321
Winkel, B., Kerp, J., Flöer, L., et al. 2016, A&A, 585, A41
Ysard, N., Abergel, A., Ristorcelli, I., et al. 2013, A&A, 559, A133

Appendix A: Best fit coefficients of the γ-ray and dust models

Table A.1. Best-fit coefficients of the γ-ray model in each energy band and of the dust model.

γ-ray	Energy band [MeV]					E(B−V)	
model	$10^{2.6} - 10^{2.8}$	$10^{2.8} - 10^{3.2}$	$10^{3.2} - 10^{3.6}$	$10^{3.6} - 10^{5}$	$10^{2.6} - 10^{5}$	model	
$q_{\rm HI\ Cet}$	1.17±0.06	1.10±0.05	1.11±0.05	1.02±0.12	1.08±0.03	$y^{\rm a}_{\rm HI\ Cet}$	1.61±0.01
$q_{\rm HI\ TauS}$	1.22±0.02	1.23±0.02	1.17±0.02	1.16±0.04	1.20±0.01	$y^{\rm a}_{\rm HI\ TauS}$	1.96±0.01
$q_{\rm HI\ TauN}$	1.10±0.02	1.04±0.02	1.06±0.02	1.13±0.05	1.05±0.01	$y^{\rm a}_{\rm HI\ TauN}$	1.70±0.01
$q_{\rm HI\ TauM}$	1.26±0.02	1.23±0.02	1.19±0.02	1.23±0.04	1.23±0.01	$y^{\rm a}_{\rm HI\ TauM}$	1.89±0.03
$q_{\rm HI\ Cal}$	1.19±0.05	1.18±0.03	1.08±0.04	1.15±0.08	1.16±0.02	$y^{\rm a}_{\rm HI\ Cal}$	2.11±0.01
$q_{\rm HI\ Per}$	1.58±0.14	1.32±0.09	1.39±0.11	1.08±0.20	1.34±0.06	$y^{\rm a}_{\rm HI\ Per}$	2.55±0.10
$q_{\rm HI\ Gal}$	0.57±0.02	0.60±0.02	0.57±0.02	0.65±0.04	0.57±0.01	$y^{\rm a}_{\rm HI\ Gal}$	0.68±0.06
$q_{\rm CO\ Cet}$	1.32±0.71	2.51±0.47	2.43±0.51	0.00±0.89	2.16±0.30	$y^{\rm b}_{\rm CO\ Cet}$	4.64±0.03
$q_{\rm CO\ TauS}$	1.91±0.20	2.10±0.15	2.08±0.16	1.68±0.30	2.01±0.09	$y^{\rm b}_{\rm CO\ TauS}$	4.14±0.02
$q_{\rm CO\ TauN}$	1.62±0.10	1.62±0.07	1.59±0.08	1.67±0.16	1.63±0.05	$y^{\rm b}_{\rm CO\ TauN}$	4.16±0.03
$q_{\rm CO\ TauM}$	1.81±0.05	1.72±0.04	1.64±0.05	1.69±0.09	1.68±0.03	$y^{\rm b}_{\rm CO\ TauM}$	3.67±0.03
$q_{\rm CO\ Cal}$	2.00±0.10	1.92±0.07	1.81±0.08	1.81±0.16	1.85±0.05	$y^{\rm b}_{\rm CO\ Cal}$	3.92±0.23
$q_{\rm CO\ Per}$	1.48±0.12	1.63±0.08	1.70±0.09	1.97±0.17	1.64±0.05	$y^{\rm b}_{\rm CO\ Per}$	2.52±0.14
$q_{\rm CO\ Gal}$	1.98±0.59	1.49±0.39	2.09±0.42	1.61±0.74	1.58±0.25	$y^{\rm b}_{\rm CO\ Gal}$	7.44±0.02
$q_{\rm ff}$	2.34±0.69	3.14±0.51	1.58±0.55	3.27±1.17	2.56±0.32	$y^{\rm c}_{\rm ff}$	2.09±0.01
$q_{\rm COsat}$	55.27±3.40	60.38±2.42	56.62±2.66	61.48±4.72	59.67±1.53	$y^{\rm a}_{\rm COsat}$	2.92±0.01
$q_{\rm DNM}$	45.82±1.46	44.53±1.06	43.23±1.19	46.84±2.38	45.03±0.67	$y^{\rm a}_{\rm DNM}$	2.77±0.01
$q_{\rm ic}$	2.88±0.77	4.54±0.64	3.88±0.65	2.48±0.84	4.20±0.36	$y^{\rm d}_{\rm iso}$	-2.61±0.01
$q_{\rm iso}$	1.39±0.25	1.12±0.28	0.70±0.28	1.70±0.27	1.07±0.14		

Notes. The q coefficients are expressed in 10^{20} cm^{-2} (K km s^{-1}) for the CO; 3.8 10^{15} cm^{-2}Jy^{-1}sr for the free-free; 10^{20} cm^{-2} mag.$^{-1}$ for the DNM and CO$_{Sat}$; other q coefficients are simple normalization factors.
The y coefficients are expressed as follows: $^{\rm a}$ in 10^{-22} cm^{2}; $^{\rm b}$ in 10^{-2} mag. K^{-1}km^{-1}s; $^{\rm c}$ in 3.8 10^{-7} mag. Jy^{-1}sr; $^{\rm d}$ in 10^{-2} mag.

Cinquième partie

Transitions de phases dans le gaz interstellaire

Les modèles théoriques d'évolution du gaz dans le milieu interstellaire prédisent l'existence d'une phase de gaz atomique neutre chaud (WNM : Warm Neutral Medium), suivie d'une phase de transition thermodynamiquement instable faisant le lien avec une phase de gaz atomique neutre froid, et optiquement épais (CNM : Cold Neutral Medium). Le CNM possède des densités volumiques de gaz plus grandes, préalablement nécessaires à la formation de gaz moléculaire (McKee & Ostriker 1977; Wolfire et al. 2003; Audit & Hennebelle 2005; Saury et al. 2014).

Les raies d'émission du Hɪ à 21cm et du CO à 2.6 mm tracent respectivement le gaz atomique et moléculaire brillant, mais elles ne tracent ni le Hɪ optiquement épais, ni le H_2 diffus constituant le gaz sombre neutre (DNM) à la transition Hɪ–H_2 (van Dishoeck & Black 1988; Grenier et al. 2005; Wolfire et al. 2010). L'intensité des raies CO manque également une partie du H_2 dense dans les directions où les raies CO saturent à cause d'une trop grande épaisseur optique ($\mathrm{CO_{sat}}$). Comme nous l'avons vu dans la partie 3, l'émission des poussières et l'émission de rayons γ sont corrélées à la quantité totale de gaz, et la modélisation conjointe de ces deux traceurs, comme une combinaison linéaire des contributions des différentes phases, permet d'extraire l'information sur le gaz supplémentaire non tracé par les observations Hɪ et CO et donc de cartographier les composantes DNM et $\mathrm{CO_{sat}}$.

L'objectif de l'analyse présentée dans l'article II est d'utiliser à la fois les observations Hɪ, CO et les cartes des composantes DNM et $\mathrm{CO_{sat}}$, obtenues par l'analyse de l'émission des poussières et des rayons γ, pour mesurer les quantités de gaz dans les différentes phases du milieu interstellaire, des milieux diffus jusqu'au cœur des nuages moléculaires. D'une part, la mesure de la fraction de gaz sombre dans la phase moléculaire permet de contraindre les modèles sur la chimie et la photo-dissociation du CO dans le milieu interstellaire. D'autre part, le suivi de la contribution des différentes phases à la quantité totale de gaz, en fonction de la densité de colonne de gaz, N_H, ou de l'extinction dans le visible, A_V permet de contraindre le seuil de la transition Hɪ–H_2 et donc les modèles de formation du H_2.

Pour étudier cette transition dans différents environnements depuis les zones diffuses jusqu'à des zones de formation stellaire, nous avons sélectionné 15 nuages appartenant aux complexes identifiés dans les régions de l'anticentre Galactique (article I) et du Chamaeleon (Planck and Fermi Collaborations 2015). Les limites de ces nuages on été choisies pour éviter toute superposition et donc toute confusion entre les différentes phases des différents nuages sur les lignes de visées. Ce point est particulièrement important pour le gaz dans le DNM qui ne peut pas être séparé en vitesse contrairement au gaz tracé par les raies d'émission Hɪ et CO. Les analyses des régions de l'anticentre Galactique et du Chamaeleon, servant de base à cette étude, utilisent la même méthode pour modéliser l'émission des poussières et des rayons γ. Néanmoins l'analyse du Chamaeleon a été réactualisée pour compter autant de mois de données γ que celle de l'anticentre et pour inclure la séparation des structures de DMN et $\mathrm{CO_{sat}}$ introduite dans l'article I. Les deux analyses s'appuient sur des cartes à la même résolution angulaire correspondant à des résolutions de 0.9 à 2.7 pc dans les différents nuages vu leurs faibles écarts en distance.

Pour chacun des nuages sélectionnés nous avons mesuré les fractions de gaz dans chacune des phases et la fraction de gaz sombre dans la phase moléculaire. Nous avons suivi leurs évolutions en fonction de la densité de colonne de gaz totale et de l'extinction afin de contraindre les seuils de la transition Hɪ–H_2 et de détection de l'émission des raies CO. Nous avons également calculé les fractions de masse moyennes pour chaque phase dans chacun des nuages afin de chercher des changements liés aux propriétés des nuages (masse, compacité, extinction moyenne,...).

Avant de résumer les résultats, quelques détails techniques importants sont à rappeler. Les densités de colonne de gaz moléculaire tracées par le CO ont été déduites à partir des facteurs de conversion, X_{CO}, estimés indépendamment pour chacun des 6 grands complexes dont font partie les 15 nuages sélectionnés. Nous avons utilisé les facteurs X_{CO} déduits des données γ, ceux déduits de l'émission des poussières étant biaisés par l'augmentation de l'opacité des poussières dans les régions moléculaires comme discuté dans les parties 3 et 4. De même nous avons utilisé préférentiellement les cartes de DNM et $\mathrm{CO_{sat}}$ déduites du modèle γ. Ceci rappelle l'importance de l'étude de l'évolution des propriétés des poussières dans notre travail. Ce point étant souligné, voici un résumé des principaux résultats de l'article II :

Concernant les masses de gaz dans les différentes phases

L'hydrogène atomique, HI, est la principale composante en masse de gaz dans ces nuages, avec des fractions allant de 50 à 80% de leurs masses totales. Le DNM représente environ 20% de la masse totale de gaz des nuages. Il rassemble de 2 à 8 fois plus de gaz que la partie visible en CO dans les nuages peu compacts ou de faible intensité CO et de 30 % à 80% de la masse visible en CO dans les nuages les plus brillants en CO.

A l'échelle des nuages la masse dans les enveloppes de DNM croît avec la masse moléculaire tracées par l'émission CO comme $M_{\mathrm{H}}^{\mathrm{DNM}} = (61.7 \pm 7.1)\left(M_{\mathrm{H_2}}^{\mathrm{CO}}\right)^{0.51\pm0.02}$. Ce résultat s'accorde relativement bien avec la tendance $M_{\mathrm{H}}^{\mathrm{DNM}} \propto \left(M_{\mathrm{H_2}}^{\mathrm{CO}}\right)^{0.4}$ mesurée dans des complexes plus massifs à $|b| > 10$ deg. Cette relation avait été établie avec une méthode d'analyse différente et des données d'émission des poussières et de rayons γ à plus basse résolution (Grenier et al. 2005) . Nos mesures à plus haute résolution tendent à confirmer la validité de cette relation, qui pourrait être utilisée pour estimer les quantités de gaz du DNM dans des régions éloignées de la Galaxie ou dans les galaxies externes. Néanmoins des tests supplémentaires sont nécessaires pour vérifier la robustesse de cette relation dans des complexes moléculaires plus massifs, dans des nuages denses et compacts mais peu massifs, et aussi dans des nuages de metallicité différentes.

Pour ce qui est de l'hydrogène moléculaire non tracé par la raie d'émission CO dans les milieux les plus denses ($\mathrm{CO_{sat}}$), il représente 30 à 50% de la densité de colonne du gaz moléculaire mesuré à des extinction $A_{\mathrm{V}} > 3$ mag.

Concernant la transition HI–$\mathbf{H_2}$

La transition du HI au $\mathrm{H_2}$ tracé par le CO est observée dans un intervalle étroit de densité de colonne $N_{\mathrm{H}} = (0.6 - 2.5) \times 10^{21}$ cm^{-2}, ce qui correspond seulement à un facteur quatre d'amplitude. La transition est marquée par la diminution rapide de la contribution du gaz atomique dès 0.4 magnitude en extinction, A_{V} (ou $(0.6 - 1) \times 10^{21}$ cm^{-2} en densité de colonne). Elle est suivie de la détection de l'émission CO à des extinctions $A_{\mathrm{V}} = 1 - 2.5$ mag. Les plus grandes fractions de DNM sont trouvées dans l'intervalle de densité de colonne intermédiaire entre la chute d'intensité HI et la montée de l'intensité CO. Au delà de 3 magnitudes en extinction l'émission CO sature significativement et donc ne trace plus tout le gaz moléculaire dense qui va être associé à la composante $\mathrm{H_2}$ de $\mathrm{CO_{sat}}$.

Concernant le gaz moléculaire sombre , CO-dark $\mathbf{H_2}$

Le gaz moléculaire sombre, noté CO-dark $\mathrm{H_2}$, correspond à la partie moléculaire du DNM à la transition HI-$\mathrm{H_2}$. A l'intérieur d'un nuage ou d'un plus grand complexe la fraction de gaz moléculaire sombre en densité de colonne, $f_{\mathrm{COdk\,H_2}}$, décroît depuis l'enveloppe jusqu'au cœur du nuage moléculaire. Cette décroissance avec une extinction croissante suit un profil semi-Gaussien qui ne varie que légèrement selon de la composition chimique du DNM (pour 50 à 100% de gaz moléculaire).

La puissance spécifique des poussières rayonnée par nucléon de gaz est définie comme $\Pi = 4\pi\ R/N_{\mathrm{H}}$ avec R l'intensité intégrée du rayonnement thermique des poussières (radiance) et N_{H} la densité de colonne de gaz (Planck Collaboration 2014a; Planck and Fermi Collaborations 2015). Elle trace indirectement l'intensité du champ de rayonnement interstellaire. Aux extinctions correspondant à la transition HI-$\mathrm{H_2}$, la puissance spécifique des poussières ne varie que de 20 % autour de la valeur moyenne et ses variations ne sont pas liées spatialement aux variations de $f_{\mathrm{COdk\,H_2}}$.

Les fractions en masse de gaz moléculaire sombre, $F_{\mathrm{COdk\,H_2}}$, mesurées d'un nuage à un autre dépendent principalement de la structure de ces nuages. Elle diminue des nuages diffus jusqu'aux nuages moléculaires denses. En particulier on note une diminution de $F_{\mathrm{COdk\,H_2}}$ pour des nuages de masse, de compacité, et de maximum d'intensité CO croissants. Pour les nuages locaux étudiés, se trouvant à moins de 500 parsecs du Soleil, on ne note pas d'évolution de la fraction $F_{\mathrm{COdk\,H_2}}$ avec la distance au centre Galactique. Par contre les nuages à plus haute latitude au-dessus du plan Galactique ont tendance à présenter des fractions de gaz sombre moléculaire plus élevées, et ce principalement en raison de leur caractère plus diffus.

Les simulations numériques modélisant la formation et de photo-dissociation du $\mathrm{H_2}$ et du CO dans le milieu interstellaire prédisent généralement des intensités d'émission CO trop faibles aux faibles densités de colonne par rapport aux observations (Bell et al. 2006; Sonnentrucker et al. 2007; Glover & Mac Low 2011; Levrier et al.

2012; Smith et al. 2014). Cet effet est discuté dans les articles I et II. Les différents résultats présentés ici, sur les seuils de la transition Hɪ-H_2 et H_2-CO, sur la relation entre la masse de gaz du DNM et de H_2 vu en CO, et sur l'évolution des fractions de gaz sombre en fonction de l'environnement, pourront aider au développement des modèles de formation et de photo-dissociation du H_2 et du CO, et à comprendre pourquoi les molécules CO sont notablement plus abondantes ou émissives en CO (au moins 10 fois plus) dans le milieu interstellaire diffus que dans les simulations modernes.

Astronomy & Astrophysics manuscript no. tau16_paper2_v4
December 4, 2016

Cosmic-rays, gas, and dust in nearby anticentre clouds : II – Interstellar phase transitions and the Dark Neutral Medium

Q. Remy$^{(1)}$, I. A. Grenier$^{(1)}$, D.J. Marshall$^{(1)}$, and J. M. Casandjian$^{(1)}$

[1] Laboratoire AIM, CEA-IRFU/CNRS/Université Paris Diderot, Service d'Astrophysique, CEA Saclay, F-91191 Gif sur Yvette, France
e-mail: `quentin.remy@cea.fr`
e-mail: `isabelle.grenier@cea.fr`

December 4, 2016

ABSTRACT

Aims. H I 21-cm and ^{12}CO 2.6-mm line emissions respectively trace the atomic and molecular gas phases, but they miss most of the opaque H I and diffuse H_2 present in the Dark Neutral Medium (DNM) at the transition between the H I -bright and CO-bright regions. Jointly probing H I , CO, and DNM gas, we aim to constrain the threshold of the H I -H_2 transition in visual extinction, A_V, and in total hydrogen column densities, N_H^{tot}. We also aim to measure gas mass fractions in the different phases and to test their relation to cloud properties.

Methods. We have used dust optical depth measurements at 353 GHz, γ-ray maps at GeV energies, and H I and CO line data to trace the gas column densities and map the DNM in nearby clouds toward the Galactic anticentre and Chamaeleon regions. We have selected a subset of 15 individual clouds, from diffuse to star-forming structures, in order to study the different phases across each cloud and to probe changes from cloud to cloud.

Results. The atomic fraction of the total hydrogen column density is observed to decrease in the (0.6–1) $\times 10^{21}$ cm^{-2} range in N_H^{tot} (A_V <0.4 magnitude) because of the formation of H_2 molecules. The onset of detectable CO intensities varies by only a factor 4 from cloud to cloud, between 0.6×10^{21} cm^{-2} and 2.5×10^{21} cm^{-2} in total gas column density. We observe larger H_2 column densities than linearly inferred from the CO intensities at $A_V > 3$ magnitudes because of the large CO optical thickness: in this regime, the additional H_2 mass on average represents 20% of the CO-inferred molecular mass. In the DNM envelopes, the fraction of diffuse CO-dark H_2 in the molecular column densities is seen to decrease with increasing A_V in a cloud. For a half molecular DNM, the fraction decreases from more than 80% at 0.4 magnitude to less than 20 % beyond 2 magnitudes. In mass, the DNM fraction varies with the cloud properties. Clouds with low peak CO intensities exhibit large CO-dark H_2 fractions in molecular mass, in particular the diffuse clouds lying at high altitude above the Galactic plane. The mass present in the DNM envelopes appears to scale with the molecular mass seen in CO as $M_H^{DNM} = (61.7 \pm 7.1) M_{H_2}^{CO\;0.51\pm0.02}$ across two decades in mass.

Conclusions. The phase transitions in these clouds show both common trends and environmental differences. These findings will help support the theoretical modelling of H_2 formation and the precise tracing of H_2 in the interstellar medium.

Key words. Gamma rays: ISM – Galaxy: solar neighbourhood – ISM: clouds – ISM: cosmic rays – ISM: dust

1. Introduction

Theoretical works on heating and cooling in the interstellar medium (ISM) predict the existence of two thermodynamically stable phases in the neutral atomic gas (Field et al. 1969; McKee & Ostriker 1977): the Warm Neutral Medium (WNM) and the Cold Neutral Medium (CNM). The volume density and kinematic temperature in the WNM are in the range of 0.03–1.3 cm^{-3}, and 4100–8800 K, respectively, while in the CNM their ranges are 5-120 cm^{-3}, and 40–200 K, respectively (Wolfire et al. 2003). Given the densities of CNM and WNM, collisions between electrons, ions, and H atoms are able to thermalize the 21 cm transition in the CNM, but not in the WNM. So the spin temperature is expected to be close to the kinematic one in the CNM and less than the kinematic one in the WNM (Deguchi & Watson 1985; Liszt 2001). Numerical simulations have shown that physical conditions in the WNM cannot trigger the transition to CNM and that an intermediate regime of thermally unstable and turbulent gas is necessary (Audit & Hennebelle 2005; Saury et al. 2014). According to simulations and observations spin temperatures are in the range of 4000–9000 K in the stable WNM and 200-5000 K in the unstable phase (Liszt 2001; Heiles & Troland 2003; Dickey et al. 2003, 2009; Roy et al. 2013; Kim et al. 2014; Murray et al. 2015).

The 21 cm emission line of the atomic hydrogen traces the whole neutral atomic gas from WNM to CNM, but, without independent measurements of the 21 cm line in absorption toward distant radio sources to determine the spin temperature, one cannot retrieve the exact column density of hydrogen. Applying a uniform spin temperature, T_S, over a cloud complex or along sight lines provides an estimate of the proportion of CNM and WNM, and only an average correction of the column densities in the dense CNM. The amplitude of column density correction with respect to the optically thin case increases with decreasing spin temperature and increasing A_V. It reaches up to 35% at $A_V \sim 3$ (Liszt 2014).

The molecular phase is mainly composed of molecular hydrogen and is commonly traced by the $J = 1 \rightarrow 0$ line emission of ^{12}CO molecules at 115 GHz, hereafter simply referred to as

CO lines. In their study of CO photo-dissociation and chemistry, van Dishoeck & Black (1988) predicted that CO emission may not trace all the molecular gas in translucent clouds. In the diffuse envelopes near the H I -H_2 transition, H_2 molecules survive more efficiently than CO against dissociation by UV radiation (Wolfire et al. 2010). Furthermore, the brightness of the ^{12}CO line depends on the abundance and the level of collisional excitation of CO molecules, which are both low in the diffuse H_2 envelopes. Large quantities of H_2 can therefore be CO-dark below the sensitivity level of the current large-scale CO surveys (of order 1 K km s^{-1}).

Chemical species precursors to CO formation, such as C II , CH, and OH, are used to trace the gas at the atomic-to-molecular transition. Magnani et al. (2003) found that the CO line intensity in the MBM16 translucent cloud weakly correlates with the stellar reddening by dust, $E(B-V)$, contrary to the CH line intensity at 3335 MHz. Similarly, C II line intensity at 158 microns and OH line intensity at 18 cm trace a larger fraction of molecular gas than CO line intensity in diffuse environments (Velusamy et al. 2010; Barriault et al. 2010). However, C II line emission also arises from the widely spread regions of atomic and ionized gas.

Blitz et al. (1990) have compiled a catalogue of clouds detected by dust emission in the far infrared (FIR) at 100 μm with IRAS, but not seen in ^{12}CO observations. These clouds at low extinction (<0.25 mag) were proposed to be made of diffuse molecular gas, here studied. Röhser et al. (2014) have studied intermediate-velocity clouds (IVCs) with and without a FIR excess compared to the H I column densities. They suggest that dim and bright IVCs in the FIR probe different stages of the transition from atomic to molecular phase.

Several studies have used the additional information provided by tracers of the total gas column density and have compared them to H I and ^{12}CO line intensities in order to map the dark gas in the Galaxy at different scales. It has been done using γ-ray emission (Grenier et al. 2005), thermal emission from large dust grains (Planck Collaboration 2011a), and stellar reddening by dust (Paradis et al. 2012). In theses studies, the H I spin temperature is not fully constrained for each line of sight, so the additional gas may include a fraction of the CNM in addition to diffuse molecular gas. The suggestion that optically thick H I fully or largely accounts for the dark gas (Fukui et al. 2015) is challenged by H I absorption, dust extinction, and γ-ray observations that we detail in the discussion part of the paper. The additional gas is thus likely to include both optically thick H I and CO-dark H_2 at the transition between the atomic and molecular phases. In the absence of extensive emission tracers for this gas, we refer to this transition as the Dark Neutral Medium (DNM).

Simulations indicate that the CO line brightness rapidly saturates at large visual extinctions, near about 4 magnitudes (Shetty et al. 2011). Similarly, observations show that CO line absorption measurements at high optical depth reveal features not seen in emission (Liszt & Pety 2012). In Remy et al. (2016) we have detected additional gas seen with both dust and γ-ray emissions toward dense regions where the ^{12}CO line emission saturates. We refer to this CO-saturated, additional, H_2 component as CO_{sat}.

In this paper we use the DNM and CO_{sat} maps derived jointly from γ-ray emission and dust optical depth at 353 GHz in addition to the H I and CO emission data in order to investigate the H I -H_2 transition from diffuse to dense molecular clouds. We provide constraints on the range in N_H^{tot} and A_V required for H_2 formation. We follow the evolution of the contribution of CO-dark H_2 to the total molecular gas inside clouds of different types. We test the range of H_2 column densities where ^{12}CO line emission saturates. In order to compare clouds of different types, we have selected a set of local clouds spanning between 140 and 420 pc in distance and with masses between 600 and 34400 solar masses. The sample includes the local anti-center clouds of Cetus, Taurus, Auriga, Perseus, California analysed in Remy et al. (2016) and the Chamaeleon cloud analysed in Planck and Fermi Collaborations (2015). These two analyses are based on the same gas tracers and same method.

The paper is organized as follows. Details on the method and on the cloud sample are given in the next section. The results and discussions are presented in Sec. 3. Section 3.1 is dedicated to the description of the gas content in the ISM phases. We focus on the transitions between the different gas phases in Sec. 3.2. The evolution of the relative contributions of the CO-dark, CO-bright, and CO-saturated H_2 to the molecular phase across a cloud is discussed in Sec. 3.3. Cloud-to-cloud variations of the average mass fractions are discussed in Sec. 3.4. The main conclusions and possible follow-on studies are listed in the last section.

2. Analyses and data

The results presented here are based on the same dust and γ-ray analyses procedures as applied to two broad regions in the anticentre (Remy et al. 2016) and in the Chamaeleon directions (Planck and Fermi Collaborations 2015) in the sky. The analysis method and multi-wavelength data used to build the γ-ray and dust models are detailed in these papers, We summarize below their main features.

To trace the total gas we have used the dust optical depth, τ_{353}, inferred at 353 GHz from the spectral energy distribution of the thermal emission of the large grains, which has been recorded between 353 and 3000 GHz by *Planck* and *IRAS* (Planck Collaboration 2014a). We have also used six years of Pass 8 photon data from the *Fermi* Large Area Telescope (LAT) between 0.4 and 100 GeV. Technical details on the photon selection, instrument response functions, energy bands, and the ancillary γ-ray data (local interstellar spectrum, point sources, inverse Compton and isotropic components) that we have used are given in Remy et al. (2016).

In order to display the results as a function of the visual extinction A_V in both regions, we have used the all-sky A_J map constructed by Juvela & Montillaud (2016) from the 2MASS extinction data, with the NICEST method at 12.0 arcmin resolution. A_J values are converted into A_V with a factor 3.55 according to the extinction law of Cardelli et al. (1989). Other A_V datasets are available, but they do not cover both the anticentre and Chamaeleon regions using the same extraction method. We have not modelled A_V as a total gas tracer as we have done with γ rays and τ_{353} because of significant discrepancies in the A_V values obtained with different methods in the diffuse parts of the clouds ($A_V \lesssim 1$ mag) that are the focus of this study (Rowles & Froebrich 2009; Green et al. 2015; Juvela & Montillaud 2016).

2.1. Summary of γ-ray and dust models

Galactic cosmic rays (CRs) interact with gas and low-energy radiation fields to produce γ rays. At the energies relevant for the LAT observations, the particle diffusion lengths in the interstellar medium exceed the cloud dimensions and there is no spectral indication of variations in CR flux inside the clouds studied (Planck and Fermi Collaborations 2015; Remy et al. 2016), so the interstellar γ radiation can be modelled, to first order,

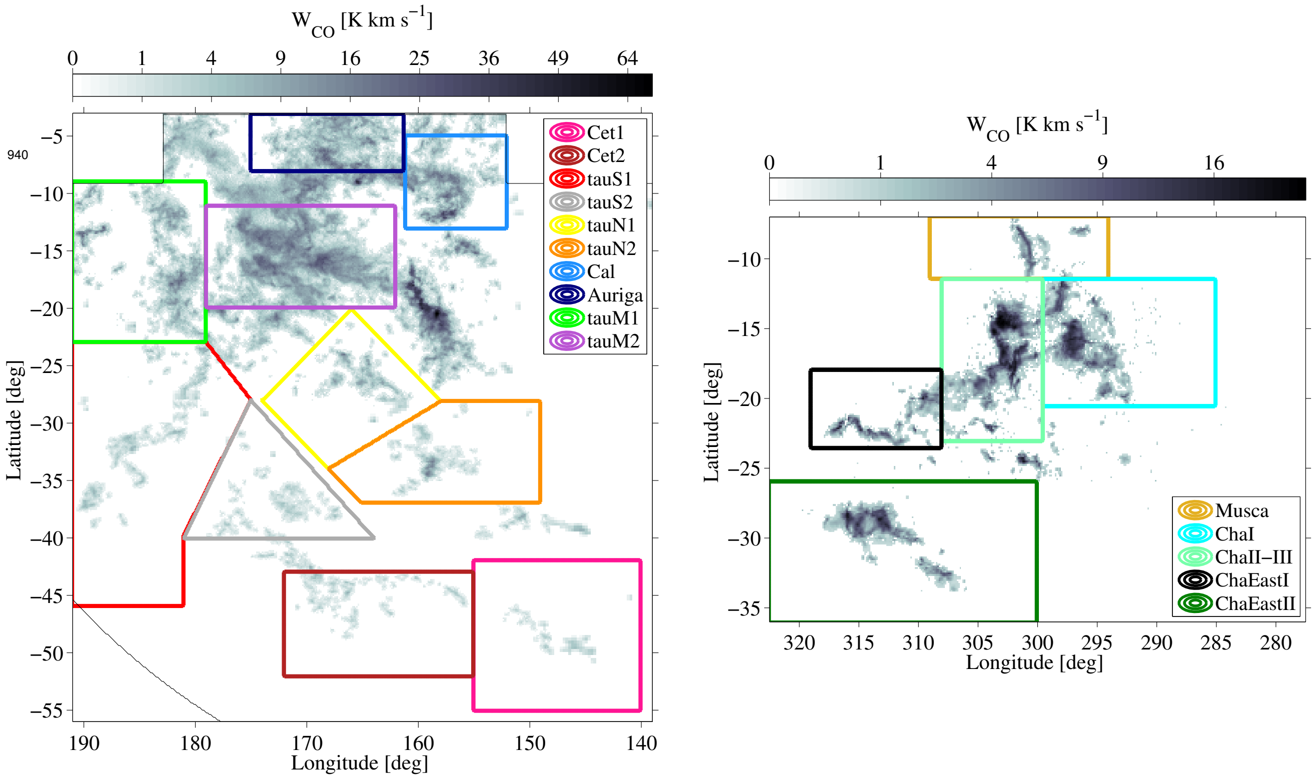

Fig. 1. Integrated CO intensity, W_{CO}, overlaid with the boundaries of the selected substructures in the anticentre (left) and Chamaeleon (right) regions.

as a linear combination of gas column-densities in the various phases and the different regions seen along the lines of sight. The model also includes a contribution from the large-scale Galactic inverse-Compton (IC) emission, an isotropic intensity to account for the instrumental and extragalactic backgrounds, and point sources (see Eq. 7 of Remy et al. 2016).

The large dust grains responsible for the thermal emission seen in the far IR and at sub-mm wavelengths are supposed to be well mixed with the interstellar gas. For a uniform mass emission coefficient of the grains, the dust optical depth should approximatively scale with the total gas column densities, so we have also modelled the optical depth map as a linear combination of gas column-densities in the various phases and in the different cloud complexes (see Eq. 6 of Remy et al. 2016).

The γ-ray intensity and the dust optical depth have been jointly modelled as a linear combination of H I -bright, CO-bright, and ionized gas components (plus the non-gaseous ancillary components of the γ-ray model mentioned above). The coefficients of the linear combination are used to scale the dust emission and γ-ray emission of gaseous origin into gas column density, and to probe independently the different gas phases and the different clouds separated in position-velocity. We have used 21-cm HI and 2.6-mm CO emission lines to respectively trace the atomic and CO-bright molecular hydrogen and we have used 70-GHz free-free emission to trace the ionised gas in the anticentre region. The contribution of ionized gas in the Chamaeleon region is negligible Planck and Fermi Collaborations (2015). The joint information from dust emission and γ rays is used to reveal the gas not seen, or poorly traced, by HI, free-free, and ^{12}CO emissions, namely the opaque HI and diffuse H_2 present in the DNM, as well as the dense H_2 to be added when the ^{12}CO line emission saturates (CO_{sat}). In the anticentre analysis we have separated the DNM and CO_{sat} components in directions inside and outside of the 7 K km/s contour in W_{CO} intensity. For the present study we have updated the analysis of the Chamaeleon region in order to incorporate separate DNM and CO_{sat} components.

Name	Distance [pc]	M_{HI} [$M_\odot$]	$M_{H_2}^{CO}$ [$M_\odot$]
Cet	190 ±30	14400 ± 2200	640 ± 140
TauM	140 ±30	29800 ± 5600	12200 ± 2300
TauS	160 ±10	35500 ± 1800	2660 ± 160
TauN	190 ±50	124500 ±33600	10000 ± 2700
Per	270 ±20	5080 ± 280	4380 ± 280
Cal	410 ±20	91000 ± 5300	34400 ± 3400
Cha	150 ±10	36700 ± 2400	3730 ± 280

Table 1. Distance to the clouds and mass in their H I and CO phases.

The residual maps (data minus model) presented in Planck and Fermi Collaborations (2015) and Remy et al. (2016) show that the best-fit models adequately describe both the *Planck-IRAS* observations in dust optical depth and the LAT observations in γ-ray intensity. Moreover jackknife tests have shown that the fitted parameters of the γ-ray and dust models apply statistically well to the whole region, both in the anticentre and Chamaeleon directions.

2.2. H I and CO data and clouds selection

H I and CO emission in the anticentre and Chamaeleon regions have been mapped by different surveys. Their relative calibrations have been verified. The Chamaeleon and anticentre analyses respectively use the CO data from the Nanten and Center for Astrophysics surveys (Mizuno et al. 2001; Dame et al. 2001; Dame & Thaddeus 2004). After correction, the integrated CO intensities, W_{CO}, recorded in the Chamaeleon region by the two surveys are close to a one-to-one correlation (Planck and Fermi Collaborations 2015). The H I survey GASS II (Kalberla et al. 2010) covers the Chamaeleon region. The GALFA and EBHIS surveys (Peek et al. 2011; Winkel et al. 2016) encompass the anticentre region. We have verified the good correlation between EHBIS and GALFA column densities in the anticentre region Remy et al. (2016). According to Kalberla & Haud (2015) and Winkel et al. (2016), the brightness temperature of GASS II is on average 4% higher than that of EBHIS. This discrepancy does not affect the column density profiles we present through single clouds (each covered by a single survey), but it induces a small shift between the gas fractions measured in the Chamaeleon region relative to the anticentre ones. Given the uncertainties, of order 5 to 10%, in the γ-ray and dust models, a 4% shift does not significantly bias our results. We can therefore compare the H I column densities and CO integrated intensities measured in both regions and merge the two samples of clouds to study cloud to cloud variations.

We have used HI and CO lines to kinematically separate cloud complexes along the lines of sight in both regions and to separate the nearby clouds from the Galactic backgrounds. Details of the pseudo-Voigt line decompositions and selection of longitude, latitude, and velocity boundaries of the complexes are given in Planck and Fermi Collaborations (2015) and Remy et al. (2016). The analyses resulted in the separation of six different complexes in the anticentre region (Cetus, South Taurus, North Taurus, Main Taurus Perseus, and California, see Fig. 1 of Remy et al. 2016) and two complexes in the Chamaeleon region (Chamaeleon, IVA, see Fig. 2 of Planck and Fermi Collaborations 2015). The complexes separated in position-velocity form coherent entities in H I and ^{12}CO to which we can associate specific distances compiled from the literature (Planck and Fermi Collaborations 2015; Remy et al. 2016). They are presented in Table 1, together with the overall masses inferred from the H I and CO data. The H I masses have been derived for optically thin conditions in the Chamaeleon region and for a spin temperature of 400 K in the anticentre region. Those conditions best match the interstellar γ-ray maps. We have applied a different CO-to-H_2 conversion factor, $X_{CO} = N_{H_2}/W_{CO}$, for each cloud complex (see below). Table 1 shows that the dataset includes faint-to-bright CO molecular clouds belonging to the solar neighbourhood, with distances ranging between 140 and 420 pc and with a large span in masses between 600 and 34400 solar masses in the CO-bright phase.

We have selected 15 clouds or sub-regions within the broader complexes in order to study phase transitions in different entities. The contours and names of the sub-regions are given in Fig. 1. When referring to those clouds, we will propagate the same names and colour scheme throughout the paper. The boundaries of the sub-regions have been chosen to avoid overlaps in direction of different complexes, so that we can study the relative contributions of the different gas phases to the total column density, in particular the DNM contribution which cannot be kinematically separated along the lines of sight. The set of sub-regions in the Chamaeleon region follow that studied in Planck and Fermi Collaborations (2015).

2.3. Estimation of the gas column density

Several studies have shown that the dust opacity, τ_{353}/N_H, rises as the gas, whether atomic or molecular, becomes denser. This opacity increase is likely due to a change in emission properties of the dust related to a chemical or structural evolution of the grains (Martin et al. 2012; Köhler et al. 2015). In the dense molecular filaments of the Taurus and Chamaeleon clouds the opacity can rise by a factor of 2 to 4 above the value found in the diffuse ISM (Stepnik et al. 2003; Planck Collaboration 2011b; Ysard et al. 2013; Planck and Fermi Collaborations 2015; Remy et al. 2016). Such a rise severely limits the use of the dust thermal emission to trace the total gas in dense media. The limit of the linear regime is estimated to be $N_H^{tot} < 2 \times 10^{21}$cm^{-2} in the Chamaeleon clouds and $N_H^{tot} < 3 \times 10^{21}$cm^{-2} in the anticentre clouds.

In all the nearby clouds studied so far and across all the gas phases we find no evidence of spectral evolution of the γ-ray emissivity of the gas relative to the local average. The latter is referred to as the Local Interstellar Spectrum (LIS). This consistency is verified in the denser molecular parts (CO_{sat}), thus indicating that, at the multi-GeV to TeV particle energies relevant for the LAT observations, the same CR flux pervades the clouds, from the diffuse atomic outskirts to the dense parts seen in ^{12}CO line emission, therefore through the bulk of a cloud volume and mass. The γ-ray emission efficiently traces the total column density of gas, contrary to the dust optical depth which is affected by the evolution of the grain emission properties. So we will preferentially estimate N_H^{tot} using γ rays.

For the calculation of the H I column densities, N_{HI}, we did not attempt to set a different H I spin temperature for each complex, but we have used a uniform average spin temperature. In the following the calculations are performed at the best-fit spin temperature of 400 K in the anticentre clouds, and for an optically thin emission in the Chamaeleon clouds (Planck and Fermi Collaborations 2015; Remy et al. 2016).

The DNM map derived from the dust distribution and τ_{353} analysis has been scaled in mass with the γ-ray emission under the assumption of a uniform CR flux permeating the H I and DNM phases. This assumption is substantiated by the uniformity of the CR spectrum found in the H I , DNM, and CO phases. By construction the DNM maps do not include the denser CO regions ($W_{CO} > 7$ K km s^{-1}) that are attributed to the CO_{sat} component.

The quantity of gas in the molecular phase is usually estimated via the ^{12}CO line emission and scaled into hydrogen column density via the N_{H_2}/W_{CO} conversion factor, X_{CO}. Our γ-ray model allows derivation of specific X_{CO} value for each cloud complex to account for potential differences in CO chemistry and excitation. Thereby we were able to report, as expected by theory, a decrease in X_{CO} from the diffuse clouds, subject to heavier photo-dissociation, to the more compact, dense, and well-shielded CO clouds (see Remy et al. 2016, for a detailed discussion). The X_{CO} factors derived from the dust analyses are systematically larger than the γ-ray estimates because of the nonlinear increase in grain opacity with N_H^{tot}, so in the following we use the X_{CO} factors derived from γ rays in each complex.

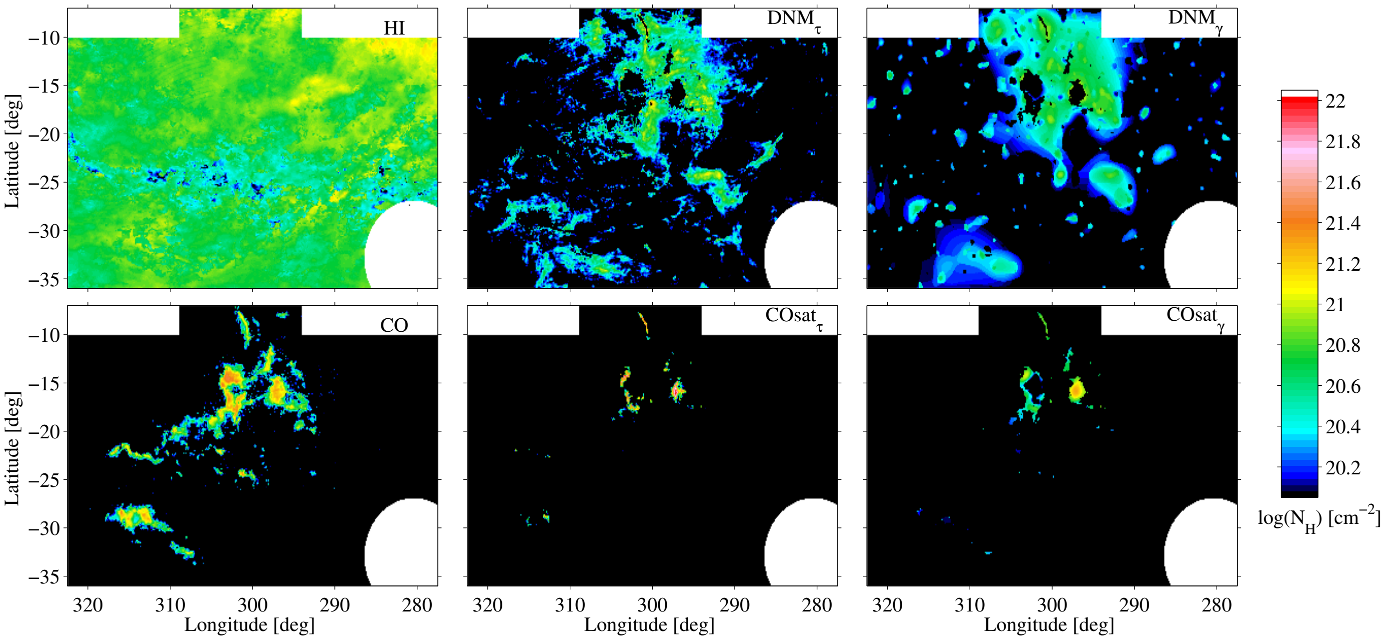

Fig. 2. Hydrogen column density maps of the HI, DNM (derived from the τ_{353} and γ-ray fits), CO-bright, and CO$_{\rm sat}$ (derived from the τ_{353} and γ-ray fits) components in the Chamaeleon region. The $X_{\rm CO}$ and $\tau_{353}/N_{\rm H}$ scale factors used in their derivation come from the γ-ray analysis for optically thin H I .

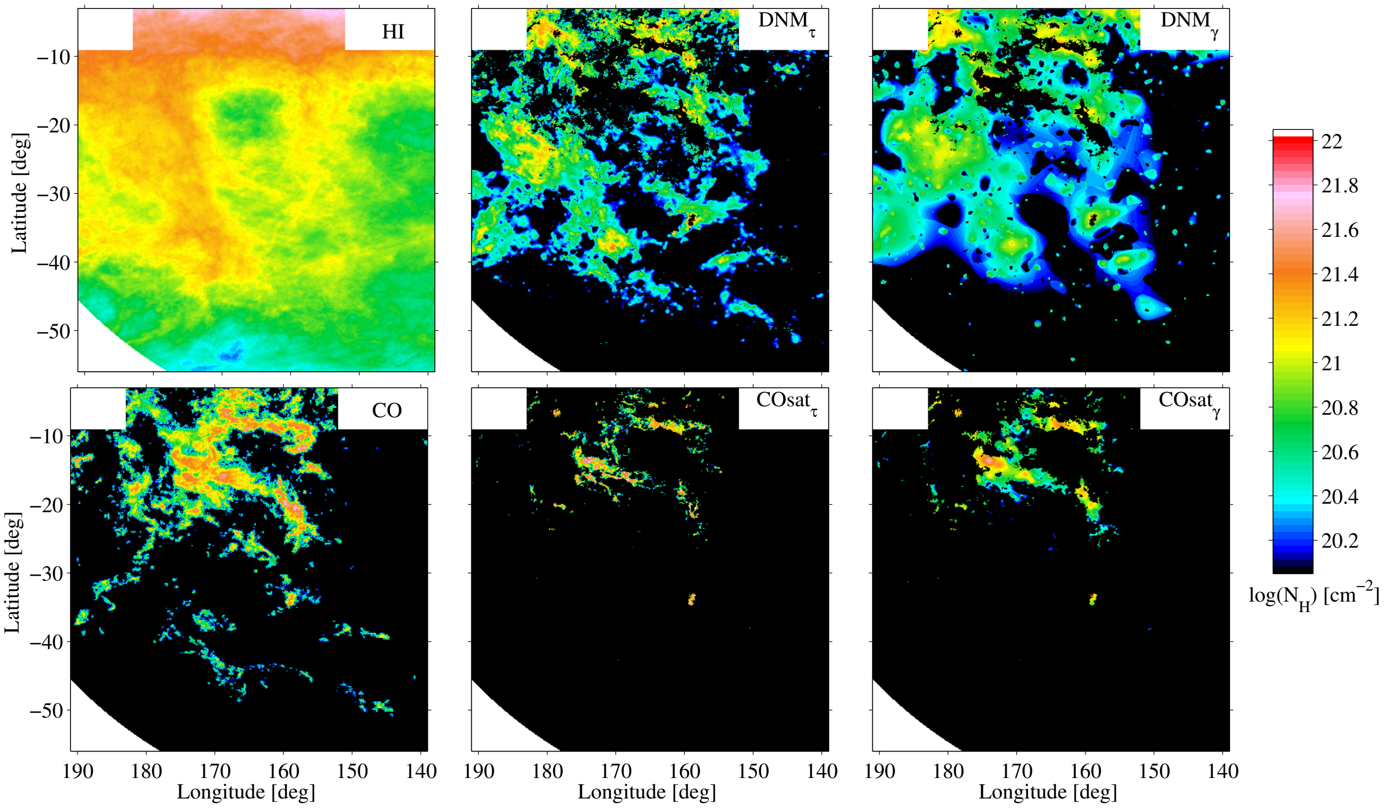

Fig. 3. Hydrogen column density maps of the HI, DNM (derived from the τ_{353} and γ-ray fits), CO-bright, and CO$_{\rm sat}$ (derived from the τ_{353} and γ-ray fits) in the anticentre region. The $X_{\rm CO}$ and $\tau_{353}/N_{\rm H}$ scale factors used in their derivation come from the γ-ray analysis with an H I spin temperature of 400K.

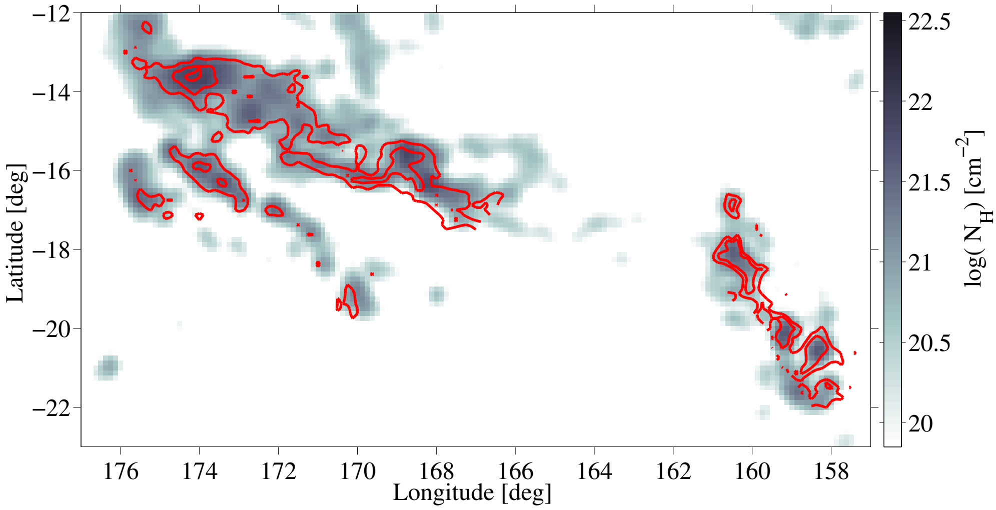

Fig. 4. Hydrogen column density map of the CO_{sat} component from the τ_{353} analysis overlaid with contours of ^{13}CO line intensities at 2 and 4 K km s^{-1} in the Taurus and Perseus clouds (Narayanan et al. 2008; Ridge et al. 2006).

3. Results

The results of the γ-ray and dust models obtained from the updated analysis of the Chameleon region compare very well with the published ones. The X_{CO} factor of (0.65± 0.02) 10^{20} cm^{-2} K^{-1} km^{-1} s derived from the γ-ray fit has not changed. The new dust opacities found in the H I , DNM, and CO phases are respectively $\overline{\tau_{353}/N_H}^{HI}$ =(15.0± 0.2) 10^{-27} cm^2 H^{-1}, $\overline{\tau_{353}/N_H}^{DNM}$ =(17.9± 0.5) 10^{-27} cm^2 H^{-1}, and $\overline{\tau_{353}/N_H}^{CO}$ =(32.9± 1.0) 10^{-27} cm^2 H^{-1}. Compared to values from the previously cited analyses the −8%, −4%, and +3% changes are not significant.

The hydrogen column-density maps obtained in the H I , DNM, CO, and CO_{sat} phases seen in the anticentre and Chamaeleon regions are shown in Fig. 2 and 3, respectively. The CO map is based on the W_{CO} data and on the X_{CO} ratios derived in γ rays for each individual cloud complex. In both regions, the column densities span from 10^{20} cm^{-2} in the atomic gas to a few times 10^{22} cm^{-2} in the molecular cores. We find comparable ranges of column densities in each phase of neutral gas. The means of the column density distributions in the anticentre clouds are larger than in the smaller Chamaeleon clouds, typically by a factor of two in the H I and DNM phases, and by a factor of three in the CO and CO_{sat} phases.

Both analyses exhibit significant quantities of gas not linearly traced by N_{HI} column densities and W_{CO} intensities, but jointly revealed by the dust mixed with gas and by the CRs spreading through it. The separation of the additional gas into DNM and CO_{sat} components according to the W_{CO} intensity in each direction (for W_{CO} > 7 K km s^{-1}) highlights the structural differences between the spatially extended, diffuse DNM gas gathering at the HI and CO interface, and the more compact, denser filaments and clumps of molecular gas in regions of large W_{CO} intensities. Figure 4 shows that the additional gas detected in the CO_{sat} component is likely due to large CO opacities because of the good spatial correspondence between the distributions of the CO_{sat} hydrogen column densities and of the intensities of the optically thinner ^{13}CO $J = 1 \rightarrow 0$ lines observed in the main Taurus and Perseus clouds (Narayanan et al. 2008; Ridge et al. 2006). Further exploiting the quantitative relation between the observed ^{13}CO intensities, the saturating ^{12}CO intensities, and the CO_{sat} column densities is beyond the scope of this paper. It requires a careful modelling of the ^{12}CO and ^{13}CO radiative transfer and of the non-linear evolution of the dust emissivities that are used with γ rays to trace the additional gas (see the discussions of the evolution of τ_{353}/N_H opacities at large N_H^{tot} in Remy et al. (2016)). We note that clouds with equivalent W_{CO} intensities may have different quantities of additional H_2 in the CO_{sat} component. For example, we observe comparable W_{CO} intensities in the filaments of Musca and ChaEastI, and in the clumps of ChamI and ChaEastII, but we find hardly any CO_{sat} gas in ChaEastI and ChaEastII whereas Musca and ChamI apparently require additional column densities as large as 10^{22} cm^{-2}.

DNM structures spatially extend between those of HI and CO clouds. The comparison between different clouds in the maps show environmental or evolutionary differences in the DNM content of clouds. This is illustrated by differences among the high-latitude translucent molecular clouds. MBM18 (l = 189°.1 b = −36°), MBM16 (l = 170°.6 b = −37°.3), MBM12 (l = 159°.4 b = −34°.3), and the chain of CO clouds along Cetus (at $b < -40°$) exhibit a rich DNM component contrary to MBM8 (l = 151°.7 b = −38°.7) and MBM6 (l = 145°.1 b = −37°.3). The proportion of optically thick H I and CO-dark H_2 in the DNM composition may also vary from clouds to clouds. An interesting structure is the DNM complex located at 170° < l < 190° and −40° < b < −20°. This is one of the largest DNM structures identifiable in the early all-sky DNM maps (Grenier et al. 2005; Planck Collaboration 2011a; Paradis et al. 2012). It extends spatially well beyond the edges of CO emission with column densities 10^{20}<N_H^{DNM} <10^{21} cm^{-2}. Its morphology is comparable to that of the H I gas in South Taurus. Its structure contrasts with the DNM found close to the CO edges of the MBM clouds and California clouds where the column densities can reach larger values near 2×10^{21} cm^{-2}. We note that the fraction of the California bubble missing in CO at l = 159°.5 and b = −10° is filled by DNM gas.

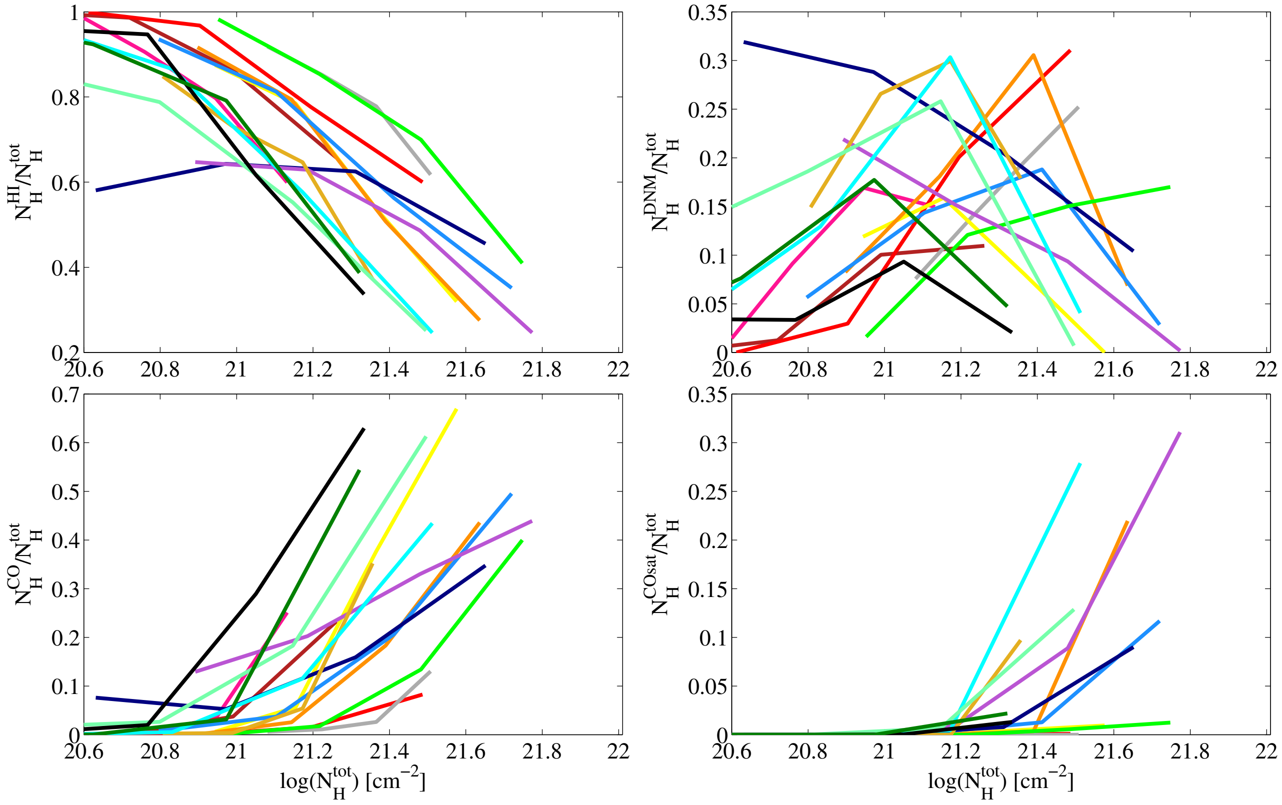

Fig. 5. Evolution with N_H^{tot} of the fractions of the total hydrogen column density in the HI (top left), DNM (top right), CO (bottom left), and CO$_{sat}$ (bottom right) components. The colors refer to the same clouds as in Fig. 1.

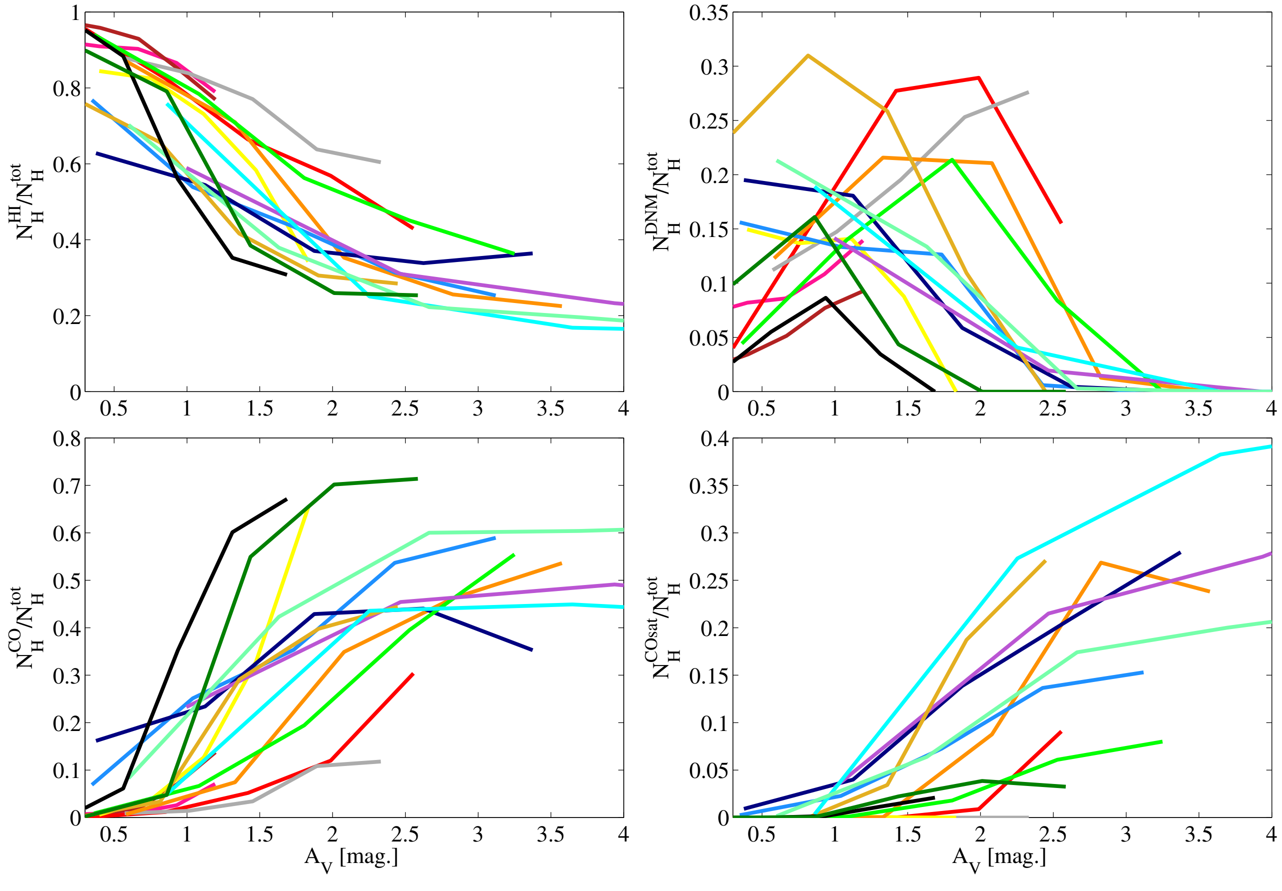

Fig. 6. Evolution with A_V of the fractions of the total hydrogen column density in the HI (top left), DNM (top right), CO (bottom left), and CO$_{sat}$ (bottom right) components. The colors refer to the same clouds as in Fig. 1.

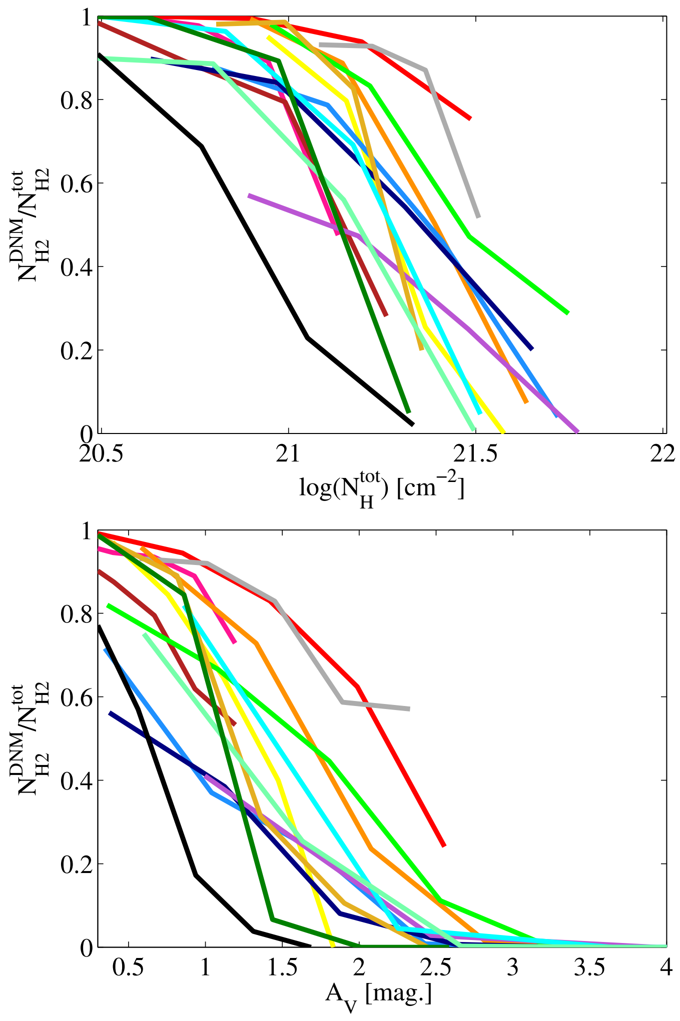

Fig. 7. Evolution of the fraction $f_{\mathrm{COdk\,H_2}}$ of molecular DNM in the total H_2 column-density as a function of the total gas column density N_H^{tot} (top) and visual extinction A_V (bottom). The DNM gas is assumed to be 50% molecular. The colors refer to the same clouds as in Fig. 1.

3.1. Phase transitions

In order to study the transition between the different neutral gas phases we have derived the ratios of the hydrogen column densities in the H I , DNM, CO-bright, and CO_{sat} components over the total column density. The ratios do not depend on cloud distances. We have plotted the ratios in the four neutral gas phases as a function of the total column density N_H^{tot} and of the visual extinction A_V in Figs. 5 and 6, respectively. Because of systematic uncertainties in the current measurements of low extinctions, we do not attempt to study the phase transitions below 0.3 magnitude in A_V.

We find that in all fifteen clouds the H I fraction in the total column density decreases for column densities greater than (0.6-1)$\times 10^{21}$ cm^{-2}, in agreement with the theoretical limit of 10^{21} cm^{-2} necessary to shield H_2 against UV dissociation for clouds of solar metallicity according to the models of Krumholz et al. (2009) and Liszt (2014). This limit is also confirmed by FUSE observations of H_2 (Gillmon et al. 2006), by OH observations (Barriault et al. 2010), and by dust observations in Perseus (Lee et al. 2012), which measure N_{HI} column densities leveling off at (0.3-0.5), (0.4-0.5), (0.8-1.4) $\times 10^{21}$ cm^{-2}, respectively. We note that, even though the H I mass of the individual clouds spans a tenfold range, the H I fractional decrease occurs over a small range in N_H^{tot}, only a factor of four wide from cloud to cloud. We also note that the slope of the decline is approximately the same in the different clouds. The column density fractions in the H I often remain large, about 30%, toward the CO-bright phase because of the turbulent 3D structure of the clouds (Valdivia et al. 2016) and because of the atomic envelopes surrounding the molecular clouds.

The CO-dark and CO-bright regimes in clouds are expected to be offset in depth because H_2 is better shelf-shielded against UV dissociation than CO at low extinction. The combination of dust screening and gas shielding is required at large extinction to protect CO molecules (Visser et al. 2009). The transition profiles of Fig. 6 do show transitions to CO-bright emission deeper into the clouds than for the H I -H_2 transition.

The DNM fraction in the total column density often peaks in the (1-3)$\times 10^{21}$ cm^{-2} range. Compared to the higher degree of organisation of the HI and CO-bright transitions, the DNM fractions show a large diversity of profiles that may be due to the large spatial overlap between the HI-bright, DNM, and CO-bright phases when integrated along the lines of sight.

The CO sensitivity threshold of the present observations are respectively 0.4 and 1.5 K km s^{-1} for the anticentre and Chamaeleon regions (Dame et al. 2001; Planck and Fermi Collaborations 2015). At that sensitivity level, the onset of CO intensities occurs for total gas column densities ranging between 0.6 and 2.5 $\times 10^{21}$ cm^{-2}, in close correspondence with the transitional drop in H I . We note again a small factor of four variation in the CO-bright transition from cloud to cloud. The transition occurs at total N_{H_2} column densities of (1.5-4)$\times 10^{20}$ cm^{-2}.

Simulations of photo-dissociation regions (PDR) by Levrier et al. (2012) show that the column density of CO molecules rises steeply after the molecular transition, at hydrogen volume densities of about 100 cm^{-3} and at N_{H_2} =(3-6)$\times 10^{20}$ cm^{-2} depending on the density profile in the PDR region. A uniform density profile shifts the transition to larger N_{H_2}. The value of 3$\times 10^{20}$ cm^{-2} corresponding to the non-uniform case agrees reasonably well with our results, as well as with CO and H_2 observations by the *HST* and *FUSE*, which indicate a transition at N_{H_2} =2.5 $\times 10^{20}$ cm^{-2} (Sheffer et al. 2008).

The saturation of the CO emission lines corresponds to a fractional increase of the column densities in the CO_{sat} component, but they contribute only 10% to 30% more gas. The saturation occurs in the main molecular clouds beyond (1.5-2.5)$\times 10^{21}$ cm^{-2} in N_H^{tot}.

3.2. Molecular gas and CO brightness

This section focuses on the transitions inside the molecular phase from the CO-dark to CO-bright and then CO-saturated regimes in each of the clouds in our sample. We distinguish the diffuse CO-dark H_2 present in the DNM from the dense H_2 implied by the CO_{sat} component to the bright CO cores in order to isolate the fraction of dark molecular gas lying at the diffuse atomic-molecular interface.

We first discuss the transition from CO-dark to CO-bright H_2 by measuring the change in the fractions of molecular DNM in the total H_2 column density, N_{H_2}. We define the CO-dark H_2 fraction in column density as:

$$f_{\mathrm{COdk\,H_2}} = \frac{N_{H_2}^{DNM}}{N_{H_2}^{tot}} = \frac{N_{H_2}^{DNM}}{N_{H_2}^{DNM} + N_{H_2}^{CO} + N_{H_2}^{COsat}} \quad (1)$$

Instead of the generic "dark gas fraction" (f_{DG}) term found in the literature for column density or mass ratios and which often implicitly assumes that the whole DNM is molecular, we use the more explicit designation of "CO-dark H_2 fraction" to restrict the fraction to the molecular part of the DNM (excluding the opaque H I) and to exclude issues with saturation of the W_{CO} intensities (CO_{sat} components).

As the DNM lies at the interface between the atomic and molecular phases, it is expected to be composed of optically thick H I and diffuse H_2 (not seen in CO), both mixed with a proportion varying as the gas becomes denser and according to the ambient conditions (e.g. H_2 volume density and kinetic temperature, intensity of the interstellar radiation field, ISRF, dust content, flux of ionizing low-energy CRs, Visser et al. 2009). The suggestion that optically thick H I fully or largely accounts for the additional gas in the DNM (Fukui et al. 2015) is challenged by several observations. Corrections of the H I column densities are too small to explain the changes observed in the $N_{HI}/E(B-V)$ ratios at $E(B-V) > 0.1$ (Liszt 2014). According to Stanimirović et al. (2014), H I absorption traces mostly the central cloud regions where CO is bright, and only to a smaller degree the CO-dark envelopes, contrary to the DNM maps that have been obtained for nearby clouds like those shown in Figs.2 and 3. Analysis of the dust thermal emission as a function of Galactic latitude and of H I spin temperature suggests that the DNM is less than 50% atomic (Planck Collaboration 2011a). Moreover, doubling the H I densities in the local ISM because of ubiquitously large H I opacities would yield a twice lower γ-ray emissivity per gas nucleon, therefore a twice lower CR flux inferred from γ rays in the local ISM. This is clearly at variance with the direct CR measurements performed in the solar system at energies of 0.1 to 1 TeV for which solar modulation is negligible (Grenier et al. 2015). Large atomic fractions in the DNM being probably the exception for our set of clouds, we have performed the calculations with a 50% or 100% molecular composition of the DNM.

Figure 7 shows the evolution profile of the CO-dark H_2 fraction in column density as a function of the total gas column density, N_H^{tot}, and of visual extinction, A_V, in each of the clouds. The CO-dark diffuse molecular hydrogen exceeds 70% of the total H_2 column density at $N_H^{tot} < 6 \times 10^{20}$ cm^{-2}, except in the TauM2 region which is centred on the extensively bright part of the Taurus CO cloud. Velusamy et al. (2010) have observed 53 transition clouds with H I and ^{12}CO emissions and no detectable ^{13}CO emission, thus containing negligible CO_{sat} H_2. In about 30% of them, the C II line emission at 1.9 THz indicates CO-dark H_2 fractions in column density exceeding 60%.

The fraction starts to decrease in the 0.4-0.9 magnitude range in visual extinction or in the (0.3-1) × 10^{21} cm^{-2} range in total gas column density. It then declines with rather comparable slopes in the different clouds. We note that CO emission in the very compact molecular filament of ChaEastI is detected at significantly lower column densities than in the other clouds, possibly because of larger H_2 volume densities, but one cannot relate filamentary CO structures to low DNM abundances since the other compact filament in our sample, Musca, retains large DNM column densities up to 2 magnitudes of extinction.

By integrating the gas over the entire anticentre or Chamaeleon regions, we find the average profiles displayed in Fig. 8 for a fully molecular composition of the DNM to allow comparisons with other observations. Systematic uncertainties in the current measurements of low extinctions limit our study of the CO-dark H_2 fraction to $A_V > 0.3$ magnitude. The rms dispersion reflects the differences in individual profiles of Fig. 7, due on the one hand to a modest difference, within a factor of 2 to 3, in the amount of extinction required to overcome CO destruction in each cloud and, on the other hand, to the difference in DNM abundance prior to the transition from CO-dark to CO-bright H_2. On average, the CO-dark H_2 dominates the column densities up to 1.5 magnitudes in visual extinction.

The individual and average $f_{\mathrm{COdk\,H_2}}$ profiles do not compare well with the model prediction of Wolfire et al. (2010) that CO emission reaches an optical depth of 1 at $A_V \gtrsim 0.7$ magnitude, well beyond the 0.1 magnitude required for the formation of H_2. Most of the profiles shown in Figs. 6 and 7 indicate a transition to the CO-bright regime deeper into the clouds, at A_V between 1 and 2.5 magnitudes, even though Wolfire et al. (2010) have modelled more massive clouds, with a total column density N_H^{tot} of 1.6×10^{22} cm^{-2}, that should screen CO molecules more effectively than the more translucent clouds in our sample. The onset of CO emission is more consistent with the approximate range near 1.5–2.5 magnitudes where the dust optical depth and dust extinction are seen to recover a linear correlation with H I and CO intensities (Planck Collaboration 2011a; Paradis et al. 2012). We note that the cloud closest to the model prediction is the very compact filament of ChaEastI, suggesting that the volume density gradient through the cloud plays an important role in addition to the integral screening through the gas columns.

We parametrize the decrease of the CO-dark H_2 fraction as a function of A_V with a half-Gaussian profile defined as :

$$f_{\mathrm{COdk\,H_2}} = \begin{cases} f_{max} & \text{if} \quad A_V \leqslant A_{V_0} \\ f_{max} \times \exp\left[-\left(\frac{A_V - A_{V_0}}{\sigma_{A_V}}\right)^2\right] & \text{if} \quad A_V > A_{V_0} \end{cases} \quad (2)$$

The results of the fits for the two analysis regions are given by the red curves in Fig. 8. We find f_{max}=0.91, A_{V_0}=0.55 mag, σ_{A_V}=1.27 mag in the anticentre region and f_{max}=0.98, A_{V_0}=0.43 mag, σ_{A_V}=0.97 mag in the Chameleon region. These parameters are derived for a fully molecular DNM, but they change only by a few percent when using a half molecular DNM composition.

Xu et al. (2016) have studied the PDR border of the main Taurus CO cloud in an approximately 0°.5-wide square, centred on $l = 172°.8$ and $b = -13°.2$, at a high angular resolution of 0.05°. This edge lies within the TauM2 sub-region of our sample. They have observed OH, ^{12}CO, and ^{13}CO line emissions and they have inferred the N_{H_2} column densities from the A_V extinction observations of Pineda et al. (2010), assuming that the hydrogen is predominately molecular and using the relation $N_{H_2}/A_V = 9.4 \times 10^{20}$ cm^{-2} mag^{-1}. Their CO-dark H_2 fraction is defined as the fraction of molecular gas not traced by ^{12}CO or ^{13}CO line emission, so it compares with our measurements of $f_{\mathrm{COdk\,H_2}}$ in the case of a fully molecular DNM composition. They have modelled the variation of the CO-dark H_2 fraction as a function of extinction with a Gaussian profile. Given the very different origins of both datasets, the close-up measurement of Xu et al. (2016) agrees remarkably well with the mean evolution of the CO-dark H_2 fraction we find in the whole anticentre region. The steeper decline of their CO-dark H_2 fraction compared to our mean trend remains compatible with the cloud-to-cloud dispersion in the sample. The discrepancy with the TauM2 profile, however, calls for further investigations in order to understand whether it is due to methodological differences (angular resolution, total gas tracers versus radiative modelling, etc) or to genuine spatial changes in the PDR profiles across TauM2.

Based on observations of C II lines at 1.9 THz with *Herschel*, Langer et al. (2014) have estimated the column densities of CO-dark H_2 in a large sample of clouds in the Galactic disc and they

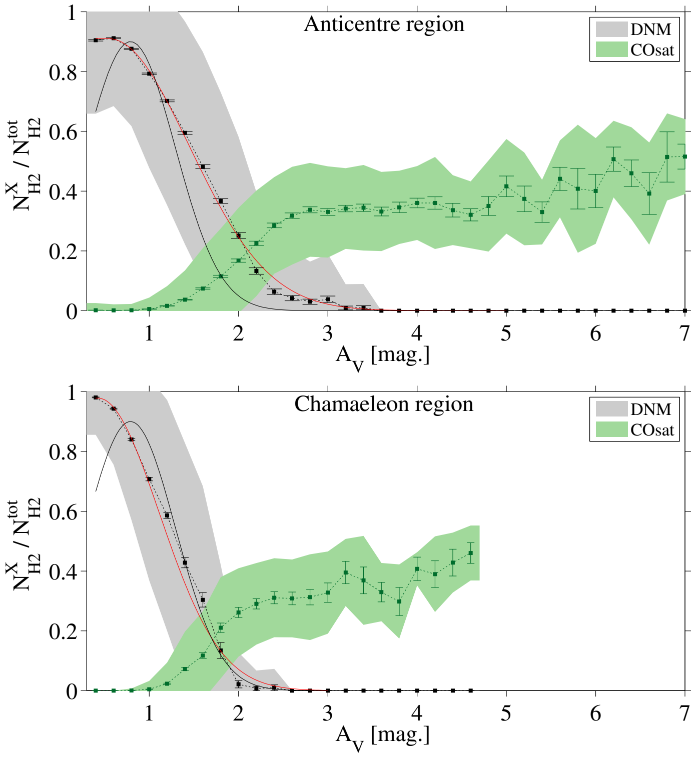

Fig. 8. Evolution with visual extinction A_V of the fraction $f_{\mathrm{COdk\,H_2}}$ of molecular DNM gas (grey) or additional CO$_{\rm sat}$ H_2 (green) in the total H_2 column-density. The DNM is assumed to be 100% molecular. The shaded areas and error bars respectively give the standard deviation in the sample and the standard error of the mean. The black line gives the Gaussian profile of Xu et al. (2016) and the red line shows the best fit by a half-Gaussian to the $f_{\mathrm{COdk\,H_2}}$ fraction.

have measured the CO-dark H_2 fraction in the total gas column density. As their estimates of the associated $N_{\rm HI}$ column densities are very low, their CO-dark H_2 fractions in the total gas are close to the $f_{\mathrm{COdk\,H_2}}$ fraction we have defined in the molecular phase. They have found a very broad range of CO-dark H_2 fractions across the whole 10^{21-22} cm^{-2} interval. The spread largely encompasses the profiles shown in Fig. 7 for $N_{\rm H}^{\rm tot} > 10^{21}$ cm^{-2}. We note, however, that the transitions we observe in the nearby clouds tend to occur at lower $N_{\rm H}^{\rm tot}$ column densities than the bulk of the Galactic sample probed with C II lines. They also occur outside the minimum and maximum fraction bounds predicted by Visser et al. (2009) and shown in Fig. 17 of Langer et al. (2014). Our observations show marked fraction declines at two to three times lower $N_{\rm H}^{\rm tot}$ column densities than the minimum model prediction, even though the nearby clouds probed in our study have the same solar metallicity and total extinction range ($A_V < 4$ mag) as the gas slabs modelled by Visser et al. (2009). Radiative modelling of those slabs is required to compare the model profiles with our data and with the recorded $W_{\rm CO}$ intensities in order to disentangle the chemical or radiative origin of this discrepancy.

Figure 9 illustrates how the CO-dark H_2 fraction relates to the structure of the molecular clouds. Generally $f_{\mathrm{COdk\,H_2}}$ progressively decreases from the DNM outskirts to the CO-bright edges, but local fluctuations imply a more complex pattern that is difficult to interpret in the 2D projection. Extended or elongated DNM-rich structures are more susceptible to photo-dissociation along the short axes of the cloud. The transition from the atomic to molecular phase is expected to occur at different column densities according to the strength of the ambient ISRF, outside and inside the cloud, according to the 3D spatial distribution of the gas and shadowing effects, and according to the 3D structure in density which impacts the ambient H_2 and CO formation rates. Theoretical predictions by Krumholz et al. (2009) indicate that the fraction of molecular gas in a galaxy depends primarily on its column density and is, to a good approximation, independent of the strength of the interstellar radiation field. According to the spherical PDR model of Wolfire et al. (2010), an increased ISRF intensity implies a modest diminution in the thickness of the diffuse H_2 envelope surrounding the CO cloud, but the ratio of H_2 and CO depths remains constant, so the CO-dark H_2 fraction remains stable against changes in ISRF intensity. Yet, this stability depends on the choice of volume density profile inside the cloud ($n_{\rm H} \propto 1/r$). For this profile they find only 30% changes in the CO-dark H_2 fraction for UV radiation fields ranging between 3 and 30 times larger than the local value of Draine (1978).

In observations we do not have a direct measure of the strength of the ISRF, but the specific power radiated by large dust grains per gas nucleon provides an indirect estimate of their heating rate by stellar radiation if the grains have reached thermal equilibrium. We have used the radiance map of Planck Collaboration (2014a) and our distributions of $N_{\rm H}^{\rm tot}$ column densities to map the specific power of the grains across the anticentre and Chamaeleon regions. We find only a 20% dispersion around the mean value of the specific power in the $0.4 < A_V < 1.5$ magnitude range that is critical for the H I -H_2 transition. We find no evidence of a spatial correlation between the distributions of the grain specific powers and those of the CO-dark H_2 fractions shown in Fig. 9. As the strength of the ISRF potentially plays a marginal role in the relative contributions of CO-dark and CO-bright H_2, the density structure of a cloud in 3D and the internal level of turbulence may be the key parameters to explain the small spread (by a factor of 4) in $N_{\rm H}^{\rm tot}$ and A_V thresholds required to overcome CO destruction and sustain a population of CO molecules dense enough to be detected by the current CO surveys. Simulation of H_2 formation within dynamically evolving turbulent molecular clouds shows that H_2 is rapidly formed in dense clumps and dispersed in low-density and warm media due to the complex structure of molecular clouds (Valdivia et al. 2016).

We now turn to the transition from CO-bright to CO-saturated H_2 that occurs in the cores of CO clouds when the optical thickness to ^{12}CO emission is large enough. Figure 5 indicates that the CO-bright part of the total hydrogen column density saturates at $A_V \sim 2$ magnitudes whereas the CO$_{\rm sat}$ fraction still increases. We follow the variation of the CO$_{\rm sat}$ fractions in the total H_2 column-density in Fig. 8. They reach 40 % at $A_V > 4$ magnitude and 50% at $A_V > 6$ magnitude. In the absence of an independent template such as ^{13}CO emission, our analysis cannot separate the additional CO$_{\rm sat}$ gas from the foreground and background DNM present along the lines of sight. Both components are summed into the CO$_{\rm sat}$ one towards the dense regions of large $W_{\rm CO}$ intensities, i.e., large A_V extinctions. The interpolation of the DNM H_2 column densities across the CO$_{\rm sat}$ regions indicates that the CO$_{\rm sat}$ H_2 fractions could be lowered by about 5-10% after subtraction of the DNM contributions.

3.3. Mass fractions and properties of clouds

We have integrated the gas masses over the extent of each cloud in each of the H I , DNM, CO, and CO$_{\rm sat}$ phases. The masses have been estimated with the DNM map and the $X_{\rm CO}$ factors derived from the γ-ray analyses, which are more robust against

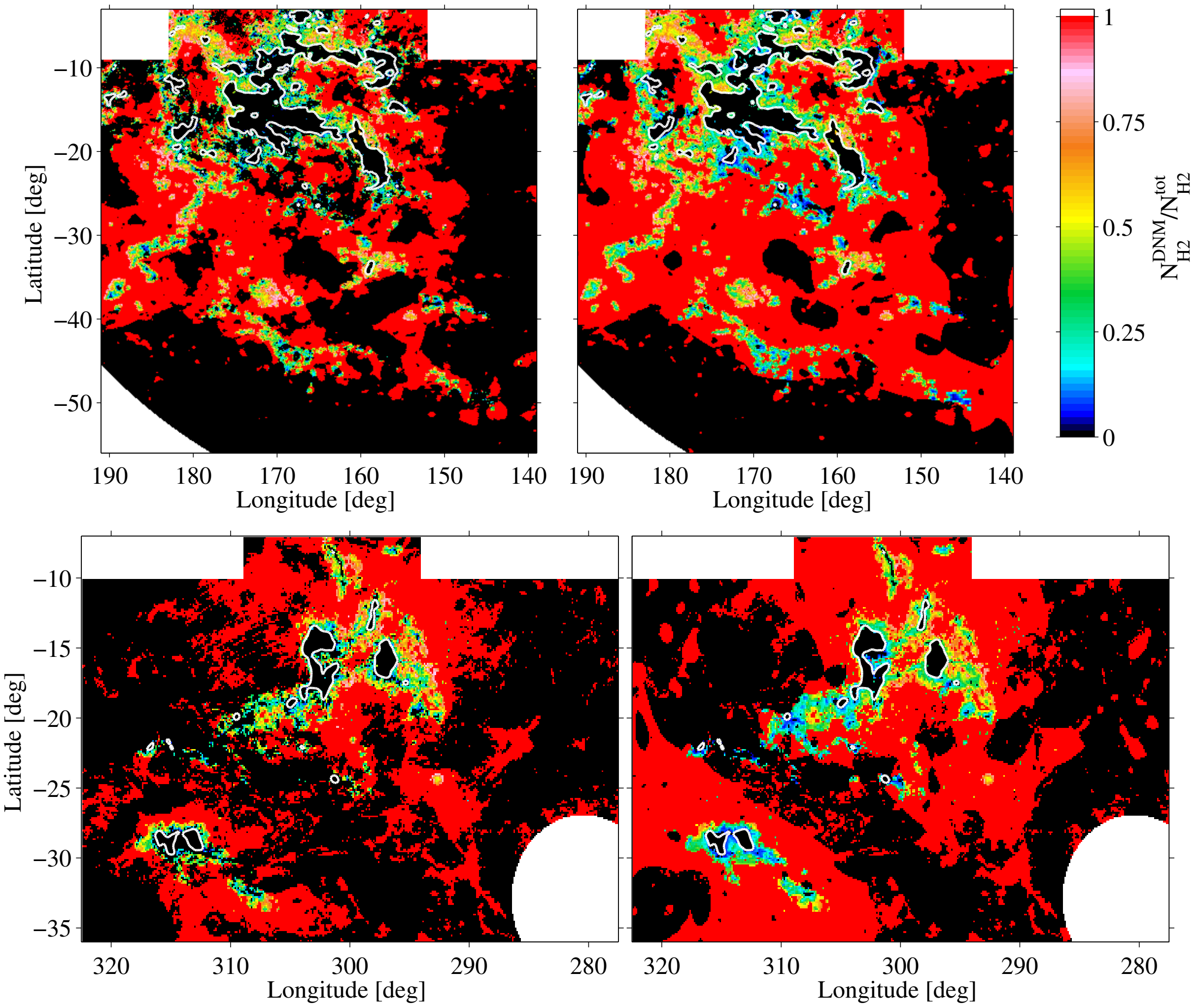

Fig. 9. Fraction of the molecular DNM in the total H_2 column-density ($f_{\mathrm{COdk\,H_2}}$) derived from the dust (left) and γ-ray (right) analyses for the anticentre (top) and Chamaeleon (bottom) regions. The DNM is assumed to be 50% molecular. The white contours outline the shapes of the CO clouds at the 7 K km s^{-1} level chosen to separate DNM and CO$_{\mathrm{sat}}$ components.

Table 2. Fractions of the total mass in the different gas phases for the 15 clouds and their CO-dark H_2 mass fractions

Name	F_{HI}	F_{DNM}	F_{CO}	F_{COsat}	$F^{50}_{\mathrm{COdk\,H_2}}$	$F^{100}_{\mathrm{COdk\,H_2}}$
Cet1	0.74 ±0.24	0.23 ±0.08	0.03 ±0.01		0.79 ±0.12	0.88 ±0.14
Cet2	0.74 ±0.24	0.19 ±0.07	0.07 ±0.03		0.60 ±0.09	0.75 ±0.12
tauM1	0.69 ±0.26	0.20 ±0.08	0.10 ±0.04	0.010 ±0.002	0.49 ±0.09	0.66 ±0.12
tauM2	0.37 ±0.13	0.12 ±0.05	0.37 ±0.16	0.14 ±0.05	0.11 ±0.02	0.19 ±0.03
tauS1	0.69 ±0.14	0.27 ±0.06	0.04 ±0.01		0.79 ±0.04	0.88 ±0.05
tauS2	0.71 ±0.15	0.25 ±0.06	0.03 ±0.01		0.82 ±0.04	0.90 ±0.05
tauN1	0.76 ±0.38	0.19 ±0.11	0.04 ±0.03		0.68 ±0.18	0.81 ±0.22
tauN2	0.77 ±0.39	0.17 ±0.10	0.05 ±0.03	0.010 ±0.005	0.61 ±0.16	0.76 ±0.20
Cal	0.43 ±0.09	0.19 ±0.04	0.30 ±0.09	0.05 ±0.01	0.22 ±0.01	0.36 ±0.02
Auriga	0.41 ±0.12	0.27 ±0.09	0.23 ±0.09	0.08 ±0.02	0.31 ±0.04	0.47 ±0.06
Musca	0.68 ±0.20	0.26 ±0.09	0.05 ±0.02	0.010 ±0.002	0.71 ±0.10	0.83 ±0.11
ChaI	0.64 ±0.19	0.20 ±0.07	0.12 ±0.04	0.03 ±0.01	0.41 ±0.05	0.58 ±0.08
ChaII-III	0.56 ±0.17	0.18 ±0.06	0.22 ±0.08	0.03 ±0.01	0.27 ±0.04	0.43 ±0.06
ChaEastI	0.77 ±0.23	0.08 ±0.03	0.14 ±0.05		0.23 ±0.03	0.38 ±0.05
ChaEastII	0.77 ±0.23	0.15 ±0.05	0.07 ±0.03		0.50 ±0.07	0.67 ±0.09

Notes. $F^{50}_{\mathrm{COdk\,H_2}}$ and $F^{100}_{\mathrm{COdk\,H_2}}$ correspond to a 50% and 100% molecular DNM composition, respectively.

dust evolution. The distance used for each cloud is the same as that of its respective parent complex given in Table 1. The mass ratios are not affected by distance uncertainties. Table 2 lists the relative contributions of the different phases to the total gas mass of clouds. The number distribution for each gas phase is shown in Fig. 10. We have also calculated the CO-dark H_2 fraction in mass, integrated over each cloud, as:

$$F_{\mathrm{COdk\,H_2}} = \frac{M_{\mathrm{H_2}}^{\mathrm{DNM}}}{M_{\mathrm{H_2}}^{\mathrm{tot}}} = \frac{M_{\mathrm{H_2}}^{\mathrm{DNM}}}{M_{\mathrm{H_2}}^{\mathrm{DNM}} + M_{\mathrm{H_2}}^{\mathrm{CO}} + M_{\mathrm{H_2}}^{\mathrm{COsat}}} \qquad (3)$$

Table 2 provides the results for 50% and 100% molecular DNM composition.

Figure 10 highlights that atomic hydrogen is the dominant form of gas by mass in all the sampled clouds. The DNM is the second most important contributor, with mass fractions often close to 20%, in close agreement with the average of 25% found in the sample of 53 clouds exhibiting CO-dark H_2 excesses in C II line emission (Velusamy et al. 2010). Bright CO clouds such as the star-forming TauM2 region or the compact ChaEastI filament gather only ~10% of their mass at the DNM interface. On the contrary, the fraction increases up to 27% in faint CO clouds such as TauS1 and TauS2. The values in Table 2 show that the relative amount of molecular gas present in the CO-dark and CO-bright regions varies greatly from cloud to cloud. Generally, the bright CO clouds, with a mean W_{CO} intensity above 4 K km s^{-1} or a maximum intensity above 20 K km s^{-1}, have more mass in the CO-bright region than in the DNM envelopes, contrary to the CO-faint and rather diffuse clouds. This is reflected by the average CO-dark H_2 fractions varying from 10% to 50% in the brighter molecular clouds (TauM, Aur, Cal, Cha) and between 50% and 90% in the diffuse clouds (Cet, TauS, TauN).

Chen et al. (2015) have studied a wider region of the Galactic anticentre that includes the clouds studied here and the Orion clouds, at an angular resolution of $0.^{\circ}1$. They have modelled the stellar extinction data as a linear combination of H I column densities from the GALFA survey and CO intensities from the Planck type 3 map, corrected for ^{13}CO contamination by multiplying the map by 0.86 (Planck Collaboration 2014b). Chen et al. (2015) used the differences between the data and model to derive the column density of DNM gas and then calculate the CO-dark H_2 mass fraction. They found this mass fraction to be 24% in Taurus, 31% in Orion, and 47% in Perseus. For the high-latitude clouds TauE2 and TauE3, which approximately correspond to the TauS2 and TauS1 clouds of our sample, they found values of 80% and 77%. For a 50-100% molecular composition of the DNM, we respectively find CO-dark H_2 mass fractions of 11–19% in Taurus (TauM2), 0.82–0.90% in TauS2, and 0.79–0.88% in TauS1, in close agreement with the results of Chen et al. (2015).

We further discuss the relative contribution of the diffuse CO-dark H_2 to the total molecular mass according to the cloud properties and location. Figure 11 shows the evolution of the CO-dark H_2 mass fraction, $F_{\mathrm{COdk\,H_2}}$, as a function of:

- the surface fraction in solid angle of dense regions with large W_{CO} intensity inside a cloud, $\mathrm{SF_{dense}} = \frac{S(W_{\mathrm{CO>5Kkms^{-1}}})}{S(W_{\mathrm{CO>1Kkms^{-1}}})}$; this parameter reflects the compactness of the molecular gas;
- the maximum CO intensity, $W_{\mathrm{CO}}^{\mathrm{max}}$, recorded in the cloud;
- the average visual extinction, $\overline{A_{\mathrm{V}}}$, of the cloud;
- the H_2 mass found in the CO-bright phase (excluding the $\mathrm{CO_{sat}}$ component), $M_{\mathrm{H_2}}^{\mathrm{CO}}$;
- the cloud height above the Galactic plane;

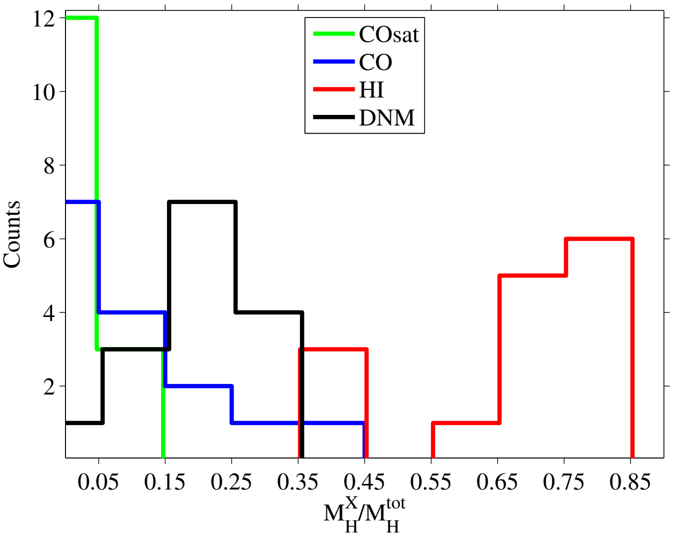

Fig. 10. Number distributions of the HI, DNM, CO, and $\mathrm{CO_{sat}}$ fractions of the total mass found in the sample of clouds for each phase.

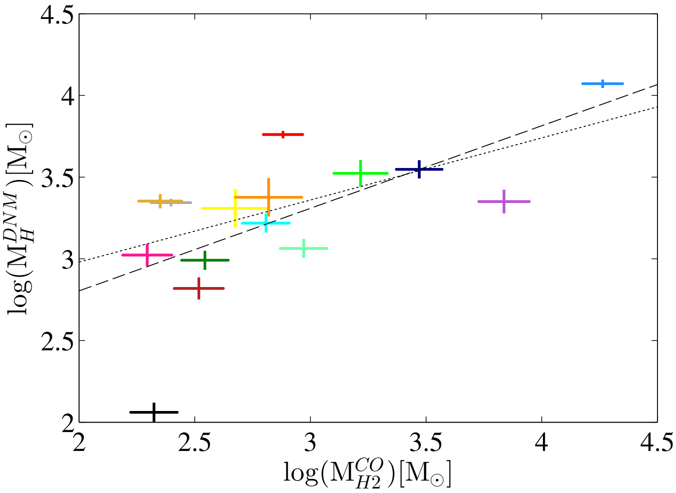

Fig. 12. Gas mass in the DNM as a function of the H_2 mass in the CO-bright phase. The dashed and dotted lines correspond to the best power-law fit respectively including and excluding the compact ChaEastI filament (black point). The colors refer to the same clouds as in Fig. 1.

- the cloud distance to the Galactic centre.

We find a significant trend for $F_{\mathrm{COdk\,H_2}}$ to decrease from 0.8 to 0.1 with increasing $\mathrm{SF_{dense}}$ and $W_{\mathrm{CO}}^{\mathrm{max}}$. A negative slope is detected with a confidence level larger than 18 σ for these diagnostics, indicating that the fraction tends to decrease from diffuse to more compact clouds. Figure 11 shows that the diffuse clouds, rich in CO-dark H_2, also tend to lie at larger heights above the Galactic plane than the brighter and more compact CO clouds.

Using the thermal emission of dust grains over the whole sky at $|b| > 5°$ and masking out CO regions with W_{CO} intensities larger than 1 K km/s, Planck Collaboration (2011a) have found an average $F_{\mathrm{COdk\,H_2}}$ mass fraction of 0.54 close to the value of 0.62 obtained at $|b| > 10°$ from dust visual extinction (Paradis et al. 2012). These high averages indeed reflect the local predominance of molecular clouds with moderate masses and diffuse structures in the sample of nearby clouds seen at medium latitudes.

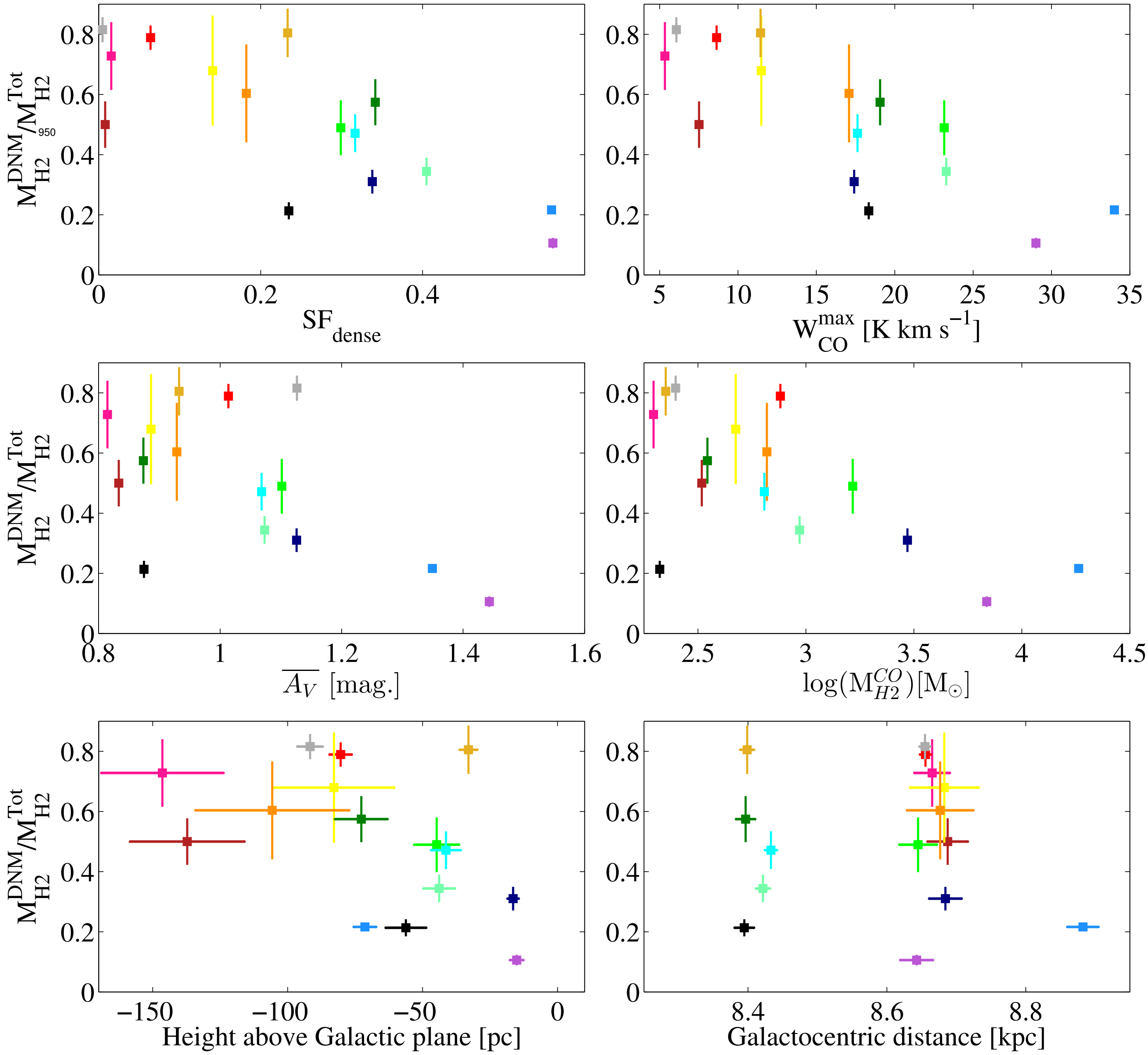

Fig. 11. Average fraction of the molecular DNM in the total H_2 mass ($F_{\mathrm{COdk\,H_2}}$) as a function of: the surface fraction of dense gas SF_{dense} in the cloud (top left), the maximum CO integrated intensity $W_{\mathrm{CO}}^{\mathrm{max}}$ recorded in the cloud (top right), the average visual extinction $\overline{A_V}$ over the cloud (middle left), the logarithm of the H_2 mass in the CO phase $M_{\mathrm{H_2}}^{\mathrm{CO}}$ (middle right), the height above the Galactic plane (bottom left), and the distance to the Galactic centre (bottom right). The DNM is assumed to be 50% molecular. The colors refer to the same clouds as in Fig. 1.

While it is clear in Fig. 11 that obscured clouds with $\overline{A_V}$ in excess of 1.2 mag have low CO-dark H_2 mass fractions, below 20%, the large scatter at low $\overline{A_V}$ indicates that this observable cannot be used to decide whether the CO-dark H_2 dominates over the CO-bright component in the molecular census. For this purpose, the peak CO intensity in a cloud may turn out to be more useful. Adding other clouds to the sample will confirm if clouds with $W_{\mathrm{CO}}^{\mathrm{max}}$ less than approximately 20 K km s^{-1} have more molecular hydrogen in the DNM than in the CO-bright parts. The model of Wolfire et al. (2010) predicts that, for a given cloud, $F_{\mathrm{COdk\,H_2}}$ is a strong decreasing function of the mean extinction of the cloud, $\overline{A_V}$. Yet, their modelled fractions remain very large, near 75%, at $\overline{A_V} = 2$ magnitudes, at variance with the low fractions we find already above ∼1.2 magnitude.

Except for the outlier CO filament of ChaEastI, compact and filamentary, which has particularly low mass, we find a significant decrease of the $F_{\mathrm{COdk\,H_2}}$ fraction with the logarithm of the $M_{\mathrm{H_2}}^{\mathrm{CO}}$ mass. The negative slope is preferred against uniform trend at a confidence level exceeding 19 σ. Figure 12 further shows that the mass present in the DNM envelopes approximately scales with the square root of the molecular mass seen in CO. We find a correlation coefficient of 0.86 between the two sets of masses on a logarithmic scale. A power-law fit yields:

$$M_{\mathrm{H}}^{\mathrm{DNM}} = (61.7 \pm 7.1) M_{\mathrm{H_2}}^{\mathrm{CO}\;0.51\pm0.02} \tag{4}$$

if we include all the clouds, and

$$M_{\mathrm{H}}^{\mathrm{DNM}} = (166.0 \pm 19.1) M_{\mathrm{H_2}}^{\mathrm{CO}\;0.38\pm0.02} \tag{5}$$

if we exclude the outlier filament of ChaEastI.

The slopes are detected at the 13 σ and 24 σ confidence levels, respectively. They compare well with the DNM mass evolution, $M_{\mathrm{H}}^{\mathrm{DNM}} \propto M_{\mathrm{H_2}}^{\mathrm{CO}\;0.4}$, found at latitudes $|b| > 5°$ in broader and more massive molecular complexes than the clouds studied here (Grenier et al. 2005). The former relation had been derived with a coarser derivation of the dust optical depth (from *IRAS* and *DIRBE*) and lower-resolution data in γ rays (from *EGRET*) and in H I lines (LAB survey, Kalberla et al. 2005). The data points in Fig. 12 strengthen the reliability of a power-law relation between the DNM mass and the CO-bright H_2 component. They also extend its application to lower CO masses. According to Larson's laws, gravitationally bound molecular clouds have masses that approximately scale with the square of the cloud linear size (Larson 1981; Lombardi et al. 2010). For bound clouds, the scaling relation of equation 4 implies that the mass present in the DNM envelopes should scale with the linear size of the molecular clouds. This can be observationally tested by using the kinematical information of the H I and CO lines when firm distances to these clouds can be inferred from the stellar reddening information from *Gaia*. This relation between masses in the DNM and CO phases can also serve to extrapolate the amount of DNM gas beyond the local ISM and in external galaxies. Its confirmation is of prime importance, but it requires further tests in giant molecular clouds of larger CO masses than in Fig. 12, in compact clouds of small size, and in clouds of different metallicity.

The PDR model of Levrier et al. (2012) yields a mass fraction of 0.32 in a cloudlet with only 9.5 $M_\odot$ in CO and illuminated by a standard UV field. The model of Wolfire et al. (2010) yields a narrow range of fractions between 0.25 and 0.33 for giant molecular clouds with masses of $(0.1 - 3) \times 10^6$ $M_\odot$ much larger than those probed in our sample and with a UV radiation field 3 to 30 times larger than the local value of Draine (1978). The theoretical studies therefore point to rather stable CO-dark H_2 fractions that should little depend on cloud mass or radiation field. Our results challenge this view by showing a wide range of mass fractions that relate to cloud properties such as the CO diffuseness ($\mathrm{SF_{dense}}$) and the CO brightness (peak W_{CO} intensity or integral of W_{CO} intensities that gives the $M_{\mathrm{H_2}}^{\mathrm{CO}}$ mass).

Cloud-dependent variations call for care in the interpretation of averages taken over large ensembles of clouds with different evolutionary or structural properties. For instance, the difference noted between the local clouds seen toward the inner and outer Galaxy by Paradis et al. (2012) does not relate to the Galactocentric distance (see Fig. 11), but to different combinations of clouds in different states. This could explain the discrepancy noted by Pineda et al. (2013) between an 'apparent decrease' of $F_{\mathrm{COdk\,H_2}}$ with Galactocentric distance in Paradis et al. (2012) and an increase with this distance in the much broader sample of clouds studied with C II lines across the Milky Way (Pineda et al. 2013). Moreover, the present trend for larger $F_{\mathrm{COdk\,H_2}}$ fractions in clouds lying higher above the Galactic plane, if confirmed, should also raise concerns for radial studies across the Galactic disc in constant latitudes bands. The rise observed in $F_{\mathrm{COdk\,H_2}}$ from about 10% at 4 kpc up to 60–80% near 10 kpc is not biased by such height variations because it is based on C II line measurements taken along the Galactic plane, at $b = 0°$ (Pineda et al. 2013).

In their simulation of the Milky Way, Smith et al. (2014) use a uniform IRSF, metallicity, and mean gas surface density, so they cannot reproduce a global variation of $F_{\mathrm{COdk\,H_2}}$ with Galactocentric radius. In conditions akin to those in the local ISM, they obtain an average fraction of 42% that is almost insensitive to the W_{CO} intensity threshold used to separate CO-bright and CO-dark gas. They have, however, found notable differences in $F_{\mathrm{COdk\,H_2}}$ between the arm and inter-arms regions. Generally the fraction is anti-correlated with the total molecular $N_{\mathrm{H_2}}$ column density. The molecular gas is predominantly CO-bright in the spiral arms ($0.1 < F_{\mathrm{COdk\,H_2}} < 0.5$), but the CO-dark H_2 mass fraction exceeds 80% in the inter-arm regions where the clouds are sheared out by the differential rotation of the disc following their passage through the spiral arm. The stretched cloud structures become more permeable to dissociating radiation. Interestingly, we find in our sample a wide range of CO-dark H_2 mass fractions responding to properties such as $\mathrm{SF_{dense}}$, $M_{\mathrm{H_2}}^{\mathrm{CO}}$, and Galactic height, that can reflect the transitory/sheared versus gravitationally well-bound state of a cloud.

Figure 13 shows the distribution of W_{CO} intensities as a function of $N_{\mathrm{H_2}}$ column densities observed in the anticentre and Chamaeleon regions. The data points above the grey line in this figure correspond to directions where $X_{\mathrm{CO}} < 10^{20}$ cm^{-2} K^{-1} km^{-1} s (as in the Chamaeleon, main Taurus, California, and Perseus clouds). The data points gathering along the horizontal axis, at very low W_{CO} up to large $N_{\mathrm{H_2}}$ values, correspond to the DNM gas. In the simulation of Smith et al. (2014) with local-ISM characteristics, CO molecules predominantly form in spiral-arm clouds, which emit mostly at $N_{\mathrm{H_2}} > 10^{21}$ cm^{-2} with $W_{\mathrm{CO}} > 10$ K km s^{-1} as shown by the blue contours in Fig. 13. As noted by Levrier et al. (2012) and illustrated in Fig. 13, simulations underproduce luminous CO emission compared to observations. They first miss CO emission at the large $N_{\mathrm{H_2}}$ column densities of a few 10^{21} cm^{-2} observed in nearby molecular clouds. This explains why they obtain twice lower X_{CO} factors than the values measured in several nearby clouds. We have discussed this discrepancy in Remy et al. (2016). It also explains why the simulated CO emission gathers primarily in giant molecular clouds in the spiral arms and why the simulations yield a sharp contrast in CO-dark H_2 abundance inside and outside of the arms. The simulations also severely under-predict CO emission in the very diffuse molecular regime, at $N_{\mathrm{H_2}} < 10^{21}$ cm^{-2}, as shown in Fig. 13. This limitation biases the simulated values of CO-dark H_2 fractions upward in column density and in mass.

4. Conclusions

We have analysed the gas, dust, and CR content of several nearby clouds in the anticentre and Chamaeleon regions. As described in Planck and Fermi Collaborations (2015) and Remy et al. (2016), in order to trace the total gas column density, we have modelled the γ-ray emission and dust optical depth at 353 GHz as linear combinations of several gaseous components associated with different phases (ionized, H I , DNM, CO, and $\mathrm{CO_{sat}}$ media). We have selected a subset of 15 clouds with no overlap in direction to avoid confusion between the separate phases of the various clouds. Thereby, we have been able to follow the relative contributions of the different gas phases to the total mass and column density, and to study phase transitions in the clouds. The main results are summarized as follows:

– **On the gas content:** H I is the dominant form of gas by mass in our sample. It contributes 50% to 80% to the total mass. The capability of CO lines to trace the total H_2 gas varies

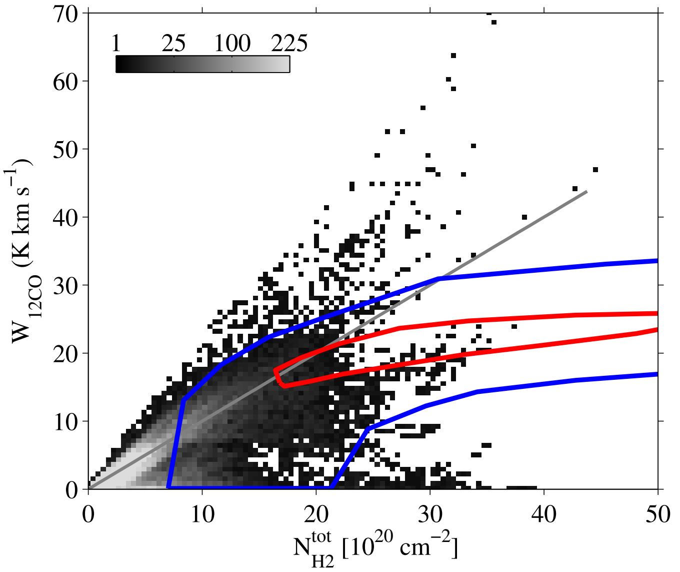

Fig. 13. Number distribution of the integrated CO intensity, W_{CO}, as a function of the total H_2 column-density derived from the γ-ray fits for the anticentre and Chamaeleon regions. The grey line corresponds to $X_{CO} = 10^{20}$ cm^{-2} K^{-1} km^{-1} s. The blue and red contours delimits the least and most populated parts of the distribution found in a simulation of the Milky Way of Smith et al. (2014) .

widely from cloud to cloud. The DNM envelopes, composed of dense optically-thick H I and diffuse CO-dark H_2 at the transition between the atomic and molecular phases, contribute about 20% to the cloud masses in our sample. The DNM mass often exceeds the H_2 mass seen in CO in diffuse clouds (see below) and it approximately scales with the square root of the CO-bright mass. The CO-saturated H_2 gas, which is seen in addition to the W_{CO}-inferred component in dense regions of large optical thickness to ^{12}CO lines, generally contributes less than 10% to the total cloud mass. It accounts for 40% of the molecular column densities at A_V >3 magnitudes.

- **On phase transitions:** The transition from the H I to H_2 composition and the onset of visible CO emission both occur in narrow intervals of total gas column density in the selected clouds, respectively at $(0.6 - 1) \times 10^{21}$ cm^{-2} and $(0.6 - 2.5) \times 10^{21}$ cm^{-2}. The H I fraction in the total column density starts to decrease below 0.4 magnitude. The CO intensities rise in the 1-2.5 magnitude range. At A_V >3 mag the ^{12}CO emission saturates significantly.
- **On the CO-dark H_2 fractions:** The $f_{\mathrm{COdk\,H_2}}$ fraction in column density is observed to decrease from the edge to the core of an individual cloud or a broader complex. The $f_{\mathrm{COdk\,H_2}}$ decrease with increasing A_V follows a half-Gaussian profile peaking at 0.4–0.6 magnitude and with a standard deviation close to 1 magnitude. The dust specific power reflecting the strength of the ISRF varies only marginally across the DNM envelopes and it does not correlate with spatial changes in $f_{\mathrm{COdk\,H_2}}$. In the solar neighbourhood, differences in the $F_{\mathrm{COdk\,H_2}}$ mass fraction primarily stem from the cloud structure: $F_{\mathrm{COdk\,H_2}}$ significantly decreases from diffuse to dense molecular clouds. The DNM molecular mass often exceeds the H_2 mass seen in CO for clouds with peak $W^{\max}_{CO}$ intensities lower than about 15-20 K km s^{-1}, with surface fractions of bright CO intensities $\mathrm{SF_{dense}}$ less than about 0.3, or with average visual extinctions $\overline{A_V}$ lower than about 1 magnitude. We note a trend for larger $F_{\mathrm{COdk\,H_2}}$ fractions in clouds located at higher latitudes above the Galactic plane.

In future studies, it will be interesting to compare maps of the total gas derived jointly from γ rays and dust optical depth, or dust extinction, to the gas traced by other species. In diffuse environments, CO precursors such as CH (Gerin et al. 2010), OH (Allen et al. 2015), and HCO (Liszt et al. 2014) can probe the CO dark H_2 in the DNM with less confusion than C II lines. In dense molecular environments, CO isotopologues such as ^{13}CO and C^{18}O, and rarer molecules routinely probe the CO-saturated molecular gas at large volume densities. Observations of these tracers are, however, still sparse and their angular extent is often inadequate for comparisons with gas maps inferred from γ-ray and dust studies. Dedicated campaigns toward individual nearby clouds are required to fully explore the relative merits and limitations of the different tracers and to constrain the DNM composition.

Additionally, extending our sample to other clouds in the local ISM, with other masses and various heights above the Galactic plane, then at larger distance in the Local Arm and in between the Local and Perseus arms, is necessary to better characterize the trends in $F_{\mathrm{COdk\,H_2}}$ discussed here. The results would greatly improve our view of the relative distributions of CO-dark and CO-bright H_2 gas across the Galaxy.

Acknowledgements. The *Fermi* LAT Collaboration acknowledges generous ongoing support from a number of agencies and institutes that have supported both the development and the operation of the LAT as well as scientific data analysis. These include the National Aeronautics and Space Administration and the Department of Energy in the United States, the Commissariat à l'Energie Atomique and the Centre National de la Recherche Scientifique / Institut National de Physique Nucléaire et de Physique des Particules in France, the Agenzia Spaziale Italiana and the Istituto Nazionale di Fisica Nucleare in Italy, the Ministry of Education, Culture, Sports, Science and Technology (MEXT), High Energy Accelerator Research Organization (KEK) and Japan Aerospace Exploration Agency (JAXA) in Japan, and the K. A. Wallenberg Foundation, the Swedish Research Council and the Swedish National Space Board in Sweden. Additional support for science analysis during the operations phase is gratefully acknowledged from the Istituto Nazionale di Astrofisica in Italy and the Centre National d'Études Spatiales in France. The French authors acknowledge the support of the Agence Nationale de la Recherche (ANR) under award number STILISM ANR-12-BS05-0016.

References

Allen, R. J., Hogg, D. E., & Engelke, P. D. 2015, AJ, 149, 123
Audit, E. & Hennebelle, P. 2005, A&A, 433, 1
Barriault, L., Joncas, G., Lockman, F. J., & Martin, P. G. 2010, MNRAS, 407, 2645
Blitz, L., Bazell, D., & Desert, F. X. 1990, ApJ, 352, L13
Cardelli, J. A., Clayton, G. C., & Mathis, J. S. 1989, ApJ, 345, 245
Chen, B.-Q., Liu, X.-W., Yuan, H.-B., Huang, Y., & Xiang, M.-S. 2015, MNRAS, 448, 2187
Dame, T. M., Hartmann, D., & Thaddeus, P. 2001, ApJ, 547, 792
Dame, T. M. & Thaddeus, P. 2004, in Astronomical Society of the Pacific Conference Series, Vol. 317, Milky Way Surveys: The Structure and Evolution of our Galaxy, ed. D. Clemens, R. Shah, & T. Brainerd, 66
Deguchi, S. & Watson, W. D. 1985, ApJ, 290, 578
Dickey, J. M., McClure-Griffiths, N. M., Gaensler, B. M., & Green, A. J. 2003, ApJ, 585, 801
Dickey, J. M., Strasser, S., Gaensler, B. M., et al. 2009, ApJ, 693, 1250
Draine, B. T. 1978, ApJS, 36, 595
Field, G. B., Goldsmith, D. W., & Habing, H. J. 1969, ApJ, 155, L149
Fukui, Y., Torii, K., Onishi, T., et al. 2015, ApJ, 798, 6
Gerin, M., de Luca, M., Goicoechea, J. R., et al. 2010, A&A, 521, L16
Gillmon, K., Shull, J. M., Tumlinson, J., & Danforth, C. 2006, ApJ, 636, 891
Green, G. M., Schlafly, E. F., Finkbeiner, D. P., et al. 2015, ApJ, 810, 25
Grenier, I. A., Black, J. H., & Strong, A. W. 2015, ARA&A, 53, 199
Grenier, I. A., Casandjian, J.-M., & Terrier, R. 2005, Science, 307, 1292
Heiles, C. & Troland, T. H. 2003, ApJ, 586, 1067
Juvela, M. & Montillaud, J. 2016, A&A, 585, A38

Kalberla, P. M. W., Burton, W. B., Hartmann, D., et al. 2005, A&A, 440, 775
Kalberla, P. M. W. & Haud, U. 2015, A&A, 578, A78
Kalberla, P. M. W., McClure-Griffiths, N. M., Pisano, D. J., et al. 2010, A&A, 521, A17
Kim, C.-G., Ostriker, E. C., & Kim, W.-T. 2014, ApJ, 786, 64
Köhler, M., Ysard, N., & Jones, A. P. 2015, A&A, 579, A15
Krumholz, M. R., McKee, C. F., & Tumlinson, J. 2009, ApJ, 693, 216
Langer, W. D., Velusamy, T., Pineda, J. L., Willacy, K., & Goldsmith, P. F. 2014, A&A, 561, A122
Larson, R. B. 1981, MNRAS, 194, 809
Lee, M.-Y., Stanimirović, S., Douglas, K. A., et al. 2012, ApJ, 748, 75
Levrier, F., Le Petit, F., Hennebelle, P., et al. 2012, A&A, 544, A22
Liszt, H. 2001, A&A, 371, 698
Liszt, H. 2014, ApJ, 783, 17
Liszt, H. S. & Pety, J. 2012, A&A, 541, A58
Liszt, H. S., Pety, J., Gerin, M., & Lucas, R. 2014, A&A, 564, A64
Lombardi, M., Alves, J., & Lada, C. J. 2010, A&A, 519, L7
Magnani, L., Chastain, R. J., Kim, H. C., et al. 2003, ApJ, 586, 1111
Martin, P. G., Roy, A., Bontemps, S., et al. 2012, ApJ, 751, 28
McKee, C. F. & Ostriker, J. P. 1977, ApJ, 218, 148
Mizuno, A., Yamaguchi, R., Tachihara, K., et al. 2001, PASJ, 53, 1071
Murray, C. E., Stanimirović, S., Goss, W. M., et al. 2015, ApJ, 804, 89
Narayanan, G., Heyer, M. H., Brunt, C., et al. 2008, ApJS, 177, 341
Paradis, D., Dobashi, K., Shimoikura, T., et al. 2012, A&A, 543, A103
Peek, J. E. G., Heiles, C., Douglas, K. A., et al. 2011, ApJS, 194, 20
Pineda, J. L., Goldsmith, P. F., Chapman, N., et al. 2010, ApJ, 721, 686
Pineda, J. L., Langer, W. D., Velusamy, T., & Goldsmith, P. F. 2013, A&A, 554, A103
Planck and Fermi Collaborations. 2015, A&A, 582, A31
Planck Collaboration. 2011a, A&A, 536, A19
Planck Collaboration. 2011b, A&A, 536, A25
Planck Collaboration. 2014a, A&A, 571, A11
Planck Collaboration. 2014b, A&A, 571, A13
Remy, Q., Grenier, I. A., Marshall, D. J., & Casandjian, J. M. 2016, submitted to A&A
Ridge, N. A., Di Francesco, J., Kirk, H., et al. 2006, AJ, 131, 2921
Röhser, T., Kerp, J., Winkel, B., Boulanger, F., & Lagache, G. 2014, A&A, 564, A71
Rowles, J. & Froebrich, D. 2009, MNRAS, 395, 1640
Roy, N., Kanekar, N., Braun, R., & Chengalur, J. N. 2013, MNRAS, 436, 2352
Saury, E., Miville-Deschênes, M.-A., Hennebelle, P., Audit, E., & Schmidt, W. 2014, A&A, 567, A16
Sheffer, Y., Rogers, M., Federman, S. R., et al. 2008, ApJ, 687, 1075
Shetty, R., Glover, S. C., Dullemond, C. P., & Klessen, R. S. 2011, MNRAS, 412, 1686
Smith, R. J., Glover, S. C. O., Clark, P. C., Klessen, R. S., & Springel, V. 2014, MNRAS, 441, 1628
Stanimirović, S., Murray, C. E., Lee, M.-Y., Heiles, C., & Miller, J. 2014, ApJ, 793, 132
Stepnik, B., Abergel, A., Bernard, J.-P., et al. 2003, A&A, 398, 551
Valdivia, V., Hennebelle, P., Gérin, M., & Lesaffre, P. 2016, A&A, 587, A76
van Dishoeck, E. F. & Black, J. H. 1988, ApJ, 334, 771
Velusamy, T., Langer, W. D., Pineda, J. L., et al. 2010, A&A, 521, L18
Visser, R., van Dishoeck, E. F., & Black, J. H. 2009, A&A, 503, 323
Winkel, B., Kerp, J., Flöer, L., et al. 2016, A&A, 585, A41
Wolfire, M. G., Hollenbach, D., & McKee, C. F. 2010, ApJ, 716, 1191
Wolfire, M. G., McKee, C. F., Hollenbach, D., & Tielens, A. G. G. M. 2003, ApJ, 587, 278
Xu, D., Li, D., Yue, N., & Goldsmith, P. F. 2016, ApJ, 819, 22
Ysard, N., Abergel, A., Ristorcelli, I., et al. 2013, A&A, 559, A133

Conclusions et perspectives

Les principaux objectifs de cette étude étaient, premièrement de tester les capacités relatives des principaux traceurs de gaz et de poussières à estimer les quantités de gaz dans les différentes phases du milieu interstellaire ainsi que la quantité totale de gaz ; deuxièmement de sonder les propriétés du gaz et des poussières dans différents nuages locaux et de chercher des effets sur les propriétés des traceurs ; troisièmement de faire le lien entre les observations et les modèles théoriques.

En exploitant l'information combinée du rougissement stellaire dû aux poussières, de leur émission thermique, des rayons γ, et des raies d'émission HI et CO, l'analyse des nuages locaux de l'anticentre Galactique nous a permis de mettre en évidence des limites à ces différents traceurs et de suivre les propriétés du gaz et des poussières des milieux atomiques diffus jusqu'aux cœurs des nuages moléculaires.

Nous avons vérifié l'accord du spectre en énergie des rayons γ avec le spectre interstellaire local dans les différentes phases du gaz. Cela témoigne d'une bonne pénétration des rayons cosmiques[21] à travers les nuages de l'anticentre Galactique et donc de la fiabilité de l'émission γ en tant que traceur du gaz interstellaire dans le milieu local.

Nous avons mesuré les densités de colonne du gaz non tracé par l'émission HI et CO, en veillant à séparer le gaz dans les enveloppes de DNM à la transition HI–H_2, et le H_2 supplémentaire à ajouter dans les parties moléculaires denses quand l'émission des raies CO sature. Les variations observées de la fraction de gaz moléculaire sombre à l'intérieur d'un nuage et d'un nuage à l'autre, peuvent servir à tester les modèles de formation et de photo-dissociation du H_2 et du CO dans les milieux diffus et les enveloppes des nuages moléculaires. La loi d'évolution de la masse de DNM en fonction de la masse de gaz moléculaire visible en CO (Grenier et al. 2005) a été confirmée et étendue à plus faible masse par cette étude. Si elle est également vérifiée dans des complexes moléculaires encore plus massifs et à des métallicités différentes, cette relation pourrait servir à estimer la masse de DNM dans les parties distantes de la Galaxie et dans les galaxies externes.

Nos mesures des rapports τ_{353}/N_H et $E(B-V)/N_H$ et l'amplitude de leurs variations avec la densité de colonne de gaz, la température de couleur des poussières et l'indice spectral d'émission des grains apportent, d'une part des contraintes sur les processus d'évolution des grains prédits par les modèles, et d'autre part des limites sur les plages dans lesquels les traceurs de poussières sont linéairement corrélés à la quantité de gaz. Les variations conjointes de ces différents paramètres restent à explorer dans d'autres régions, notamment pour contraindre le lien entre les gradients en τ_{353}/N_H et $E(B-V)/N_H$ (anti-corrélation du facteur d'extinction R_V avec l'index spectral et corrélation avec la température de couleur, discutées dans l'article III). Elles apporteront un éclairage complémentaire sur le fait que le rapport $E(B-V)/N_H$ ne semble pas chuter nettement dans les cœurs moléculaires alors que les modèles prédisent un accroissement significatif de la taille des grains et du facteur R_V .

L'analyse des nuages de l'anticentre Galactique a permis de mettre en évidence une tendance à ce que le rapport X_{CO} moyen d'un nuage diminue lorsque le nuage est plus brillant et plus compact, mais pas avec la masse visible en CO. Cette tendance systématique est compatible avec la forte diminution du facteur X_{CO} prévue par les modèles depuis les enveloppes diffuses, plus exposées à la photo-dissociation, jusqu'aux cœurs moléculaires denses, mieux écrantés. Les valeurs de X_{CO} inférieures à 10^{20} cm^{-2} K^{-1} km^{-1} s qui caractérisent l'ensemble des nuages locaux étudiés dans cette thèse (et précédemment en rayons γ) sont difficiles à atteindre dans les modèles. Elles ne sont atteintes que pour des densités volumiques de gaz et des extinctions A_V nettement supérieures à celles sondées dans notre étude. Ces différences confirment que les simulations prédisent généralement une émission CO trop peu lumineuse à faible densité de colonne. Cette différence est connue mais son origine reste à clarifier.

Par ailleurs, le fait que les valeurs de X_{CO} déduites de l'émission des poussières soient systématiquement plus grandes que celles déduites du rougissement dû aux poussières et de l'émission de rayons γ, et ce d'autant plus à mesure que l'opacité des grains τ_{353}/N_H augmente, révèle un biais dû à l'évolution des propriétés d'émission des grains.

Indépendamment des résultats sur les propriétés du milieu interstellaire, la méthode d'analyse couplant traceurs de poussières et rayons γ a été améliorée pour l'analyse des nuages locaux de l'anticentre Galactique, en incluant

---

[21] ayant des énergies de quelques GeV à quelques TeV correspondant aux observations γ utilisées

la séparation des composantes de DNM et CO_{sat}, et en ajoutant une composante free-free extraite de l'émission à 70 GHz mesurée par Planck. Ces implémentations seront exploitées pour des analyses du même type dans d'autres nuages. De plus les techniques de décomposition en position et vitesse des nuages, développées pour cette étude, peuvent être appliquées à d'autres régions du ciel.

La méthode de séparation des nuages locaux que nous proposons, basée sur l'algorithme DBSCAN, permet une décomposition des structures équivalente, voire supérieure aux méthodes existantes (comme CLUMPFIND, CROPS, SCIMES) et ce en utilisant uniquement l'information en position-vitesse contenue dans les données, sans hypothèses supplémentaires.

Les vitesses centrales des raies Hɪ et CO issues de notre méthode de décomposition peuvent être utilisées pour isoler les nuages locaux mais aussi les différentes composantes Galactiques en comparant ces vitesses à celles prédites par les modèles de structure spirale. La décomposition préliminaire à basse résolution sur l'ensemble du ciel donnent des indications intéressantes qui pourraient être ciblées par des études dédiées à plus hautes résolutions spatiales et spectrales grâce aux nouvelles cartographies Hɪ (GASS III, Kalberla & Haud 2015, EBHIS, Winkel et al. 2016) et CO (NANTEN 2, MOPRA, Burton et al. 2013). Par exemple, on note une possible extension du bras de Scutum jusqu'à l = 150° à 20 kpc du centre Galactique visible dans l'émission Hɪ et marginalement dans l'émission CO, à confirmer. On note également, à la fois dans l'émission Hɪ et CO, la présence de gaz entre les bras de Persée et Carina, dans la prolongation du bras local (à 5 kpc soleil dans la direction l = 270°). On pourrait donc comparer l'évolution des propriétés du milieu interstellaire entre les bras et l'inter-bras comme par exemple le facteur X_{CO} et la fraction de gaz moléculaire sombre, tel que nous l'avons suggéré dans l'article II.

Les cartes d'émission des poussières et des rayons γ ne donnent qu'une information sur la quantité totale de gaz intégrée sur les lignes de visée. La cartographie du milieu interstellaire basée sur l'exploitation des raies d'absorption dans les spectres stellaires et en particulier des DIBs (Zasowski et al. 2015) apporte une information en vitesse supplémentaire. Pour l'instant cette cartographie est très parcellaire et couvre rarement les grandes étendues (en angle solide) du DNM et du gaz moléculaire des nuages locaux. Dans ces directions hors du plan Galactique il y a moins de confusion possible entre les différents nuages sur les lignes de visée ce qui facilite l'étude des propriétés du milieu interstellaire. De futures observations ciblées sur les nuages locaux permettraient de comparer la largeur équivalente des DIBs avec les densités de colonne dans les différentes phases de gaz et en particulier dans le DNM. L'information en vitesse apportée par les DIBs pourrait permettre de séparer différentes composantes dans le DNM, comparables à celles séparées dans l'émission Hɪ et CO et ainsi de mieux contraindre la structure des nuages dans les différentes phases du milieu interstellaire.

Le milieu interstellaire Galactique a été observé intensivement et très précisément en 2D à de multiples longueurs d'onde, ou en 2+1D (position-vitesse). Aujourd'hui la cartographie 3D du milieu interstellaire se développe rapidement sous l'impulsion de grands relevés stellaires en photométrie ou spectroscopie. Les mesures du télescope *Gaia* seront un catalyseur essentiel de cette révolution. *Gaia* offrira au cours des prochaines années un nombre sans précédent d'informations sur notre galaxie combinant des données astrométriques, photométriques et spectroscopiques de plus d'un milliard d'étoiles. Le calcul de la magnitude absolue à partir des données de Gaia nécessite une estimation de l'extinction. C'est pourquoi la construction d'une carte d'extinction 3D est une priorité pour pouvoir exploiter tout le potentiel de *Gaia*. Au cours des dernières années plusieurs études ont proposé des cartes 3D de l'extinction dans la Galaxie : dans les 500 pc du voisinage solaire (Lallement et al. 2014), ou jusqu'à quelques kiloparsecs (Marshall et al. 2006; Green et al. 2015). Les résolutions angulaires et en distance de ces cartes varient fortement en fonction de la méthode ou des données utilisées et des échelles ou régions sondées. De nouvelles techniques bayésiennes ont récemment été proposées pour améliorer la précision de ces cartes 3D. Par exemple afin de localiser plus précisément des nuages locaux, Marshall et al. (2015) propose une nouvelle approche bayésienne dérivée de sa méthode combinant des données photométriques et le modèle de population stellaire de Besançon pour contraindre simultanément l'extinction et la distance (voir section 4.1). Le désavantage de cette méthode reste de dépendre d'un modèle de population stellaire, en effet l'extinction peut être localement biaisée en direction d'un amas d'étoile où les densités stellaires sont supérieures à celles prédites par le modèle. En parallèle une méthode de déconvolution bayésienne est en cours de développement pour permettre de déterminer simultanément la distribution de l'extinction et de la densité stellaire le long de la ligne de visée Babusiaux et al. (2016).

La cartographie 3D des poussières basée sur ces méthodes représentera une avancée importante, cependant les problématiques essentielles liées au milieu interstellaire, à savoir les relations entre les propriétés d'extinction et d'émission des poussières, l'évolution des différentes phases de gaz, ainsi que les conditions de la formation stellaire ne peuvent être abordées que si l'on dispose également de la cartographie 3D de la composante gazeuse et des liens gaz-poussières à toutes les échelles spatiales, des cœurs de nuages aux bras spiraux. La comparaison de l'information apportée par les raies d'émission du gaz (Hɪ, CO) et les raies d'absorption interstellaires dans les spectres stellaires (DIBs, Na, K...) peut permettre d'identifier des composantes en vitesses similaires correspondant aux mêmes nuages. La détection ou non-détection de ces composantes en fonction de la distance des étoiles (mesurée avec *Gaia*) apportera une contrainte sur la distance des nuages. Ces estimations de distances pourront être comparée à celles apportées par les méthodes de cartographie 3D de l'extinction (causée par les poussières). Cette comparaison de la tomographie des poussières avec la tomographie du gaz permettrait d'identifier de possibles biais dans la détermination de l'extinction en fonction de la distance et donc d'améliorer les cartes d'extinction mais aussi d'étudier les propriétés des poussières et du gaz dans le milieu interstellaire en trois dimensions.

Remerciements

Tout d'abord je tiens à remercier ma directrice de thèse Isabelle Grenier pour ses conseils tout au long de ces trois années, l'expertise qu'elle m'a transmise pour l'analyse des nuages, et les corrections apportées aux articles et au manuscrit de thèse. Je remercie aussi mes principaux collaborateurs Douglas Marshall et Jean-Marc Casandjian pour leur contribution à cette étude et leurs conseils. Un grand merci aux membres de la collaboration *Fermi* LAT ayant suivi notre travail et en particulier aux rapporteurs internes Seth Digel et Tsunefumi Mizuno pour leurs commentaires et corrections.

L'Agence Nationale de la Recherche est remerciée pour le financement du Projet Stilism auquel cette thèse est associée. Je tiens également à remercier les membres du projet Stilism à l'Observatoire de Paris-Meudon, Rosine Lallement, Ana Monreal-Ibero, et Meriem El Yajouri, avec lesquelles j'ai fréquemment échangé sur les questions relatives aux DIBs et à la corrélation des vitesses du gaz vues par les raies d'émission et d'absorption.

Merci au personnel de l'école doctorale STEP'UP pour son assistance dans les étapes administratives et pour veiller au bon déroulement des thèses. Un grand merci aux membres du jury de thèse, Francois Boulanger, Jacques Le Bourlot, Gilles Joncas, Rosine Lallement pour avoir accepté de juger ce travail et d'assister à la soutenance.

Je remercie également mes professeurs des Universités de Toulouse et Montpellier pour la compréhension de la physique qu'ils m'ont permis d'acquérir, ainsi que mes encadrants de stages de Master Denis Puy (M1), et Benoit Semelin (M2), en particulier pour leurs recommandations.

Je remercie les membres du personnel du laboratoire AIM, du Service d'Astrophysique, et plus généralement du CEA Saclay pour leur accueil et l'aide qu'ils ont pu m'apporter au cours de ces trois années, aussi bien sur les plans scientifique, technique, qu'administratif.

Et à toutes celles et ceux que je ne citerai pas, mais qui savent ce que je leur dois... Merci.

Références

Abdo, A. A., Ackermann, M., Ajello, M., et al. 2010, ApJ, 710, 133

Ackermann, M., Ajello, M., Allafort, A., et al. 2012a, ApJ, 756, 4

Ackermann, M., Ajello, M., Allafort, A., et al. 2012b, ApJ, 755, 22

Ankerst, M., Breunig, M. M., peter Kriegel, H., & Sander, J. 1999, in (ACM Press), 49–60

Atwood, W. B., Abdo, A. A., Ackermann, M., et al. 2009, ApJ, 697, 1071

Audit, E. & Hennebelle, P. 2005, A&A, 433, 1

Babusiaux, C., Fourtune-Ravard, C., Arenou, F., Sartoretti, P., & Gomez, A. 2016, in prep.

Bell, T. A., Roueff, E., Viti, S., & Williams, D. A. 2006, MNRAS, 371, 1865

Benjamin, R. A., Churchwell, E., Babler, B. L., et al. 2005, ApJ, 630, L149

Bignami, G. F., Boella, G., Burger, J. J., et al. 1975, Space Science Instrumentation, 1, 245

Brand, J. & Blitz, L. 1993, A&A, 275, 67

Brunthaler, A., Reid, M. J., Menten, K. M., et al. 2011, Astronomische Nachrichten, 332, 461

Burton, M. G., Braiding, C., Glueck, C., et al. 2013, PASA, 30, e044

Cardelli, J. A., Clayton, G. C., & Mathis, J. S. 1989, ApJ, 345, 245

Casandjian, J.-M. 2012, in American Institute of Physics Conference Series, Vol. 1505, American Institute of Physics Conference Series, ed. F. A. Aharonian, W. Hofmann, & F. M. Rieger, 37–45

Casandjian, J.-M. 2015, ApJ, 806, 240

Cecchi-Pestellini, C., Cacciola, A., Iatì, M. A., et al. 2010, MNRAS, 408, 535

Cesarsky, C. J., Casse, M., & Paul, J. A. 1977, A&A, 60, 139

Cesarsky, C. J. & Volk, H. J. 1978, A&A, 70, 367

Clemens, D. P. 1985, ApJ, 295, 422

Colombo, D., Rosolowsky, E., Ginsburg, A., Duarte-Cabral, A., & Hughes, A. 2015, MNRAS, 454, 2067

Cordes, J. M. & Lazio, T. J. W. 2002, ArXiv Astrophysics e-prints

Dame, T. M., Hartmann, D., & Thaddeus, P. 2001, ApJ, 547, 792

Dame, T. M. & Thaddeus, P. 2004, in Astronomical Society of the Pacific Conference Series, Vol. 317, Milky Way Surveys : The Structure and Evolution of our Galaxy, ed. D. Clemens, R. Shah, & T. Brainerd, 66

de Zeeuw, P. T., Hoogerwerf, R., de Bruijne, J. H. J., Brown, A. G. A., & Blaauw, A. 1999, AJ, 117, 354

Delhaye, J. 1965, in Galactic Structure, ed. A. Blaauw & M. Schmidt, 61

Dermer, C. D. 1986, A&A, 157, 223

Dermer, C. D. 2012, Physical Review Letters, 109, 091101

Dickey, J. M., McClure-Griffiths, N. M., Gaensler, B. M., & Green, A. J. 2003, ApJ, 585, 801

Dickey, J. M., Strasser, S., Gaensler, B. M., et al. 2009, ApJ, 693, 1250

Dobashi, K., Marshall, D. J., Shimoikura, T., & Bernard, J.-P. 2013, PASJ, 65

Draine, B. T. 2003, ARA&A, 41, 241

Draine, B. T. & Li, A. 2007, ApJ, 657, 810

Elyajouri, M., Monreal-Ibero, A., Remy, Q., & Lallement, R. 2016, ApJS, 225, 19

Ester, M., Kriegel, H. P., Sander, J., & Xu, X. 1996, in Proceedings of the Second International Conference on Knowledge Discovery and Data Mining, ed. E. Simoudis, J. Han, & U. M. Fayyad (AAAI Press), 226–231

Ewen, H. I. & Purcell, E. M. 1951, Nature, 168, 356

Fich, M., Blitz, L., & Stark, A. A. 1989, ApJ, 342, 272

Flagey, N., Noriega-Crespo, A., Boulanger, F., et al. 2009, ApJ, 701, 1450

Foster, J. B., Mandel, K. S., Pineda, J. E., et al. 2013, MNRAS, 428, 1606

Glover, S. C. O. & Mac Low, M.-M. 2011, MNRAS, 412, 337

Green, G. M., Schlafly, E. F., Finkbeiner, D. P., et al. 2014, ApJ, 783, 114

Green, G. M., Schlafly, E. F., Finkbeiner, D. P., et al. 2015, ApJ, 810, 25

Green, J. A., Caswell, J. L., McClure-Griffiths, N. M., et al. 2011, ApJ, 733, 27

Grenier, I. A., Black, J. H., & Strong, A. W. 2015, ARA&A, 53, 199

Grenier, I. A., Casandjian, J.-M., & Terrier, R. 2005, Science, 307, 1292

Heiles, C. & Troland, T. H. 2003a, ApJS, 145, 329

Heiles, C. & Troland, T. H. 2003b, ApJ, 586, 1067

Heyer, M. & Dame, T. M. 2015, ARA&A, 53, 583

Jones, A. P., Fanciullo, L., Köhler, M., et al. 2013, A&A, 558, A62

Juvela, M. & Montillaud, J. 2016, A&A, 585, A38

Kalberla, P. M. W., Burton, W. B., Hartmann, D., et al. 2005, A&A, 440, 775

Kalberla, P. M. W. & Haud, U. 2015, A&A, 578, A78

Kalberla, P. M. W., McClure-Griffiths, N. M., Pisano, D. J., et al. 2010, A&A, 521, A17

Kanbach, G., Bertsch, D. L., Favale, A., et al. 1989, Space Sci. Rev., 49, 69

Kerr, F. J. & Lynden-Bell, D. 1986, MNRAS, 221, 1023

Kim, C.-G., Ostriker, E. C., & Kim, W.-T. 2014, ApJ, 786, 64

Köhler, M., Ysard, N., & Jones, A. P. 2015, A&A, 579, A15

Lallement, R., Vergely, J.-L., Valette, B., et al. 2014, A&A, 561, A91

Lebrun, F., Bennett, K., Bignami, G. F., et al. 1983, ApJ, 274, 231

Lebrun, F. & Paul, J. A. 1978, A&A, 65, 187

Levine, E. S., Blitz, L., & Heiles, C. 2006, Science, 312, 1773

Levrier, F., Le Petit, F., Hennebelle, P., et al. 2012, A&A, 544, A22

Liszt, H. 2001, A&A, 371, 698

Liszt, H. S., Pety, J., & Lucas, R. 2010, A&A, 518, A45

Marshall, D. J., Montier, L. A., Ristorcelli, I., et al. 2015, Mem. Soc. Astron. Italiana, 86, 589

Marshall, D. J., Robin, A. C., Reylé, C., Schultheis, M., & Picaud, S. 2006, A&A, 453, 635

Martin, P. G., Roy, A., Bontemps, S., et al. 2012, ApJ, 751, 28

McClure-Griffiths, N. M. & Dickey, J. M. 2007, ApJ, 671, 427

McKee, C. F. & Ostriker, J. P. 1977, ApJ, 218, 148

Mizuno, A. & Fukui, Y. 2004, in Astronomical Society of the Pacific Conference Series, Vol. 317, Milky Way Surveys : The Structure and Evolution of our Galaxy, ed. D. Clemens, R. Shah, & T. Brainerd, 59

Morris, M. & Rickard, L. J. 1982, ARA&A, 20, 517

Morrison, P. 1958, Il Nuovo Cimento (1955-1965), 7, 858

Muller, C. A. & Oort, J. H. 1951, Nature, 168, 357

Murray, C. E., Stanimirović, S., Goss, W. M., et al. 2015, ApJ, 804, 89

Oort, J. H. & Muller, C. A. 1952, Monthly Notes of the Astronomical Society of South Africa, 11, 65

Paradis, D., Dobashi, K., Shimoikura, T., et al. 2012, A&A, 543, A103

Peek, J. E. G., Heiles, C., Douglas, K. A., et al. 2011, ApJS, 194, 20

Perrot, C. A. & Grenier, I. A. 2003, A&A, 404, 519

Persic, M., Salucci, P., & Stel, F. 1996, MNRAS, 281, 27

Planck and Fermi Collaborations. 2015, A&A, 582, A31

Planck Collaboration. 2011, A&A, 536, A19

Planck Collaboration. 2014a, A&A, 571, A11

Planck Collaboration. 2014b, A&A, 571, A13

Planck Collaboration. 2014c, A&A, 566, A55

Reid, M. J., Menten, K. M., Brunthaler, A., et al. 2014, ApJ, 783, 130

Renault-Tinacci, N., Grenier, I. A., Harding, A. K., et al. 2016 in prep., (Fermi internal review)

Robin, A. C., Reylé, C., Derrière, S., & Picaud, S. 2003, A&A, 409, 523

Rosolowsky, E. & Leroy, A. 2006, PASP, 118, 590

Rosolowsky, E. W., Pineda, J. E., Kauffmann, J., & Goodman, A. A. 2008, ApJ, 679, 1338

Rowles, J. & Froebrich, D. 2009, MNRAS, 395, 1640

Roy, A., Martin, P. G., Polychroni, D., et al. 2013a, ApJ, 763, 55

Roy, N., Kanekar, N., Braun, R., & Chengalur, J. N. 2013b, MNRAS, 436, 2352

Saury, E., Miville-Deschênes, M.-A., Hennebelle, P., Audit, E., & Schmidt, W. 2014, A&A, 567, A16

Schlafly, E. F., Green, G., Finkbeiner, D. P., et al. 2014a, ApJ, 789, 15

Schlafly, E. F., Green, G., Finkbeiner, D. P., et al. 2014b, ApJ, 786, 29

Schlafly, E. F., Meisner, A. M., Stutz, A. M., et al. 2016, ApJ, 821, 78

Schlegel, D. J., Finkbeiner, D. P., & Davis, M. 1998, ApJ, 500, 525

Skilling, J. & Strong, A. W. 1976, A&A, 53, 253

Smith, R. J., Glover, S. C. O., Clark, P. C., Klessen, R. S., & Springel, V. 2014, MNRAS, 441, 1628

Sonnentrucker, P., Welty, D. E., Thorburn, J. A., & York, D. G. 2007, ApJS, 168, 58

Stepnik, B., Abergel, A., Bernard, J.-P., et al. 2003, A&A, 398, 551

Sullivan, W. 1982, Classics in Radio Astronomy, 1st edn., Studies in the History of Modern Science 10 (Springer Netherlands)

Trumpler, R. J. 1930, PASP, 42, 214

van de Hulst, H. C. 1945, Ned. tijd. natuurkunde, 11, 210

van de Hulst, H. C., Muller, C. A., & Oort, J. H. 1954, Bull. Astron. Inst. Netherlands, 12, 117 van Dishoeck, E. F. & Black, J. H. 1988, ApJ, 334, 771

van Leeuwen, F. 2007, A&A, 474, 653

Wainscoat, R. J., Cohen, M., Volk, K., Walker, H. J., & Schwartz, D. E. 1992, ApJS, 83, 111

Williams, J. P., de Geus, E. J., & Blitz, L. 1994, ApJ, 428, 693

Wilson, R. W., Jefferts, K. B., & Penzias, A. A. 1970, ApJ, 161, L43

Winkel, B., Kerp, J., Flöer, L., et al. 2016, A&A, 585, A41

Wolfire, M. G., Hollenbach, D., & McKee, C. F. 2010, ApJ, 716, 1191

Wolfire, M. G., McKee, C. F., Hollenbach, D., & Tielens, A. G. G. M. 2003, ApJ, 587, 278

Ysard, N., Abergel, A., Ristorcelli, I., et al. 2013, A&A, 559, A133

Zasowski, G., Ménard, B., Bizyaev, D., et al. 2015, ApJ, 798, 35

A Catalogue de la DIB à 1.5273 μm dans les spectres des étoiles de calibration APOGEE

The Astrophysical Journal Supplement Series, 225:19 (16pp), 2016 August doi:10.3847/0067-0049/225/2/19

A CATALOG OF 1.5273 μm DIFFUSE INTERSTELLAR BANDS BASED ON APOGEE HOT TELLURIC CALIBRATORS

M. Elyajouri[1], A. Monreal-Ibero[1], Q. Remy[2], and R. Lallement[1]
[1] GEPI Observatoire de Paris, PSL Research University, CNRS, Université Paris-Diderot, Sorbonne Paris-Cité, Place Jules Janssen, F-92195 Meudon, France; meriem.el-yajouri@obspm.fr
[2] Laboratoire AIM, IRFU/Service d'Astrophysique CEA/DSM CNRS Universite Paris Diderot, CEA-Saclay, F-91191 Gif-sur-Yvette, France

Received 2016 February 19; revised 2016 April 26; accepted 2016 April 26; published 2016 August 5

ABSTRACT

High resolution stellar spectroscopic surveys provide massive amounts of diffuse interstellar bands (DIBs) measurements. Data can be used to study the distribution of the DIB carriers and those environmental conditions that favor their formation. In parallel, recent studies have also proved that DIBs extracted from stellar spectra constitute new tools for building the 3D structure of the Galactic interstellar medium (ISM). The amount of details on the structure depends directly on the quantity of available lines of sight. Therefore there is a need to construct databases of high-quality DIB measurements as large as possible. We aim at providing the community with a catalog of high-quality measurements of the 1.5273 μm DIB toward a large fraction of the Apache Point Observatory Galactic Evolution Experiment (APOGEE) hot stars observed to correct for the telluric absorption and not used for ISM studies so far. This catalog would complement the extensive database recently extracted from the APOGEE observations and used for 3D ISM mapping. We devised a method to fit the stellar continuum of the hot calibration stars and extracted the DIB from the normalized spectrum. Severe selection criteria based on the absorption characteristics are applied to the results. In particular limiting constraints on the DIB widths and Doppler shifts are deduced from the H I 21 cm measurements, following a new technique of decomposition of the emission spectra. From ∼16,000 available *hot telluric* spectra we have extracted ∼6700 DIB measurements and their associated uncertainties. The statistical properties of the extracted absorptions are examined and our selection criteria are shown to provide a robust dataset. The resulting catalog contains the DIB total equivalent widths, central wavelengths and widths. We briefly illustrate its potential use for the stellar and interstellar communities.

Key words: dust, extinction – ISM: lines and bands

Supporting material: machine-readable table

1. INTRODUCTION

The spectra of stars viewed through one or several interstellar clouds display a plethora of relatively weak non-stellar absorption features of unknown origin, the so-called diffuse interstellar bands (DIBs, see Herbig 1995; Sarre 2006, for a review). First DIBs were discovered around the early 20's by Heger (see McCall & Griffin 2013, for a review of the history of the DIBs discovery) and their interstellar origin was established in the 30's (Merrill 1934, 1936). Today, more than 400 optical DIBs (400–900 nm) are known (e.g., Jenniskens & Desert 1994; Hobbs et al. 2009). The first near-infrared (NIR) DIB was discovered by Joblin et al. (1990). Currently, ∼25 NIR DIBs have been identified (Foing & Ehrenfreund 1994; Geballe et al. 2011; Cox et al. 2014; Hamano et al. 2015, 2016), including the strong band at 1.318 μm. NIR DIBs are particularly useful since they allow to make use of highly reddened target stars and explore the densest areas of the interstellar medium (ISM). Most measured DIBs have a Galactic origin. Still, they have also been detected in the Magellanic clouds, M31 and M33 (Ehrenfreund et al. 2002; Welty et al. 2006; Cordiner et al. 2008a, 2008b, 2011; van Loon et al. 2013) and in a few line of sights toward e.g., starburst galaxies or in SNe Ia spectra (Sollerman et al. 2005; Cox & Patat 2008; Heckman & Lehnert 2000; Phillips et al. 2013). Recently a DIB gradient was established for the first time in a 160 Mpc distant galaxy (Monreal-Ibero et al. 2015).

In spite of the number and ubiquity of DIBs, the carrier of most DIBs (i.e., the agents that originate these features) remains unidentified. Carbon is involved in most of the proposed candidates and among them we can find hydrocarbon chains (e.g., Maier et al. 2004), polycyclic aromatic hydrocarbons (PAHs, e.g., Crawford et al. 1985; Leger & D'Hendecourt 1985; van der Zwet & Allamandola 1985; Salama et al. 1996; Kokkin et al. 2008), and/or fullerenes (Sassara et al. 2001; Iglesias-Groth 2007). See Cox (2011) for a recent review on the DIB-PAH hypothesis. Today the situation is particularly promising in this regard, since the carrier for two DIBs at 9577 and 9632 Å was recently for the first time unequivocally identified with C_{60}^{+} (Campbell et al. 2015), confirming earlier results of Foing & Ehrenfreund (1994). C_{60}^{+} was also detected in emission toward NGC 7023 by Berné et al. (2013), and C60 and C70 have also been identified in emission in young planetary nebulae (Cami et al. 2010). Besides, first insights on the physical properties of the environments that are favorable or not for DIB formation are being obtained from high-quality absorption data (Cox & Spaans 2006; Vos et al. 2011; Cordiner et al. 2013).

An interesting property of these features is that they are correlated with the amount of interstellar matter along the line of sight. Various correlations with neutral hydrogen, extinction and interstellar Na I D and Ca H&K lines have been established (e.g., Herbig 1993; Friedman et al. 2011). As a result, DIBs can be used to trace the structure of the ISM in the same way than others species, and they even offer certain advantages when used instead of (or in addition to) other tracers. For example, given their intrinsic weakness, they are ideal tracers in conditions where other features (e.g., Na I D) saturate, like very dense molecular clouds or regions seen through a large amount of extinction. Encouraged by this correlation between DIBs and IS matter, several teams have recently presented works that made use of the information provided by the different spectroscopic surveys to study the Galactic ISM structure and extinction in 2D or 3D by using the strength of different DIBs as a proxy (e.g., Kos et al. 2014; Yuan et al. 2014; Baron et al. 2015; Lan et al. 2015; Puspitarini et al. 2015).

In the near-IR, the 1.5273 μm band (hereafter, we will also use 15273 Å and refer to vacuum wavelengths) falls in the spectral range observed by the Apache Point Observatory Galactic Evolution Experiment (APOGEE, Wilson et al. 2010; Majewski 2012), and this high resolution, high signal, massive survey was used by Zasowski et al. (2015) to trace the 3D structure of the ISM at the large scale based on an unprecedented number of extracted NIR DIBs. Such pioneering work has demonstrated the potential of these methods and consequently that increasing the number of measurements will result in more accurate mapping.

In this article we present a work based on a fraction of the spectra of the most recent APOGEE's target sample made publicly available. The entire dataset comprises ~160,000 stars, most of them cool K and M giants ($T_{\rm eff}\sim$ 3500–5000 K). As part of the observing strategy and calibration plan of the survey, ~17,000 *hot telluric* stars were also observed (see details in Section 2). By definition these are the bluest stars on a given pointing, and thus, most of the times early (i.e., O- to F-type) stars. As such, their almost featureless continua make them ideal targets to extract the information associated to the 1.5273 μm DIB. Our work has been focused on these calibration stars. We have devised a method to fit their stellar continua and we present the resulting catalog of DIB measurements extracted from their spectra. This catalog complements the existing extensive catalog of Zasowski et al. (2015) based on the APOGEE main, cool targets.

The paper is structured as follows: Section 2 contains the technical aspects regarding the data used in this work. Section 3 describes the methods used for continuum fitting and DIB parameter extraction, whereas a detailed description of our criteria to validate a DIB detection and estimate uncertainties is included in Section 4. Section 5 describes the resulting catalog and its validation. Section 6 illustrates some potential applications. Conclusions are summarized in Section 7.

2. THE DATA

2.1. APOGEE Overview

The SDSS-III APOGEE is one of the four Sloan Digital Sky Survey III (SDSS-III, Aihara et al. 2011; Eisenstein et al. 2011) experiments operated from 2011 to 2014. APOGEE uses a 300-fiber multi-object spectrograph working in the near-infrared (H-band, 1.51–1.70 μm) at high spectral resolution ($R\sim$ 22,500, Wilson et al. 2010). The spectrograph is attached via a fiber optic train to the SDSS 2.5 m telescope at Apache Point Observatory (Gunn et al. 2006). Since the effects of extinction at near-IR wavelengths are reduced, APOGEE has a strong potential to explore dust obscured regions of the Galaxy that are beyond the reach of optical surveys, in particular the inner Galaxy and bulge.

In a given observation, about 230 (out of 300) fibers are allocated for scientific targets selected from the source catalog the Two Micron All Sky Survey (2MASS, Skrutskie et al. 2006). The ~160,000 selected scientific targets are distributed across all Galactic environments. Most of them are red giant stars but there are also special subsamples including stars with measured parameters and abundances from other spectroscopic studies, cluster members, etc. associated to several APOGEE ancillary science programs (see Zasowski et al. 2013, for a detailed description of the different target classes).

In addition to the science targets, a sample of hot stars, also called telluric standards stars (TSSs) or *hot telluric* calibrators are observed (35/300 fibers) to allow for the correction of the telluric absorption lines (see below). Finally, the remaining ~35 fibers are allocated for observing blank sky positions to enable sky emission subtraction.

2.2. The APOGEE Telluric Standard Stars

The total number of TSSs in the APOGEE survey is nearly ~17,000. Ideally, for a good telluric correction one would like to have bright O, B and A stars because of their featureless spectra. Therefore, to maximize the chances of observing stars of these types, the TSSs were selected as the bluest stars on a given plate having a magnitude in the range $5.5\leqslant H\leqslant 11$ and ensuring a uniform distribution over the plate (see Zasowski et al. 2013, for details of TSS selection). Their spectra are used to adjust in an exquisite way the atmospheric transmission and its variability throughout the field, a transmission that is used to remove the telluric lines in all observed targets.

It is important to note that the TSSs are corrected for telluric absorption lines in the same way as the science targets. In other words, they benefit from the correction tool they have themselves produced. An interesting point about these stars is that, in addition to their use as tools to decontaminate the telluric absorption, they constitute a highly valuable dataset for ISM studies since their smooth continua are ideal to extract the information associated with DIBs. Here we focus on the strongest 1.5273 μm DIB. Work is in progress on the weaker absorption bands.

The TSS can easily be identified in the APOGEE data products by means of the `APOGEE_TARGET2` bitmask since all these stars are flagged as `APOGEE_TELLURIC` (bit 9).

2.3. Used Information Extracted from the APOGEE Archive

This work is based on the products from the SDSS data release 12 (DR12, Alam et al. 2015). This release includes all the data taken between 2011 April and 2014 July. The spectra can be downloaded from the Science Archive Server (SAS) as described on the data access page.[3] There are three different types of reduced spectra available (see Holtzman et al. 2015; Nidever et al. 2015). Here, we use the calibrated, well-sampled, and pseudo continuum-normalized combined 1D spectra. These are available as fits files with four separate extensions: the first one carries the information about the star and the derived stellar parameters, the second one contains the observed spectra, the third one saves the error pixels and the

---

[3] http://data.sdss3.org/sas/dr12/apogee/spectro/redux/r5/stars/l25_6d/v603/

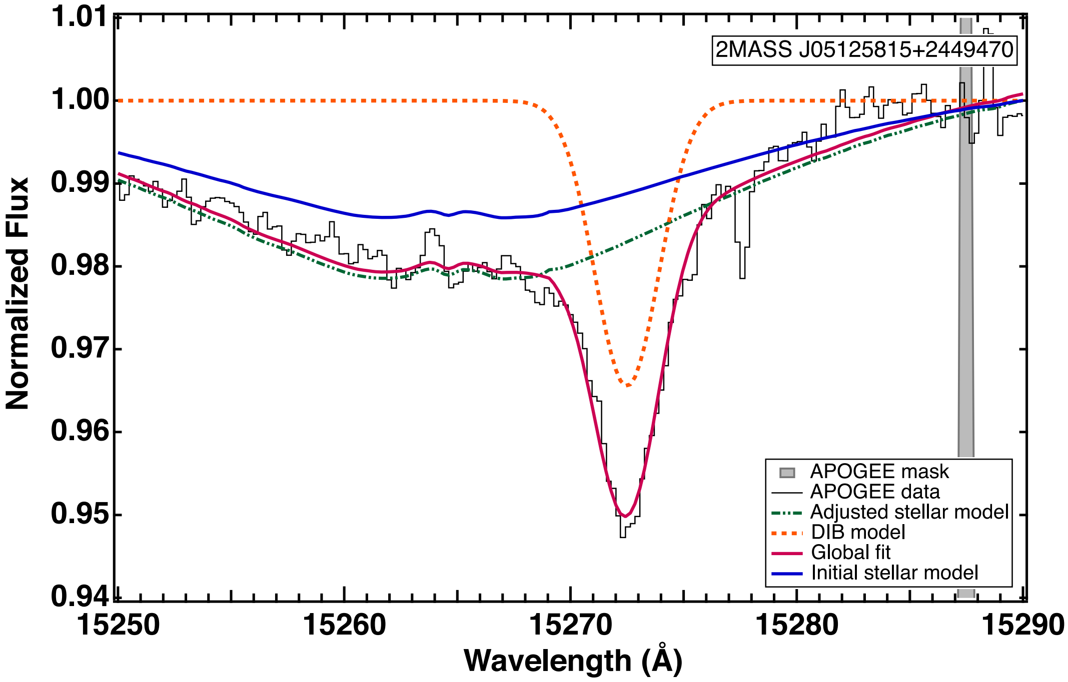

Figure 1. Example illustrating our fitting method. Data as provided by the APOGEE survey are shown in black while the final stellar+DIB modeled spectrum appears in magenta. The initial stellar model provided by APOGEE and the model obtained after application of the scaling factor α are shown in solid blue and dash–dot green lines, respectively. The DIB absorption alone is represented with a dashed orange line. A gray band in the red part of the spectrum shows an example of masked region.

fourth one has a state-of-the-art modeled spectrum S_λ adjusted to the observed one (García Pérez et al. 2016). The modeled spectra are interpolated from a grid of spectra, itself based on a large sample of model atmospheres (Mészáros et al. 2012). These modeled spectra are optimized for stars at temperature $3\,800\,\mathrm{K} < T < 5250\,\mathrm{K}$ (Ahn et al. 2014). The TSSs are a priori hotter, and therefore as shown below, small adjustments to the provided modeled spectra were needed.

All the spectra are sampled at same rest wavelength pixel scale, with a constant dispersion in log λ, as

$$\log \lambda_i = 4.179 + 6 \times 10^{-6}\, i \tag{1}$$

with 8575 total pixels ($i = 0$–8574), giving a rest wavelength range of 15100.8–16999.8 Å (Nidever et al. 2015).

We also use the table that summarizes all the parameters derived from the APOGEE spectra (for DR12, allStar-v603.fits), including for each observed individual star its mean barycentric radial velocity, the standard deviation of the mean velocity, the mean ASPCAP parameters and abundances as derived from the combined spectra, and a compilation of ancillary targeting data (see Holtzman et al. 2015; Nidever et al. 2015, for a full description of the data in these files).

3. DATA ANALYSIS

The aim of this work is analyzing the series of ~16,000 DR12 TSS spectra than can be downloaded from the APOGEE site to determine the presence (or absence) of the DIB at 15273 Å and measuring its equivalent width (EW) in case of positive detection. Given the volume of data, this needs to be done with as less as possible human intervention. For that, we took as starting point the methodology presented by Puspitarini et al. (2013) for optical spectra, and adapted it to the peculiarities of APOGEE spectra. At the end, we had a fully automated DIB extraction method able to measure DIB EWs without any user interaction during the fit. The code was developed using the IGOR PRO environment.[4] Note that the reduced pseudo-normalized spectra of DR12 are corrected from telluric lines contamination. Thus, no telluric correction is needed. In the following, we give the details of our fitting technique, we explain how we extracted the EW of the DIB and how we estimated their associated uncertainties.

3.1. Profile Fitting

We fit each TSS spectrum to a model made out of the product of several components as follows:

$$M_\lambda = [S_\lambda]^\alpha \times \mathrm{DIB}[\sigma, \lambda, D] \times (1 + [A] \times \lambda) \tag{2}$$

with:

1. $[S_\lambda]^\alpha$, *an adjusted stellar spectrum*: S_λ is the initial stellar model provided by the APOGEE project. As we mentioned above, this model is not optimized for the TSSs that are hotter than the main targets. Therefore, even if the velocity of each target star was accurately determined and the global shape of the spectrum was most of the times adequate, the depth of the stellar atmospheric lines was not properly estimated (see Figure 1). We included a scaling factor (α) in order to take this into account and to adjust the model depth to the data.
2. *DIB*$[\sigma, \lambda_c, D]$, *the DIB profile*: It was modeled as a Gaussian function with three free parameters associated to its width (σ), central wavelength (λ_c) and depth (D).

---

[4] http://www.wavemetrics.com

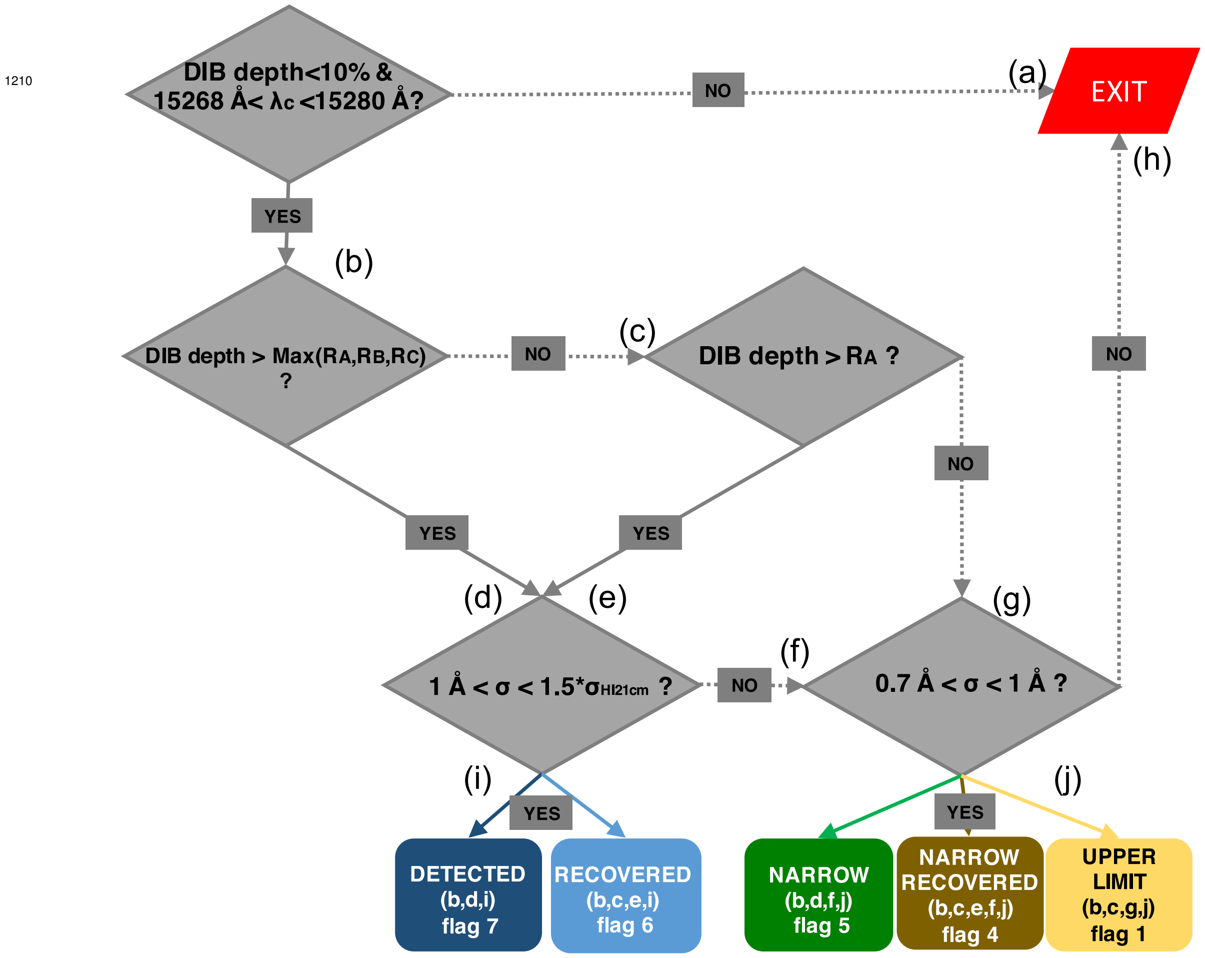

Figure 2. Flowchart compiling our decision criteria to create our catalog. Any spectrum able to reach the bottom part of the flow has a positive DIB detection. The path followed by a given spectrum to be classified has been indicated in the corresponding box with small letters. Flags numbers in each box at bottom are detailed in Section 5 and included in the catalog.

3. $(1 + [A] \times \lambda)$, *a local continuum*: this was a simple 1° polynomial introduced to model as closely as possible the continuum around the DIB.

We selected a pre-defined spectral range for the fit restricted to the vicinity of the DIB [15260–15290] Å to determine the above coefficients α, σ, λ_c, D and A. Note that this range was large enough to ensure an adequate sampling of the neighboring Bracket 19-4 stellar line at 1.52647 μm. Errors provided by APOGEE were used to mask those spectral ranges affected by artifacts due to imperfect sky emission correction or other sources of uncertainty. We use the Levenberg–Marquardt algorithm implemented in IGOR PRO to compute the coefficients that minimize the chi-square χ^2. An example illustrating our fitting procedure is shown in Figure 1.

3.2. DIB EW and Error Estimates

In the following, we explain how we extracted the DIB EW from our fits and how we estimated the uncertainties associated to each of the parameters presented in the catalog.

1. *Computation of the DIB EW:* Since none of the previous or present observations reveals any asymmetry of the 15273 Å DIB, and for our sightlines the linear regime prevails, we assume that the actual DIB absorption has a shape that is similar to the mono-Gaussian model. We also neglect the small departures from a Gaussian that result from multiple cloud superimposition that is small compared to other sources of uncertainties. Subsequently, assuming that the continuum $I_0(\lambda)$ is reasonably fitted, the DIB EW is the area of the fitted Gaussian and can be simply analytically derived from its parameters as the product of the model DIB's depth D by the coefficient σ:

$$\mathrm{EW} = \int_{\mathrm{DIB}} \frac{I_0 - I_\lambda}{I_0}\, d\lambda = \sqrt{2\pi}\; D\sigma \tag{3}$$

where $I(\lambda)$ is the observed spectrum.

2. *Computation of standard deviations in residuals:* We calculated the standard deviation of the fit residuals, *data-model*, in a region close to the DIB (region A = [λ_c−10, λ_c + 10] Å). In addition to this, we performed a second fit using the same function as the one presented in Equation (2) but over the whole spectral range covered

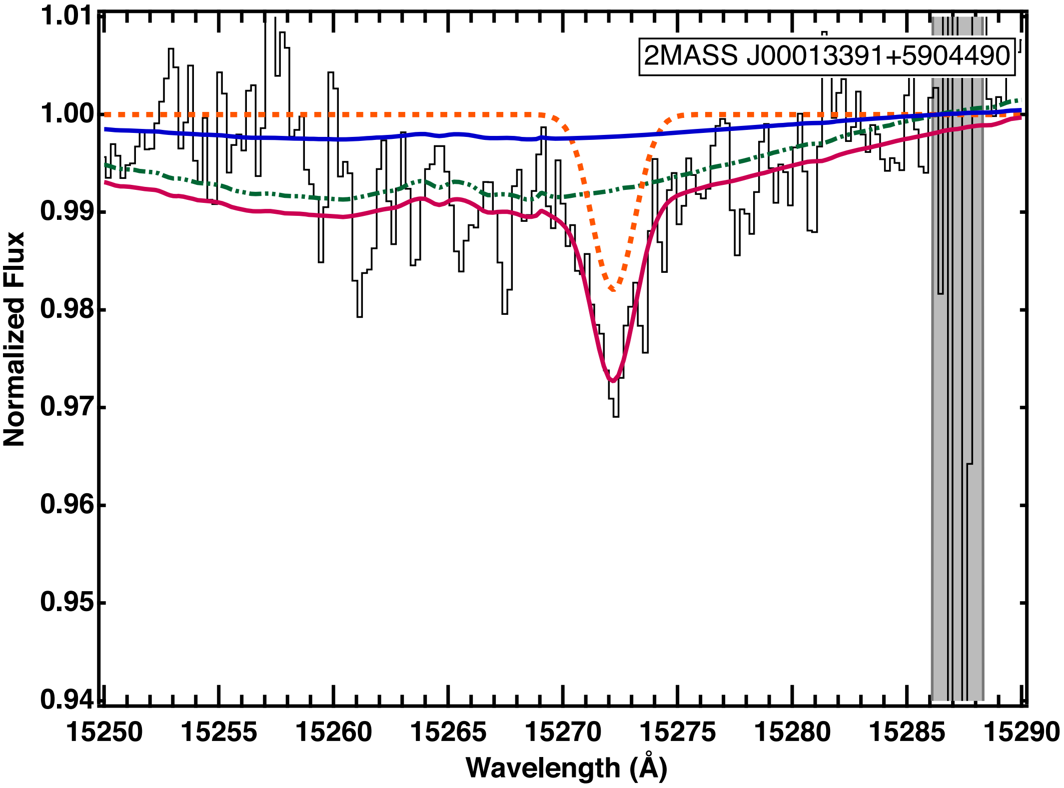

Figure 3. Example of detection of narrow DIB (0.7 Å < σ < 1 Å): 2MASS J00013391+5904490 with $\sigma = 0.9 \pm 0.1$ Å, $\lambda_c = 15272.2 \pm 0.1$ Å, and EW $= 0.041 \pm 0.021$ Å. Color and symbol code is as in Figure 1.

by APOGEE. As a matter of fact, we found that the first and third terms of Equation (2) are good enough to represent continuum and Bracket lines in the entire APOGEE spectral region. For this fit the DIB term in the equation has the same restrictions as in the local fit. The DIB is fitted to ensure an optimum placement of the continuum in the DIB region and subsequently everywhere. As a matter of fact, omitting the DIB could bias the continuum in its spectral region and react on the whole fit. The residuals from this additional fit were used to obtain two additional measurements of the standard deviation. The first one was calculated over a *clean* (i.e., free from DIB absorption, strong stellar lines and telluric residuals) spectral range (region B = [15892–15959] Å). The second one (region C = [15200–15250] Å) corresponds to a region relatively close to the DIB (and also free of DIB) and potentially contaminated by stellar residuals.

Hereafter, we will call the standard deviation R for all the three regions, R_A, R_B and R_C. These were used for the selection criteria discussed in Section 4. Also, the standard deviation R_A in the narrow spectral range around the DIB is used below to estimate the uncertainty on the DIB EW.

3. *Uncertainties on the DIB central wavelength and width:* The IGOR algorithm uses data and fitted model to evaluate the *data-model* standard deviation in the spectral range used for the fit, within the implicit assumption that the fitting function is ideally adapted to the data and the data are characterized by random Gaussian noise. If there are telluric line residuals or any other artifacts that amplify the signal fluctuations, the estimated standard deviation is correspondingly increased and treated as random noise. Based on the standard deviation and the mutual influence of the parameters the algorithm estimates one sigma errors on each parameter. We use these error estimates on both the central wavelength and the width.
4. *Uncertainty on the DIB EW:* For this quantity we estimated the error in a very conservative way in order to take into account the departures from Gaussian noise and the ideal fitting function, as well as potential subsequent misplacements of the continuum level. As a matter of fact in a number of cases telluric absorption or sky emission correction residuals are present and for a number of targets the stellar line shapes are not perfectly fitted. This may result in slight displacements of the fitted continuum that do not impact the line center and impact the width in a negligible way but may impact the depth. For the most conservative estimate of the error we used the standard deviation of region A, coupled to the maximum DIB width deduced for each sightline from H I 21 cm data (see Section 4). The maximum error was estimated as the EW of a Gaussian with the maximum width of the H I 21 cm line and a depth equal to R_A:

$$\mathrm{err(EW)} = \sqrt{2\pi}\ R_A\ \sigma_{\mathrm{H\,I\,21\,cm}}. \tag{4}$$

We checked that this conservative error is appropriate to all types of spectra and data quality, including those cases where there are clear residuals linked to stellar or telluric lines. Figure 9 shows the estimated error as a function of the EW for all targets of the catalog. It can be seen from the figure that due to our method based on H i, for the same EW the error is significantly larger in directions where the ISM radial velocity range is very large, mainly here at Galactic longitudes smaller than 70°. This confirms that our quoted values are very conservative.

4. VALIDATION CRITERIA

4.1. Selection of Fitted Absorptions

We applied a series of tests to the fitted Gaussian absorptions based on the fitted parameters, the signal quality in the DIB region and elsewhere, and finally the lines of sight (LOS) direction and the corresponding Galactic gas. The series of tests is schematically represented in Figure 2.

1. *First global test*: the first selective test eliminates those absorptions that are deeper than 10% of the continuum (arrow (a) in Figure 2). Those depths are extremely unlikely for Galactic DIBs and especially for the TSSs that are nearby. Indeed, we checked a posteriori that all those cases correspond to spurious detections (stellar lines for the coolest or most metallic objects, unusually strong telluric residuals, etc.). We also eliminated simultaneously absorptions centered outside the spectral range [15268–15280] Å. In the red, the corresponding large Doppler shifts of $\geqslant +137$ km s^{-1} are unrealistic for the nearby ISM. In the blue, the test excludes a tiny fraction of fits with unrealistically high negative Doppler shifts caused by a stellar line (see the histogram in Figure 5).
2. *Test on the absorption depth*: as a second test for the selected targets (the arrow (b)), we compared the depth of the fitted absorption line with the standard deviation on the residuals. This comparison was done in a one- or two-step process. We first compare the absorption depth with the maximum of the three standard deviations R_A, R_B and R_C described in Section 3.2. If it is larger (arrow (d)), then start directly the tests on the width. If the depth is smaller that this maximum, i.e., if the spectrum is globally too noisy to detect the DIB (the arrow (c)) or the DIB is very shallow, we also compared the absorption depth with the local standard deviation R_A only. This second step allows to detect those spectra that are noisy in those spectral ranges far from the DIB but that have a good enough signal to noise in the DIB neighborhood to ensure a detection, i.e., the use of the maximum of the three R_A, R_B and R_C deviations is too restrictive. Absorptions that pass successfully the test (arrow (e)) are then examined for their widths in the same way than the previous ones (arrow(d)) but are flagged differently. The difference in the flags serves to evaluate the quality of the spectrum and identify those targets for which models have a shape incompatible with the measurements outside the DIB region. They will be visually inspected one by one. Absorptions who still appear too shallow (arrow (g)) are examined in a different way.
3. *Criterion on the width in case of shallow absorptions:* as a third test for those absorptions that appear small with respect to the noise, both locally and in the three spectral regions (i.e., from arrow (g)), we selected the DIBs with a width, σ, within predefined limits. The lower limit of 0.7 Å is deduced from the results of Zasowski et al. (2015) and in particular from the σ histogram of the whole APOGEE dataset shown in their Figure 6. This histogram shows that a very abrupt decrease occurs at $\simeq$1 Å implying that the intrinsic DIB width maybe as small as this value. Taking into account our typical uncertainties on the DIB width, err(σ) $\simeq$ 0.35, we finally imposed a lower limit on the width of 0.7 Å. This criterion has been checked a posteriori to eliminate spurious detections associated to bad pixels or telluric residuals, and simultaneously to keep actual detections of narrow DIBs. A typical example of such narrow absorptions that pass successfully the test is shown in Figure 3. It can be seen from the figure that it looks convincingly like an actual DIB. The upper limit of 1.0 Å is chosen for the following reasons: for those absorptions that are very shallow (arrow (g)), this maximum value eliminates flat and elongated features of uncertain origin. Conversely, those very shallow absorptions that are reasonably wide pass the test and are falling in the *upper limit* category (yellow box in Figure 2). For those absorptions that are deeper and correspond to arrow (f), this maximum value will result in definitely rejecting those features that are broader than $1.5\sigma_{\rm H\,I\,21\,cm}$ (see below).
4. *Limits on the width σ based on H i 21 cm emission spectra*: For all absorptions that exceed the noise level, either globally or locally (arrows (d) and (e)), a subsequent test on the DIB width is performed based on radio 21 cm H i spectra. As a matter of fact the velocity range for some fitted absorptions is clearly not compatible with the velocity distribution in the Galaxy. Such unrealistic absorption widths are caused by an improper modeling of the stellar lines, residuals of telluric lines, or a locally increased level of noise. In order to eliminate these spurious or biased detections from the catalog we added the following constraint on the DIB width based on the radial velocities of the atomic hydrogen gas. Indeed as the H i is the most common and widespread form of gas in the galaxy, its extent in velocity should encompass the velocity extent of the DIB, as verified in previous DIB measurements (see, e.g., Puspitarini et al. 2015; Zasowski et al. 2015).

We estimated the maximal radial velocity width of the DIB by constructing a *virtual*, composite DIB based on the H i spectra. To do so we used the results of the H i line decomposition method presented in Planck et al. (2015). We briefly recall the principle of this decomposition. The first step is to detect the significant lines in the brightness temperature $T_B(v)$ spectra of the LAB Survey (Kalberla et al. 2005). We measured the dispersion in temperature, $T_{\rm rms}$, outside the bands with significant emission. In order to limit the number of false detections caused by strong noise fluctuation we clipped the data to zeros except if $T_B(v) > T_{\rm rms}$ in 3 channels (3 km s^{-1}). Then, using the 5-point-Lagrangian differentiation twice, we computed the curvature d^2T_B/dv^2 in each channel. Lines are detected as negative minima in d^2T_B/dv^2. False detections triggered by the edges of the clipped regions were eliminated. Then each spectrum is fitted by a sum of pseudo-Voigt functions, one for each detected line. The pseudo-Voigt

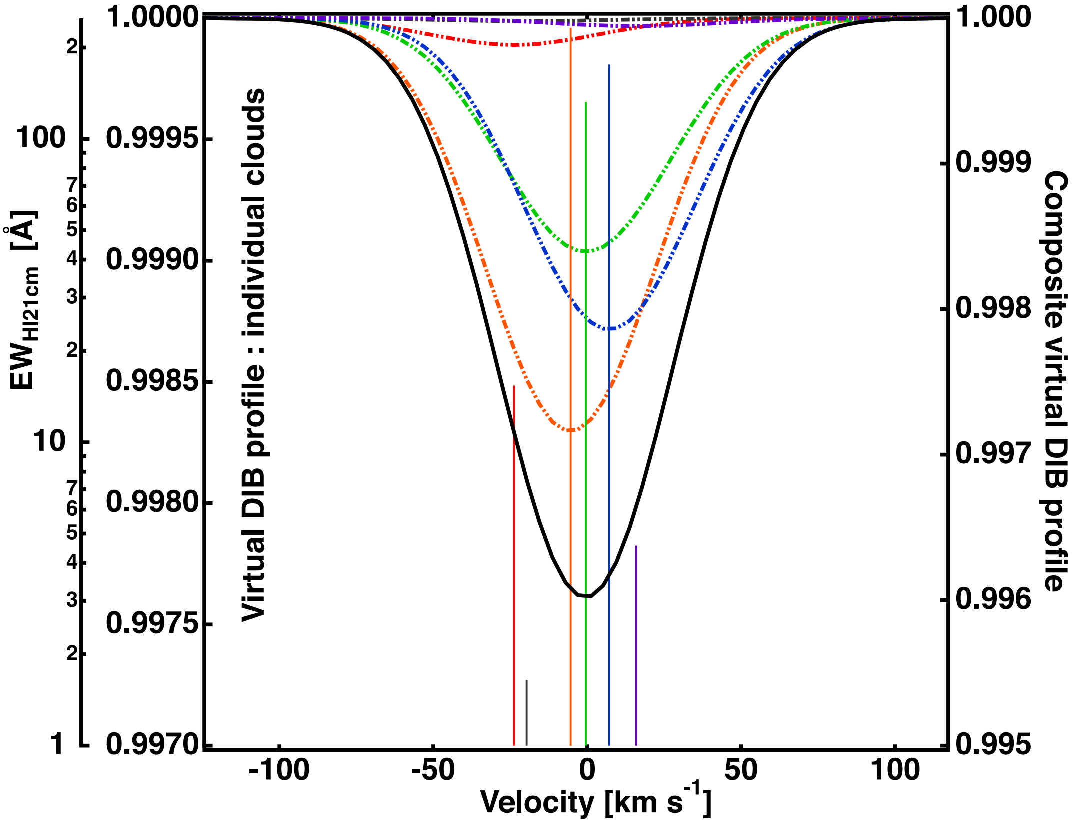

Figure 4. Example illustrating our construction of a *virtual* DIB for a typical LOS with 6 H I clouds. Vertical lines in different colors mark the strength and velocity of the 6 individual H I 21 cm components. The corresponding individual Gaussians for the synthetic DIBs are shown using the same colors. The function representing the total *virtual* DIB through the H I disk is plotted in black. Note that for a better visualization, the scales for the total DIB and individual components are different.

Table 1
Summary with Statistics of the Selected Sample

	λ_c (Å)	σ (Å)	EW (mÅ)
Mean	15272.42	1.50	78
Std Dev	1.13	0.40	49
Median	15272.43	1.47	69

function is defined as

$$\mathrm{PV} = \eta \mathrm{L} + (1 - \eta)\mathrm{G} \tag{5}$$

with $0 < \eta < 1$ the shape factor, L a Lorentzian, and G a Gaussian respectively defined as

$$L = \frac{h}{1 + \left(\frac{v - v_0}{\sigma}\right)^2} \tag{6}$$

and,

$$G = h \exp\left(\frac{v - v_0}{\sigma}\right)^2 \tag{7}$$

where v_0 is the position of the line, σ the width and h the height parameter.

In order to take into account the detection uncertainties, the position of the line v_0 is allowed to vary in a ±4 km s^{-1} range around the initial position. For each detected line the free parameters η, h, σ, and v_0 are fitted by means of a χ^2 minimization.

For each LOS the computed H I decomposition is used to construct a *virtual* DIB, the one that would be measured in the spectrum of a star located beyond all the H I clouds, i.e., at the periphery of the Galactic H I disk. To do so, each H I component is associated to a DIB that has a width $\sigma_0 = 1.4$ Å and a radial velocity equal to the one of the H I line. The chosen width σ_0 corresponds to an upper limit on the intrinsic DIB width that can be derived from the Figure 6 of Zasowski et al. (2015). To convert the H I line into a DIB EW we use the following relationships:

(i) The H I column density is calculated in the optically thin limit:

$$N_{\mathrm{H\,I}} = 1.823 \times 10^{18} \int T_b(v)dv \tag{8}$$

where $T_b(v)$ is the the 21 cm line brightness temperature at radial velocity v.

(ii) The H I column density is transformed into reddening using the $N_{\mathrm{H\,I}} - E(B - V)$ empirical relation from Gudennavar et al. (2012) and the average $R_v = A_v/E(B - V)$ value of $= 3.1$:

$$A_v = 3.1 \times 1.6 \times 10^{-22} \times N_{\mathrm{H\,I}} \tag{9}$$

and finally.

(iii) The extinction is converted into a DIB EW using the relation derived by Zasowski et al. (2015):

$$EW_{\mathrm{DIB}} = 0.102 \times A_v^{1.01}(\text{Å}). \tag{10}$$

Table 2
Sample Stars with 15273 Å DIB Detection

2MASS ID	GLON	GLAT	$\lambda_c \pm \mathrm{err}(\lambda)$	$\sigma \pm \mathrm{err}(\sigma)$	EW ± err(EW)	Flag	$\mathrm{EW}_{\mathrm{H\,I\,21\,cm}}$
00001687 + 5903034	116.390	−03.169	15274.0 ± 0.2	1.1 ± 0.2	041 ± 018	7	219
00001877 + 5938132	116.500	−02.595	15272.3 ± 0.1	1.4 ± 0.1	075 ± 019	7	231
00005414 + 5522241	115.740	−06.791	15271.1 ± 0.3	1.9 ± 0.3	058 ± 018	7	109
00010331 + 1549325	105.570	−45.340	15272.0 ± 0.4	0.8 ± 0.5	010 ± 021	1	017
00010512 + 5651581	116.060	−05.332	15271.9 ± 0.4	1.4 ± 0.4	027 ± 014	6	148
00011569 + 6314329	117.320	+00.919	15274.5 ± 0.1	1.5 ± 0.2	097 ± 020	7	313
00013391 + 5904490	116.550	−03.172	15272.2 ± 0.1	0.9 ± 0.1	042 ± 022	5	219
00013919 + 7005554	118.690	+07.639	15272.8 ± 0.2	1.6 ± 0.2	062 ± 011	7	187
00022269 + 6254032	117.380	+00.559	15273.5 ± 0.1	2.0 ± 0.2	128 ± 025	7	279
00023939 + 7109185	118.970	+08.659	15271.7 ± 0.3	1.7 ± 0.3	053 ± 010	7	138
00024298 + 5748303	116.460	−04.450	15272.4 ± 0.2	1.2 ± 0.2	033 ± 016	7	190
00024671 + 1605384	106.240	−45.194	15272.8 ± 0.2	0.7 ± 0.2	016 ± 012	5	017
00024931 + 5709106	116.350	−05.096	15272.7 ± 0.3	1.7 ± 0.3	049 ± 013	6	158
00024931 + 5709106	116.350	−05.096	15272.7 ± 0.2	1.3 ± 0.2	058 ± 017	7	158
00025231 + 5841372	116.650	−03.584	15272.9 ± 0.2	1.8 ± 0.2	069 ± 017	7	223
00025606 + 7014169	118.820	+07.754	15273.2 ± 0.3	1.2 ± 0.3	029 ± 013	7	164
00032397 + 7310282	119.420	+10.631	15268.4 ± 0.5	0.8 ± 0.6	008 ± 016	1	103
00042334 + 5626552	116.430	−05.828	15273.0 ± 0.2	0.8 ± 0.2	024 ± 022	4	141
00044189 + 6939114	118.860	+07.152	15274.4 ± 0.3	0.9 ± 0.3	021 ± 013	4	216
00044627 + 0132128	099.672	−59.211	15271.4 ± 0.6	0.9 ± 0.6	008 ± 009	1	013
00045177 + 5933503	117.060	−02.775	15272.5 ± 0.4	2.2 ± 0.4	066 ± 027	7	230
00045306 + 7048114	119.090	+08.280	15273.6 ± 0.8	1.4 ± 0.8	014 ± 007	6	138
00050083 + 6349330	117.840	+01.414	15271.9 ± 0.1	2.0 ± 0.1	175 ± 030	7	313
00051293 + 5811530	116.860	−04.127	15272.7 ± 0.1	1.2 ± 0.1	060 ± 013	7	223
00051873 + 5758464	116.830	−04.345	15274.0 ± 0.2	1.6 ± 0.2	070 ± 024	7	193
00052394 + 6347207	117.870	+01.370	15271.9 ± 0.1	1.7 ± 0.1	135 ± 019	7	313
00052888 + 5717190	116.730	−05.028	15272.0 ± 0.3	1.2 ± 0.3	026 ± 014	7	158
00052965 + 5722141	116.750	−04.948	15272.3 ± 0.3	1.4 ± 0.3	043 ± 024	7	158
00053673 + 7530446	120.010	+12.901	15272.2 ± 0.2	1.7 ± 0.2	082 ± 023	7	110
00054538 + 6234237	117.700	+00.167	15274.7 ± 0.1	1.4 ± 0.1	133 ± 029	7	293
00060064 + 7001540	119.040	+07.504	15271.3 ± 0.3	1.4 ± 0.3	036 ± 011	7	193
00060945 + 6412287	118.030	+01.768	15272.1 ± 0.1	1.7 ± 0.1	130 ± 023	7	335
00061415 + 0127198	100.290	−59.414	15271.8 ± 0.2	0.8 ± 0.2	023 ± 016	5	014
00063033 + 5719168	116.870	−05.021	15272.8 ± 0.2	0.8 ± 0.2	021 ± 015	5	172
00064418 + 7541165	120.110	+13.062	15271.0 ± 0.4	2.3 ± 0.4	071 ± 026	6	110
00064478 + 0025574	099.822	−60.418	15271.6 ± 0.2	0.7 ± 0.2	024 ± 017	4	019
00064971 + 5737102	116.970	−04.734	15272.7 ± 0.4	2.1 ± 0.5	048 ± 016	7	193
00065832 + 5726544	116.960	−04.906	15272.2 ± 0.4	1.8 ± 0.4	040 ± 017	7	172
00071354 + 5804306	117.100	−04.295	15272.8 ± 0.2	1.2 ± 0.2	041 ± 023	7	193
00072008 + 6241381	117.900	+00.254	15272.9 ± 0.1	1.4 ± 0.1	139 ± 033	7	296
00074256 + 6318026	118.040	+00.845	15271.3 ± 0.1	1.4 ± 0.1	120 ± 022	7	304
00074657 + 5722435	117.050	−04.993	15272.0 ± 0.2	1.4 ± 0.3	043 ± 014	7	172
00074863 + 7040220	119.310	+08.109	15271.7 ± 0.6	0.9 ± 0.6	009 ± 010	4	167
00080292 + 7332356	119.820	+10.934	15271.8 ± 0.2	0.9 ± 0.2	025 ± 022	3	099
00081304 + 6315383	118.090	+00.796	15273.9 ± 0.1	1.3 ± 0.1	085 ± 023	7	304
00085840 − 0015231	100.410	−61.257	15273.3 ± 2.5	0.9 ± 2.7	002 ± 014	1	016
00090905 + 5737124	117.270	−04.786	15271.8 ± 0.2	0.9 ± 0.2	036 ± 015	5	177
00091817 + 7022314	119.380	+07.795	15272.6 ± 0.2	1.2 ± 0.2	038 ± 011	7	167
00092728 + 7447408	120.130	+12.152	15271.4 ± 0.2	0.9 ± 0.2	038 ± 012	5	108
00094423 + 0117063	101.810	−59.865	15272.6 ± 0.4	1.7 ± 0.5	033 ± 014	7	013

Note. The central wavelength is in the stellar frame.

(This table is available in its entirety in machine-readable form.)

The depth of each individual DIB is computed from the EW and the width. The final *virtual* DIB is the product of those individual DIBs and as such it is broadened to match the velocity distribution of the H I spectrum for the entire path through the Galaxy. Figure 4 illustrates the construction of the *virtual* DIB for a typical LOS with 6 H I clouds. This *virtual* DIB is fitted to a Gaussian and the resulting width $\sigma_{\mathrm{H\,I\,21\,cm}}$ is used to impose a limit on the APOGEE absorption width. Such a limit is ensuring the compatibility between the measured DIB width and the velocity spread seen in H I. Absorptions that do not pass the test (i) as shown in Figure 2 enter test (f). The broad absorptions will be discarded as discussed above and the narrow lines are reconsidered and classified as shown in Figure 2.

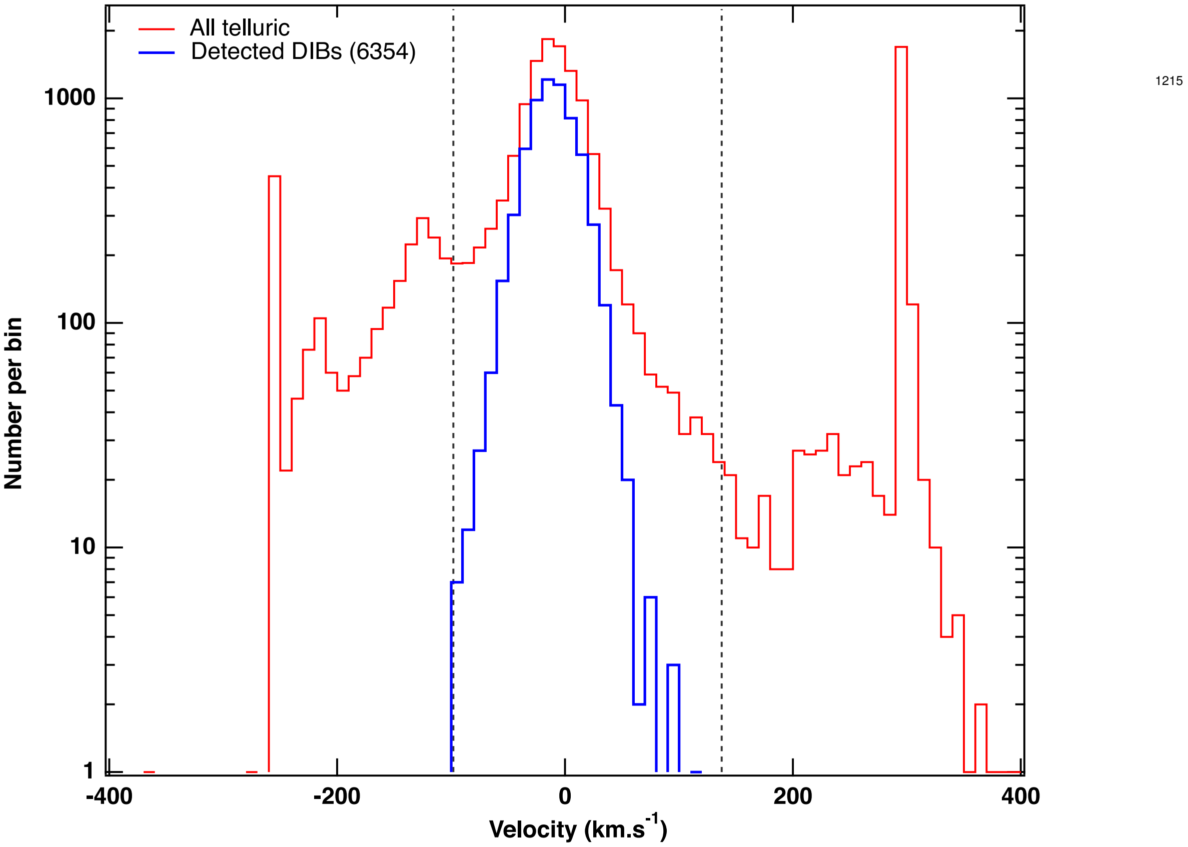

Figure 5. Histogram of the Doppler velocities for all fitted lines (red) and for selected DIBs only (blue). The limiting values used in the first selection step are shown as black vertical lines. Note the exclusion of all unrealistic Doppler velocities falling in the first and last bins and the disappearance of the secondary maximum at $\simeq$130 km s^{-1} that corresponds to false detections produced by a strong stellar line falling at this wavelength.

4.2. Special Cases

We applied target selection criteria and considered separately Be Stars and stars from the field 4529 because they can yield difficulties in fitting. To do so we used the Chojnowski et al. (2015) catalog of Be stars and the information contained in the APOGEE tables. All these spectra have been the subject of one by one visual inspection and only those where the DIB was clearly unambiguously and accurately detected were kept. Figure 14 contains an example of a Be star spectrum and a spectrum from a star in plate 4259.

The different possible outcomes after the selection criteria described in Sections 4.1 and 4.2 have been flagged from 1 to 7. Figure 14 presents one representative example for each category.

5. THE CATALOG

Statistical properties of the whole catalog of all detected DIBs are shown in Table 1. We present a fraction of this catalog in Table 2. For the total of 6716 detections or upper limits the catalog lists the 2MASS identification, then the EW, central wavelength in the stellar frame and DIB Gaussian width and associated errors. The flag allowing to identify the selection criteria for each target is also added. Finally, we included for completeness the estimated EW for the *virtual DIB* as calculated from the emission in the H I 21 cm line. The various categories (1) Upper limit (2) Stars from plate 4529 (3) Be Stars (4) Narrow recovered DIBs (5) Narrow DIBs (6) Recovered (7) Detected comprise 362, 11, 52, 122, 473, 572 and 5124 TSS targets respectively. Figure 10 shows the location of all TSSs on a sky coordinates plot, distinguishing those that are included in the catalog. It can be seen that at Galactic latitudes smaller than $\simeq$15° all APOGEE fields contain TSSs with detected DIBs, while at higher latitude some fields have no targets included in this catalog, due to the weakness of the IS column.

The comparison between the velocity distributions of the original sample and the one included in this catalog is presented in Figure 5. Both of them peak at ~ -20 km s^{-1}. However, while the final distribution resembles to a Gaussian distribution, the original one is quite irregular, with several secondary peaks. In particular those at ~ -260 and -130 km s^{-1} correspond to very strong stellar absorption features that have been successfully eliminated. Note that the final sample presents a relatively small (i.e., $\lesssim$30) number of detections with high velocities (i.e., $\sim$100 km s^{-1}). After visual inspection of the corresponding spectra, we did not see any evidence for a spurious detection. Therefore we kept those detections in the catalog. They will be the subject of further work. We cannot exclude a similar high velocity tail in the blue due to the threshold imposed to remove spurious identifications due to stellar lines.

Figure 6 displays the distribution of the DIB widths. Only a very small fraction of selected DIBs have sigma above 3 Å. In the same way, Figure 7 shows that there are very few DIBs

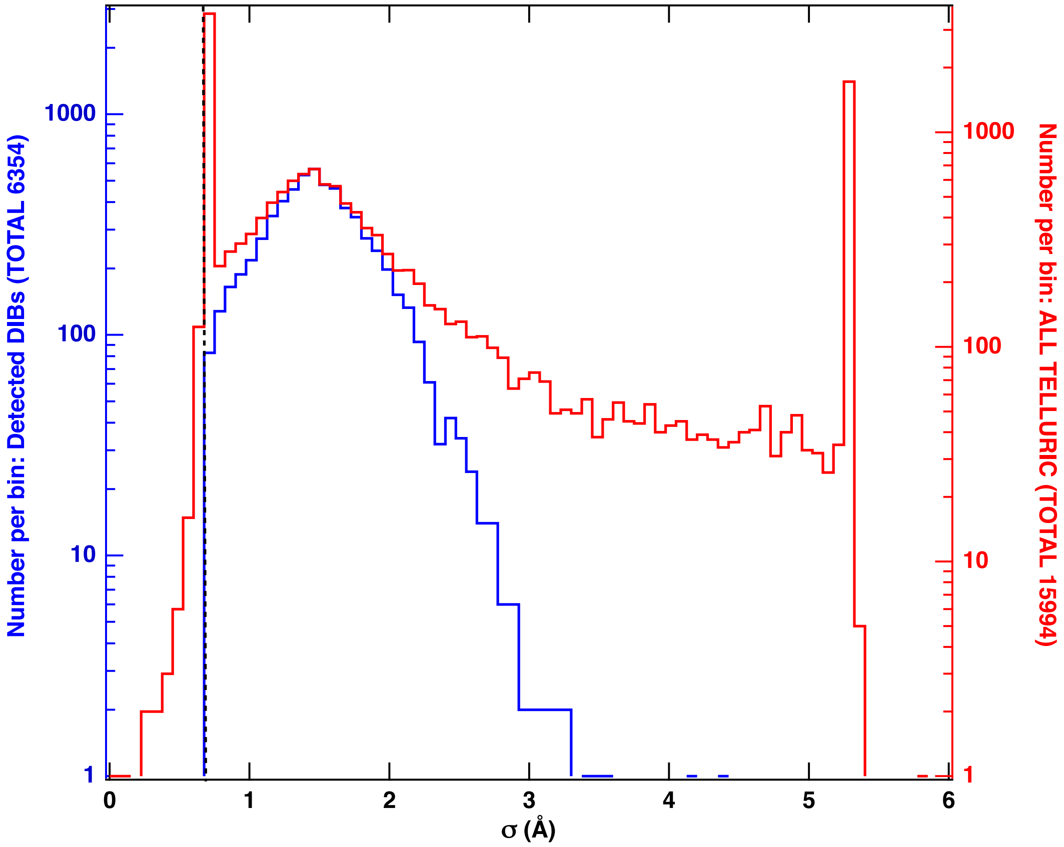

Figure 6. Same as Figure 5, but for the DIB width σ. The limiting value 0.7 Å used in the selection step is shown as a black vertical line.

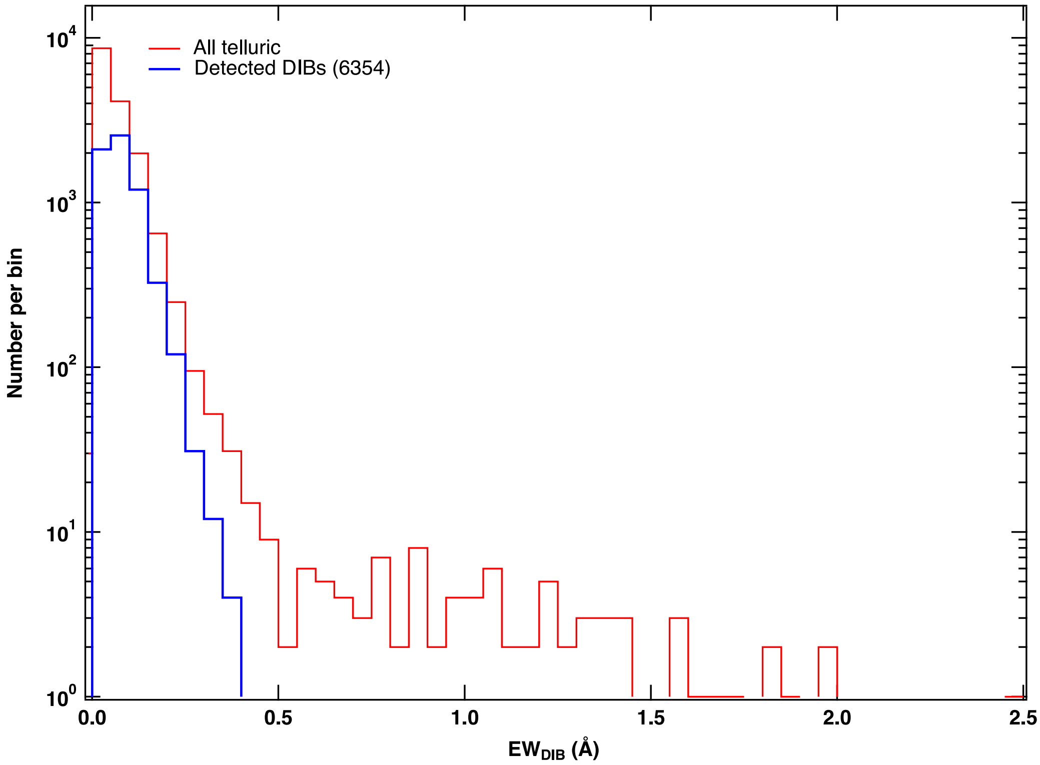

Figure 7. Same as Figure 5, but for the DIB equivalent width.

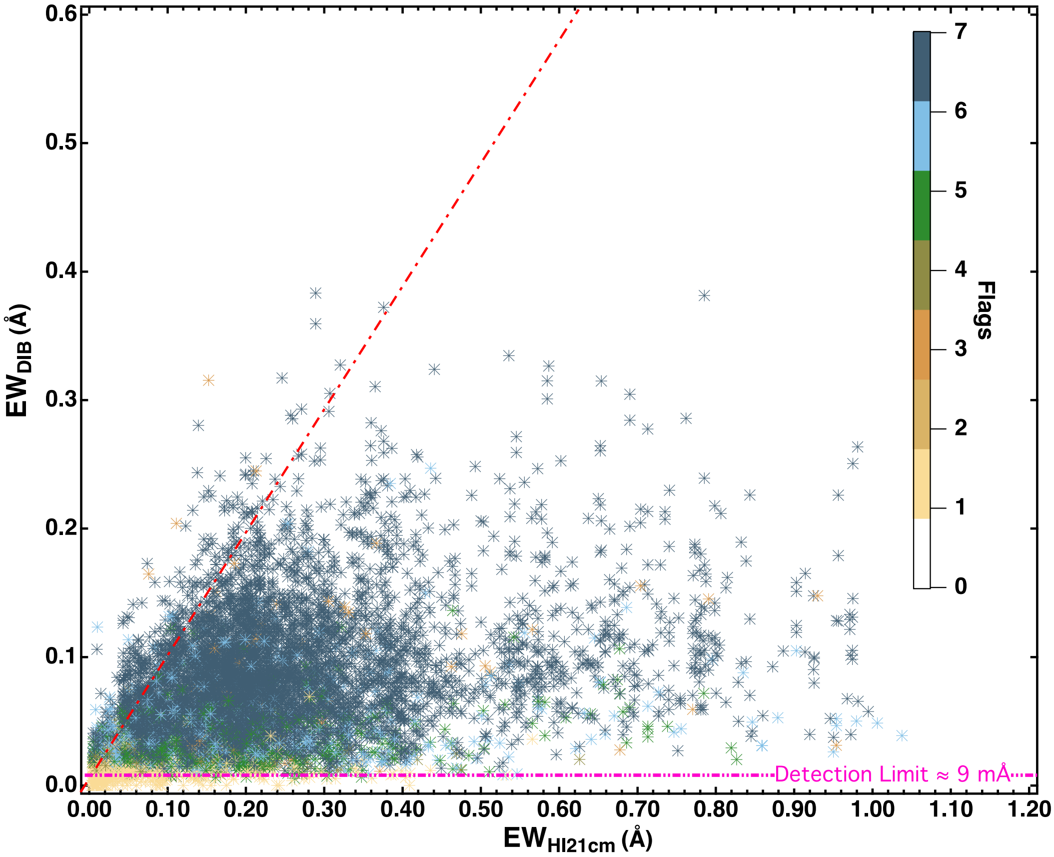

Figure 8. DIB equivalent width as a function of the *virtual* DIB equivalent width that is proportional to the total H I column. The dotted red line is the one-to-one relation (see the text). The color code is the same as in Figure 2 with 2 additional colors indicating the special cases of Be stars (orange) and stars from field 4529 (camel) from Section 4.2. A clear detection limit is found at around 9 mÅ indicated by a pink dashed line.

(∼167) with EW > 200 mÅ. This is not unexpected since TSS are relatively nearby stars, much closer than the APOGEE targets full sample. Finally, we show in Figure 8 a comparison between the APOGEE measured EWs and the EWs of the *virtual* DIBs described in Section 4 that are proportional to the total hydrogen column from the LAB Survey (Kalberla et al. 2005), converted into an EW according to Equation (4). The figure shows that, within the error bars, there is an envelope to all the data points that corresponds roughly to a one-to-one relation. This supports the robustness of our method and the choice of the conversion factor. Data points close to the envelope very likely correspond to target stars located beyond all the H I clouds seen in emission, while points well below the envelope correspond to targets that are in front of at least one cloud. Locations of the TSS targets and corresponding DIB strengths are displayed in Figure 10.

6. POTENTIAL APPLICATIONS

In the following, we illustrate the potential of this catalog by means of two examples: as a proxy for the extinction and as tool for ISM tomography.

The 15273 Å DIB is correlated with the extinction over at least three orders of magnitudes (Zasowski et al. 2015). Thus, it can be used as an independent approach to estimate it or as an initial guess in absence of better information. We crossmatched the present TSS catalog with the compilation of reddening measurements provided by Lallement et al. (2014) used to build local 3D maps of the ISM. Figure 11 shows the comparison between the APOGEE 1.5273 μm DIB EW and the reddening for the 221 stars in common. There is a clear positive correlation showing that the fitted absorptions contain valuable information on the intervening ISM. The figure also presents the linear fit derived by Zasowski et al. (2015) for the APOGEE cool stars. Our data points cluster around this relationship in solid agreement with the results obtained for the late-type stars. We note however that the number of *outliers* with very weak DIBs is significantly higher than the number of *outliers* with strong DIBs. A possible explanation to this trend could be that UV radiation field of the early-type stars acts on the intervening matter. This influence of the star temperature has already been noticed in the past (Vos et al. 2011; Raimond et al. 2012).

Likewise, the catalog can be crossmatched with spectra available for the targets. Being relatively bright many of them have been the subject of specific investigations, allowing comparisons with other DIBs and atomic or molecular lines. We have found at least 100 targets that have been observed at very high resolution and are available from public archives.

Finally, as mentioned in the introduction, our main interest in this (or similar) catalogs is the potential for use in ISM tomography. Compared with the extended catalog of Zasowski et al. (2015) that allows mapping the Galactic scales, the TSSs are more appropriate for the nearby ISM. As a proof-of-concept we explored this use in the Taurus-Perseus region. This is illustrated in Figure 12 that shows the dust optical thickness measured by Planck in this area (Planck Collaboration

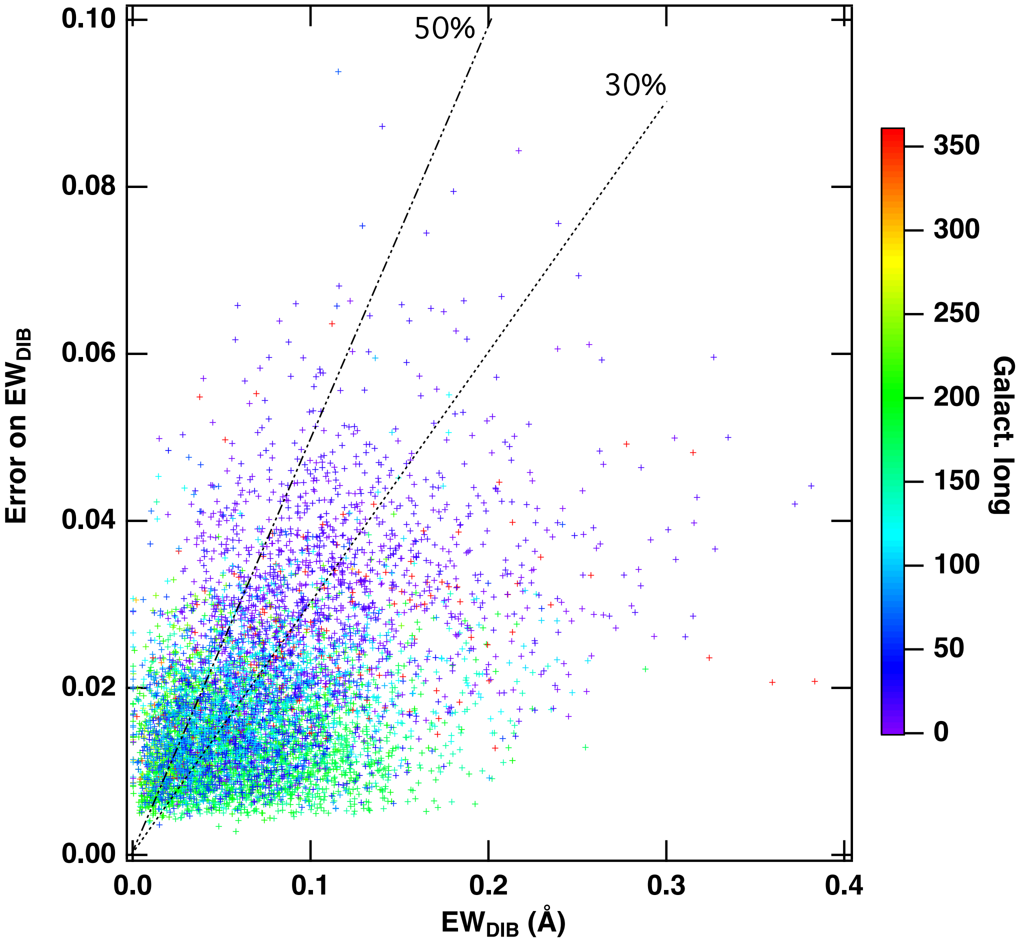

Figure 9. Estimated error on the DIB equivalent width EW for all the targets of the catalog. Above (resp. below) dashed lines relative errors are larger (resp. smaller) than 30% and 50%. The color scale refers to the Galactic longitude of the target star. Due to our method, relative errors are overestimated for targets at lower longitudes (violet, dark blue signs, see the text).

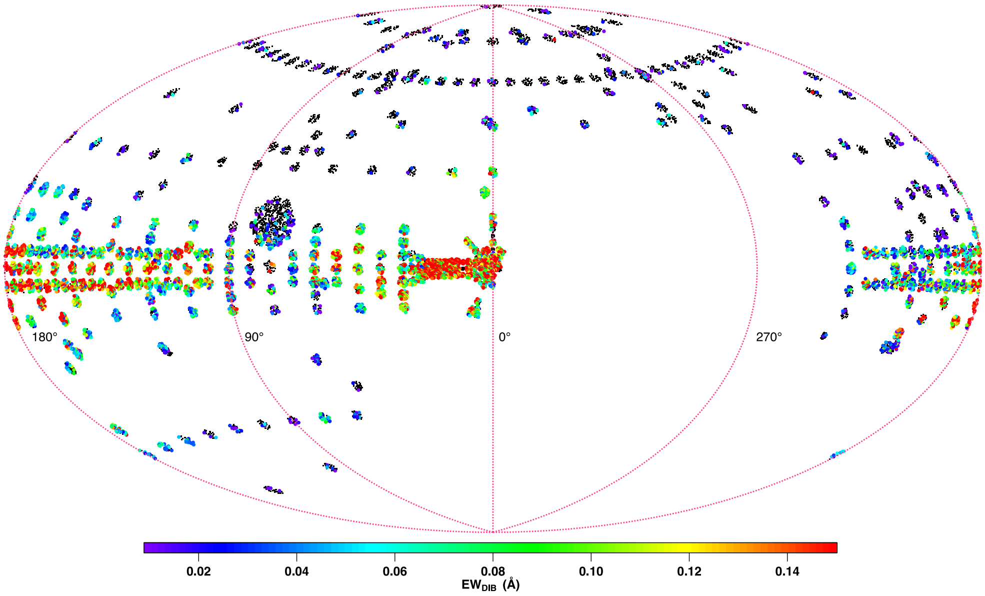

Figure 10. Location of all TSS targets on a sky coordinates plot, distinguishing those that are included in the catalog (colored circles, color representative of the EW) from those not included (black circles).

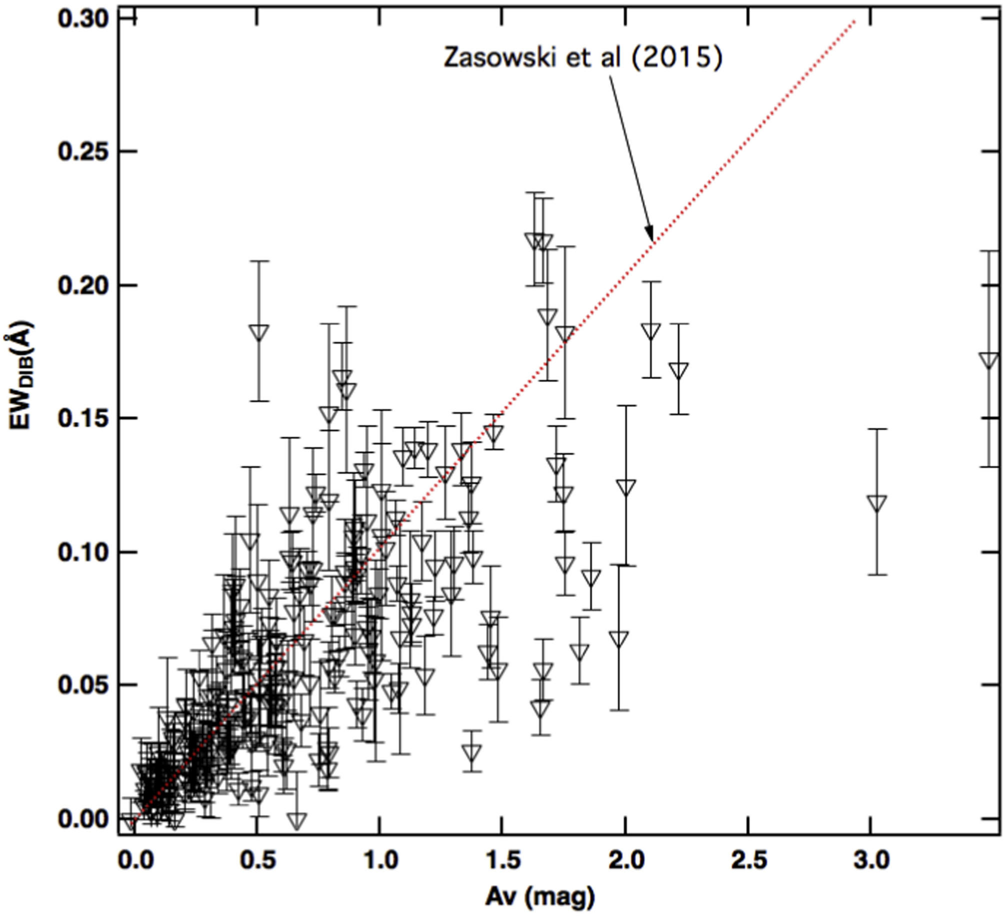

Figure 11. DIB equivalent width as a function of the color excess for the subset of 221 targets described in Section 5. The linear relationship (red curve) is the one fitted to the whole set of APOGEE late-type stars by Zasowski et al. (2015).

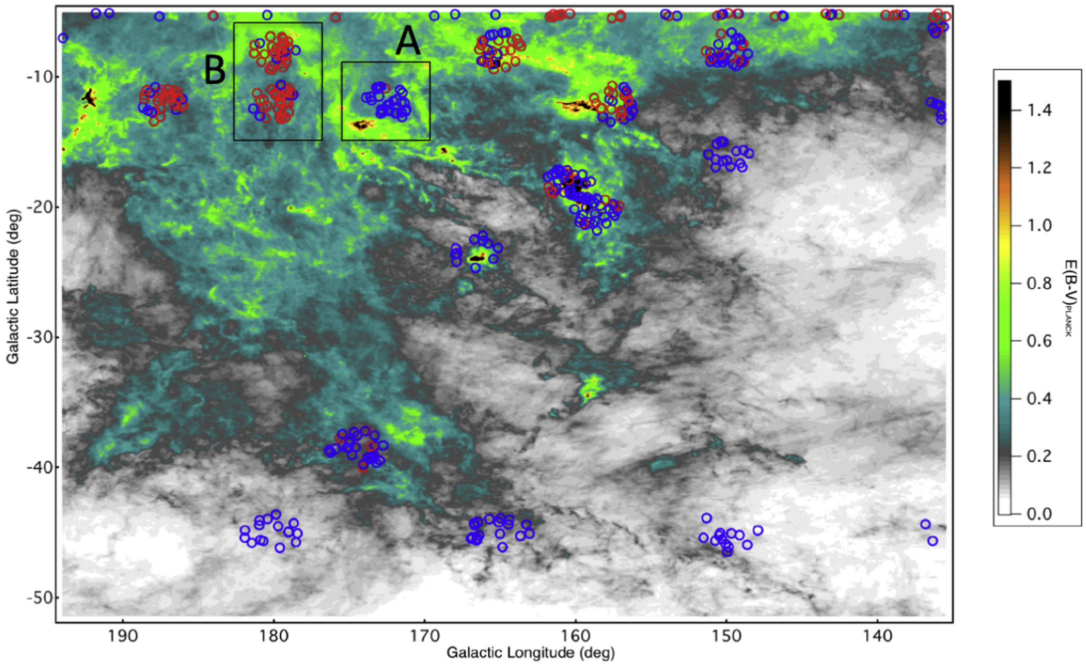

Figure 12. Planck dust optical depth in the Taurus-Perseus region with superimposed APOGEE TSS targets selected for the catalog. Blue (resp. red) markers correspond to a DIB equivalent width lower (resp. higher) than a threshold of 50 mÅ. In regions devoid of dust (white or pale gray) DIBS are uniformly below the threshold. Toward dense clouds there is a mixed composition that reflects the location of the target (see Figure 13).

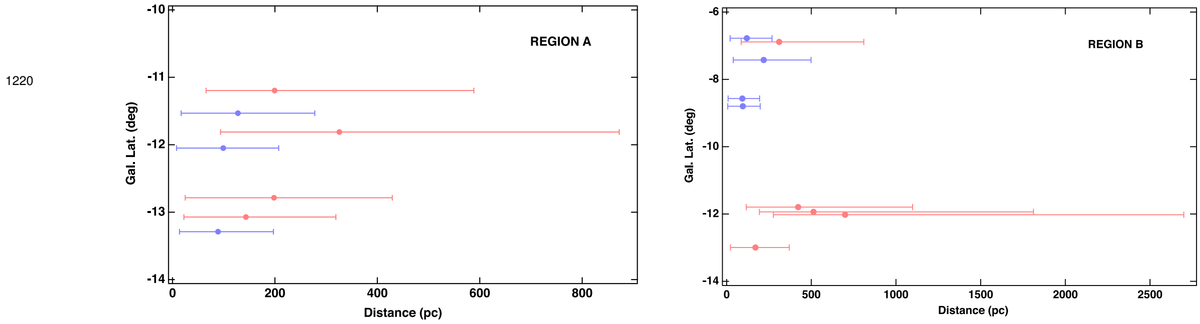

Figure 13. Example of future 3D mapping based on DIBs: DIB strengths and target *Hipparcos* distances for the two regions A and B from Figure 12. Blue (resp. red) markers correspond to a DIB equivalent width lower (resp. higher) than a threshold of 50 mÅ. The closest (resp. most distant) targets show consistently negligible (resp. strong) absorption. Accurate and more numerous parallaxes should allow to bracket the distance to the clouds.

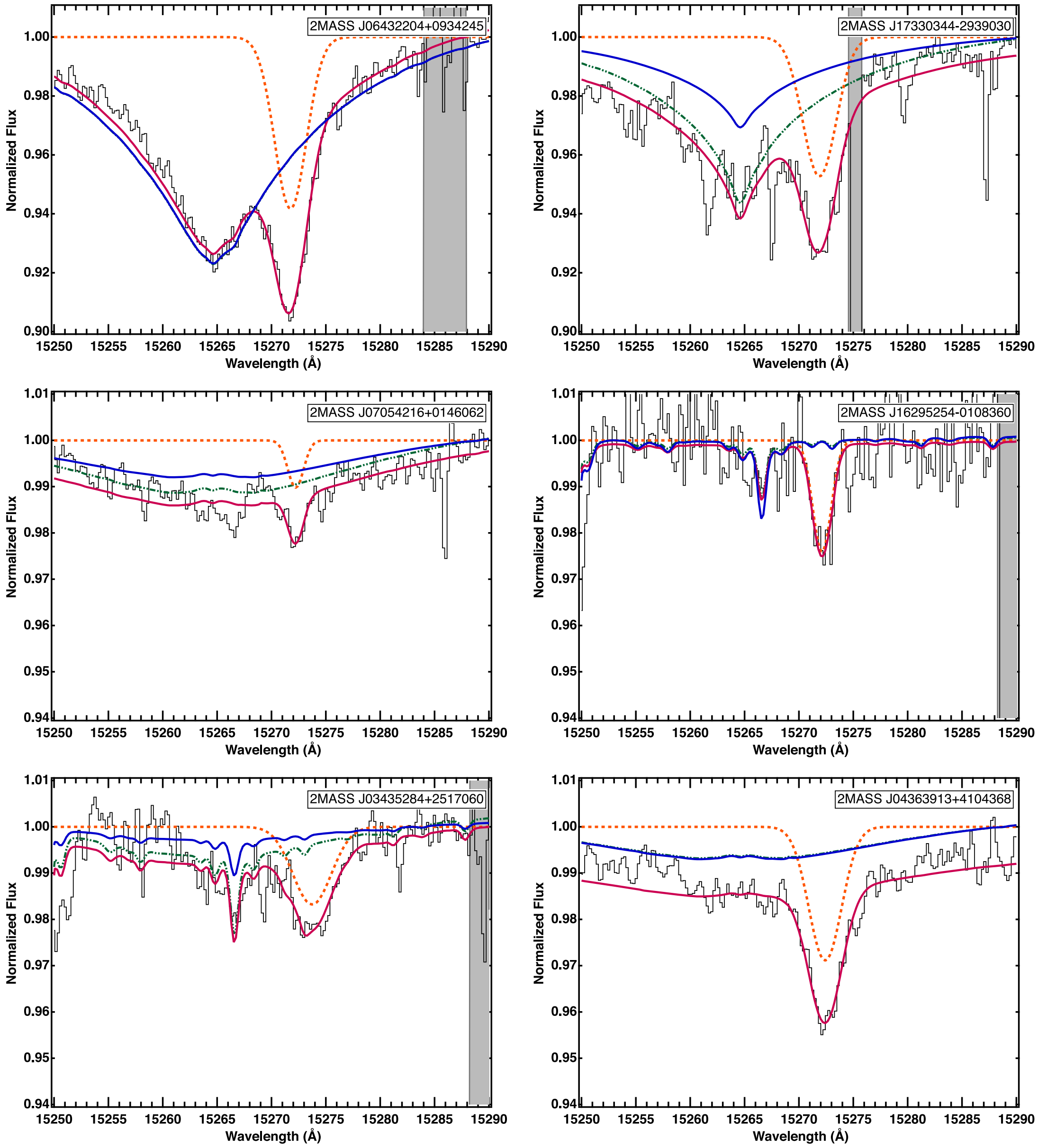

Figure 14. Illustration of the various categories of selected absorptions: (top left) Detected-flag7; (top right) Recovered-flag6; (center left) Narrow-flag5; (center right) Recovered Narrow DIBs-flag4; (bottom left) Stars from plate 4529-flag3; (bottom right) Be Stars-flag2. Color and symbol code is as in Figure 1.

et al. 2014). Superimposed on the map are the TSS targets color-coded according to the detection (or non-detection) of a DIB with an EW higher than 50 mÅ. The strength of the DIB is always small in regions with negligible or small dust emission while the contrary is seen toward opaque clouds. We selected two regions, marked as A and B in Figure 12, to explore the use of this catalog to locate the molecular clouds along the line of sight. For that, we used the subset of targets in these areas with *Hipparcos* parallax (Perryman et al. 1997; van Leeuwen 2007). Figure 13 shows a comparison between the detection (or absence) of a DIB toward a given target and the distance to it. For both cases there is a clear cut-off in distance between this two categories. This allows to bracket the distance to the main absorbing cloud: targets without detection are in front of the clouds while those with detection are well beyond. For our particular cases the main clouds are at about 150 pc, in agreement with the detailed tomography of Schlafly et al. (2014). This illustrates the potential of this catalog to build detailed 3D maps of the ISM once the more accurate and numerous parallaxes provided by *Gaia* will become available.

7. SUMMARY AND PERSPECTIVES

We have analyzed the series of SDSS/APOGEE NIR spectra of the calibration stars used to decontaminate data from telluric absorption lines. Those targets are generally blue stars and the APOGEE Stellar Parameters and Chemical Abundances Pipeline (ASPCAP, García Pérez et al. 2016) stellar models cannot be used straight away. We have used them as a starting point and allowed the model broad stellar features to vary in depth to reproduce the observed continuum. In the region of the 1.5273 μm DIB this adjustment has proven to be good enough to allow the extraction of the DIB EW and central radial velocity through Gaussian fitting of the DIB absorption. Careful and severe examinations of the DIB parameters, the continuum shape and the quality of the adjustment were done. This result in a conservative selection of reliable DIB parameters. In particular all DIB candidates that contradict radial velocity limiting values based on the H I 21 cm spectra have been excluded. A total of 6716 lines of sight are selected and the results are presented in a catalog that will be available from CDS, Strasbourg. The statistical properties of the resulting DIB database show that our selection criteria are fully appropriate.

Since most of the calibration stars are nearby objects (say, within the first kpc), such a DIB catalog can be used to improve 3D maps of the nearby ISM and to complement maps at larger scale. We have compared our DIB detections in the Taurus-Perseus region with the distribution of dust as traced by Planck, finding a good agreement between the strength/existence of the DIBs and the location of the clouds in the plane of the sky. Likewise, we showed how used jointly with existing parallax (i.e., distances) of the stars they can be used to assign a distance to the clouds. A step forward would be the application to the DIBs of inversion methods to recover the 3D structure, as already attempted based on optical absorption lines and extinction (e.g., Vergely et al. 2010; Lallement et al. 2014; Sale & Magorrian 2014). A strong advantage of NIR DIBs is the potential use of highly reddened target stars and the exploration of dense IS clouds. Moreover, nowadays instrumentation is becoming more and more NIR–IR oriented and large datasets in this spectral range are foreseen. 3D maps of the Galactic ISM are tools of wide use and their quality is expected to increase considerably in future once the *Gaia* distances will be available. Independently, DIB-based maps can be compared with dust and gas 3D distributions, providing new diagnostics of the conditions of their formation, ionization and destruction. They can also help interpreting small-structure of ISM clouds and of UV radiation impact on DIBs revealed by high spatial or temporal resolution spectroscopic data (Cordiner et al. 2013; Smith et al. 2013).

R.L., A.M.-I. and Q.R. acknowledge support from Agence Nationale de la Recherche through the STILISM project (ANR-12-BS05-0016-02). M.E.Y. acknowledges funding from the Region Ile-de-France through the DIM-ACAV project.

Funding for the Sloan Digital Sky Survey IV has been provided by the Alfred P. Sloan Foundation, the U.S. Department of Energy Office of Science, and the Participating Institutions. SDSS-IV acknowledges support and resources from the Center for High-Performance Computing at the University of Utah. The SDSS web site is www.sdss.org.

SDSS-IV is managed by the Astrophysical Research Consortium for the Participating Institutions of the SDSS Collaboration including the Brazilian Participation Group, the Carnegie Institution for Science, Carnegie Mellon University, the Chilean Participation Group, the French Participation Group, Harvard-Smithsonian Center for Astrophysics, Instituto de Astrofísica de Canarias, The Johns Hopkins University, Kavli Institute for the Physics and Mathematics of the universe (IPMU)/University of Tokyo, Lawrence Berkeley National Laboratory, Leibniz Institut für Astrophysik Potsdam (AIP), Max-Planck-Institut für Astronomie (MPIA Heidelberg), Max-Planck-Institut für Astrophysik (MPA Garching), Max-Planck-Institut für Extraterrestrische Physik (MPE), National Astronomical Observatory of China, New Mexico State University, New York University, University of Notre Dame, Observatário Nacional/MCTI, The Ohio State University, Pennsylvania State University, Shanghai Astronomical Observatory, United Kingdom Participation Group, Universidad Nacional Autónoma de México, University of Arizona, University of Colorado Boulder, University of Oxford, University of Portsmouth, University of Utah, University of Virginia, University of Washington, University of Wisconsin, Vanderbilt University, and Yale University.

APPENDIX
VARIOUS CATEGORIES OF SELECTED ABSORPTIONS

The various types of detections or upper limits resulting from the criteria shown in Figure 2 are illustrated in Figure 14. We assigned a flag in the catalog to each of the different categories.

REFERENCES

Ahn, C. P., Alexandroff, R., Allende Prieto, C., et al. 2014, ApJS, 211, 17
Aihara, H., Allende Prieto, C., An, D., et al. 2011, ApJS, 193, 29
Alam, S., Albareti, F. D., Allende Prieto, C., et al. 2015, ApJS, 219, 12
Baron, D., Poznanski, D., Watson, D., Yao, Y., & Prochaska, J. X. 2015, MNRAS, 447, 545
Berné, O., Mulas, G., & Joblin, C. 2013, A&A, 550, L4
Cami, J., Bernard-Salas, J., Peeters, E., & Malek, S. E. 2010, Sci, 329, 1180
Campbell, E. K., Holz, M., Gerlich, D., & Maier, J. P. 2015, Natur, 523, 322
Chojnowski, S. D., Whelan, D. G., Wisniewski, J. P., et al. 2015, AJ, 149, 7
Cordiner, M. A., Cox, N. L. J., Evans, C. J., et al. 2011, ApJ, 726, 39
Cordiner, M. A., Cox, N. L. J., Trundle, C., et al. 2008a, A&A, 480, L13
Cordiner, M. A., Fossey, S. J., Smith, A. M., & Sarre, P. J. 2013, ApJL, 764, L10
Cordiner, M. A., Smith, K. T., Cox, N. L. J., et al. 2008b, A&A, 492, L5

Cox, N. L. J. 2011, in EAS Publications Ser. 46, PAHs and the Universe: A Symposium to Celebrate the 25th Anniversary of the PAH Hypothesis, ed. C. Joblin, & A. G. G. M. Tielens (Les Ulis: EDP Sciences), 349
Cox, N. L. J., Cami, J., Kaper, L., et al. 2014, A&A, 569, A117
Cox, N. L. J., & Patat, F. 2008, A&A, 485, L9
Cox, N. L. J., & Spaans, M. 2006, A&A, 451, 973
Crawford, M. K., Tielens, A. G. G. M., & Allamandola, L. J. 1985, ApJL, 293, L45
Ehrenfreund, P., Cami, J., Jiménez-Vicente, J., et al. 2002, ApJL, 576, L117
Eisenstein, D. J., Weinberg, D. H., Agol, E., et al. 2011, AJ, 142, 72
Foing, B. H., & Ehrenfreund, P. 1994, Natur, 369, 296
Friedman, S. D., York, D. G., McCall, B. J., et al. 2011, ApJ, 727, 33
García Pérez, A. E., Allende Prieto, C., Holtzman, J. A., et al. 2016, AJ, 151, 144
Geballe, T. R., Najarro, F., Figer, D. F., Schlegelmilch, B. W., & de La Fuente, D. 2011, Natur, 479, 200
Gudennavar, S. B., Bubbly, S. G., Preethi, K., & Murthy, J. 2012, ApJS, 199, 8
Gunn, J. E., Siegmund, W. A., Mannery, E. J., et al. 2006, AJ, 131, 2332
Hamano, S., Kobayashi, N., Kondo, S., et al. 2015, ApJ, 800, 137
Hamano, S., Kobayashi, N., Kondo, S., et al. 2016, ApJ, 821, 42
Heckman, T. M., & Lehnert, M. D. 2000, ApJ, 537, 690
Heger, M. L. 1922, LicOB, 10, 141
Herbig, G. H. 1993, ApJ, 407, 142
Herbig, G. H. 1995, ARA&A, 33, 19
Hobbs, L. M., York, D. G., Thorburn, J. A., et al. 2009, ApJ, 705, 32
Holtzman, J. A., Shetrone, M., Johnson, J. A., et al. 2015, AJ, 150, 148
Iglesias-Groth, S. 2007, ApJL, 661, L167
Jenniskens, P., & Desert, F.-X. 1994, A&AS, 106, 39
Joblin, C., D'Hendecourt, L., Leger, A., & Maillard, J. P. 1990, Natur, 346, 729
Kalberla, P. M. W., Burton, W. B., Hartmann, D., et al. 2005, A&A, 440, 775
Kokkin, D. L., Troy, T. P., Nakajima, M., et al. 2008, ApJL, 681, L49
Kos, J., Zwitter, T., Wyse, R., et al. 2014, Sci, 345, 791
Lallement, R., Vergely, J.-L., Valette, B., et al. 2014, A&A, 561, A91
Lan, T.-W., Ménard, B., & Zhu, G. 2015, MNRAS, 452, 3629
Leger, A., & D'Hendecourt, L. 1985, A&A, 146, 81
Maier, J. P., Walker, G. A. H., & Bohlender, D. A. 2004, ApJ, 602, 286
Majewski, S. R. 2012, BAAS, 219, 205.06
McCall, B. J., & Griffin, R. E. 2013, RSPSA, 469, 20120604
Merrill, P. W. 1934, PASP, 46, 206
Merrill, P. W. 1936, ApJ, 83, 126
Mészáros, S., Allende Prieto, C., Edvardsson, B., et al. 2012, AJ, 144, 120
Monreal-Ibero, A., Weilbacher, P. M., Wendt, M., et al. 2015, A&A, 576, L3
Nidever, D. L., Holtzman, J. A., Allende Prieto, C., et al. 2015, AJ, 150, 173
Perryman, M. A. C., Lindegren, L., Kovalevsky, J., et al. 1997, A&A, 323, L49
Phillips, M. M., Simon, J. D., Morrell, N., et al. 2013, ApJ, 779, 38
Planck, Fermi Collaborations, Ade, P. A. R., et al. 2015, A&A, 582, A31
Planck Collaboration, Abergel, A., Ade, P. A. R., et al. 2014, A&A, 571, A11
Puspitarini, L., Lallement, R., Babusiaux, C., et al. 2015, A&A, 573, A35
Puspitarini, L., Lallement, R., & Chen, H.-C. 2013, A&A, 555, A25
Raimond, S., Lallement, R., Vergely, J. L., Babusiaux, C., & Eyer, L. 2012, A&A, 544, A136
Salama, F., Bakes, E. L. O., Allamandola, L. J., & Tielens, A. G. G. M. 1996, ApJ, 458, 621
Sale, S. E., & Magorrian, J. 2014, MNRAS, 445, 256
Sarre, P. J. 2006, JMoSp, 238, 1
Sassara, A., Zerza, G., Chergui, M., & Leach, S. 2001, ApJS, 135, 263
Schlafly, E. F., Green, G., Finkbeiner, D. P., et al. 2014, ApJ, 786, 29
Skrutskie, M. F., Cutri, R. M., Stiening, R., et al. 2006, AJ, 131, 1163
Smith, K. T., Fossey, S. J., Cordiner, M. A., et al. 2013, MNRAS, 429, 939
Sollerman, J., Cox, N., Mattila, S., et al. 2005, A&A, 429, 559
van der Zwet, G. P., & Allamandola, L. J. 1985, A&A, 146, 76
van Leeuwen, F. 2007, A&A, 474, 653
van Loon, J. T., Bailey, M., Tatton, B. L., et al. 2013, A&A, 550, A108
Vergely, J.-L., Valette, B., Lallement, R., & Raimond, S. 2010, A&A, 518, A31
Vos, D. A. I., Cox, N. L. J., Kaper, L., Spaans, M., & Ehrenfreund, P. 2011, A&A, 533, A129
Welty, D. E., Federman, S. R., Gredel, R., Thorburn, J. A., & Lambert, D. L. 2006, ApJS, 165, 138
Wilson, J. C., Hearty, F., Skrutskie, M. F., et al. 2010, Proc. SPIE, 7735, 77351C
Yuan, H.-B., Liu, X.-W., Xiang, M.-S., et al. 2014, in Proc. IAU Symp. 298, Setting the scene for Gaia and LAMOST, ed. S. Feltzing et al. (Cambridge: Cambridge Univ. Press), 240
Zasowski, G., Johnson, J. A., Frinchaboy, P. M., et al. 2013, AJ, 146, 81
Zasowski, G., Ménard, B., Bizyaev, D., et al. 2015, ApJ, 798, 35